Magnetization dynamics in chiral thin films probed by x-ray resonant magnetic resonant scattering

Cyril Léveillé

université PARIS-SACLAY

Magnetization dynamics in chiral thin films probed by x-ray resonant magnetic scattering

Dynamique de la chiralité dans des multicouches observées par diffusion magnétique résonante des rayons X

Thèse de doctorat de l'université Paris-Saclay

École doctorale n° 564, physique en Île-de-France (PIF)
Spécialité de doctorat : Physique
Graduate School : Physique. Référent : Faculté des sciences d'Orsay

Thèse préparée dans les unités de recherche :
Synchrotron Soleil (Université Paris-Saclay),
Unité mixte de physique CNRS/Thales (Université Paris-Saclay, CNRS),
sous la direction de **Nicolas Jaouen**, Responsable ligne de lumière,
la co-direction de **Nicolas Reyren**, chargé de recherche

Thèse soutenue à Paris-Saclay, le 18 novembre 2022, par

Cyril LEVEILLE

Composition du Jury

Alexandra MOUGIN Directrice de recherche, LPS	Présidente
Thorsten HESJEDAL Professeur, Oxford university	Rapporteur & Examinateur
Christoforos MOUTAFIS Professeur associé, Manchester	Rapporteur & Examinateur
Christine BOEGLIN Directrice de recherche, ICPMS CNRS	Examinatrice
Mathias KLÄUI Professeur, JGU Mayence	Examinateur
Grégory MALINOWSKI Chargé de recherche, IJL CNRS	Examinateur
Nicolas JAOUEN Docteur, Synchrotron SOLEIL	Directeur de thèse

THESE DE DOCTORAT
NNT : 2022UPASP124

université PARIS-SACLAY

ÉCOLE DOCTORALE
Physique en Île-de-France (PIF)

Titre : Dynamique de la chiralité dans des multicouches observée par diffusion magnétique résonante des rayons X.

Mots clés : Chiralité, magnétisme, dynamique ultra-rapide, diffusion magnétique des rayons X, multicouches

Résumé : Les notions de chiralité et de topologie des textures magnétiques ont récemment émergé en nanomagnétisme dans le cadre de l'étude des parois de domaines chirales ou des skyrmions dans une perspective de nouvelles technologies de stockage de l'information. Au-delà de la course vers la reduction de la taille des bits magnétiques, l'accélération de la dynamique de l'aimantation est un autre défi à surmonter pour de futurs application de l'éctronique de spin, la spintronique.

Dans ce travail de doctorat, l'étude de différents systèmes allant des échantillons antiferromagnétiques synthétiques (SAF) aux skyrmions et parois de domaine chiraux dans des multicouches ferromagnétiques (FM) a été réalisée par diffraction résonante magnétique des rayons X (XRMS).

Dans un premier temps, les résultats expérimentaux non dépendants du temps réalisés sur des échantillons FM par XRMS sont descrits. Cette partie est suivie par la démonstration que la XRMS est possible sur des échantillons SAFs. Les SAFs sont constitués de couches FM couplées antiferromagnétiquement et bien qu'ils permettent d'atteindre des vitesses de déplacement de texture magnétiques supérieures au FM, leur caractérisation avec des techniques conventionnelles est difficile due à l'aimantation totale nulle dans la multicouche.

Ce travail doctorale montre que la XRMS est une des rares techniques très sensible pour sonder la chiralité dans ces systèmes.

Dans un deuxième temps, l'étude résolue en temps sur des échantillons FM ayant des parois de domaines chirales, est effectuée en mode pompe et sonde au laser à électrons libres de FERMI. Nous avons trouvé que les parois de domaines se désaimantent plus et se réaimantent plus vite que les domaines. Un modèle fondé sur l'action d'un couple induit par les électrons chauds polarisés en spin et venant des domaines vers les parois a été proposé pour expliquer cette évolution temporelle.

Finalement, une étude préliminaire résolue en temps sur des échantillons FM présentant un réseau de skyrmion sous champ magnétique a été réalisée. Nous n'avons trouvé aucune différence significative entre l'état domaine et l'état skyrmionique dans les dix première picosecondes. Cependant, après trente picosecondes, un changement significatif de comportement est observé en champ. La compréhension de ce nouveau résultat est discutée mais n'est pas complète, et mérite des études complémentaires.

Title : Magnetization dynamics in chiral thin films probed by x-ray resonant magnetic resonant scattering.

Keywords : Chirality, magnetism, ultra-fast dynamics, x-ray resonant magnetic scattering, multilayers

Abstract : Chirality and topology have recently emerged in nanomagnetism, both for studying new magnetic textures with alluring properties such as chiral domain walls (DW) or magnetic skyrmions, and for looking at new routes towards future disruptive spintronic devices. Besides the race towards ultimate size magnetic bits, revealing how the magnetization can be altered at the ultimate timescale is another key question to address the actual challenges of future data storage, spin logic or even neuromorphic spintronic technologies.

In this PhD work, the study of different system ranging from Synthetic Antiferromagnets (SAF) and chiral skyrmions or DW in ferromagnetic multilayers (FM) has been performed by X-ray Resonant Magnetic Scattering (XRMS).

First, static experiment have been performed and the XRMS techniques description on FM is followed by the demonstration that this approach can also be used on SAF samples that allows higher displacement velocities of magnetic textures than FM. SAFs are made of FM layers coupled antiferromagnetically to each other and are difficult to study with conventional techniques due to the zero net magnetization in the multilayer, this PhD demonstrates that XRMS is one of the few very sensitive technique to probe the chirality in such system.

Secondly, time-resolved study on FM with chiral DWs is performed in pump and probe mode at FERMI free electron laser. We found that the DWs demagnetizes more and recovers faster than the domains. A hot electron induced torque model has been proposed to explain this time evolution.

Finally, preliminary time-resolved experiments on a skyrmions lattice state in FM has been also performed. We found no significant difference between DW and skyrmions in the ultra-fast timescale (<10 ps). However, at longer timescale (>30 ps), a significant change of behaviour with field is observed. The understanding of this new result is being discussed but is still not yet complete and deserves future study.

Notation table

3TM	Three temperature model
AFM	Antiferromagnet(ic).
AGFM	Alternating gradient force magnetometer
CCW	Counterclockwise.
CGR	Compound growth rate
CW	Clockwise.
DMI	Dzyaloshinskii-Moriya interaction
DW	Domain wall
HDD	Hard disk drives
HM	Heavy metal
FCC	Face-centered cubic
FEL	Free electron laser
FM	Ferromagnet(ic)
GMR	Giant magnetoresistance
IEC	Interlayer exchange coupling
IP	In-plane
KB	Kirkpatrick-Baez
MFM	Magnetic force microscopy
MOKE	Magneto-optical Kerr effect
OOP	Out-of-plane
PMA	Perpendicular magnetic anisotropy
RKKY	Ruderman-Kittel-Kasuya-Yoshida
SAF	Synthetic antiferromagnet
SOT	Spin orbit torque
STT	Spin transfer torque
TMR	Tunnel magnetoresistance
VNA-FMR	Vector network analyzer ferromagnetic resonance
XMCD	X-ray magnetic circular dichroism
XRMS	X-ray resonant magnetic scattering
XRR	X-ray (resonant) reflectivity

List of symbols

A	Heisenberg exchange interaction stiffness	J m^{-1}
B	Magnetic induction	T
C_i	Specific heat of the bath I (spin, electron or lattice)	J m^{-3} K^{-1}
CL	Circular left polarization of the light	
CR	Circular right polarization of the light	
DIFFERENCE	Designates the image obtained after subtraction of CL and CR images.	
d_{ij}, D	Dzyaloshinskii-Moriya interaction parameter	J, J m^{-2}
E	The system energy	J
f_i	Scattering amplitude factor	
G_{ij}	Coupling constant between the bath i and j (spin, electron or lattice)	W m^{-3} K^{-1}
$\mathcal{H}$	Hamiltonian operator	J
H_{dem}	Demagnetizing field	A m^{-1}
H_{eff}	Effective PMA field	A m^{-1}
H_x	Hamiltonian operator of x	J
$\hbar$	Reduced Planck constant	6.626×10^{-34} J s
J	Total electron angular momentum axial vector	J s
j	Total electron angular momentum amplitude	J s
K_{eff}	Effective PMA parameter	J m^{-3}
K_u	Uniaxial magnetic anisotropy parameter	J m^{-3}
L	Electron orbital magnetic angular momentum	J s
M_s	Saturation magnetization	A m^{-1}
M	Magnetization axial vector	A m^{-1}
m	Normalized magnetization direction	
m	Reduced magnetic moment	
q	Scattering vector	m^{-1}
S	Electron spin angular momentum	J s
SUM	Designates the image obtained after addition of CL and CR images	
T	Temperature	K
α	Magnetic damping	
γ	Electron gyromagnetic ratio	1.761×10^{11} rad T^{-1} s^{-1}
δ	Domain wall width	m
ε	Energy density	J m^{-3}
μ	Absorption coefficient	m
μ_0	The vacuum magnetic permeability	$4\pi \times 10^{-7}$ H m^{-1}
π'	Vertical light polarization	
ρ	Charge density	A s m^{-3}
σ'	Horizontal light polarization	
λ	Light wavelength	m
Γ	Energy width of a level	eV

Table of content

Remerciements

Mes premiers remerciements vont à Nicolas Jaouen et ACDssy (désolé pour le jeu de mot pourri) qui m'ont tous deux fait confiance à différentes étapes de ce doctorat. Merci également à Nicolas Reyren d'avoir répondu patiemment à mes question d'ignorants et d'avoir corrigé RIGOUREUSEMENT ce manuscrit.

Je tiens aussi à remercier toutes les personnes avec qui j'ai pu discuter et partager des bêtises (pour rester polie). Horia pour son alarme ventrale réglée à 11h30 pétante. Merci à Roland de m'avoir facilité l'accès à la 5G « naturelle », en espérant que tu passesseras une bonne retraite (comme quoi un Normand peut souhaiter du bon à un breton…) !

Merci également à Myriam pour toutes ces discussions d'après covid ainsi que pour m'avoir fait connaître deux doctorants voisins de lignes. J'ai nommé Antoine, la plaque tournante des Ulis et Raphaël le trollo-décolonio-intégriste. Ce fût un plaisir de partager ce savoureux mélange de sérieux et de bêtise avec vous trois.

Dans une note plus sérieuse, un énorme merci à Yanis qui m'a probablement fourni la moitié des échantillons étudiés pendant ce doctorat. Merci également à Vincent Cros pour sa participation intellectuelle (en plus des deux Nicolas) à l'interprétation de nos résultats. Merci à Vincent Garcia et Stéphane Fusil pour la consommation de science avec modération sur la ligne :^). Merci à Erick et Samuel qui ont participé à ce travail de longue haleine.

Un grand merci à Jean-Yves qui a été mon compagnon de voyage au début de ma thèse ainsi qu'à Michel pour les discussion scientifiques et tennistiques. En Parlant de Tennis, un petit merci à Eric et Philippe, qui n'ont rien à voir avec ma thèse mais qui ont partagé un temps (fou ?) sur le terrain avec moi pendant ces trois années.

Merci également au Jury de prendre de votre temps pour relire et évaluer mon travail de thèse.

Enfin, merci à Pascaline de m'avoir supporté et soutenu 😊

Introduction

The first evidence of a magnetic effect has been discovered more than two thousand years ago. The capacity of Lodestone to attract Iron has been noticed by the Chinese and Greeks. Later, the Chinese carved Lodestone and noticed that some asymmetric sculptures, like a spoon, spontaneously pointed toward the South[1]. The use of magnetic material as compass to navigate started but it is on 1600 that William Gilbert gave a proper context for the compass operation as he described earth as a giant magnet. He also described the influence of heat on iron magnetism. The next step in the fundamental understanding of magnetism was achieved thanks to the discovery of electricity. During the XIXth century, Oersted found that an electric current flowing close to a compass can make it move. Electromagnetism was born and few decades later, Maxwell gathered the work on electricity and magnetism by reducing them in four equations. The first use of magnetism for information storage application is the telegraphone. It records the intensity of the electric current produced by a sound transducer in a moving magnetic wire and offer the possibility to read back the stored information. The magnetic medium and the reading process improved in the second half of the XXth century, fuelled by the invention of computer. IBM commercialised the first memory disk in 1956, which laid the foundations of the modern HDD. In HDD, the magnetic medium encodes the information in magnetic domains which were initially magnetized IP. In this magnetization orientation, the dipolar energy scales with the ratio of the magnetic medium thickness over the domain's width, which limits the storage density. A solution is to use perpendicularly magnetized layers, which allow to stabilize smaller domains. In those systems, the magnetic layer has to be few nanometer thin but the thickness can't be too small, otherwise the dipolar energy diverges. Magnetic materials with a strong uniaxial anisotropy are needed, but not too strong so that writing is still possible. The main storage density limitation was due to the reading and writing head. The discovery of the GMR by Fert[2] and Gründberg[3] stretched this limitation as spin-valve devices, consisting in the variation of the multilayer resistivity depending on the relative orientation of two saturated magnetic layers, increased the sensitivity of the reading process and, consequently, increased the storage density. It also opened a new field of study (spintronics) that exploits the electron's intrinsic angular moment degree of freedom, the spin, for future information and communication technologies. Note that only ten years separates the discovery and the first commercial GMR-based read head. It was soon followed by TMR, that further improved the spin-valves based reading step. Now the bit size approach 60 nm².

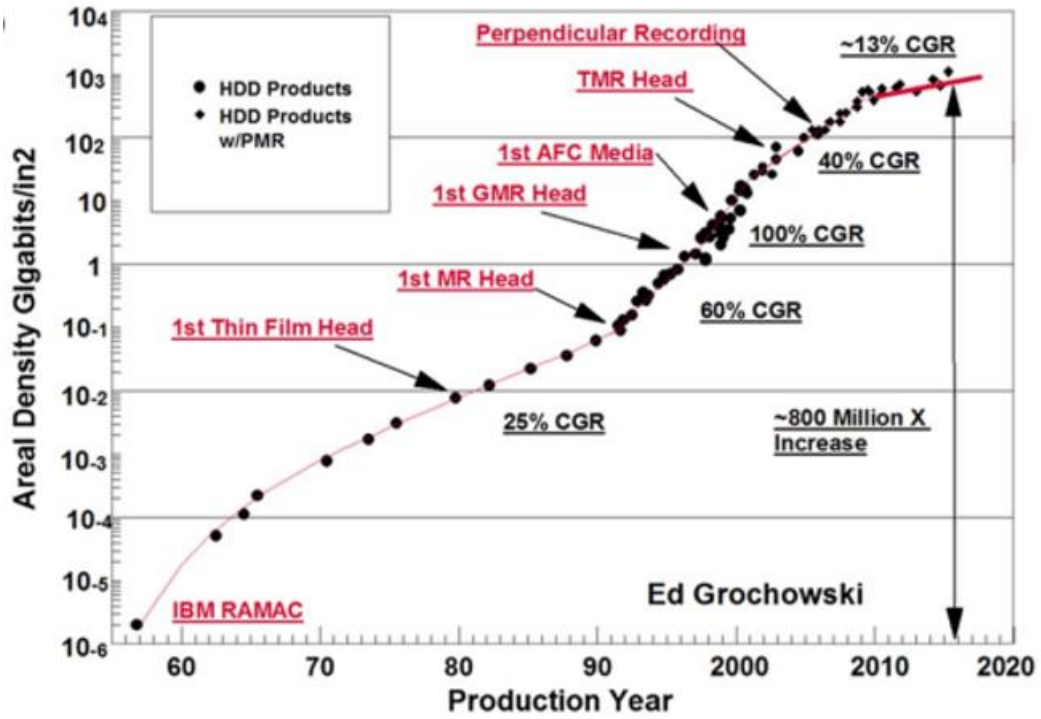

Figure 1 Evolution of the areal density of commercial HDD products from 1955 and 2016. The figure is extracted from Fullerton and Childress, Proc. IEEE 104, 1787-1795 (2016)[4].

The still growing demand for bigger storage devices pushes the research toward different solutions. One of them is the displacement of magnetic domains with chiral DWs. Chiral magnetic textures can be stabilized by the DMI (see chapter 1 for more details), which needs a broken inversion symmetry in the sample. Magnetic chirality is defined by the magnetization steady sense of rotation within the sample. It is an important concept for storage devices as it determines the direction of propagation of the magnetic textures with a cycloidal winding and allows higher velocities[5]. A Racetrack memory data storage devices has been designed to use the displacement of domains with static writing and reading heads[6]. It would make HDD more resilient against mechanical impact. The DMI can be found in bulk materials (B20 structures) or at the interfaces in multilayers with an asymmetric stacking order. Multilayers are versatile as it is possible to tune the different magnetic contributions to, for instance, decrease the energy associated to the creation of a DW for instance. Together with DMI, it can induce the nucleation of smaller chiral magnetic textures such as skyrmions, which are two-dimensional and localised spin textures in a magnetically saturated environment. Isolated skyrmions can be nucleated at RT[7–9]. A part of the current research on skyrmions focuses on reducing their size down to few nanometers as well as on their efficient current induced-displacement[10,11]. In FM multilayers, skyrmions displacement is hampered by a transverse deflection toward the track edges. It is linked to its topology but can be cancelled in AFM coupled skyrmions[12]. Moreover, SAF samples can exhibit more efficient and higher magnetic texture displacement velocity up to 750 m s^{-1} which increases as the total net magnetization in the multilayer decreases[13].

Despite the perspectives in the reduction of the magnetic texture size, the displacement speed and efficiency are limited by the drop of the efficiency with current (walker breakdown

for domains and deformation for skyrmions) or by the current impulsion length that doesn't decrease below 100 ps, rise time and pulse width combined[14]. To overcome this last limitation, the magnetization manipulation assisted by light heating has been proposed but is limited in density and speed due to heat diffusion. Moreover, the precessional switching of the magnetization in FM hardly falls in the THz range which is one order of magnitude slower than in AFM materials[15].

In 1996, Beaurepaire *et al*.[16] found a sub-picosecond demagnetization with a subsequent picosecond remagnetisation dynamic in a nickel FM single layer after a 60 fs laser excitation. Before that pioneer work, the interaction between lasers and magnetic material was thought to be mediated by heat transfer from the lattice to the spin. In bulk transition metals, the magnetic anisotropy energy value is around 100 µeV per atom. The Heisenberg uncertainty principle, $\Delta t \approx \hbar/\Delta E$, gives a characteristic time of ~40 ps, which is two orders of magnitude higher than the demagnetization time found by Beaurepaire *et al* (~ 250 fs). The ultrafast reaction of the spins to a visible light pulse paves the way to a new paradigm for magnetization manipulation. The femtomagnetism field has expanded in different branches that discovered and now exploit various phenomena such as coherent spin precession triggered by the optical generation of ultrafast spin currents in FM/HM[17] and AFM/HM[18] layers or the magnetization switching by a laser pulse[19,20] (all optical switching in ferrimagnets for instance) which can be helicity dependent. The later process as well as STT and SOT based switching could be particularly important for future magnetic recording device as they are expected to be more efficient than the Oersted-induced switching[21].

Ultrafast experiments are performed in pump and probe mode. It consists in the stroboscopic repetition of the pump (laser) and probe beams with a delay between the two that varies throughout the experiment. Thus, only the strictly reproducible phenomena can be probed on the same sample. As discussed in chapter 1, the pump wavelength changes the absorption efficiency but not the intrinsic ultrafast mechanism(s). The probe is usually a visible or an X-ray light as their interaction with the matter in almost instantaneous. Most of the ultrafast studies focused on the magnetization evolution in magnetically saturated materials and used visible light MOKE. It has the advantage to be sensitive to all the magnetic moment in the topmost layers of the sample. However, the different models used to explain the flow of angular momentum, described in chapter 2, don't vary in the same manner with depth and at the interfaces. Thus, the element selectivity that X-rays provide (but also some resonant MOKE set-up) seems a promising technique to study the ultrafast regime, even though a large scale facility is required. XMCD relies on the difference of absorption between the two circular polarizations performed at two absorption edges of the magnetic element and will be described also in more details in chapter 1. It can disentangle the spin and orbital angular momentum[22], which is thought to be the first angular momentum transfer step[23,24]. The element selectivity also unveiled another spin transfer mechanism optical inter-site spin transfer (OISTR) mechanism[25,26] in alloys and multilayers which accelerates (increases) the demagnetization (quenching).

Prior to this PhD work, most of the studies focused on the ultrafast evolution of saturated magnetic state. Here, we focused on the off-specular signal evolution from non collinear spin

textures in multilayers. In the **first chapter**, the different magnetic contributions present in amorphous transition metal magnetic layers at remanence are presented. The equilibrium between the different magnetic interaction for nucleating some non collinear spin textures is also briefly discussed. Then, an introduction about the different mechanism that intervene in the ultrafast demagnetization process is given. This part treats the local mechanism and slowly shift toward the non-local process, both being supported by theoretical or experimental evidence. MOKE has been widely used in that purpose but in our case, we worked with X-rays tuned at a magnetic element absorption edge. The third part of this chapter presents the electron and matter interactions in the soft-X-ray regime followed by the particular case of reflectivity. Finally, the facilities used to perform the experiment during this PhD work are briefly presented.

The study of magnetic chirality is done by XRMS. In **chapter 2**, the XRMS formalism in the case of circularly polarized light is presented. Formal calculations results are described in both transmission and reflection geometry. The diffraction pattern obtained in the DIFFERENCE and SUM images for both DWs type and chirality are calculated. However, the two images can only be quantitatively compared within a sample. The asymmetry ratio (DIFFERENCE / SUM) allows a comparison between samples as its value depends on the magnetic texture. Numerical calculations, varying the incident angle and the DWs width are performed. It shows a dependence of the asymmetry ratio to the relative DWs and domains widths. Then, experimental results obtained before this PhD work in FM multilayers are presented. It is followed by the angular and temperature dependent studies of the XRMS signal in SAF samples.

In the **last chapter**, the time-resolved study on FM multilayers with chiral textures is presented. After a discussion on the effect of the FEL beam fluence on the sample, the DIFFERENCE and SUM signals obtained in a known [Pt/Co/Al]-based multilayer system with chiral DWs are compared. MOKE, VNA-FMR and magnetic mode calculations have been performed to find the origin of a GHz oscillation in the hundred’s picosecond regime. Then, the effect of the pump circular polarization is explored on the same sample at different fluences. Finally, this PhD work explores the sub-nanosecond dynamic of skyrmion lattice systems at different field.

Chapter 1: State of the art

1.1 Magnetic interactions

The humanity discovered magnetic effects more than two thousand years ago. The compass was the very first use of it, but no fundamental macroscopic comprehension has been achieved until Maxwell work in the nineteenth century. The advent of quantum mechanics treatment of atomic and matter properties opened the way to a deeper understanding of magnetic phenomenon. It was even formalised, by the Bohr-Van Leeuwen theorem, that magnetism can't be explained by a classical point of view[27,28]. From the second half of the twentieth century, thanks to the progress in growth techniques, it is now possible to deposit subnanometer thin layers, so that one system dimension can be smaller than the typical spin relaxation length. Various interface dependent magnetic phenomena have been discovered (such as GMR, TMR, exchange bias…) and some are now at the forefront of the research interest for storage application. The growing complexity of magnetic structures has increased the need of simulating the non collinear spin texture resulting from the interplay between magnetic contributions.

In this first chapter part, the main magnetic interactions relevant in spintronic devices are described as well as the sample engineering allowing (chiral) magnetic textures to be obtained. Then, we concentrate on the ultrafast magnetization dynamics field, a spintronic subfield, sometimes referred as femtomagnetism. The mechanism proposed for the angular momentum transfer as well as the different experimental evidence are described. Finally, the different facilities used for the results presented in this PhD work are presented.

1.1.1 The macroscopic magnetization

The magnetization **M** is an axial vector describing the induced or permanent magnetic property of the matter expressed in amperes per meter (A m^{-1}). It is defined by the ratio between the elementary magnetic moment d**M** and the elementary volume that it occupies dV. In micromagnetic simulations, the reduced magnetic moment $\boldsymbol{m} = \frac{\boldsymbol{M}}{M_s}$ is often used to reduce the degree of freedom since you define once the magnetization amplitude for a magnetic layer (usually the magnetization at saturation M_s) and allow the angles to move freely. In the following, only the nucleus contribution to the magnetization is neglected as the proton and neutron gyromagnetic ratio is ~1000 times smaller than the electron one. The electron magnetic moment has two distinct atomic components. The orbital angular momentum through the magnetic quantum number of the electron state and its intrinsic angular momentum, the spin, is equal to $\pm\frac{\hbar}{2}$ often referred as spin up (↑) or down (↓). The total angular momentum is the vectorial sum of the two contributions $\boldsymbol{J} = \boldsymbol{L} + \boldsymbol{S}$ and contributes to the magnetic moment as:

$$M = g_j \mu_B \sqrt{j(j+1)} \quad (1)$$

With j the amplitude of the total angular momentum $\boldsymbol{J}$ and g_j the Landé factor. Noteworthy, the electron magnetic moment has an opposite sign to the electron spin due to electron negative charge that appears in the expression of the Bohr magneton μ_B. In the samples studied during this thesis, metallic transition metal atoms cannot be considered isolated. It modifies the orbital spherical harmonics expression depending on the atom environment symmetry and their sensitivity to it. Due to fermionic properties of electrons (Pauli exclusion principle), the magnetism is linked to the unpaired electrons inside the crystal field sensitive *d* shell, meaning that the different atomic *d* orbitals aren't anymore the eigenstates. The new orbitals are a linear combination of the latter. As a result, the orbital angular momentum is quenched (but not zero) and the magnetic moment only results from the intrinsic electron spin contribution[29,30]. The spin orientation depends on various magnetic interaction at short or long range.

1.1.2 Exchange interaction

The 3d shell density of states' spin polarization, in the itinerant model, results from the electrons-electrons interactions. Depending on the balance between the orbitals overlap, the electron-ion attractive force and the electron-electron repulsion, the exchange interaction can favour a ferromagnetic or antiferromagnetic state. The general atomic and continuous limit expressions for the exchange interaction assuming a small angle shift between neighbour atoms is[31]:

$$\mathcal{H}_{\text{ex}} = -\sum_{\langle i,j \rangle} J_{ex} \left(\boldsymbol{S}_i \cdot \boldsymbol{S}_j \right) \qquad E_{ex} = \int A(\nabla \boldsymbol{m})^2 dV$$

(2)

Here, $\boldsymbol{S}_i$ express the spin vector on atom site *i*. The exchange stiffness *A* scales with the coupling strength J_{ex} which can be positive or negative depending on the above-mentioned energy contributions. In the case where the Coulomb repulsion energy cost dominates the kinetic energy gain resulting from the band split, the element coupling strength is positive and favours a ferromagnetic coupling[32]. It has a short range and saturates at the bulk value for a thickness of 3 or 4 atoms[33], meaning that the exchange stiffness can be controlled reducing the layer thickness. Another way to control its strength can be to alloy the magnetic layer with other elements[34–37].

1.1.3 Dipolar and Zeeman interactions

The magnetic moments emit a stray field at long-range. The dipole-dipole interaction can play a considerable role in the magnetic texture, especially due to its long-range order. The dipolar energy is expressed as a self-demagnetizing field $\mathbf{H_{dem}}$ that originates from the magnetization distribution in the sample:

$$E_d = -\frac{1}{2}\mu_0 M_S \int \mathbf{H_{dem}} \cdot \mathbf{m} dV$$

(3)

The demagnetizing field energy is expressed analogously to the Zeeman effect ($E_Z = -\mu_0 M_s \int \mathbf{m} \cdot \mathbf{H_{ext}} dV$) which favours a parallel alignment of the magnetic moment with an applied external field[38]. The competition between exchange energy and the dipolar interaction can lead to the formation of domains pointing in opposite directions[39]. It also contributes to an anisotropic orientation of the magnetic moment through the so-called shape anisotropy. In general, it favours the alignment of the spins parallel to the sample's longest side. In thin films with planar geometry, which is the case of all samples studied during this work, it favours an in-plane configuration of the spins. However, as soon as the sample deposition techniques allow to grow ultrathin films (few atomic layers), new interfacial effects start to emerge.

1.1.4 Interfacial magnetic anisotropy

Possible large magneto crystalline surface contributions to the magnetic properties have been first pointed out in Néel[40] pioneering work and experimentally observed in NiFe single layer by Gradmann and Muller in 1968[41]. The atoms located at the film surface experience a different environment affecting the symmetry of the orbital orientation due to chemical bonds or strain effect[42]. Since the 3*d* orbitals are subjected to spin-orbit coupling, it also affects the spin orientation and can favour either a uniaxial perpendicular anisotropy or an in-plane magnetic anisotropy. The first observations of perpendicular magnetic anisotropy in multilayers were realized in Co-based multilayers[43–45]. The general expression of the anisotropy energy is expressed as:

$$E_K = -VK_u m_z^2$$

(4)

With V the FM volume and K_u the magnetic anisotropy parameter positive (negative) advantaging a perpendicular (in-plane) orientation of the spins. It typically contains a surface (K_s) and volume (K_v) contributions.

$$K_u = \frac{K_s}{t_{FM}} + K_v$$

(5)

The surface term can be enhanced by reducing the FM layer thickness. It is an important feature as it allows to tune the magnetic anisotropy of magnetic layers. Moreover, the quality of the interface (roughness, intermixing) affects the value of the interfacial anisotropy. The volume term is often small in the samples used in this thesis, where the magnetic anisotropy is dominated by the FM/Pt interface[46], favouring a perpendicular easy axis with respect to the sample plane. The sample planar geometry results in a competition between the interfacial magnetic anisotropy and the dipolar interaction. Usually, an effective anisotropy K_{eff} can be defined in a saturated sample as:

$$K_{eff} = K_u - \frac{\mu_0 M_s^2}{2}$$

(6)

This expression is then inserted into the magnetic anisotropy energy contribution, with parameters estimated from magnetometry techniques. However, the shape anisotropy has only a few known analytical macroscopic solutions in samples with a magnetic texture such as domain and domain walls, and then only numerical approach can simulate properly the dipolar field influence on a magnetic texture at remanence. If only the three above magnetic interactions dominate in the sample, it is possible to estimate the domain wall width with a one-dimensional approach. It gives a value that scales with the square root of the exchange stiffness over the anisotropy ($\sqrt{A/K}$), where $K = K_{eff}$ in the thin film limit. The domain wall can be of two types, either Néel (cycloidal rotation of the spin) or Bloch (helicoidal). In perpendicularly magnetized planar sample, Bloch type domain wall is generally favoured. However, it is possible to obtain the Néel configuration by narrowing the lateral size of the sample (nanowire) or by using a non-centrosymmetric sample, which allows asymmetric chiral exchange such as the DMI, either by structure or by stacking.

1.1.5 Dzyaloshinskii-Moriya interaction

Dzyaloshinskii studied the presence of a weak ferromagnetic moment in some bulk antiferromagnetic samples. He stated that if such a phenomenon is present, with an interaction favouring a canting of the neighbour spins, there must be a breaking of inversion symmetry in the structure as well as a strong spin lattice interaction[47]. Moriya gave a microscopic explanation deriving the superexchange interaction, that consists in the (AFM) coupling between two magnetic atoms mediated by a non-magnetic one, with a spin orbit coupling perturbation[48]. The Dzyaloshinskii-Moriya interaction (DMI) is then a three-site mechanism that can also appear via non-magnetic impurities[49] or at interfaces. Indeed, the breaking of inversion symmetry can also be realised by a non-symmetric thin film stacking. Thus, a ferromagnetic layer interfaced with a non-magnetic layer made of a heavy element, for a strong spin orbit coupling, can also exhibit DMI[42]. A renewed interest in materials presenting a strong DMI emerges and intense researches are now performed[5,50–56]. DMI favours a specific tilt of the magnetization between neighbouring spins, and can hence stabilize chiral DWs of the Bloch type (typically for B20 materials with a broken bulk inversion symmetry) or of the Néel type (typical for interfaces, but can also occur for some bulk structures). Its expression is written in the discrete interaction case as:

$$\mathcal{H}_{DM} = -\sum_{\langle i,j \rangle} \boldsymbol{d}_{ij} \cdot (\boldsymbol{S}_i \times \boldsymbol{S}_j)$$

$$E_{\mathrm{DMI}} = t_{\mathrm{FM}} \int_S D \left(m_{\mathrm{x}}\, \partial_{\mathrm{x}} \mathrm{m}_{\mathrm{z}} - m_z \partial_x m_x + m_y \partial_y m_z - m_z \partial_y m_y \right) \mathrm{d}x\mathrm{d}y$$

(7)

Here, $\boldsymbol{S_i}$ expresses the spin vector on atom site *i* and $\boldsymbol{d}_{ij}$ is the DMI vector that defines the magnetic layer chirality if strong enough. We express the DMI energy in the micromagnetic form for the specific case of the interfacial DMI, which is relevant for the rest of the thesis (the expression is different for other symmetries). In B20 crystal structure (bulk DMI), $\boldsymbol{d}_{ij}$is parallel to the unit displacement between two spin sites $\boldsymbol{u}$, favouring an helicoidal canting (Bloch) of the magnetic moment, while in multilayers $\boldsymbol{d}_{ij}$is perpendicular to both, $\boldsymbol{u}$ and magnetic moments, resulting in a cycloidal spin rotation (Néel). In the latter case, the corresponding *D* value in the micromagnetic framework changes of sign upon inversion of the stacking order. The chiral nature of the interaction determines the electrically induced DW direction of propagation[5]. Moreover, the Walker breakdown field scales linearly with the *D* value, which extends the DW steady regime where its velocity increases linearly with the field/current. Tailoring multilayers with the highest DMI possible has another interesting feature. Indeed, the antisymmetric interaction is partly responsible for the stabilisation of skyrmion lattice state often obtained at low temperature in bulk samples[57–59] and isolated skyrmions observed in multilayers at room temperature[7–9,12,60–62].

1.1.6 Ruderman-Kittel-Kasuya-Yoshida interaction

Historically, the Ruderman-Kittel-Kasuya-Yoshida (RKKY) interaction was introduced to describe the indirect coupling between nuclear magnetic moment mediated by conduction electron[63–65]. It has been later adapted to explain the indirect exchange coupling between two ferromagnetic layers interaction through non-magnetic metallic layers[66,67]. They added the treatment of the Friedel-like spin density oscillation propagation in the metallic spacer to the existing *s-d* band mixing model[68,69]. The expression of the RKKY energy per unit area obtained by considering a potential between conduction electrons of the spacer layer and the ferromagnetic layers is given by:

$$\mathcal{H}_{\mathrm{RKKY}} = \sum_{i,j} J(R_{i,j}) \boldsymbol{S}_i \cdot \boldsymbol{S}_j \qquad E_{\mathrm{RKKY}} = \int_S A_{\mathrm{RKKY}}\, \boldsymbol{m}_1 \cdot \boldsymbol{m}_2 dxdy$$

(8)

Where $\boldsymbol{S}_i$ and $\boldsymbol{S}_j$ are the spins of the two different ferromagnetic layers. The coupling strength $J(R_{i,j})$ depends on the distance between two magnetic moments. It encapsulates the quantum interference effect occurring in the spacer layer due to spin dependent confinement in the spacer layer. In the micromagnetic expression of the RKKY, A_{RKKY} is the RKKY factor in J m^{-2}. The RKKY model explains well the oscillating behaviour of the interaction with respect to the non-

magnetic spacer layer thickness. Moreover, it qualitatively reports the modification in the oscillation or coupling strength due to structural imperfections at the interface (i.e. dislocations, roughness or strain) or depending on the spacer element[67]. However, quantitative predictions of the coupling strength value as well as its phase differs from the experimental data due to the need of an accurate knowledge of the interface and fermi surfaces properties.

The RKKY interaction has been central for the elaboration of spin valve devices, that has boosted the storage density capabilities[2,3,70].

1.1.7 The different spin textures

Depending on the relative magnetic interaction energy values, different magnetic textures are stabilized. At remanence, a uniform OOP uniform magnetization state is energetically favoured when the exchange interaction and the PMA dominate. The formation of domains with opposite magnetization direction reduces the dipolar energy contribution but comes at the cost of the formation of DWs. The energy cost of a DW is expressed as:

$$\varepsilon_{DW} = 4\sqrt{AK} - \pi D$$

(9)

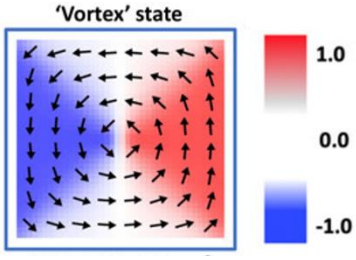

Figure 2: Simulation of a vortex state. Image taken from A. Barman *et al*. Journal of Applied Physics **128,** 170901 (2020)[71].

Non-collinear spin textures are favoured by reducing the DW formation energy cost which is equivalent to reduce the anisotropy K and/or the exchange energy and/or to increase D from equation 9. The number of magnetic domains and their size depends on the amount of dipolar energy gained versus the energetic cost of DWs. In systems where the dipolar energy is of the same order of magnitude than the exchange interaction, it is possible to obtain non collinear spin texture without DMI. For instance, in square magnets with negligible PMA, the system reduces the demagnetizing field by orientating the magnetization parallel to the system edge. These magnetic vortices, depicted in figure 2, are stabilized when the lateral dimension of the system is equivalent to the exchange length $l_{ex} = \sqrt{A/K_d}$. Here, K_d is the shape anisotropy resulting from the demagnetizing field.

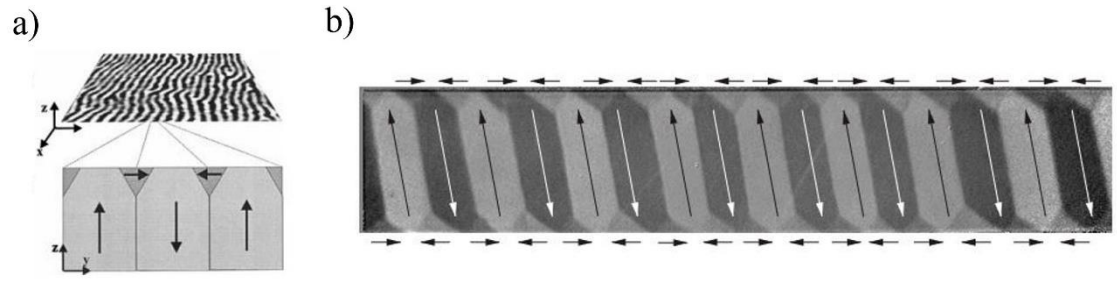

Figure 3: Closure domains in samples with OOP easy axis (a) and IP easy axis (b). Image (a) and (b) are taken from H.A. Dürr *et al.* Science **284**, 2166 (1999)[72] and O. Fruchart, Lectures on nanomagnetism, European School of Magnetism[73], respectively.

When the lateral dimensions of the planar system are smaller than the exchange length, a uniform magnetization state is observed. For l_{ex} small compared to the system dimension, a domain pattern is observed. Closure domains can stabilize in systems with a non-negligible dipolar energy contribution even in the domain pattern state for samples with OOP (a) and IP (b) easy axis, as depicted in figure 3.

The closure domains presented in figure 3 (a) exhibit a magnetic pattern with a steady sense of winding at the surface, i.e., chirality induced by the dipolar interaction. Chiral magnetic patterns can also be favoured by the DMI and are at the forefront of the spintronic research, especially in multilayers. Indeed, the chirality induced by the interfacial DMI allows to deterministically control a magnetic pattern with an electrical current and to achieve higher displacement velocity. A large DMI amplitude reduces the DWs' formation energy cost. In multilayers, a high DMI energy term and a vanishing effective anisotropy can be achieved, making the DW energy cost negative. A spin spiral magnetic state, consisting of a sinusoidal rotation of the magnetization is stabilized. The nucleation of such texture favours the apparition of small isolated (meta)stable skyrmions at low fields (~100 mT) that are theoretically more resilient against field and temperature annihilation than magnetic bubbles[74]. Skyrmion is a chiral and localized 2D swirling arrangements of the spins in the middle of a uniform magnetization. They are different from magnetic vortices and bubbles. Despite sharing a cylindrical symmetry, magnetic vortices can potentially be infinite in size. Magnetic bubbles are also localized and stabilized in perpendicularly magnetized material, but they generally aren't chiral and are generally few µm big. Skyrmions are often smaller than magnetic bubbles. They have been first observed in skyrmion lattice state in bulk[57,59]and later in thin films[58] samples lacking inversion symmetry at cryogenic temperatures. However, the chiral vector orientation differs between the two types of samples. In bulk systems, the DMI often favours a helicoidal (Bloch) type of winding whereas the interfacial DMI generates a cycloidal (Néel) one. The CW or CCW sense of winding is determined by the sign of the DMI parameter as long as the dipolar is small enough in comparison. The Skyrmion lattice state exist in a restricted range of temperature and applied field. This is due to the different evolution of the magnetic parameters with temperature. Multilayers offer more possibilities to tune the different magnetic parameter contributions. The first observations of isolated skyrmions at RT were performed on a Pt/Co/Ir based multilayer[9] and other Pt/Co based multilayers[8]. Note that RT skyrmions were found in bulk compounds before multilayers but in the lattice state[75]. Due to the cylindrical symmetry of the skyrmions, they are

vertically replicated in the magnetic layers. It increases the skyrmions magnetic volume making them more resilient against thermal fluctuation. Increasing skyrmion stability at RT fuel the research toward the stabilization of magnetic skyrmion with a size below ten nm as well as their efficient motion.

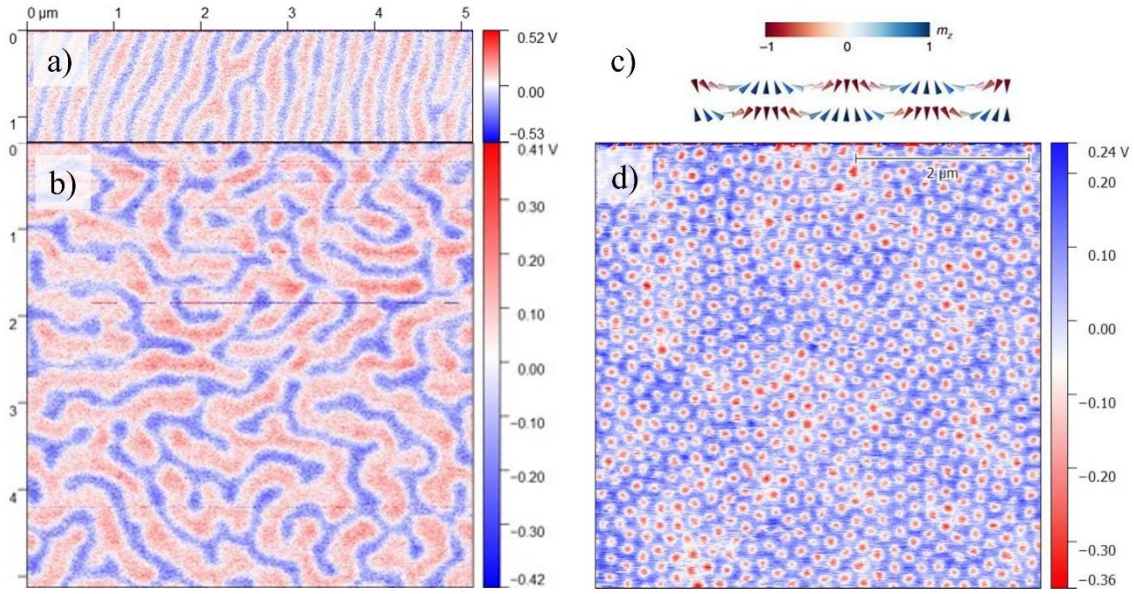

Figure 4: MFM images showing a magnetic domain pattern taken at zero field after an IP (a) and OOP (b) demagnetization procedure. (c) Simulation of two spin spirals AFM coupled. (d) MFM image of a skyrmion lattice obtained on a twenty repetitions CoFeB/Al_2O_3/Pt multilayer for an external OOP magnetic field of 75 mT. Image (c) is taken from W. Legrand *et al*., Nat. Mater. 19, 34-42 (2020)[12] and image (d) from the PhD work of William Legrand[76].

In this section, the different magnetic interactions and their role in some spin textures have been briefly presented. Future spintronic storage-based devices aim to reduce the size of the magnetic texture, the power consumption as well as to accelerate the magnetization dynamic. In that regard, the ultrafast magnetization dynamic induced by a femtosecond optical excitation fuel intense research.

1.2 Ultrafast magnetization dynamics

The magnetization dynamics is governed by the precessional movement, even in the THz regime. It is well described by the Landau-Lifshitz-Gilbert equation[77,78] and still used to describe the action of spin transfer torque[79] or spin-orbit torque[80,81] on magnetic texture.

$$\frac{d\mathbf{M}}{dt} = -\gamma\left(\mathbf{M}\times\mathbf{H}_{\text{eff}} - \alpha\mathbf{M}\times\frac{d\mathbf{M}}{dt}\right)$$

With γ the electron gyromagnetic ratio, α the material damping parameter and $\mathbf{M}$ the magnetization. The effective field $\mathbf{H}_{\text{eff}}$ combines the different magnetic interactions and the external field. In ferromagnetic transition metals[82], it usually takes few nanoseconds for the magnetization to switch by STT. Recently, it has been demonstrated that this dynamics can be reduced

down to several hundreds of picosecond for the magnetization to switch with SOT[83,84]. In antiferromagnet, the exchange-enhanced switching dynamics is well established in the THz regime[85–87]. However, the ultrafast demagnetization isn't governed by a spin precession and the magnetization amplitude isn't conserved which compromises the use of the LLG equation in the sub-picosecond regime. The advances in shortening laser pulse length toward hundreds of femtoseconds during the 90s fuelled the exploration of the electron-phonons dynamics and coupling. Experiments performed on noble metals estimated an electron-electron relaxation time of about 500 fs and subsequent electron-phonon energy transfer process occurring few picosecond later[88–90]. In the meantime, studies on magnetic materials found no evidence of ultrafast demagnetization using tens of picosecond pump and probe pulses, even when samples melted[91]. They concluded that the spin and lattice interaction characteristic time scale was larger than the pulse length as observed in Gadolinium[92]. However, in 1996, Beaurepaire *et al.*[16] found a sub-picosecond demagnetization in a Ni single layer[16] using a 60 fs pump and probe beams. They fit their results with a thermodynamic three temperatures model (3TM), which assumes an exchange of energy between the spin, lattice and electron reservoirs. The temperature of each subsystem is described by three coupled differential equations:

$$\begin{aligned} C_e(T_e)\frac{dT_e}{dt} &= -G_{el}(T_e - T_l) - G_{es}(T_e - T_s) + P(t) \\ C_s(T_s)\frac{dT_s}{dt} &= -G_{es}(T_s - T_e) - G_{sl}(T_s - T_l) \\ C_l(T_l)\frac{dT_l}{dt} &= -G_{el}(T_l - T_e) - G_{sl}(T_l - T_s) \end{aligned}$$

(10)

With T_i, the temperature of the bath i, i designating the electronic (e), spin (s) or lattice (l) subsystem. C_e, C_s and C_l are the electronic, spin and lattice specific heat, respectively. G_{el}, G_{es} and G_{sl} describe the coupling interaction between electron-lattice, electron-spin and spin-lattice baths. A linearly polarized laser pulse, with a power density P(t), is absorbed by the near Fermi level electrons. It first creates a non-thermal electronic distribution that thermalizes in hundreds of femtoseconds by electron-electron scattering. In the picosecond regime, electron-phonon scattering dominates and the baths exchange energy before reaching equilibrium. The lattice temperature increases slowly since its heat capacity is larger than the electron and spin ones, the latter being the smaller. In the limit of small fluence, instantaneous electron bath temperature increase and negligible spin specific heat ($C_s \to 0$), the model admits a simple solution[93] which can be used to fit ultrafast demagnetization curves up to tens of picosecond:

$$-\frac{\Delta M}{M(t < t_0)} = [(D_1 - D_2 - D_3)\Theta(t - t_0)] * \Gamma(t)$$

With:

$$D_1 = \frac{A_1}{\left(t/\tau_0 + 1\right)^{\frac{1}{2}}}$$

$$D_2 = \frac{(A_2\tau_E - A_1\tau_M)}{\tau_E - \tau_M} e^{-\frac{t}{\tau_M}}$$

$$D_3 = \frac{\tau_E(A_1 - A_2)}{\tau_E - \tau_M} e^{-\frac{t}{\tau_E}}$$

(11)

Where M is the total magnetization. $D_{1,2,3}$ are dimensionless quantities related to the lattice, spin and electron baths thermalization times. The three contributions are multiplied by a Heaviside function $\Theta(t - t_0)$ and convoluted by the temporal gaussian shape of the probe beam $\Gamma(t)$. A_1 corresponds to the magnetization variation value when the baths are at equilibrium and A_2 is proportional to the electronic temperature. $\tau_M$and τ_E are the demagnetization and magnetization recovery time constants while τ_0 is the characteristic timescale for the lattice thermalization.

The 3TM explains the loss of magnetization by the increase of the spin temperature relative to the Curie temperature by means of energy exchange between the baths. However, this thermodynamic model doesn't consider the heat diffusion inside the sample and the action of non-thermal electrons during the first femtosecond[94,95]. Importantly, it lacks a microscopic explanation on how the angular moment is carried away from the magnetic layer since the angular moment should also be conserved and that a laser induced dipolar transition doesn't invert the spin quantum number.

1.2.1 The microscopic approach of the ultrafast demagnetization

The conservation of angular momentum holds true as long as the system is invariant by rotation of the coordinates set. Thus, even highly out of equilibrium phenomena should obey it. Illg *et al.* proposed an expression for the total angular momentum (**J**) conservation[96]:

$$\Delta\langle \boldsymbol{J} \rangle = \Delta\langle \boldsymbol{L}_e \rangle + \Delta\langle \boldsymbol{S}_e \rangle + \Delta\langle \boldsymbol{L}_{ph} \rangle + \Delta\langle \boldsymbol{L}_{EM} \rangle = 0$$

(12)

Here, Δ significates a variation while $\langle X \rangle$ stands for the average value over the system. The equation suggests a possible transfer of angular momentum between the electron orbital angular momentum $\boldsymbol{L}_e$, electron spin $\boldsymbol{S}_e$, lattice (phonons) $\boldsymbol{L}_{ph}$ and photons $\boldsymbol{L}_{EM}$ (EM = electromagnetic). In the following, the transfer of angular momentum as an origin of the optically induced ultrafast demagnetization observed in transition metals is discussed based on the last equation. A separation between local and non-local dissipation of angular momentum is made. Local

demagnetization means that the effect is visible only in the area excited in opposition to transport mechanism, considered as non-local.

1.2.1.1 Local effects

The first (local) effect that could come in mind is due to the pump, which is often a red visible Titane:Saphire crystal laser with a wavelength around 800 nm. Different authors proposed a mechanism based on the interaction between the electromagnetic field of the pump and the spin-orbit coupling[97–99]. Alone, the laser induced dipolar transition is conservative in spin, which shouldn't result in an ultrafast loss of angular momentum. In association with spin-orbit coupling, transition with spin inversion isn't forbidden anymore. Moreover, coherent switching effect of circularly polarized light, carrying angular momentum to the system, has been found in weak ferromagnetic samples[100,101] and was theoretically predicted in other materials[19]. Koopmans *et al.*[102,103], stated that the angular momentum carried by the laser field should be too small and no evidence of the inverse Faraday effect[19] or of a polarization change in the photonic system[104] has been found in bulk ferromagnetic samples with a polarized laser pump[93]. In addition, the pump length is usually ∼100 fs or less which is lower than the time at which the demagnetization reaches its maximum value ∼300-500 fs in transition metals.

Noteworthy, in multilayers or alloys made of a ferromagnetic element with a nonmagnetic element having *d* shell energy close to the ferromagnetic element one, a spin selective charge transfer can occur. The optical inter-site spin transfer (OISTR) consists in the transfer of minority electrons from a heavy metal (for instance Pt or Pd) toward the ferromagnetic element[25,105] and has a lifetime corresponding to the pump duration. Moreover, the ferromagnetic elements experiencing the OISTR effect demagnetizes more and faster than the same bulk element during the first tens of femtoseconds[23] but then catch the same trend. As further discussed in the chapter dedicated to the X-ray matter interaction, circularly polarized X-ray tuned at a resonant edge of a magnetic element with spin orbit coupling can be selective in spin. This phenomenon is used to retrieve the spin and orbital part of the angular momentum in magnetic transition metals or rare-earth elements[106–108] by integration of the difference between both circular polarization absorption spectra realized on two transition edges sharing the same initial state. The integral amplitude is linked to the average spin and orbital momentum by the sum rules. For instance, it was used to detect the OISTR effect. Apparently, the sum rules, allowing to disentangle the two contributions, still holds during the ultrafast transient state[109] despite changes detected in the band structure and exchange splitting[110–112]. Stamm *et al*. performed the first subpicosecond resolved pump probe experiment using X-ray magnetic circular dichroism (XMCD) on a bulk nickel sample and found no significative evidence of a transfer from the spin to the orbital bath as both decreases[113]. This observation has been reproduced in different systems[22,114,115] but the lack of direct coupling between the spin angular momentum and other channel, excepting the orbital degree of freedom, suggested a dynamic requiring hundreds of attosecond time resolution[116]. A two-step mechanism, relying on the spin-orbit assisted exchange of angular momentum between the spin and orbital baths followed by a coulomb interaction mediated orbital to lattice transfer have been imagined. It is fuelled by the experimental evidence for the second step via the ultrafast Einstein-de Haas effect[117]. A recent study noticed

a systematic slower demagnetization dynamics of the easy axis in an epitaxial hexagonal cobalt thin film[118]. The ab initio calculations performed in the same study indicates a large magneto-crystalline anisotropy in the electron-lattice coupling which could explain the dynamics anisotropy. Moreover, the different demagnetization rate between metallic Tb (high orbital momentum) and Gd (quenched orbital momentum)[119] as well as the extrinsic spin-orbit coupling contribution depending on the laser pulse itself[105] indicate a possible path for the spin-lattice coupling mediated by orbital momentum. The in-depth study of this model relies on the pump and probe' shortening duration length[120].

The classical sub-picosecond demagnetization dynamics observed in ferromagnetic sample can also be induced by hot electrons produced in a different layer. Multiple experiments[121–123] showed that a ferromagnetic layer capped with a sufficiently thick layer that absorbs almost totally the pump pulse, also experience ultrafast demagnetization. The onset loss of magnetization is delayed compared to uncapped samples, with a delay scaling linearly with the low scattering layer (like copper) thickness placed between the pump-absorbing (like platinum) and the ferromagnetic layer[123]. The laser pump excitation excites primarily the electrons around the Fermi level. A transient non-thermal electron distribution takes place and thermalize (in term of Fermi-Dirac distribution as depicted in figure 5) within 100 fs by electron-electron scattering[124].

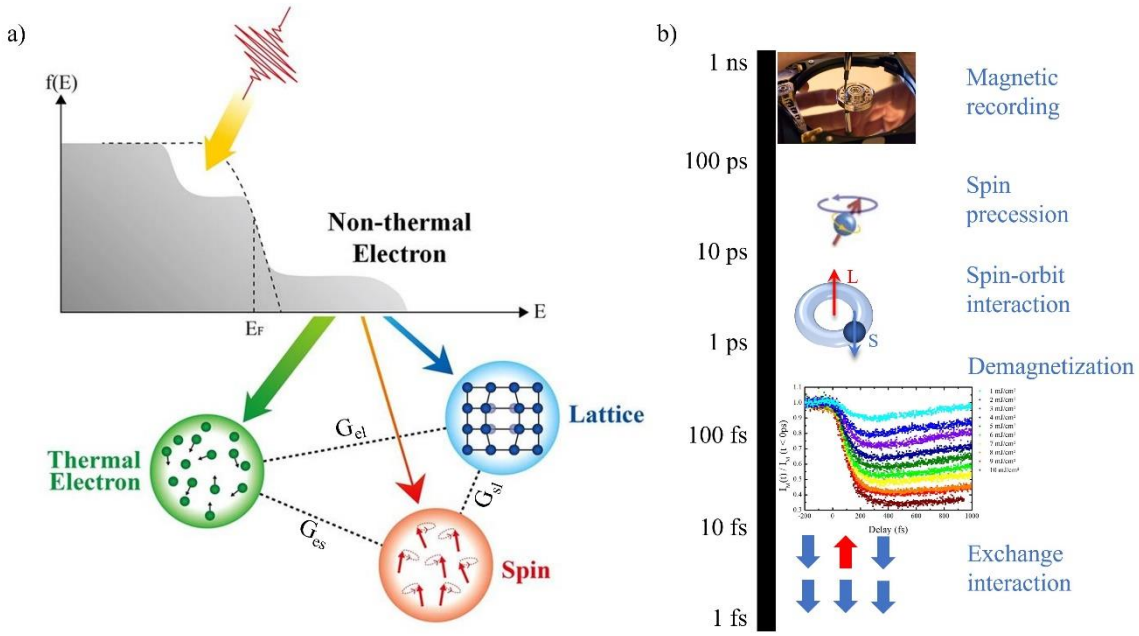

Figure 5: (a) Scheme of a non-thermal electron distribution optically induced. The usual shape of thermalized electrons distribution (Fermi-Dirac) is indicated by the dotted curve in the graph. The arrows represent the energy transfer from non-thermal electrons toward thermal electrons (green), lattice (blue) and spin system (red). The arrows' thickness qualitatively indicates the amount of energy exchanged. Dotted lines between the three baths depict their relative coupling. Figure taken from Shim *et al*[95]. (b) Typical timescales found in magnetization dynamics.

Depending on the pump wavelength, the non-equilibrium profile should change and gives insight on the non-thermalized electrons role in ultrafast demagnetization. Gort *et al.*[125] performed a time and spin resolved photoemission spectroscopy experiment indicating a

different dynamics between states around the Fermi level and deeper one. But recent magneto-optical studies revealed no change in the demagnetization time as well as in the recovery upon varying wavelength from visible-infrared[126] to THz excitation[127] with equal demagnetization amplitude. Both stated that for the same fluence, longer wavelength are more effective producing hot electrons. In the next section, hot electrons spin-flip scattering with local (quasi)particles as a demagnetization channel is discussed.

1.2.1.2 Electron-(quasi)particles scattering

The first scattering events after the optical excitation are the inelastic electron-electron collision that can produce secondary excited electrons but also thermalizes the electron distribution. However, this scattering event conserves the angular momentum and spin-orbit assisted Coulomb scattering has to take place[128,129]. Spin-orbit interaction mixes the spin states, so that an electron Bloch wavefunction is not a pure majority or minority spin state[22]. Moreover, the corresponding quantum operator enables spin-flip scattering through the "spin decrease-orbital increase" S^-L^+ term since more minority electron states are available. However, the electron-electron spin-flip scattering cannot explain the total loss of demagnetization alone. In transition metal single layers, the spin-orbit interaction is small due to the quenched orbital moment[130]. Also, the model struggles to explain the (fast) magnetization recovery rate, and electron-phonon scattering with a non-zero spin-flip probability is needed to absorb the electronic excess of energy[131].

The electron-phonon scattering process acts primarily as an energy sink due to the high heat capacity of the lattice compared to the electron bath one. Koopmans *et al*. proposed a decomposition of the Elliot-Yafet[132] type of scattering (probability of spin-flip at a scattering event with no spin precession in-between) to explain the demagnetization dynamics[133]. The spin-dependent part involves, once again, spin-orbit coupling due to local "hot spot" in the transition metal band structure[134] or to the presence of (magnetic) impurities. The majority spin being more excited than the minority population, the number of spin-flip transition from majority to minority is thus greater in both cases. It leads to a reduction of the macroscopic magnetization. The angular momentum is then transferred to the lattice by the absorption or emission of a phonon[135]. A microscopic three temperatures model (M3TM) has been developed to model demagnetization curve by implementing a spin-flip probability in the electron-phonon scattering events[136]. The model successfully reproduces the different demagnetization dynamics governing either elemental transition metal ferromagnets and rare-earth metals. However, some *ab initio* studies argue that the electron-phonon spin-flip scattering requires a too large amount of non-thermal electron after hundreds of femtosecond to reproduce the experimental data in ferromagnetic transition metals[96,137].

The Elliot-Yafet mechanism debate on its efficiency brought the attention on the band structure variation[138,139]. Several works focused on the transient exchange splitting role in ultrafast demagnetization. Surprisingly, they found collective spin fluctuations in the sub picosecond timescale and concluded that it is a more likely demagnetization mechanism than a strong exchange splitting change[110,140,141].

The fact that nickel demagnetizes more than cobalt for a same fluence has been interpreted a possible thermal fluctuation mechanism by magnons generation mediated by hot electron, as their Curie temperature indicates (~620 K for Ni and ~1300K for Co)[142]. A magnon is a coherent spin wave excitation (quasiparticle) of the magnetization, behaving like a boson. The emission of a magnon reduces the total magnetization. It can scatter with an electron resulting from the exchange interaction between the electron spin and the local scattering effective spin direction. Since magnons carry a well-defined and non-zero spin angular momentum (contrary to phonons), the electron-magnon spin-flip scattering does not necessarily needs spin-orbit coupling[143]. However, it cannot explain the ultrafast demagnetization dynamics alone and is probably associated with electron-phonon spin-flip scattering[96,143–145].

The different electron-(quasi)particles scattering and their respective outcomes are schemed in figure 6.

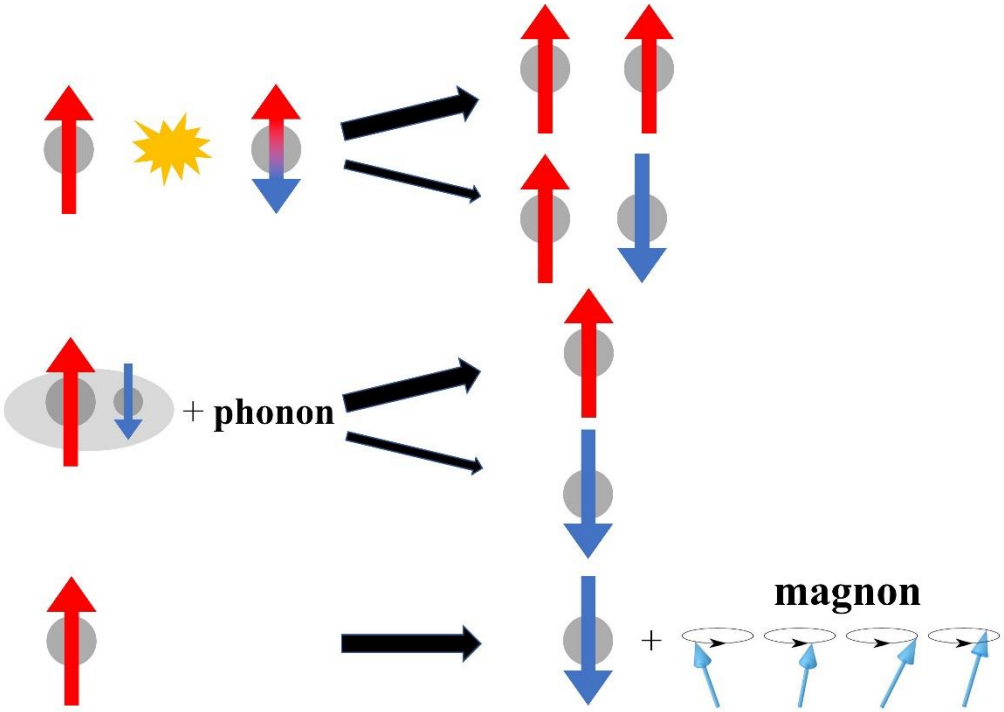

Figure 6: Schemes of the different scattering mechanism responsible for the demagnetization. On the top, representation of a majority hot electron scattering with a d electron, yielding two hot electrons whose final spin relative orientation depends on the d polarization. The thickness of the black arrows qualitatively depicts the relative probability of the event considering the up electrons as the majority electrons. In the middle, a mixed spin state due to spin orbit coupling scatters with a phonon. It results in either a spin-independent electron-phonon scattering or an Elliott-Yafet like spin-flip mechanism. At the bottom, a majority hot electron flips its spin with the emission of a magnon.

Spin-orbit coupling is an essential feature for the spin angular momentum dissipation. Its weak bulk value in transition metals struggle to explain the ~100 fs demagnetization observed in nickel, cobalt and iron. Additionally, Malinowski *et al.*[146] demonstrated that an interlayer transfer of spin angular momentum from a ferromagnetic layer to another speeds up and increases the demagnetization process when the two layers are polarized in spin antiparallel to each other. The effect was visible for a conducting spacer layer and not with an insulating one.

1.2.1.3 Nonlocal spin transport

A spin transport demagnetization model could explain the ultrafast demagnetization process without the need for a spin-flip process. Battiato *et al*. developed a model based on the transport of spin polarized hot electrons as well as spin conserving electron scattering[147,148]. It describes the transport of mobile *s-p* electrons and treat the d electrons as quasi-localized magnetic moments. The excited electrons have different velocities, lifetime and mean free path depending on their relative spin orientation with respect to the local one[149,150] but also to their displacement regime[137,151]. Thus, minority electrons are less mobile and scatter more while majority electrons carry away from the ferromagnetic layer (or the laser spot) their angular momentum. The latter can consequently induce a spin torque on another magnetic layer[152].

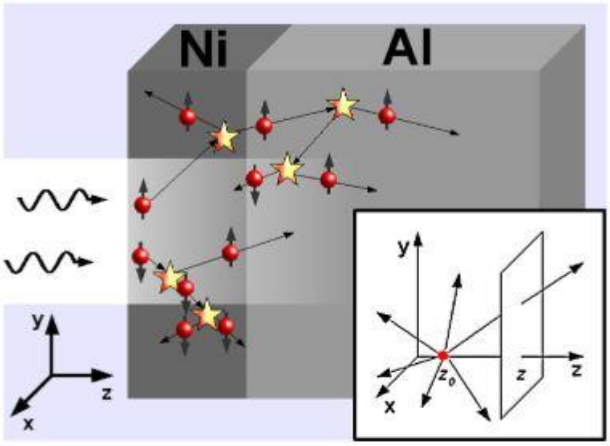

Figure 7: Scheme of the different superdiffusive processes after an optically induced electron excitation. The different mean free path between majority and minority electrons is represented by the number of collisions experienced. The generation of cascade electrons by inelastic scattering is depicted. The inset represents the geometry used in the electron flux calculation performed in Battiato et al. work whose image is also from[148].

This interpretation can explain the different dynamic between transition metal and gadolinium, since the spin polarized 4f band are localized and not directly affected by the optical excitation. It qualitatively describes the slower dynamics observed in insulators, compared to transition metal, due to the lack of superdiffusive spin current. The superdiffusive qualification of the model comes from the different electrons regime that are initially moving in a ballistic way ($\sqrt{\langle R^2 \rangle} \propto t$) after the laser pulse and after losing energy due to spin conservative diffusion, move in a diffusive manner ($\sqrt{\langle R^2 \rangle} \propto t^{1/2}$). The model predicts the polarization of a metallic neighbour layer due to the net spin current flowing at the interface. Moreover, due to the charge conservation, an electronic backward surge toward the ferromagnetic layer can happen[153]. With their lower mean free path, minority electrons should accumulate at the interface and induce a local demagnetization. Thus, the magnetization profile should not be homogeneous, especially at the ferromagnetic interfaces. This particular magnetization shape has been confirmed by time resolved X-ray resonant reflectivity[154,155].

Despite the experimental confirmations[156–159] in fully metallic samples, the superdiffusive spin transport model is unable to explain the ultrafast demagnetization in ferromagnetic bulk and ferromagnetic thin film containing or deposited on insulating layers[93,148,160]. Thus, both local and non-local mechanisms are needed to account for the sub picosecond demagnetization in transition metals.

The above presentation focused on the different microscopic demagnetization mechanism but the remagnetization process is also not fully understood. After the maximum demagnetization amplitude (~500 fs for transition metals), the first recovery stage takes place with a characteristic time of few picoseconds. It has been verified experimentally that the pump wavelength does not play a role in the demagnetization and recovery process[126]. It was expected since the excitation pulse isn't in the same time window as both dynamics, but a careful normalization to the maximum demagnetization amplitude had to be performed. Indeed, longer wavelength produces more hot electrons, which increases the demagnetization efficiency with respect to the fluence[127]. The increased efficiency (or fluence) results in longer demagnetization time[136] as well as longer recovery time[142]. It is well known since experiments on non-magnetic metals that the electron-phonon relaxation time increases with the fluence[161,162] or with temperature[163] and is typically around a picosecond. Thus, the different dynamics also have an extrinsic component that depends on the total energy absorbed by the system. Shim *et al*[164]. stated that the recovery dynamics depends on the different baths temperature after absorption of the optical pump since the exchange stiffness decreases non linearly with the temperature[165,166]. The nonlinear dependence of the exchange interaction in temperature could explain the highly reduced recovery dynamics at high fluence (or ambient temperature)[167], where the electron and spin temperature could thermalize above the Curie point. The magneto crystalline anisotropy should not play a significant role in the recovery process according to their simulations[164]. On the other hand, in a study focusing on the ultrafast of an epitaxial hexagonal close-packed cobalt thin film (15 nm) the authors found a different behaviour between the easy and hard axis[118]. A difference has been observed in both, the demagnetization process and in the recovery phase, where the hard axis systematically has a faster dynamic than the easy axis. The ratios between the hard over the easy axis demagnetization and the corresponding recovery times were approximately the same, suggesting a similar microscopic mechanism perturbation. It was further reinforced by a different delay shift between the reflectivity curves and the magnetization, the shift being shorter for the hard axis. They ascribed this result to the larger electron-phonon coupling and Elliott-Yafet spin-flip scattering in the hard axis, supported by simulations. Extrinsic contributions, other than pump related properties, can also modify the picosecond dynamics. The applied magnetic field influences the recovery dynamic but has no influence on the demagnetization rate. Indeed, the higher is the external magnetic field, the faster the magnetization recovers[168]. The study[168] observed the same tendency for the few picoseconds dynamic as well as for the slow recovery (τ_{slow}~200 ps), where the LLG equation usually works. In that time scale, damped oscillations of the magnetization can be observed[133] which are ascribed to spin precession.

All the above experiments were performed on saturated samples. The first time-resolved experiment on a sample (Co/Pt multilayer) at remanence with magnetic domains, has been done

in transmission geometry by Pfau *et al*[169]. They used small angle X-ray scattering (SAXS) and looked at the first order diffracted signal that originates from the labyrinthic domains, acting like a magnetic grating, that form a ring isotropic in intensity. The diffracted intensity integrated over the ring, decreases and recovers in a similar time scale as in saturated samples. However, a shift in the momentum transfer q_{peak}, which is linked to the domain periodicity in real space and correspond to the position of peak maximum, suggests that the demagnetization isn't homogeneous. The ultrafast q_{peak} decrease reaches a minimum at 0.5 ps with a time constant of 300 fs. The variation corresponds to a 4% shift and would corresponds to an average domain expansion of 2.8 nm over the probed area (250×250 µm²). If the hypothetic rearrangement process is homogeneous in the probed area, that is a 4% change of the domain boundaries, it would necessitate a domain wall velocity of 10^7m s^{-1}. Considering inhomogeneous domain annihilation, growth and expansion, it corresponds to a domain wall velocity of 10^{-4}-10^{-5}m s^{-1}. Those speeds are orders of magnitude larger than the one reported on domain walls[170] and also larger than the velocities (group and phase) of magnons[171]. Finally, the effective momentum transfer shift has been ascribed to a DW blurring due to the asymmetric spin dependent lateral transport across domain walls. The softening of the domain boundaries profile due to minority spin accumulation, similar to the superdiffusive transport prediction at the ferromagnetic layer interfaces[147,148], reproduce the drop in the peak position[169]. This shift of the diffracted peak position has been reproduced in transmission geometry on a CoFe/Ni multilayer, also exhibiting PMA and a maze domain pattern, by Zusin *et al*[172]. They performed the same analysis as Pfau *et al*. on the first, third and fifth diffraction order and found a 6% domain dilatation but within 1.6 ps this time. In their case, they attributed this (slower) shift to electron-magnon interactions. However, two other studies performed on a Co/Pd multilayer[173] and $Co_{88}Tb_{12}$ amorphous film (50 nm) multilayers[174] with stripped domains, also in transmission geometry, found no significant shift in the diffraction peak position at the picosecond timescale. Both noticed a faster demagnetization time, independent of the laser fluence, in contrast to experiments performed on similar saturated samples. It suggests, as stated by Pfau *et al*., a spin transport exchange from inversely oriented domains, accelerating the demagnetization. However, the absence of a peak shift in the ultrafast regime doesn't corroborate the DW blurring effect, even though the demagnetization level reached in Hennes *et al*. work[174] report the same observation as Pfau *et al*. in the small fluence regime[169].

The diffracted signal maximum position behaviour in the ultrafast regime is as controversial as the microscopic mechanism responsible from the demagnetization. In the former, information about the domain walls has been obtained by comparing the evolution of different diffraction order peaks. The domain dynamics was mainly probed and no information on the ultrafast internal domain wall magnetic order evolution has been retrieved. This thesis aims to study the chirality dynamic and to compare it with the domain one. It is achieved by performing time resolved SAXS but in reflection geometry.

1.3 X-rays and matter

In 1846, Michael Faraday studied the final polarization of a linearly polarized light passing through a transparent material placed in a magnetic field parallel to the beam propagation and used a Nichol's prism as analyser. M. Faraday found a rotation of the light's polarization depending on the magnetic field applied, which is the very first evidence of an interaction between light and magnetism[175]. However, the effect was subtle and performed on dielectric transparent materials.

At the beginning of the twentieth century, experiments on ferromagnetic sample have been carried out to study what we call the magnetic texture and were performed by observing the movement of microscopic colloidal particles above a magnetic material. But the domains visualisation was limited as the particles had to be small relative to the domains size. It was a profuse period for ferromagnetism theory and the need of an experimental tool that probes the distribution of the magnetic moment at the nanometer scale was much needed. The discovery of neutrons in 1932 and the subsequent use of its spin, combined with the wave-particle duality announced by De Broglie, paved the way for magnetic samples studies. The first scattering experiments made on magnetic materials were done with neutrons, since Bloch[176], Schwinger[177] and Halpern and Johnson[178] first pointed out the non-negligible interaction between the neutron spin with the atomic magnetic moments of a magnetic substance.

X-rays had been discovered before neutrons, but they were essentially used to probe the electronic density. The first studies involving the magnetic property of a substance and X-rays, were carried out on single crystals of Iron based oxides and on pure iron polycrystal[179–182] during the first quarter of the XXth century. Platzman and Tzoar[183] first point out the theoretical possibility to probe the spin distribution in antiferromagnets with elastic scattering of hard X-rays, analogously to what was already done with neutrons. The magnetic Bragg scattering signal was evidenced experimentally by de Bergevin and Brunel[184] 2 years after, launching the interest in X-rays for spin distribution studies. Even if the cross section of the magnetic signal is 6 orders of magnitude smaller than the charge, making experiments long enough to achieve a good signal over noise ratio, X-rays sources are far more easily available in comparison to neutron sources. The democratisation of synchrotron light sources, allowing to change the energy and the polarisation of the incoming photons combined with a higher flux of photons, has changed the way magnetic samples are nowadays studied.

In the following, I present the different photon-matter interaction processes with a focus on the X-ray regime and the associated techniques that I used to explore multilayers properties. I begin with the x-ray (resonant) reflectivity (XRR) that probes the electronic distribution in the sample and can also give the average magnetic moment orientation of different layers in the sample. Then, I will present a 2D diffraction resonant techniques that gives access to in-plane distribution of the magnetization. One gives access to the averaged magnetic depth profile of the sample, the other can give information about the 3D magnetic texture.

1.3.1 Photon-matter interaction

A photon can interact in multiple ways with the matter with a probability that depends on the energy of the incoming photons with respect to the element considered. At very high photon energies, of the order of 10^9 eV, interactions with the nucleus dominate, while around 10^6 eV, it is the inelastic Compton scattering regime that usually prevails as seen in figure 8. The soft X-ray regime used in this thesis is dominated by the photo electric effect that puts the absorption of a photon at stake on the contrary to the Rayleigh scattering. Noteworthy, the break in the carbon photo electric cross section around 300 eV corresponds to the K edge transition between the 1*s* and a 2*p* level.

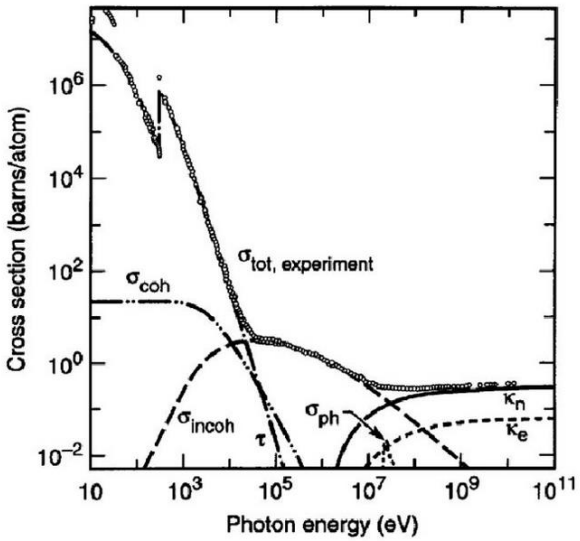

Figure 8 : Cross section of the different processes in the carbon total cross section. The global cross section is dominated by the photo-electric effect (τ) until 10 keV where the coherent scattering (σ_{coh}) plays a significant role. After 10 keV, Compton scattering (σ_{incoh}) is the main contribution until high energies (10^7 eV for carbon) where nucleus-photon interactions start to take over: κ_n for the pair production in the nuclear field, κ_e the pair production in the electron field and σ_{ph} the photonuclear absorption. The figure was taken from Hubbell *et al*. J. Phys. Chem. Ref. Data **9**, 1023 (1980)[185].

Neutrons had been privileged to probe the magnetism while X-rays were mainly used to probe the electronic charge distribution in solids. The electromagnetic nature of the light should be sensitive to magnetism but until 1970, Compton scattering with polarization analysis[186] was the unique solution to study magnetic order with X-rays. Platzman and Tzoar[183] derived a mildly relativistic expression for the cross section in Bragg condition, which is sensitive to magnetic distribution analogously to neutron Bragg scattering. Two years later, De Bergevin and Brunel[184] confirmed experimentally the theoretical results on ferro and ferrimagnetic compounds with a maximum in the relative intensity between the charge and magnetic signal of 10^{-3}. However, the theoretical breakthrough in the way magnetism is probed by X-rays today find its foundation in Blume seminal work[187,188].

1.3.2 Non-relativistic quantum description of the interaction

On the contrary to the relativist Hamiltonian developed by Platzman and Tzoar, Blume considered the resonant effects using an electronic Hamiltonian that relies on the kinetic and potential operators, the quantification of the electromagnetic field, the spin-orbit interaction, and the photon magnetic field action on the spin angular momentum:

$$\mathcal{H} = \sum_j \frac{1}{2m}\left(\boldsymbol{P}_j - \frac{e}{c}\boldsymbol{A}(r_j)\right)^2 + \sum_j V(r_j) + \sum_{k\lambda} \hbar\omega_k (C^+(\boldsymbol{k}\lambda)C(\boldsymbol{k}\lambda) + \frac{1}{2}) - \frac{e\hbar}{2(mc)^2}\sum_j \boldsymbol{s}_j \cdot \boldsymbol{E}(r_j) \times \left(\boldsymbol{P}_j - \frac{e}{c}\boldsymbol{A}(r_j)\right) - \frac{e\hbar}{2mc}\sum_j \boldsymbol{s}_j \cdot \nabla \times \boldsymbol{A}(r_j)$$

(13)

Replacing $\boldsymbol{E} = -\nabla\boldsymbol{\phi} - \frac{1}{c}\dot{\boldsymbol{A}}$ in the spin orbit term of equation 13 gives:

$$-\frac{e\hbar}{2(mc)^2}\sum_j \boldsymbol{s}_j \cdot \boldsymbol{E}(r_j) \times \left(\boldsymbol{P}_j - \frac{e}{c}\boldsymbol{A}(r_j)\right) \approx \frac{e\hbar}{2(mc)^2}\left(\sum_j \boldsymbol{s}_j \cdot \left(-\nabla\boldsymbol{\phi} \times \boldsymbol{P}_j\right) + \sum_j \boldsymbol{s}_j \cdot \frac{e}{c^2}[\dot{\boldsymbol{A}}(r_j) \times \boldsymbol{A}(r_j)]\right)$$

(14)

Terms linear in $\boldsymbol{A}$ are omitted, since the spin orbit contribution is of order $(v/c)^2$. The first term corresponds to the ordinary spin-orbit coupling from electrons while the second represent the spin dependent scattering.

The total expression can be reorganised in 3 different contributions $\mathcal{H} = \mathcal{H}_0 + \mathcal{H}_R + \mathcal{H}'$

$$\mathcal{H}_0 = \sum_j \frac{1}{2m}P_j^2 + \sum_j V(r_j) + \frac{e\hbar}{2(mc)^2}\left(\sum_j \boldsymbol{s}_j \cdot \left(-\nabla\boldsymbol{\phi} \times \boldsymbol{P}_j\right)\right.$$

$$\mathcal{H}_R = \sum_{\boldsymbol{k}\lambda} \hbar\omega_k (C^+(\boldsymbol{k}\lambda)C(\boldsymbol{k}\lambda) + \frac{1}{2})$$

$$\mathcal{H}' = \frac{e^2}{2mc^2}\sum_j A^2(r_j) - \frac{e}{mc}\sum_j \boldsymbol{A}(r_j) \cdot \boldsymbol{P}_j - \frac{e\hbar}{mc}\sum_j \boldsymbol{s}_j \cdot [\nabla \times \boldsymbol{A}(r_j)] - \frac{e\hbar}{2(mc)^2}\frac{e^2}{c^2}\sum_j \boldsymbol{s}_j \cdot [\dot{\boldsymbol{A}}(r_j) \times \boldsymbol{A}(r_j)] = H_1' + H_2' + H_3' + H_4'$$

With the vector potential $\boldsymbol{A}$ expanded as:

$$\boldsymbol{A}(r) = \sum_{q\sigma}\left(\frac{2\pi\hbar c^2}{\mathrm{U}\omega_k}\right)^{1/2}[\boldsymbol{\epsilon}(\boldsymbol{k}\sigma)C(\boldsymbol{k}\sigma)e^{i\boldsymbol{k}\cdot\boldsymbol{r}} + \boldsymbol{\epsilon}^*(\boldsymbol{k}\sigma)C^+(\boldsymbol{k}\sigma)e^{-i\boldsymbol{k}\cdot\boldsymbol{r}}]$$

U is a quantization volume, σ indicates the two polarizations and ϵ is the unit polarization vector of the wave with a wave vector $\boldsymbol{k}$.

The term $\mathcal{H}_0$describes the kinetic, potential and spin orbit energy contributions to the electron's Hamiltonian. $\mathcal{H}_R$represents the quantified electromagnetic energy of one photon.

Let's consider a single photon interaction in detail. The initial quantum state $|a\rangle$ of the system corresponds to the eigenstate of $\mathcal{H}_0$with a single photon present. The probability of transition toward a state $|b\rangle$ is induced by the interaction Hamiltonian $\mathcal{H}'$ and given by the Fermi Golden rule up to the second order.

$$w = \frac{2\pi}{\hbar}\left|\langle b|\mathcal{H}'|a\rangle + \sum_n \frac{\langle b|\mathcal{H}'|n\rangle\langle n|\mathcal{H}'|a\rangle}{E_a + \hbar\omega_k - E_n}\right|^2 \times \delta(E_a - E_b + \hbar\omega_k - \hbar\omega_{k'})$$

(15)

$\mathcal{H}_1'$ and $\mathcal{H}_4'$ contribute to the first order term as they are quadratic in $\boldsymbol{A}$ while $\mathcal{H}_2'$ and $\mathcal{H}_3'$ contribute to the second order. Considering only the elastic events, i.e., $\omega_{k'} \sim \omega_k$

$$w = \frac{2\pi}{\hbar}\left|\langle b|\mathcal{H}_1' + \mathcal{H}_4'|a\rangle + \sum_n \frac{\langle b|\mathcal{H}_2' + \mathcal{H}_3'|n\rangle\langle n|\mathcal{H}_2' + \mathcal{H}_3'|a\rangle}{E_a + \hbar\omega_k - E_n}\right|^2 \times \delta(E_a - E_b)$$

Developing the first order term gives the Thomson charge scattering and a second contribution that depends on the Fourier transform of the spin density but smaller by a factor $\frac{\hbar\omega}{mc^2}$ ~ 0.002 for 1keV X-rays compared to the charge signal.

This magnetic contribution is small compared to the charge one, but it was used in the hard X-ray regime to study magnetism. The work of Blume sheds light on the second order term in the Fermi golden rule, the one linear with the potential vector, that involves a 'virtual transition' toward an intermediate state, *n*. It corresponds mathematically to a photon annihilation-emission and emission-annihilation processes.

The scattering cross section is calculated multiplying ω by the density of final states (at the Fermi level) $\rho(E_f)$ and dividing by the incident flux I_0:

$$\frac{d^2\sigma}{d\Omega dE} = w \cdot \frac{\rho(E_f)}{I_0} \propto I(\omega, \boldsymbol{q})$$

(16)

The general expression in the Born approximation for the scattered intensity, which is equivalent to a non-normalized cross section, is given by:

$$I(\omega, \boldsymbol{q}) \propto \left| \sum_n f_n(\omega) \mathrm{e}^{\mathrm{i}\mathbf{q}\cdot\mathbf{r_n}} \right|^2$$

(17)

With $\boldsymbol{q} = \boldsymbol{k}' - \boldsymbol{k}$ the scattering vector, where $\boldsymbol{k}(\boldsymbol{k}')$ is the wave vector of the incident (scattered) photons. The summation is over the different atomic sites with a position vector r_n. f_n is the scattering amplitude of the site n that is considered as a unique element in the following.

The resonant term in the cross section, causing anomalous dispersion, can be expressed as:

$$\frac{d^2\sigma}{d\Omega dE} = \left(\frac{e^2}{mc^2}\right)^2 \left| \langle b|H_1' + H_4'|a\rangle + \frac{\hbar^2}{m} \sum_n \sum_{ij} \left(\frac{\left\langle b\left| \left(\frac{\epsilon' \cdot P_i}{\hbar} - i(k' \times \epsilon') \cdot s_i\right) e^{-ik'\cdot r_i} \right| n \right\rangle \left\langle n\left| \left(\frac{\epsilon \cdot P_j}{\hbar} - i(k \times \epsilon) \cdot s_j\right) e^{ik\cdot r_j} \right| a \right\rangle}{E_a + \hbar\omega_k - E_n - \frac{i\Gamma_n}{2}} + \frac{\left\langle b\left| \left(\frac{\epsilon \cdot P_j}{\hbar} - i(k \times \epsilon) \cdot s_j\right) e^{ik\cdot r_j} \right| n \right\rangle \left\langle n\left| \left(\frac{\epsilon' \cdot P_i}{\hbar} - i(k' \times \epsilon') \cdot s_i\right) e^{-ik'\cdot r_i} \right| a \right\rangle}{E_a + \hbar\omega_k - E_n - \frac{i\Gamma_n}{2}} \right) \right|^2 \times \delta(E_a - E_b)$$

The term Γ_n has been added in the denominator to take into account the energy level width, which is especially important when $\hbar\omega_k \sim E_a - E_n$. The gain in the second order cross section contribution can reach up to 6 orders of magnitude at a resonance edge of some of the actinide elements[189]. The magnetic signal enhancement depends on the strength of the transition that relies on the levels wave function overlap and on the difference in the Fermi level density of states between majority and minority spins caused by exchange splitting. In transition metals, the transition between a localized s shell towards a 3*d* level is considerably weaker than the transition $2p \rightarrow 3d$, where the overlap is large. In rare-earth elements, even if the 4*f* orbital is more localized than the 3*d* one, the transition with a *p* level is still relatively high due to the high polarizability of the 4*f* shell. In this work, only metallic iron and cobalt have been studied at the L ($2p \rightarrow 3d$) and M ($3p \rightarrow 3d$) edges. Around the cobalt $M_{2,3}$ edge (λ~20.8 nm), the attenuation length is ten times smaller than at the L edge (λ~1.6 nm). Thus, the signal mostly originates from the first layers while it will be more sensitive to buried magnetic signal at the L edge. The L_3 transition has been preferred to the L_2 since the $2p_{3/2}$ level has twice the number of electrons of the $2p_{1/2}$. The spin orbit coupling separates the $2p$ orbitals into the two aforementioned levels, having the orbital and spin angular momentum parallel and antiparallel to each other respectively. Circularly polarized light carries an angular momentum, which, together with spin orbit coupling, makes the absorption dichroic since no spin inversion occurs during the transition.

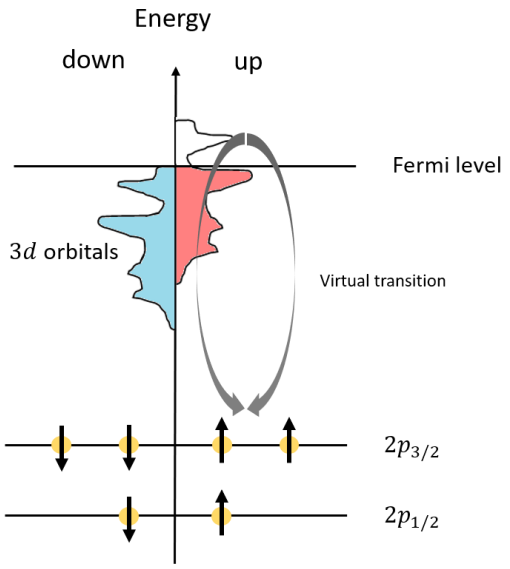

Figure 9: Illustration of the virtual transition at one of the L edges due to the Fermi golden rule second order perturbation contribution in a transition metal. The exchange coupling causes a difference in the Fermi density of state between spin up and down. The 2p levels can be considered as a reservoir of spins. They are split in two levels of energy due to spin orbit coupling. The $2p_{1/2}$ level has its orbital momentum antiparallel to its electrons spin momentum, while in the case of the $2p_{3/2}$ levels, they are parallel to each other. Since circularly polarized light carries an angular momentum, a dichroic effect in the absorption can be observed resulting from the different virtual transition probability between the two circular polarizations.

Hannon *et al.*[190] pursued development of Blume and expressed the coherent scattering amplitude for an electric 2^L pole transition (L=0 for a monopole, L=1 for a dipole…) that depends on the spherical harmonics (Y_{LM}) and on a term that describes the strength of the transition $F_{LM}(\omega)$:

$$f_{EL}^{xres}(\boldsymbol{k'}, \boldsymbol{e}_f, \boldsymbol{k}, \boldsymbol{e}_0, \omega) = 2\lambda f_D \sum_{M=L}^{L} \left[\boldsymbol{e}_f^* \cdot \boldsymbol{Y_{LM}}(\boldsymbol{k'}) \boldsymbol{Y_{LM}^*}(\boldsymbol{k}) \cdot \boldsymbol{e}_0\right] F_{LM}(\omega)$$

(18)

Where $k_f, e_f (k_0, e_0)$ are the wave vector and the polarization vector of the out-going (in-going) photon. f_D is the Debye-Waller factor that describes the attenuation in the diffracted intensity due to thermal agitation.

The $F_{LM}(\omega)$ factor has the form of a Lorentzian function that depends on multiple parameters:

$$F_{LM}(\omega) = \sum_{a,n} \left[\frac{p_a p_a(n) \Gamma_x(aMn; L)}{2(\epsilon(n) - \epsilon(a) - \hbar\omega - \frac{i\Gamma(n)}{2})} \right]$$

(19)

In the numerator, p_a corresponds to the probability that the system is in the initial state $|a\rangle$ while $p_a(n)$ describes the probability that the final state n is unoccupied. $\Gamma_x$stands for the partial width for the corresponding radiative decay $|n\rangle \rightarrow |a\rangle$. The total energy width of the excited state $\Gamma(n)$ is typically of order $\approx 1-10\ eV$which gives a scattering characteristic time of about 10^{-16}s. The polarization dependence of the scattering comes from the vector product between the spherical harmonics and the polarization vector of the ingoing and outgoing photon. In the electric dipole transition, the phase variation is neglected within the average radius $\bar{r}$ of the orbital considered for the transition with respect to the nucleus, i.e. $\bar{r}/\lambda$ <<1. This approximation is valid in the soft X-rays regime, where $\lambda \sim 100\bar{r}$ for the iron 2p orbitals. It leads to selection transition rules where there is a unit change in the azimuthal number L of $1\hbar$ and no spin inversion. In the dipolar approximation, the resonant scattering amplitude has been expressed by Hannon[190] as:

$$f_{EL}^{xres} \approx \frac{3}{8\pi}\lambda f_D\{\boldsymbol{e_f^*}\cdot\boldsymbol{e_0}[F_{11}+F_{1-1}] - i(\boldsymbol{e_f^*}\times\boldsymbol{e_0})\cdot\boldsymbol{m}[F_{11}-F_{1-1}] + (\boldsymbol{e_f^*}\cdot\boldsymbol{m})(\boldsymbol{e_0}\cdot\boldsymbol{m})[2F_{10}-F_{11}-F_{1-1}]\} = \frac{3}{8\pi}\lambda f_D\{\boldsymbol{e_f^*}\cdot\boldsymbol{e_0}[f_0] - i(\boldsymbol{e_f^*}\times\boldsymbol{e_0})\cdot\boldsymbol{m}[f_1] + (\boldsymbol{e_f^*}\cdot\boldsymbol{m})(\boldsymbol{e_0}\cdot\boldsymbol{m})[f_2]\}$$

(20)

Where F_{10}, F_{11} and $F_{1-1}$are the transition strength factor for a unit increment of the angular momentum $\Delta L = 1\hbar$ that also implies a change in the magnetic orbital number M of 0,1 and -1 respectively. $\boldsymbol{m}$ represents the direction of the ion local moment. f_0, f_1 and f_2 correspond to the charge, magnetic and quadrupolar amplitude factor.

The first term depends on the ingoing and outgoing photon polarization vector scalar product. The second term is linearly proportional to the magnetization direction and responsible from the first harmonic satellites studied in this thesis. The last contribution is quadratic with respect to the magnetization and can give second order harmonics in rare earth, multiferroic and/or antiferromagnetic compounds, such as $BiFeO_3$[191]. However, in transition metals, it is negligible due to the near zero pre factor (f_2), reflecting the high symmetry point group and quenched orbital momentum. It won't be detailed in the matrix formalism expressed thereafter.

It is worth to note that the expression 20 considers that the atom environment has a punctual group with a symmetry than can be as low as C_{4h}. It typically describes a cubic symmetry broken by a magnetic moment. The valence shell spin orbit has been neglected because it would distort the orbitals and then lower the symmetry. A strong spin orbit coupling would induce an electronic anisotropy in the valence shell that should give rise to a linear magnetic dichroism[192,193].

The amplitude factors can be written as the sum of a dispersive and an absorption contribution:

$$f_0 = f_0' + if_0''$$

(21)

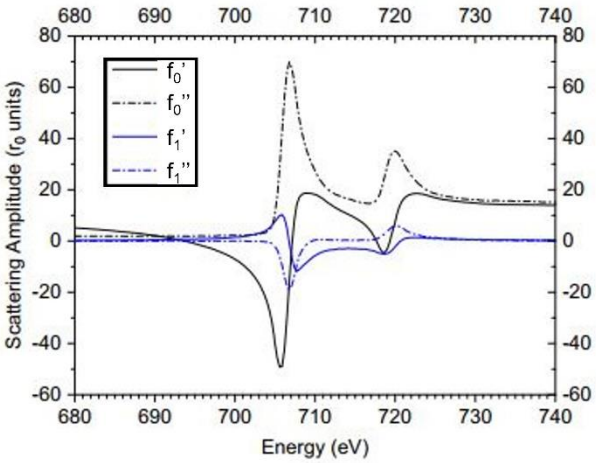

Figure 10: Real (′) and imaginary (") part of the charge (f_0) and pure magnetic (f_1) scattering amplitude at the iron $L_{2,3}$ edges taken from M. Elzo *et al*[194].

The real and imaginary part are linked with each other by the Kramers-Kronig relation and depend strongly on the energy as shown in figure 10.

The relative variation of the dispersive and absorption part changes the penetration depth which allows the magnetic texture depth dependence study. Coupling the energy and angle dependence of the diffracted signal with an off specular software simulation fed by micromagnetic simulations of the in-depth magnetic texture could retrieve the depth variation of the magnetic texture in multilayers. It is of particular interest in thick ferromagnetic multilayers where the dipolar interaction can induce a hybrid chirality within the sample such as in Legrand *et al*.[62] paper. However, due to the smaller length of absorption in the soft X-ray regime, multiple scattering occurs, and the Born approximation must be reconsidered. A recent contribution from Flewett *et al*.[195] uses a distorted wave born approximation (DWBA) simulation program that takes into account absorption and weight the magnetic layers contribution to the off specular scattering. It is of particular interest for 3D magnetization texture refinement and has been used to determine the depth of the ferromagnetic sample's Bloch part, located between the Néel CW and CCW chiral textures.

The use of increasingly complex and thick asymmetric multilayers, with individually thin layers, that can stabilize magnetic skyrmions makes x-ray resonant magnetic scattering (XRMS) a tool of choice or 3D magnetization distribution studies. Reflectivity curves should be performed in order to verify the multilayer quality, especially the roughness at the interfaces and pick up the appropriate incident angle to maximize the magnetic constructive interference effect coming for XRMS images.

1.3.3 A particular case: X-ray reflectivity

X-rays has been first widely used to characterize the electronic density of solids. In 1954, L.G Parratt[196] is the first to use X-ray reflectivity for evaporated copper on a glass substrate, effectively estimating the copper oxide thickness on top. The "Eigenwave" model presented hereafter is based on the classical propagation of eigenwave through the media that use

the quantum description of the photon-matter interaction presented above. This description is similar to other approaches[197–199] but is particularly useful for the simulation of multilayers.

The electromagnetic wave propagation is described by Maxwell equations with the approximations that the medium response to an electric field is proportional to the dielectric permittivity tensor $\hat{\varepsilon}$ and that the magnetic permeability μ is a scalar:

$$\boldsymbol{D} = \varepsilon_0 \hat{\varepsilon} \boldsymbol{E} \; and \; \boldsymbol{B} = \mu_0 \mu \boldsymbol{H}$$

(22)

Where $\boldsymbol{D}$ is the electric displacement, $\boldsymbol{E}$ the electric field, $\boldsymbol{B}$ the magnetic field and $\boldsymbol{H}$ the magnetizing field. A further supposition considers that the medium modifies the amplitude and the direction of the wavevector in addition to the absorption. The propagation equation gives solutions with a propagating vector $\boldsymbol{k}$ equal to:

$$\boldsymbol{k} = \frac{2\pi}{\lambda} \boldsymbol{n}$$

(23)

The anisotrope refractive index $\boldsymbol{n} = (n_x, n_y, n_z)$ is imposed by Maxwell equations and depends on the dielectric permittivity, which is here obtained by a quantum treatment of the atomic scattering amplitude as done by Hannon[190]. The relation between the latter two is given by:

$$\hat{\varepsilon} = 1 + \hat{\chi}$$

$$\hat{\chi} = \frac{4\pi}{{k_0}^2} \sum_a \rho_a f_a$$

(24)

With ρ_a the number of atoms a per volume unit and f_a the scattering amplitude of the atoms a which can be expressed in the dipolar approximation as:

$$f = (\boldsymbol{e'}^* \cdot \boldsymbol{e}) f_0 - i(\boldsymbol{e'}^* \times \boldsymbol{e}) \cdot \boldsymbol{m} f_1$$

(25)

$$f_0 = -r_0 f_{th} + (\frac{3}{4k})[F_{11} + F_{1\bar{1}}]$$

$$f_1 = (\frac{3}{4k})[F_{11} - F_{1\bar{1}}]$$

Where **e = E**/E and **e'** are the polarization vectors of incident and refracted photons respectively. The first term in the f_0 expression corresponds to the Thomson contribution, with r_0 the classical electron radius and f_{th} the Fourier transform of the electronic charge density. f_{1m} terms

corresponds to the photon absorption probability by an atom with a change of m in the angular momentum projected on the unitary quantification axis vector $\boldsymbol{m} = \boldsymbol{M}/|\mathrm{M}|$, chosen as the local magnetic moment direction. Noteworthy, this expression of the scattering amplitude neglects higher terms in the multipolar expansion of the vector potential ($e^{-i\boldsymbol{k}\cdot\boldsymbol{r}} \approx 1 - \cancel{i\boldsymbol{k}\cdot\boldsymbol{r}} + \cdots$), which is correct for soft X-rays. However, in the hard X-rays regime, a correction from the quadripolar term, $i\boldsymbol{k}\cdot\boldsymbol{r}$, is needed and gives a $\Delta L = 2$ contribution, which is usually smaller than the dipolar one.

The permittivity matrix expression in the ortho-normalized ($\hat{x}$, $\hat{y}$, $\hat{z}$) basis gives an antisymmetric matrix with diagonal terms proportional to the Thompson contribution and off diagonal to the magnetic one. Then, it can be injected in equation 24 to give the expression of the dielectric tensor:

$$\hat{\varepsilon} = \begin{pmatrix} \varepsilon & \varepsilon_{xy} & \varepsilon_{xz} \\ -\varepsilon_{xy} & \varepsilon & \varepsilon_{yz} \\ -\varepsilon_{xz} & -\varepsilon_{yz} & \varepsilon \end{pmatrix}$$

(26)

Where $\varepsilon = 1 + \frac{4\pi}{k_0^2}\rho f_0$; $\varepsilon_{xy} = -i\frac{4\pi}{k_0^2}\rho m_z f_1$; $\varepsilon_{xz} = i\frac{4\pi}{k_0^2}\rho m_y f_1$; $\varepsilon_{yz} = -i\frac{4\pi}{k_0^2}\rho m_x f_1$

This dielectric permittivity is then injected in Maxwell classical equations of wave propagation.

Maxwell equations leads to a propagation equation, which in the case of a monochromatic wave with a wave vector $\mathbf{k} = (2\pi/\lambda)\mathbf{n}$, $\boldsymbol{n} \times (\boldsymbol{n} \times \boldsymbol{E}) + \hat{\varepsilon}\boldsymbol{E} = \boldsymbol{0}$[194]. It constrains the refractive index with respect to the permittivity $|n^2\delta_{ik} - n_i n_k - \varepsilon_{ik}| = 0$.

Resolving the equation in a referential attached to a wave vector $\boldsymbol{k}$ which propagates along the $\hat{\boldsymbol{z}}$ axis and considering the permittivity off-diagonal terms negligible compared to the diagonal ones ($\varepsilon_{ik} \ll \varepsilon$) at the second order yields:

$$n^{\pm} \approx \sqrt{\varepsilon \pm i\varepsilon_{xy}} = \sqrt{1 + \frac{4\pi}{k_0^2}\rho(f_0 \pm m_z f_1)} \approx 1 + \frac{2\pi}{k_0^2}\rho(f_0 \pm m_z f_1)$$

(27)

The general refractive index expression is given by:

$$n^{\pm} = \sqrt{1 + \frac{4\pi}{k_0^2}\rho(f_0 \pm \boldsymbol{k}\cdot\boldsymbol{m}f_1)} \approx 1 + \frac{2\pi}{k_0^2}\rho(f_0 \pm \hat{\boldsymbol{k}}\cdot\boldsymbol{m}f_1)$$

(28)

The planar component of the in and out-going wave vectors are conserved. The electric **E** and excitation fields **H** can be expressed as a function of the dielectric tensor and of.

$$\boldsymbol{E} = \hat{\varepsilon}^{-1}\boldsymbol{D}$$

$$\boldsymbol{H} = \boldsymbol{n} \times \boldsymbol{E} = \boldsymbol{n} \times (\hat{\varepsilon}^{-1}\boldsymbol{D})$$

(29)

The two equations give six expressions for the electromagnetic field components. The planar components are linked by the boundary conditions at the interfaces which imposes the conservation of the planar components of $\boldsymbol{E}$ and $\boldsymbol{H}$. The reflected and transmitted waves are calculated using a 4×1 vector $\mathfrak{D}$ that contains both in-going and out-going beam polarizations. At each interface, a 4×4 boundary matrix A_m decomposes $\boldsymbol{E}$ and $\boldsymbol{H}$ planar components in the medium m. The polarization change through the m to m+1 interface is ensured by the $A_{m+1}^{-1}A_m$ matrix product, which gives $\mathfrak{D}_{m+1} = A_{m+1}^{-1}A_m\mathfrak{D}_m$.

In case of a multilayer, the polarization state in the last layer is expressed as[194]:

$$\mathfrak{D}_f = \widehat{M}\mathfrak{D}_i = A_f^{-1}\prod_m A_m P_m A_m^{-1} A_0 \mathfrak{D}_i$$

(30)

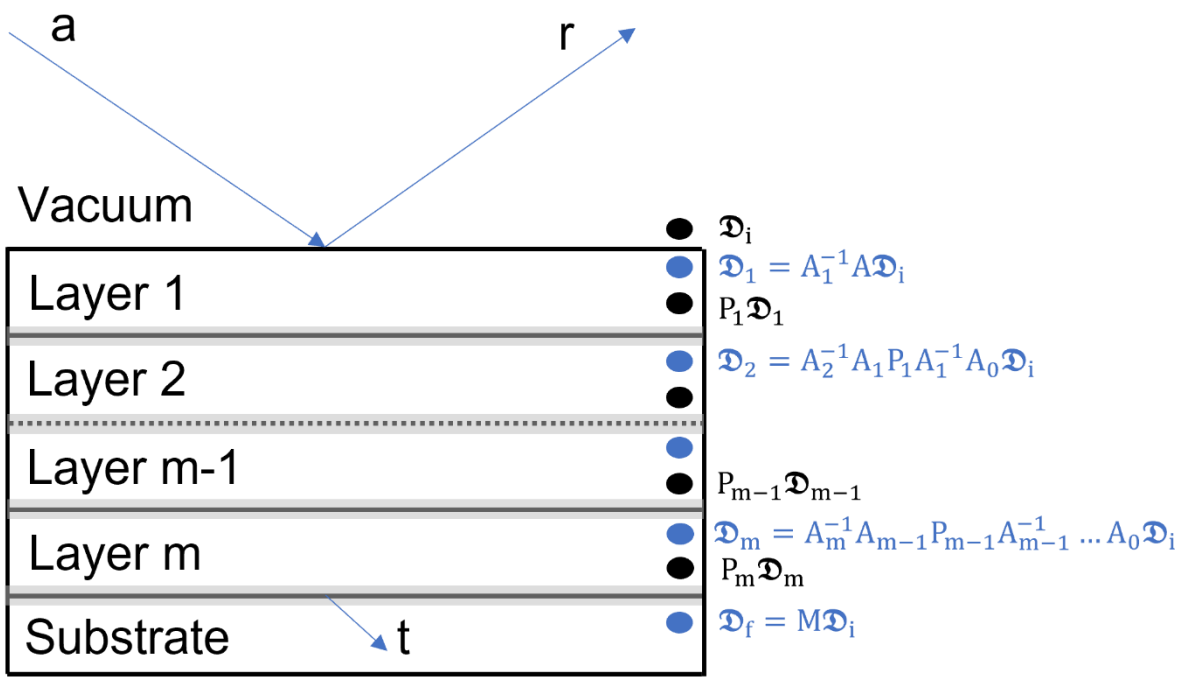

Figure 11: Scheme of the reflectivity calculation. a is the incoming beam, $\mathfrak{D}_i$ the pseudo vector containing the polarization state in the vacuum and the reflected beam r. t is the transmitted beam. $A_m^{-1}A_m$ transmits the polarization states on both side of the interface. P_m is the operator that propagates the wave in a medium. The grey areas at the interfaces represents the electronic roughness which is modelized by an error function, erf.

P_m is a propagation matrix between two interfaces that contains the phase shift and amplitude attenuation experienced by the wave while propagating in a medium.

Noteworthy, the roughness is considered as a $\hat{z}$ variation in the electronic density and must be smaller than the thickness of the layer. Its effect is considered in the interface propagation $A_{m+1}^{-1}A_m$.

The aim is then to solve the following equation considering that only the reflected wave is taken into account at the interface with the last medium:

$$\mathfrak{D}_i = M^{-1}\mathfrak{D}_f = \begin{bmatrix} a_{p_1} \\ a_{p_2} \\ r_{p_1} \\ r_{p_2} \end{bmatrix} = M^{-1} \begin{bmatrix} t_{p_1} \\ t_{p_2} \\ 0 \\ 0 \end{bmatrix}$$

(31)

With r and t, the reflectivity and transmission coefficient for polarization state p_1 or p_2 and a_p the initial polarization state of the incident photons. The interested reader can read Elzo *et al*[194]. work for more details on the matrix formalism notably used in the magnetic reflectivity fit software dyna.

In that section, the photon and matter interactions were briefly discussed and followed by the quantum formalism of the photon-in, photon-out resonant process giving the scattering factor amplitude. The square of the latter is proportional to the diffracted intensity. The particular case of the x-ray resonant reflectivity (XRR) has been briefly presented with a matrix formalism that allows shorter calculation time for the computer. XRR is a powerful tool to study the quality of the multilayer growth and to determine the in-depth magnetic layer to layer magnetization variation.

1.4 Experimental description

XRR needs the photon energy to be tuned at the magnetic element resonant edge. This versatility can be obtained in synchrotron and free electron laser (FEL) facilities. The different experimental set-up and beamlines used during this PhD work as well as the production of the synchrotron radiation are discussed in the following parts.

1.4.1 Synchrotron radiation

The synchrotron radiation has been visually observed in 1947 for the first time by Elder *et al.*[200] at the General Electric 70 MeV electron synchrotron, after its theoretical prediction[201]. It is emitted when a relativistic charged particle is accelerated perpendicularly to its direction of motion. At first, it was seen as a parasitic radiation for particle physics since it represents a loss of energy. However, as particle accelerators went higher in energy, the synchrotron radiation was exploited as a by-product.

It is in 1968 that the first storage ring dedicated to the synchrotron radiation source exploitation has been commissioned[202]. It was a 240 MeV storage ring with an injection current of 50 mA and an average radius of 1.5 meter. It was fed by a fixed small field alternating

gradient accelerator electron synchrotron at 50 MeV. The electrons were injected in an off central orbit, then accelerated by radiofrequency cavities to reach 240 MeV and had a half-life that don't exceed two hours. This dedicated synchrotron radiation source showed the superiority of the electron storage ring. The second generation of synchrotron storage ring were bigger in size and higher in energy. The interest lies in the fact that it increases the brilliance of the beam as the angular emission decreases with the storage ring energy and that it shifts the spectral distribution of the synchrotron radiation towards smaller wavelengths as seen in figure 12. The synchrotron radiation source (SRS) at Daresbury is the figurehead of this generation as it was the first multi-user X-ray synchrotron radiation facility[203]. This period saw the advent of insertion devices, such as wigglers or undulators, producing a brighter synchrotron radiation[204].

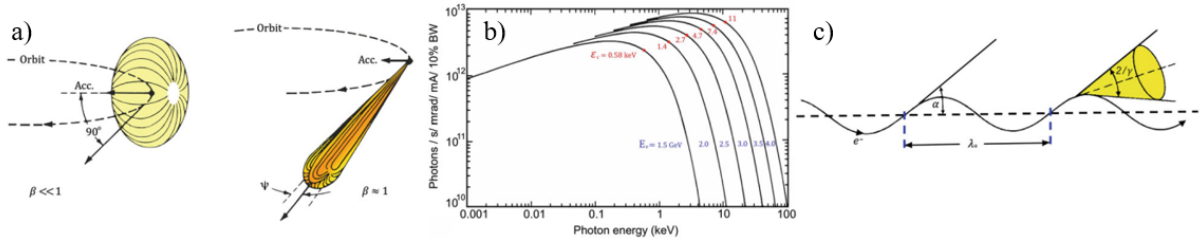

Figure 12: (a) Scheme of the radiation emitted by a charged particle in the non-relativistic case ($\beta = \frac{v}{c} \ll 1$) and in the relativistic case ($\beta \approx 1$). (b) Brilliance spectral distribution of the synchrotron radiation for different storage ring energies. The critical energy ε_c, depends on the storage ring parameters (i.e., electron energy and size of the storage ring) and separate the curve into two parts containing each 50% of the energy emitted. (c) Sketch of the electron motion in an insertion device (wiggler or undulator) with its magnetic periodicity λ_u, the electron wiggling angle α and the synchrotron radiation emission cone depicted in yellow. The cone angle depends on the electron velocity through $\gamma = \frac{1}{\sqrt{1-\beta^2}}$. All figures are taken from Balerna *et al*[204].

Wigglers and undulators consists in two jaws, placed symmetrically with respect to the electron beam in the vertical direction, containing each a periodic arrangement of permanent magnets installed on the storage ring' straight sections. The electrons oscillate perpendicularly to their direction of motion and emit synchrotron radiation (figure 12.c). The small bending radius of the electron beam results in a shift of the emitted photon towards smaller wavelength, an increase of the radiated intensity and brightness. The difference between an undulator and a wiggler can be quantified by a dimensionless parameter K:

$$K = \alpha\gamma \tag{32}$$

With α the wiggling angle and $\gamma = \frac{1}{\sqrt{1-\frac{v^2}{c^2}}} = \frac{1}{\sqrt{1-\beta^2}}$ the Lorentz factor which depends on the electron energy. γ is also the inverse of the synchrotron radiation emission angle. In both, the electron moves in a sinusoidal magnetic field, so that K can be expressed as:

$$K = \frac{e}{2\pi mc}\lambda_u B = 93.4\,\lambda_u B$$

Where λ_u is the magnetic period of the insertion device, expressed here in meter and B the magnetic field in Tesla. In the wiggler case, the deflection parameter $K \gg 1$, which means that the wiggling angle α is large compared to the natural opening angle γ^{-1} of the synchrotron radiation. The main implication is that the radiation emitted at each magnetic periodicity isn't coherent. Thus, the total intensity corresponds to the sum of all individual pole contributions multiplied by number of electrons per bunch. An undulator has a deflection parameter $K \approx 1$. The wiggling angle is then close to the photon emission angle. Knowing that the electron path is sinusoidal, there is an interference effects occurring between photons emitted at different point of the trajectory. It leads to a different spectral distribution of the flux compared to wigglers or bending magnets. Indeed, if the radiation is observed with an angle θ with respect to the undulator axis, the constructive interference gives a condition on the wavelength[205]:

$$\lambda_n = \frac{\lambda_u}{2n\gamma^2}\left(1 + \frac{K^2}{2} + \gamma^2\theta^2\right)$$

Where n is the harmonic number. This expression differs from the wavelength equation obtained for a bending magnet or a wiggler by the factor $\frac{K^2}{2}$ inside the parenthesis. It means that with an undulator, it is possible to tune the wavelength by changing the gap between the two magnetic arrays which modifies the K factor, since it depends on the magnetic field B. Moreover, the intensity of the synchrotron radiation increases as the square of the undulator's magnetic periods number. Undulators opened the way for increasingly coherent synchrotron radiation sources.

The third generation of storage ring have been optimized to maximize the brilliance and reduce the emittance of the source, especially the vertical one. Soleil is one of the most recently built third generation synchrotron. The electrons are extracted from an electron gun and sent toward a 27 meters long linear accelerator. Electrons reach an energy of 100 MeV and are directed toward a 157 meters long circular accelerator, called booster, where they reach the storage ring energy. At SOLEIL, it is a 2.75 GeV storage ring (γ=5400) with a circumference of 354 meters. It has a rectangular shape, the inner vertical size being only 10 mm large. Along the ring, several apparatuses compensate the electron beam perturbations caused by the loss of energy and to the electrostatic repulsion inside the electron bunches. To compensate the beam's energy loss, two cryomodules are installed. They contain each two accelerating cavities that works with superconducting elements cooled at 3 K. Quadrupoles and sextupoles are placed down and upstream each insertion device (wiggler or undulators). They focus the beam and correct the chromatic as well as the geometric aberrations, respectively. It reduces the size and the divergence of the source, which is an important feature for experimental techniques using a coherent beam, such as XRMS. With the third generation of synchrotron and the use of undulators, it is now easier and less costly in photon flux to reach the spatial coherence condition.

In order to study the magnetic chirality in transition metals, it is necessary to use a circularly polarized beam (detailed in chapter 2). For this purpose, the APPLE-II undulators[206] are used. It consists in a 4 jaws undulator that has 4 different arrays of magnets with the same magnetic periodicity that can be displaced with respect to each other. The insertion devices are

installed in the storage ring straight section prior to a beamline. The synchrotron radiation emitted arrives toward the beamlines, where it is exploited.

1.4.2 Description of the SEXTANTS beamline & RESOXS diffractometer

The static experiments were performed at the soft x-ray experiment resonant scattering (SEXTANTS) beamline at SOLEIL synchrotron. Its energy range starts from 50 eV to 1700 eV but is fully optimized in the 70-1200 eV range. It is equipped with two 1.6 m long Apple-II undulators with a 44 mm and 80 mm periodicity that provide a full control on the beam polarization, either linear or circular with a polarization efficiency of 99%. The light arrives on two water cooled mirrors, using a closed-circuit thermostatic bath, that absorb up to 90% of the thermal load coming from the source (undulators). The secondary functions of the two mirrors consist in the fine adjustment of the deviation angle to compensate an eventual displacement of the source position and in the radiation safety fulfilment by displacing the beam with respect to the source axis. They are placed in an aluminium chamber with motors placed outside the chamber preventing any carbon deposition from dust cracking under the intense beam which can happened even in ultra-high vacuum. The beam is then monochromatized by selecting one diffraction order of a grating. There are five different interchangeable variable line spacing (VLS) gratings, all mounted in the same baseplate for rotation (energy selection) and translation (grating selection). They are all water cooled as well as the spherical mirror M2 that focuses the radiation coming from the grating in use towards a vertically occulting exist slit. The monochromator hutch is thermalized at 20°C with a tolerance inferior to 0.1°C. The monochromatic beam is sent into one of the two branches of the beamline using two horizontally deviating toroidal mirrors mounted on the same hexapod device. One mirror (M3) feeds the inelastic part and the M6 send the beam in the elastic one. The switching between the two working positions is realised by a control software that controls the hexapod position. The two branches aim to study the electronic and magnetic properties of the matter using photon-in/photon-out techniques. The resonant inelastic x-ray scattering (RIXS) part probes low electronic excitations with an energy resolution above $5000 < \frac{E}{\Delta E}$ that can reach 20 000 depending on the grating and on the energy[207,208]. During this thesis, only elastic scattering experiments have been carried out.

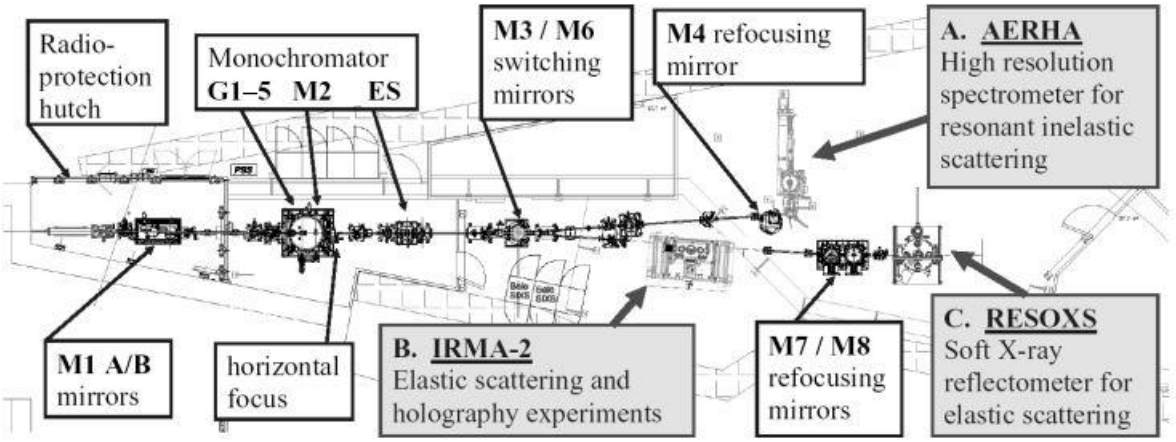

Figure 13: Scheme of the SEXTANTS beamline with the main optical elements and the three end-stations designed with A, B and C. Image taken from Sacchi *et al*[208].

After the M6 mirror, the IRMA-2 location exploits the beam to perform coherent x-ray imaging on magnetic domains, using mainly Fourier transform holography (FTH) or Ptychography techniques in the COMET end-station[209]. It is equipped with four permanent magnets in NdFeB mounted on four rotatable arms. The gap between the magnets and the sample varies by using an Archimedean spiral system which is driven by a single stepper motor. The field at the sample location can reach 1T in the closest gap configuration. The diffracted beam is collected either by a diode or by a CCD camera (mainly used) that can move parallel to the beam axis. After the COMET detection compartment, two plane silica mirrors in Kirkpatrick-Baez (KB) configuration (M7 and M8) mounted on mechanical benders can displace and focus the beam focal point into the C working point.

RESOXS is a diffractometer dedicated to X-ray resonant magnetic scattering in the soft X-ray regime, meaning that it is on UHV condition like the rest of the beamline since air attenuates x-rays strongly at those energies[210]. The motors that rotate or translate the sample and the detector are placed outside the chamber to minimize the vacuum level, which is important when the sample is cooled. The goniometer is mounted in two parts in a way that the sample and detector stages can rotate independently. The sample can be moved in three orthogonal directions, rotate around the Y axis, making an angle θ with the incident beam, and rotate (within a $\pm 3°$ range) around the propagation beam axis. Those rotations are key to correct the sample misalignment due to non-planar sticking on the sample holder. The θ rotation, contrary to the χ one, also affects the two pairs of poles placed in the Y'Z' plane at 45° from Y' and Z' axis. The cylindrical poles are made of pure iron and guide the magnetic flux emitted by the 620 turns coil that surrounds it. Orthogonal poles pairs are supplied independently, which allows different in-plane field configurations. The field generated increases linearly until 0.12 T, corresponding to a current of 2 A, and reach an upper limit of 0.2 T for I = 8 A. The magnetic field produced varies by 3.5% within a volume of 2 mm^3 in the middle of the poles. This volume is far greater than the usual beam size and is of the same order than the sample size usually studied. The remanent bias field has been measured to approximately 3 mT at the middle but, in case the sample is very sensitive to small magnetic field, the magnets can be moved by a rotation around

the Z' axis (not shown in the sketch below). In a near future, the magnet stage will be replaced by a quintupole made of electromagnets which is able to produce an in-plane and out of plane magnetic field that, according to calculations, could reach 0.6 T in the three directions. Noteworthy, all SEXTANTS motors are controlled by a Linux Tango environment.

The sample holder is made of the same material as the cold finger (green part on the figure 14 (a)), that is in high purity copper, preventing any detrimental magnetic forces while measuring and maximizing thermal conductance. The cold finger is the final part of a cryostat system that uses continuously flowing helium to cool the sample. It can reach temperature as low as 30 K, which is sufficient for most magnetic compounds.

The second part of the goniometer holds the detection stage. It is equipped with two detectors. A 21.5 mm sensitive area silicon photodiode (Canberra-Eurisys IP 300-PH-CER) with an electrometer for the signal readout. It is usually used for the reflectivity curves while the diffraction patterns have been collected on a 2D Peltier-cooled 2048x2048 pixels PI-MTE3 CCD detector. The latter covers 6.1° at a working distance of 26 cm from the sample and has a pixel size of 13.5 µm. It is equipped with a beamstop that can moves in the two directions of the detector plane in order to avoid damaging the CCD. The flux produced by the undulator source can exceed 1×10^{19} photons s^{-1} mm^{-2} $mrad^{-2}$ for a 0.1% energy band width. The beam must be fully coherent for imaging techniques, such as holography but not necessarily for XRMS experiments. Also, the absence of magnetic speckles isn't important for the XRMS signal analysis.

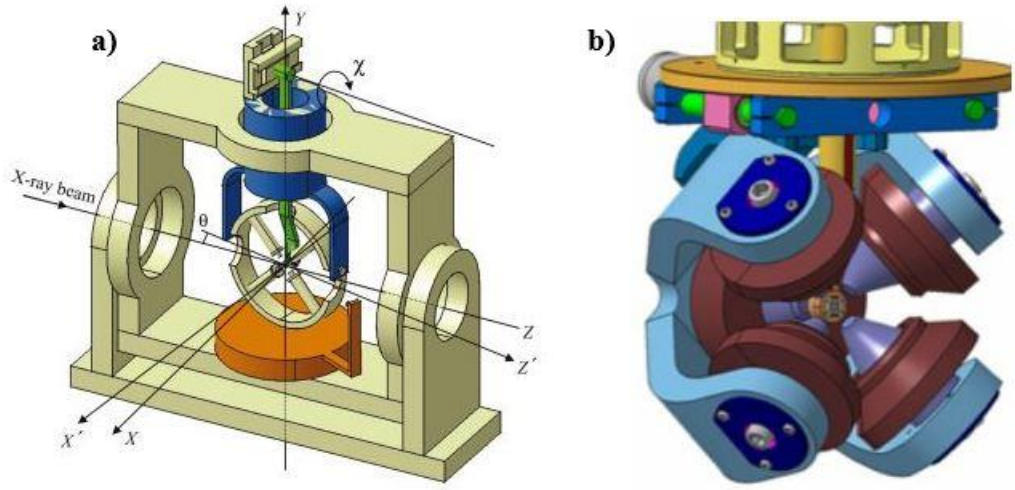

Figure 14: a) Sketch of the goniometer with the movements possible for the sample stage. $\widehat{X,Y,Z}$ represents the X-ray beam basis and $\widehat{X',Y',Z'}$ the sample translations. The mismatch between the two referential can be compensated by the θ and χ rotations. The green part corresponds to the cold finger that hosts the sample holder and is the only one rotating around Z' (χ rotation). The blue part holds the magnetic device which turns around Y the same way as the cold finger. The image is taken from Jaouen *et al*[210]. b) Sketch of the future magnet with the sample holder and the cold finger passing through in the middle of the coils.

The coherence of a beam is described by a spatial and temporal component. The characterization of the spot size has been realized at the intermediate focal point (IRMA-2 or COMET) using a YAG and a CCD detector, yielding a spot size of 80×50 μm^2 (h×v). The coherence properties of the beam were realized in the same chamber under multiple energy and beamline angular acceptance[211]. To do so, a mask containing eleven 200 nm diameter holes distributed in a way that cross-correlation images do not overlap has been used. The beamline angular acceptance has been tuned by varying a 4-jaw aperture placed 10 m after the undulator source.

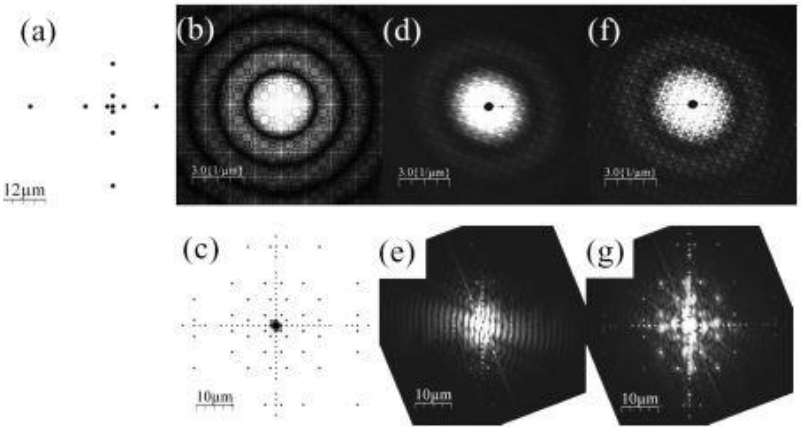

Figure 15: (a) Representation of the mask used for the coherence characterization with its calculated diffraction diagram (b) and the associated 2D Fourier transform (c). Images with their respective 2D Fourier transform (d)-(e) and (f)-(g) were taken with a vertical and horizontal beamline acceptance of 150 μrad and 40 μrad respectively. The same grey scale has been applied for all the experimental data. Figure taken from Sacchi *et al*[211].

The scattering pattern obtained for a 40 μrad acceptance is better defined than the 150 μrad one, resulting in a more defined 2D Fourier transform reconstruction, indicating a better horizontal and transverse coherence of the beam. The spatial coherence is limited by the diffraction limit that depends on the wavelength λ and on the emittance of the beam ϵ:

$$\epsilon \leq {}^{\lambda}/_{4\pi}$$

(33)

The emittance can be expressed as the product of the source size root mean square (rms) σ with its divergence σ' also in rms. The coherence condition must be fulfilled in both directions. In the 3rd synchrotron generation, the electron beam emittance is lower and approaches the diffraction limit[212]. For instance, it can reach 3.9 nm rad at SOLEIL or 2.7 nm rad at Diamond in the horizontal direction, while in the vertical one the emittance is as low as 39 pm rad. The coupling between the vertical and horizontal emittance is around 1%. The energies that have been used during this PhD work corresponds to the Co and Fe L_3 edges which give a diffraction limit equal to ~0.13 nm rad. Thus, since the value of the emittance given earlier is the minimum achievable emittance value, the horizontal direction is not in the required coherent condition. Fortunately, by cutting the beam in the same direction, it is possible to recover the limit at the cost of intensity. It plays on the divergence of the beam and reduces the effective emittance coming at the end station. SEXTANTS beamline is located on a medium straight

section with a source size (divergence) of 350 µm (16.5 µrad) in the horizontal direction. Assuming a gaussian beam shape, the divergence of the photon beam is given by:

$$\sigma'(ph) = \sqrt{{\sigma'_e}^2 + {\sigma'_R}^2}$$

Where σ'_R is the divergence due to the diffraction effect. It is linked to the undulator length and to the desired wavelength by $\sigma'_R = \sqrt{\frac{\lambda}{2L}}$ which is equal to ~23.4 µrad. It gives a photon divergence of ~28.6 µrad. The coherence length, taken at the working position (RESOXS end station in that case) is expressed as:

$$\Lambda \approx \frac{\lambda D}{\pi\sqrt{2}\sigma}$$

(34)

D is the distance between the source and the sample, which is an optical intermediate point at ~ 6 m for RESOXS, λ the wavelength used and σ the size of the source. Taking the experimental parameters at the Fe L_3 edge, it gives a spatial coherence length of ~6 µm in the horizontal direction (while it is of the hundreds of µm order in the vertical one). These figures are theoretical as they don't consider the optical artifacts and the mirrors acceptance angle. The beam is at least 100 µm large in the RESOXS end station, depending on the mirror focus, confirming that the coherent condition is not fulfilled. However, it is possible to use a pinhole located at the entrance of the RESOXS end station if coherent diffraction imaging technique is performed. It is the case for ptychography that can be performed in the IRMA-2 end station, that was previously located at the current COMET location (IRMA-2 location in the original scheme of the beamline).

The future generation of synchrotron facilities will focus on the horizontal emittance reduction to increase the beam spatial coherent as well as its brightness. SOLEIL is nowadays starting a process to upgrade the machine. It aims to reduce the beam horizontal size and divergence with a small increase on the beam vertical properties which should stay in the diffraction limited condition.

The other important component of the coherence is the longitudinal (energy) coherence. The beam emitted from undulator isn't monochromatic and the emission cone is narrow so that the angle spread between the different energies is small. The formula that gives the condition required for the longitudinal coherence is obtained by a simple reasoning. Considers a beam that contains two wavelengths. The first wavelength λ performs N oscillations while the second one, equals to $\lambda + \Delta\lambda$, performs N-1 periods. It yields:

$$N\lambda = (N-1)(\lambda + \Delta\lambda)$$

(35)

A rapid reorganisation gives $\lambda + \Delta\lambda = N\Delta\lambda$. Defining the coherence length as the distance from which, the shift between the two wavefront is equal to half the wavelength, it links the length necessary to perform a full phase shift between the two waves $N\lambda$ and the coherent length, which is half of this value. The longitudinal coherent length is thus given by $l_{coh} = N\lambda/2$, that can be expressed as:

$$l_{coh} = \frac{(\lambda + \Delta\lambda)\lambda}{2\Delta\lambda} \approx \frac{\lambda^2}{2\Delta\lambda}$$

(36)

The second part of the expression has been obtained by considering $\lambda^2 \gg \lambda\Delta\lambda$. It holds true for a sufficiently large resolving power ($\frac{\lambda}{\Delta\lambda}$). In SEXTANTS case, the monochromator is usually above 10 000. The coherent length is thus $l_{coh} \geq \lambda * 5000$ which is equal to 8.75 µm. This length has to be compared with the maximal optic path difference that can exist in the sample studied. The sample used during this work were more than 10 times thinner than 8 µm. Another way to see it, is to compare the length to the penetration depth at the resonance. At the Fe L_3 edge, the absorption coefficient μ is equal to 80 nm, meaning that, if the Fe is the only element that strongly absorbs in the sample, 370 nm is sufficient to attenuate the beam by 99%. The longitudinal coherent condition is thus fulfilled.

In the next years, SEXTANTS beamline will be able to perform time resolved study on the beamline elastic branch, using a femtosecond 1kHz pulsed laser. However, the SOLEIL synchrotron radiation has a limited time resolution of ~50 ps due to the length of the electron bunch. Noteworthy, the issue is common to all synchrotron facilities. It is possible for the machine to work in a low momentum compaction factor (low-α) mode. It consists in a hybrid filling pattern with small and large bunches. In the $\alpha/100$ mode, the small bunches are separated by 2.8 ns and account for a 2 mA current in total compared to the 500 mA on the "normal" operation mode. They are followed by a single bunch of 15 µA shifted by 295.3 ns with respect to the last small bunch. The low-α mode reduces the bunch length to 7 ps. However, it is still too long for probing ultrafast demagnetization behaviours in transition metals that usually occurs at the hundreds of fs timescale. Free electron laser (FEL) facilities can provide such a short bunch length with a high beam peak brilliance that exceeds by at least 6 orders of magnitude the synchrotron one.

1.4.3 The principle of free electron lasers

The principle of a FEL has been invented and demonstrated by J. Madey's group at Stanford University during the 70s[213,214]. The principle is the same as for synchrotron for the injection and LINAC part but differs in the design shape. A FEL is a linear electron accelerator that can be more than two km long (EUXFEL, LCLS) and can be seeded by a laser or not.

During this work, experiments have been mainly performed at Fermi FEL in Italy, on the Elettra synchrotron campus. It is a 320 meters long FEL, optimized for the UV/XUV wavelengths. FEL that emits in the higher energy range, i.e., soft/hard X-ray regime, are usually longer. Fermi is a seeded FEL, which provides a smaller variation in the bunch-to-bunch intensity. After the first 10 m LINAC that increases the electron beam energy to 100 MeV, electrons are sent into a series of LINACs, bunch compressors and a focusing system that provide a 1.2 GeV beam with the minimum transverse emittance. A UV laser (260 nm) is synchronized with the electron bunch to induce an energy modulation inside a short two jaws undulator, called modulator. The modulated bunch passes through a dispersive section that converts the energy modulation into a spatial modulation. The pre-bunched electron beam is finally sent toward a series of undulators, called radiator level, tuned at a harmonic wavelength of the seed laser and separated by quadrupoles that correct the electrons trajectory. Passing through the undulators, the electrons emit a synchrotron radiation, characteristic to the undulator strength, parallel to their trajectory. The photons field interacts and imprints its periodic structure on the electrons beam since its velocity is close to the speed of light. As a result, the initially pre-bunched beam is spatially modulated by the emitted electromagnetic field. Indeed, the periodic electric field accelerates the electrons, that loose or gain energy depending on its position in the bunch. During this period, the light emitted increases linearly as it moves inside undulators. At some point, a denser bunch forms, following the synchrotron radiation wavelength, and emits coherently with it, which reinforces the electric field. In turn, the strengthen radiation forms other dense bunches which emit coherently. During this second phase, the radiation power increases exponentially with the undulator length. Finally, the electron beam is fractioned into small bunches and the emission enhancement saturates, as seen in figure 16. The modulation of the electron density in small bunches by the synchrotron radiation that they produce inside undulators is called microbunching. The total intensity FEL radiation scales as the square of the total number of undulators poles multiplied by the square of the number of electrons inside each microbunch. This process is called self-amplified spontaneous emission (SASE).

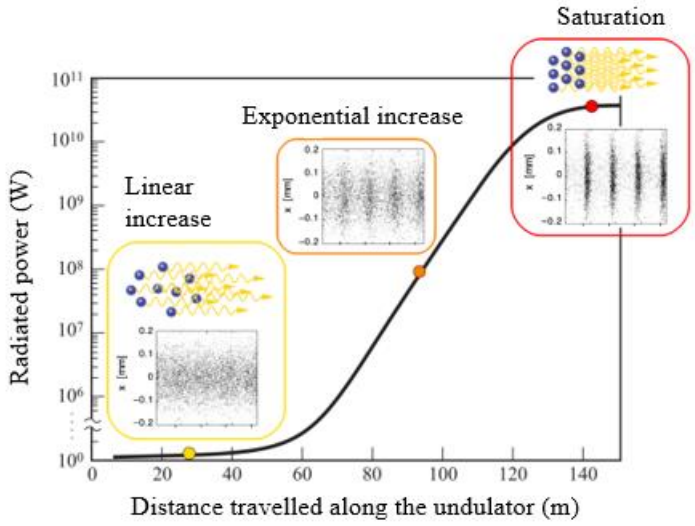

Figure 16: Plot of the radiated power by the electron versus the distance spent inside the undulator to describe the SASE effect. The three graphics are numerical simulations of the electron density distribution[215]. The yellow dot is on the area where there is no modulation in the electron beam (blue dots). The power of the beam increases

linearly with the distance. At the orange dot, a modulation appears, but is still not perfect. The photon flux increases exponentially. Finally, at the red dot, the microbunching is achieved. The photons (yellow arrows) are emitted coherently but the radiated power saturates. The image is taken from Valentin Chardonnet PhD work[155].

Some FEL facilities use two radiator levels to emit shorter wavelength[216]. The pulse from the first shorter radiator level is used as a seed before the electrons enters a dispersive section and the last long radiator section (self-seeded FEL). The seeding process increases the flux emitted per pulse and reduces the shot-to-shot intensity variation between each electron injection compared to SASE FEL. Moreover, with a seeded FEL, the wavelength bandwidth is narrower and the temporal duration of the FEL pulse is mostly determined by the UV seed laser[217]. The FEL pulse duration is usually inferior to 100 fs. After the last radiator level, the electron beam is sent toward a beam dump through magnetic dipoles, while the FEL pulse continues toward the experimental section.

The results presented in this manuscript have been obtained on DiProI end station[218]. It is alternatively fed by both FEL branch (FEL-1 and FEL-2), that covers a spectral range from 100 to 4 nm wavelength in the first harmonic, with a transition between the two complementary FEL lines at 20 nm. FEL-1 has been used for experiment at the cobalt $M_{2,3}$ edge (20.8 nm) since it can produce a degree of circularly polarized X-ray between 92-95%[219]. The change is realized by a switching mirror. A gas cell, equipped with up and downstream intensity monitors, can attenuate the FEL pulse by more than three orders of magnitude. Solid state filters (Al, Zr and Pd) can provide additional attenuation of the intensity. Further downstream, two variable-line spacing plane gratings provides information on the FEL spectral features such as wavelength, spot distribution and at least the relative shot-to-shot intensity. A split and delay device, made of grazing incidence mirrors, can split the FEL pulse in two part to perform FEL-pump FEL probe experiments, with a delay ranging from -2 to 30 ps. The FEL pulse focus is made with two bendable mirrors in KB configuration that can focus the beam down to a 5×6 µm² full width at half maximum spot, which represents several J.cm^{-2} per pulse. In stroboscopic experiments, such as pump-probe, the FEL pulses are coupled with an infrared pump beam, coming from a part of the femtosecond seed laser. Thus, the time jitter between the IR and FEL pulses is as low as 10 fs inside the DiProI end-station. The delay between the pump and probe is realized by a translation stage that provide a $\pm$570 ps delay range. Two thin films polarizers are used to tune the IR pulse energy and a lens telescope can adjust the beam size on the sample. Finally, waveplates can modify the pump polarization.

DiProI end-station is versatile, as it is adapted for transmission or small angle scattering geometry in static or time resolved experiments. The sample holder can move in all directions as well as rotate with respect to the perpendicular to the scattering plane. In particular, the directions perpendicular to the incident beam can move with a precision of 100 nm, which is particularly useful for experiments realized in transmission where samples are deposited on small membranes (usually 500×500 µm²). The sample holder can host multiple samples at the same time. A Si_3N_4 film and an Yttrium Aluminium Garnet (YAG) sample are integrated for the spatial and temporal overlaps between pump and probe beams. A first image of the FEL beam is taken with a visible sensitive camera that is not shielded with an aluminium foil and which integrates more than 20 ms, that corresponds to the FEL and laser repetition rate. The

FEL spot is detected thanks to the YAG luminescence. The wavelength as well as the transition width depends on the doping element, but it is often located around 800 nm. Then, the pump laser beam is moved with a set of mirrors until achieving the spatial overlap. The laser beam size is often 1.5 or 2 times bigger in each direction compared to the FEL beam, so that the probed area is uniformly pumped. Then, the sample holder moves to the Si_3N_4 film to perform the temporal overlap. The laser induced an ultrafast variation of the transmitted or reflected (both are possible) FEL signal of a Si_3N_4 film. The signal is monitored by a photodiode as the delay line moves and compared to the tabulated ultrafast variation of the Si_3N_4 film at the corresponding angle. The moment where the two beams match is called t_0.

Once both spatial and temporal overlaps are performed, the two beams' intensities are adjusted to not destroy or degrade the sample. A 1 mm ball-shaped beamstop placed at 35 mm from the sample holder block either the direct FEL beam in transmission geometry or the specular reflection in reflection scattering. It increases the signal to noise ratio of scattered beam collected on the 2048×2048 pixels Princeton instrument MTE2048 CCD detector. The camera is mounted on a xz translation stage allowing to change the maximum collection angle. It ranges from 14.5° when the sample to CCD distance is equal to 55 mm to 5.1° when the distance is moved to 150 mm. For a distance of 100 mm, the beamstop covers an angle of about $\pm 0.8°$ at the diffraction pattern's center. Finally, an aluminium foil covers the CCD chip to stop any IR laser stray light.

In that chapter, the different magnetic interactions and spin textures that can exist in our multilayers have been detailed. Then, the debate on the mechanism responsible for the ultrafast dynamic has been presented. At the moment, there is a convergence toward the coexistence of multiple mechanism as not a single one can explain the different results found in a variety of samples. Usually, the study of the ultrafast magnetization behaviour is performed at saturation with MOKE. Few studies focused on the evolution of the magnetic domain pattern, but the characteristic time for the demagnetization is similar to the saturated state. The study of the off-specular scattering peak position, related to the magnetic texture periodicity, shows different behaviours. In some studies, the periodicity increases (in real space) in the sub-picosecond time scale, while other found a variation after few picoseconds or none. XRR, presented in the third sub-chapter, is a powerful technique to study magnetic properties in multilayers. To maximize the magnetic contrast, the energy of the photon has to be tuned at the resonance edge involving a spin polarized shell and a relatively strong transition that is linked with the orbitals overlap between the two levels. The synchrotron radiation, produced in synchrotron or FEL facilities, is a versatile source that fulfil the photon energy tuning. The various means to product the synchrotron radiation have been reviewed as well as the different facilities and experimental chambers which have been used during this PhD.

Chapter 2: Probe the magnetic chirality

The word "chirality" has been first introduced into science by Lord Kelvin in the middle of the 19th century. In magnetic samples, the first X-ray observation of dipolar-induced chiral closure domains has been performed by Dürr *et al*.[72] in 1999 on a 40 nm FePd film deposited on MgO and capped by a 2 nm Pd layer. The prediction of interfacial DMI[42,49] (as discussed in chapter 1) and its subsequent application in multilayers offer the possibility to engineer the magnetic parameters by tuning the stacking order, the layer composition and thickness. More recently, it has been shown that magnetic texture chirality determines the electrically driven propagation direction of the DWs and enables higher velocities[5]. XRMS is well suited to easily determine the periodicity of the magnetic texture, the type and the chirality of the DWs.

In this chapter, the XRMS theory is presented with an emphasis to its capacity to probe magnetic chirality illustrated for a simple single magnetic layer with different magnetic textures. In a second part, the different results previously obtained for FM multilayers are presented. This chapter will finish with a new study performed on SAF samples.

2.1 XRMS formalism

The theoretical results presented in this chapter can be expressed in a σ, π linear polarization basis (see figure 17 below). It is a more convenient way to present the results as it gives direct insight of the different polarization channels in the diffracted beam.

The linear polarization basis used in the following can be expressed as:

$$\begin{pmatrix} \sigma \rightarrow \sigma' & \pi \rightarrow \sigma' \\ \sigma \rightarrow \pi' & \pi \rightarrow \pi' \end{pmatrix}$$

With σ, π (σ', π') are respectively the incoming and outgoing linear polarization perpendicular and parallel to the scattering plane respectively which is defined by **k** and **k'**:

$$\begin{pmatrix} \boldsymbol{k} \\ \boldsymbol{k'} \end{pmatrix} = \begin{pmatrix} \cos(\theta) & -\sin(\theta) \\ \cos(\theta) & \sin(\theta) \end{pmatrix} \begin{pmatrix} \boldsymbol{x} \\ \boldsymbol{z} \end{pmatrix} ; \ \boldsymbol{k'} \times \boldsymbol{k} = -\hat{\boldsymbol{y}} \sin(2\theta) \text{ and } \boldsymbol{q} = \boldsymbol{k'} - \boldsymbol{k}$$

(37)

Where $\widehat{x, y, z}$ is an orthogonal and normalized basis defined with the sample plane as depicted below:

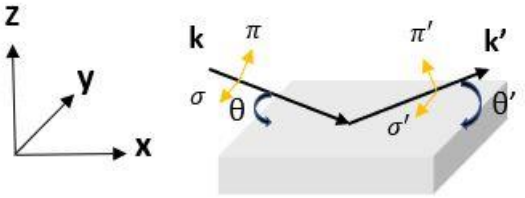

Figure 17: Scheme of the orthogonal basis used with respect to the sample plane.

The expression of the intensity depends on the Fourier transform of the scattering amplitude. The later contains 3 different contributions, as seen in chapter 1 paragraph 3.2:

$$F(\boldsymbol{q}) = M_c(\boldsymbol{q}) + M_m(\boldsymbol{q}) + M_Q(\boldsymbol{q})$$

The charge, magnetic and quadripolar terms can be written in the σ, π basis:

$$M_c(\boldsymbol{q}) = F_0\hat{\rho}(\widehat{\boldsymbol{e}'}^* \cdot \widehat{\boldsymbol{e}}) = F_0\hat{\rho}\begin{pmatrix}1 & 0\\ 0 & \boldsymbol{k}'\cdot\boldsymbol{k}\end{pmatrix} = F_0\hat{\rho}\begin{pmatrix}1 & 0\\ 0 & \cos 2\theta\end{pmatrix}$$

(38)

$$M_m(\boldsymbol{q}) = -iF_1\left(\widehat{\boldsymbol{e}'}^* \times \widehat{\boldsymbol{e}}\right)\cdot\widehat{\boldsymbol{m}} = -iF_1\begin{pmatrix}0 & \boldsymbol{k}\cdot\widehat{\boldsymbol{m}}\\ -\boldsymbol{k}'\cdot\widehat{\boldsymbol{m}} & (\boldsymbol{k}'\times\boldsymbol{k})\cdot\widehat{\boldsymbol{m}}\end{pmatrix}$$
$$= -iF_1\begin{pmatrix}0 & \widehat{m_x}\cos\theta + \widehat{m_z}\sin\theta\\ -\widehat{m_x}\cos\theta + \widehat{m_z}\sin\theta & -\widehat{\mathrm{m}_\mathrm{y}}\sin 2\theta\end{pmatrix}$$

(39)

$$M_Q(q) = F_2(\widehat{\boldsymbol{e}'}^* \cdot \widehat{\boldsymbol{m}})(\hat{\boldsymbol{e}}\cdot\widehat{\boldsymbol{m}})$$
$$= F_2\begin{pmatrix}\widehat{m_y^2} & -\widehat{m_y}(\widehat{m_x}\sin\theta - \widehat{m_z}\cos\theta)\\ \widehat{m_y}(\widehat{m_x}\sin\theta + \widehat{m_z}\cos\theta) & -\cos^2\theta\,(\widehat{m_x^2}\tan^2\theta + \widehat{m_z^2})\end{pmatrix}$$

(40)

F_0, F_1 and F_2 are the Fourier transform of the transition strength factor f_0, f_1, f_2, respectively. $\widehat{m}$ and $\hat{\rho}$ are the magnetization and charge density Fourier transform. The diagonal matrix in the charge contribution indicates that the polarization won't rotate on the contrary to the magnetic linear part. The expression of the total intensity in the matrix formalism, which is equivalent to equation17, is given by:

$$I(\boldsymbol{q}) = Tr[F\cdot\bar{\mu}\cdot F^\dagger]$$

(41)

With F ($F^\dagger$) the (transposed and complex conjugate) scattering amplitude and $\bar{\mu}$ a density matrix that stands for the polarization of the incident beam. In the Cartesian linear polarization coordinates, it can be written as[220]:

$$\bar{\mu} = \frac{1}{2}(P_0 I_0 + \boldsymbol{P}\cdot\bar{\boldsymbol{\sigma}}) = \frac{1}{2}\begin{pmatrix}P_0+P_1 & P_2 - iP_3\\ P_2 + iP_3 & P_0 - P_1\end{pmatrix} = \frac{1}{2}\begin{pmatrix}P_\sigma & P_2 - iP_3\\ P_2 + iP_3 & P_\pi\end{pmatrix}$$

(42)

In the equation above, I_0 is the unit matrix, $\bar{\boldsymbol{\sigma}}$ is the Pauli matrix vector while $\boldsymbol{P} = (\boldsymbol{P_1}, \boldsymbol{P_2}, \boldsymbol{P_3})$ expresses the polarization in the Poincaré-Stokes's representation. The table below indicates the P vector combination for each polarization state.

Table 1: Pure polarization states expressed in the Stokes-Poincaré formalism. Table is taken from Van der Laan, C.R physique 2008[220].

	P_0	P_1	P_2	P_3
σ polarization	1	1	0	0
π polarization	1	−1	0	0
Linear polarization at ±45°	1	0	±1	0
Circular polarization	1	0	0	±1
Polarization averaged	1	0	0	0
Linear dichroism	0	1	0	0
Circular dichroism	0	0	0	1

In this thesis, circular polarized light has been used to study the magnetism of magnetic layers of 3*d* transition metal. Neglecting the term quadratic with the magnetic moment we can derive the following expression for the scattered intensity:

$$I(q) = Tr\left[M_c \cdot \bar{\mu} \cdot M_c^{\dagger}\right] + Tr\left[M_m \cdot \bar{\mu} \cdot M_m^{\dagger}\right] + Tr\left[M_m \cdot \bar{\mu} \cdot M_c^{\dagger} - M_c \cdot \bar{\mu} \cdot M_m^{\dagger}\right] \equiv I_c(\boldsymbol{q}) + I_m(\boldsymbol{q}) + I_i(\boldsymbol{q})$$

(43)

Where the three intensities I_c, I_m and I_i refer to the charge, magnetic and interference between the two, respectively. The charge term won't change with the polarization reversal, thus I_c is not developed. I_m and I_i are expressed taking $P_0 = 1$, $P_1 = P_2 = 0$ and $P_3 = \pm 1$.

$$I_m(\boldsymbol{q}) = \frac{|F_1|^2}{2}\left[|\boldsymbol{k}' \cdot \widehat{\boldsymbol{m}}|^2 + |\boldsymbol{k} \cdot \widehat{\boldsymbol{m}}|^2 + |(\boldsymbol{k}' \times \boldsymbol{k}) \cdot \widehat{\boldsymbol{m}}|^2 + 2P_3 \Im m[(\boldsymbol{k}' \cdot \widehat{\boldsymbol{m}^*})(\boldsymbol{k}' \times \boldsymbol{k}) \cdot \widehat{\boldsymbol{m}}]\right]$$

(44)

$$I_i(\boldsymbol{q}) = \Im m\left[F_0^* \widehat{\rho^*} F_1\left(\widehat{\boldsymbol{m}} \cdot (\boldsymbol{k}' \times \boldsymbol{k})(\boldsymbol{k}' \cdot \boldsymbol{k})\right)\right] + P_3 \Re e\left[F_0^* \widehat{\rho^*} F_1\left(\boldsymbol{k} \cdot \widehat{\boldsymbol{m}} + (\boldsymbol{k}' \cdot \widehat{\boldsymbol{m}})(\boldsymbol{k}' \cdot \boldsymbol{k})\right)\right]$$

(45)

From equation 44, we can see that the magnetic intensity is proportional to the square of the magnetization while the interference contribution (45) is linear with the magnetic moment.

2.2 Example of applications with circularly polarized light

In this section, we will discuss the different possible results that can be obtained with XRMS on a magnetic single layer. In the first part, the transmitted signal obtained in the direct beam or diffraction pattern is briefly discussed. Then, the off-specular signal coming from a striped magnetic domain pattern with chiral DWs is calculated. The XRMS signal coming from Bloch and Néel DW types (depicted in figure 18) with magnetic stripes oriented along or perpendicular to the scattering plane are treated. The asymmetry ratio (defined thereafter) of different magnetic textures is calculated. Finally, the experimental results obtained on chiral FM multilayers with XRMS are described.

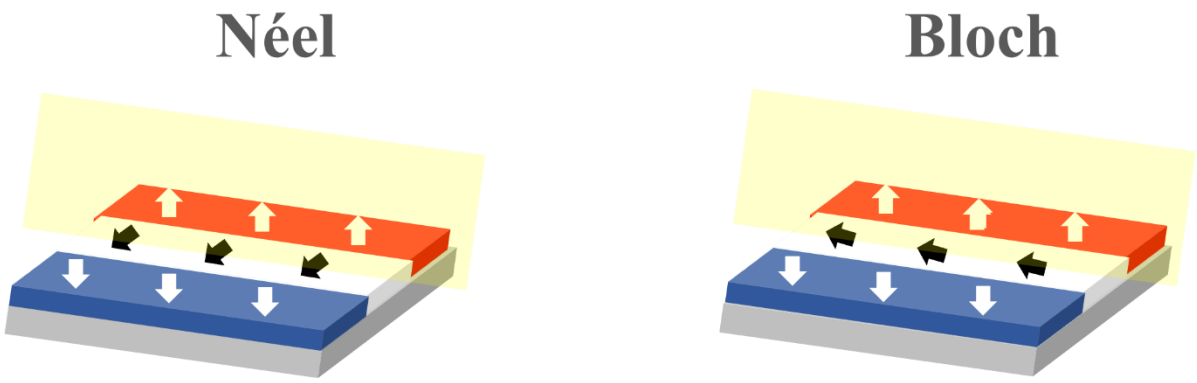

Figure 18: Scheme of the cycloidal rotation (Néel) and of the helicoidal (Bloch) rotation of the spin through a DW. The domains are in stripes and parallel to the scattering plane (yellow rectangle).

2.2.1 Case of the transmission geometry

2.2.1.1 In the transmitted direct beam

As defined in equation 43, the signal originates from the addition of a charge, magnetic and an interference term between the charge and the magnetic contributions. A way to cancel the charge contribution is to look at the dichroic signal. The dichroism is defined as the DIFFERENCE of the circular left and the circular right polarization (CL – CR) intensities. In this geometry, the X-ray beam is normal to the sample surface, meaning that the scattered and incident wavevectors are equal $\boldsymbol{k}' = \boldsymbol{k}$. This implies that their cross-product cancels out, $\boldsymbol{k}' \times \boldsymbol{k} = \boldsymbol{0}$. The circular polarization is the only parameter that should change (P_3) during the signal acquisition. In the direct beam, the magnetic and interference intensities yield:

$$I_m^{CL}(\boldsymbol{q}) - I_m^{CR}(\boldsymbol{q}) = I_m^{CL-CR}(\boldsymbol{q}) = 0$$

$$I_i^{CL-CR}(\boldsymbol{q}) = 4Re[F_0^* \widehat{\rho^*} F_1(\boldsymbol{k} \cdot \widehat{\boldsymbol{m}})]$$

$$I_m^{CL+CR}(\boldsymbol{q}) = |F_1|^2[|\boldsymbol{k}\cdot\widehat{\boldsymbol{m}}|^2]$$

$$I_i^{CL+CR}(\boldsymbol{q}) = 0$$

The pure magnetic term in the DIFFERENCE and the interference term in the SUM cancel out because of the $\boldsymbol{k}'\times\boldsymbol{k}$ cross product. The remaining intensity originates from the interference term for the DIFFERENCE and the magnetic contribution in the SUM. Both depend on the scalar product $\boldsymbol{k}\cdot\widehat{\boldsymbol{m}}$. Note that, contrary to the SUM, no charge signal is left in the dichroic result. As the wavevector $\boldsymbol{k}$ is perpendicular to the sample surface, only the Fourier transform component of the magnetization parallel to $\boldsymbol{k}$ and corresponding to a non-zero charge distribution in the same direction is probed. Thus, only the net magnetic moment in the sample is probed in the transmitted direct beam, that corresponds to the zero-order beam. It is the particular case of x-ray magnetic circular dichroism (XMCD) that allow to probe the magnetic moment in a sample at saturation (using an external field).

2.2.1.2 In the transmitted diffraction geometry

For a sample at remanence, i.e., in the presence of alternating magnetic domains, it is possible to obtain a diffraction pattern in transmission geometry because the sample acts as a magnetic grating. The scattering angle is usually small (few degrees) due to the magnetic period of few hundreds of nanometers relative to the light wavelength (20.8 nm maximum). meaning that the incident and scattered wavevectors are still equivalent. To simply illustrate analytically the possible results, the magnetic pattern is taken as a perfectly aligned Néel CW ($\mathcal{X}=1$) spin spiral with a periodicity along y, perpendicular to the scattering plane with no depth dependence. The normalized magnetic vector is written:

$$\boldsymbol{m} = \begin{pmatrix} 0 \\ \mathcal{X} m_y \sin\, k_y y \\ \mathrm{m_z} \cos\, k_y y \end{pmatrix} = \begin{pmatrix} 0 \\ m_y \sin\, k_y y \\ \mathrm{m_z} \cos\, k_y y \end{pmatrix}$$

(46)

The amplitude of the magnetization wavector $\boldsymbol{k_y}$ is equal to $2\pi/p_y$ with p_y the periodicity of the magnetic texture in the $\boldsymbol{y}$ direction. The magnetization components amplitude m_y= m_z=1 is written to distinguish the geometrical components in the intensity latter. The magnetic vector Fourier transform gives the following components referred previously as ($\widehat{m}_x$, $\widehat{m}_y$, $\widehat{m}_z$):

$$\widehat{\boldsymbol{m}} = \begin{pmatrix} 0 \\ -im_y\left(\delta(q-k_y)-\delta(q+k_y)\right) \\ m_z\left(\delta(q-k_y)+\delta(q+k_y)\right) \end{pmatrix}$$

(47)

With the Dirac delta function referred as $\delta(\boldsymbol{q})$. This expression is injected into I_i for the cases $\boldsymbol{q}=\boldsymbol{k}_y$ and $\boldsymbol{q}=-\boldsymbol{k}_y$.

$$I_i^{CL-CR}(\boldsymbol{q}=\boldsymbol{k_y}) = 4\Re e[F_0^*\hat{\rho}^* F_1(m_z)] = 0 = I_i^{CL-CR}(\boldsymbol{q}=-\boldsymbol{k_y})$$

$$I_m^{CL-CR}(\boldsymbol{q}=\boldsymbol{k_y}) = 0 = I_m^{CL-CR}(\boldsymbol{q}=-\boldsymbol{k_y})$$

$$I_i^{CL+CR}(\boldsymbol{q}=\boldsymbol{k_y}) = 0 = I_i^{CL+CR}(\boldsymbol{q}=-\boldsymbol{k_y})$$

$$I_m^{CL+CR}(\boldsymbol{q}=\boldsymbol{k_y}) = 2|F_1|^2[|\boldsymbol{k}\cdot\widehat{\boldsymbol{m}}|^2] = I_m^{CL+CR}(\boldsymbol{q}=-\boldsymbol{k_y})$$

No magnetic dichroism is obtained at $\boldsymbol{q}=\pm\boldsymbol{k_y}$ due to the Fourier transform of the charge density distribution, $\hat{\rho}^*$, that has no in plane component in homogenous layers and that the transmission geometry cancels the cross product in I_m. However, in the SUM image of CL + CR polarization, the pure magnetic term gives a scattering at $\pm\boldsymbol{k_y}$ with the same intensity on both side of the direct beam.

2.2.2 Case of the reflection geometry:

2.2.2.1 Case of a Néel spin spiral stripes

2.2.2.1.1 Magnetic stripes parallel to the scattering plane

In this paragraph, we will illustrate the fact that in reflection geometry one can probe the in-plane component of the magnetization. It is the geometry privileged during the thesis since it ultimately gives access to the type and to the chirality of the DWs or closure domains, which is the quantity we want to have access.

In the formal calculations below, the scattering plane is assumed to be defined by the (x,z) vectors as depicted in figure 17. The same spin spiral magnetic texture is assumed with $\boldsymbol{k}$ and $\boldsymbol{k}'$ defined by equation 37. The focus is brought on the off-specular diffracted intensity, as the specular signal corresponds to the magnetic reflectivity which has been presented in the first chapter. In the off-specular scattering, the interference term between the charge and the magnetic signal cancels if there is no common IP modulation, which is in general valid. A $\boldsymbol{y}$ periodic CW Néel stripy spin spiral texture is used on equation 44. The $\boldsymbol{q}$ dependent magnetic signal for each circular light helicity is given by:

$$I_m^{CR}(\boldsymbol{q}=\boldsymbol{k_y}) = \frac{|F_1|^2}{2}\left[2m_z^2\sin^2\theta + m_y^2\sin^2 2\theta + 2(\mathrm{m_z}\sin\theta)(-m_y\sin 2\theta)\right]$$

$$I_m^{CL}(\boldsymbol{q}=\boldsymbol{k_y}) = \frac{|F_1|^2}{2}\left[2m_z^2\sin^2\theta + m_y^2\sin^2 2\theta - 2(\mathrm{m_z}\sin\theta)(-m_y\sin 2\theta)\right]$$

$$I_m^{CR}(\boldsymbol{q}=-\boldsymbol{k_y}) = \frac{|F_1|^2}{2}\left[2m_z^2\sin^2\theta + m_y^2\sin^2 2\theta + 2(\mathrm{m_z}\sin\theta)(+m_y\sin 2\theta)\right]$$

$$I_m^{CL}(\boldsymbol{q} = -\boldsymbol{k_y}) = \frac{|F_1|^2}{2}\left[2m_z^2 \sin^2\theta + m_y^2 \sin^2 2\theta - 2(\mathrm{m_z}\sin\theta)(+m_y \sin 2\theta)\right]$$

(48)

One notices quickly that the intensity in one diffraction spot of one helicity is equal to the other spot intensity in the other circular helicity.

$$I_m^{CR}(\boldsymbol{q} = \boldsymbol{k_y}) = I_m^{CL}(\boldsymbol{q} = -\boldsymbol{k_y})$$

$$I_m^{CL}(\boldsymbol{q} = \boldsymbol{k_y}) = I_m^{CR}(\boldsymbol{q} = -\boldsymbol{k_y})$$

The intensity of the two diffraction spots when taking the DIFFERENCE yields:

$$I_m^{CL-CR}(\boldsymbol{q} = \boldsymbol{k_y}) = -\,I_m^{CL-CR}(\boldsymbol{q} = -\boldsymbol{k_y}) = -2|F_1|^2[(\mathrm{m_z}\sin\theta)(m_y \sin 2\theta)]$$

(49)

It results that in the theoretical DIFFERENCE image, schemed in figure 19, there is a dichroism in the diffraction spots at $\boldsymbol{q} = \pm\boldsymbol{k_y}$ resulting from the interference of the m_y and m_z components of the magnetization.

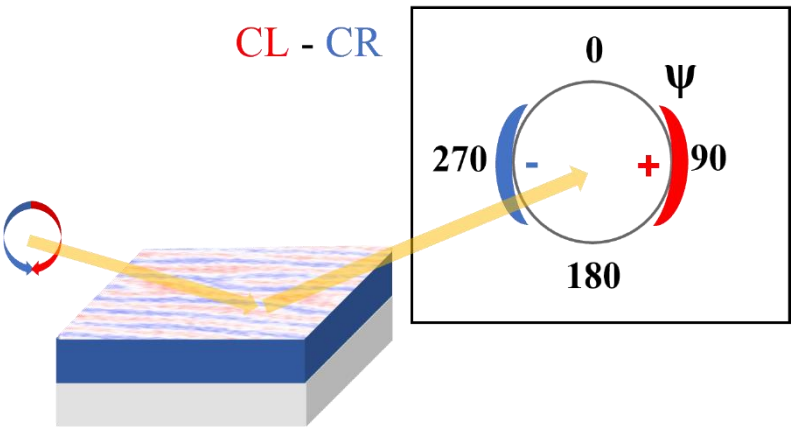

Figure 19: Scheme of the theoretical DIFFERENCE image obtained for a CW and Néel type stripes that are aligned with the scattering plan. The image is looked from the photon direction of propagation (in front of the sensor).

For a Néel CCW ($\mathcal{X} = -1$) DWs, the m_y component would be opposite to the CW chirality in equation 46. It leads to an opposite dichroism in the DIFFERENCE image compared to the Néel CW DWs as depicted in figure 20.

$$I_m^{CL-CR}(\boldsymbol{q}=\boldsymbol{k_y}) = -I_m^{CL-CR}(\boldsymbol{q}=-\boldsymbol{k_y}) = 2|F_1|^2[(\mathrm{m_z}\sin\theta)(m_y \sin 2\theta)]$$

(50)

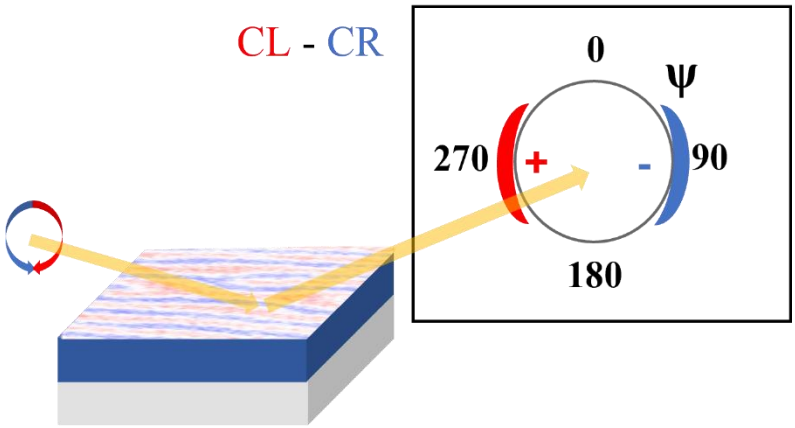

Figure 20: Scheme of the difference image obtained in the same experimental conditions as figure 19 except that the magnetization rotation is CCW in the DWs.

However, the SUM intensity doesn't change and can be written as:

$$I_m^{CL+CR}(\boldsymbol{q}=\boldsymbol{k_y}) = I_m^{CL+CR}(\boldsymbol{q}=-\boldsymbol{k_y}) = |F_1|^2[2m_z^2 \sin^2\theta + m_y^2 \sin^2 2\theta]$$

(51)

The intensity in the SUM signal is of the same amplitude for $\boldsymbol{q} = \pm\boldsymbol{k_y}$. It depends on the square of the z and y components of the magnetization, which are of the same amplitude in a spin spiral texture. The SUM signal is dominated by the z component in more usual magnetic patterns simply because the domains, oriented along the $\pm\boldsymbol{z}$ axis, are larger (few hundreds of nanometers) than the DWs (few tens of nanometers). The consequence of this on the SUM and DIFFERENCE intensities will be discussed later in that chapter. In that part, the cases of Néel type spin spiral stripes aligned with the scattering plane has been explored. In the following sub-section, the theoretical signal when the stripes are perpendicular to the scattering plane is developed.

2.2.2.1.2 Magnetic stripes perpendicular to the scattering plane

The magnetic pattern is identical to the previous paragraph but simply rotated by 90°. The perfectly aligned Néel CW spin spiral texture has now a periodicity along $\boldsymbol{x}$. We consider for simplicity also a constant depth dependence and a magnetic pattern invariant by translation parallel to the $\boldsymbol{y}$ axis. The normalized magnetic vector is now written:

$$\boldsymbol{m} = \begin{pmatrix} m_x \sin(k_x x) \\ 0 \\ m_z \cos(k_x x) \end{pmatrix}$$

The Fourier transform of the magnetization vector is given by:

$$\widehat{\boldsymbol{m}} = \begin{pmatrix} -im_x\big(\delta(q-k_x) - \delta(q+k_x)\big) \\ 0 \\ m_z\big(\delta(q-k_x) + \delta(q+k_x)\big) \end{pmatrix}$$

Inserting the last expression into equation 44 with the same wavevectors yields:

$$I_m^{CL-CR}(\boldsymbol{q} = \boldsymbol{k_x}) = 2|F_1|^2[Im[(\boldsymbol{k'} \cdot \widehat{\boldsymbol{m}^*})(\boldsymbol{k'} \times \boldsymbol{k}) \cdot \widehat{\boldsymbol{m}}]] = I_m^{CL-CR}(\boldsymbol{q} = -\boldsymbol{k_x}) = 0$$

$$I_m^{CL+CR}(\boldsymbol{q} = \boldsymbol{k_x}) = I_m^{CL+CR}(\boldsymbol{q} = -\boldsymbol{k_x}) = 2|F_1|^2[m_x^2 \cos^2\theta + m_z^2 \sin^2\theta]$$

(52)

The consequence is that due to the $(\boldsymbol{k'} \times \boldsymbol{k}) \cdot \widehat{\boldsymbol{m}}$ term, the dichroic signal is zero at $\pm\boldsymbol{k_x}$. This implies that when dealing with magnetic stripes, the chirality is accessible with XRMS if there is a magnetic contribution parallel ($\boldsymbol{k'} \cdot \widehat{\boldsymbol{m}^*}$) and perpendicular ($(\boldsymbol{k'} \times \boldsymbol{k}) \cdot \widehat{\boldsymbol{m}}$) to the scattering plane as it is the product of the two that build the dichroic signal.

For the SUM (CL + CR), the diffracted intensity isn't strongly affected by the azimuthal angle.

The Néel type DW is mostly found in multilayers or thin films, while the Bloch type can be found in bulk material with a broken inversion symmetry. In the next sub-section, a similar treatment is applied.

2.2.2.2 Case of a Bloch spin spiral stripes

2.2.2.2.1 Magnetic stripes parallel to the scattering plane

A Bloch type DW consists in the helical rotation of the magnetization from one domain to another. In opposition to the Néel DW, the magnetization acquires a component parallel to the DW direction. If one considers a CW Bloch type spin spiral parallel to the scattering plan, the magnetization vector is written:

$$\boldsymbol{m} = \begin{pmatrix} m_x \sin\ k_y y \\ 0 \\ \mathrm{m_z} \cos\ k_y y \end{pmatrix}$$

The stripes periodicity is along the $\boldsymbol{y}$ axis but no magnetization component is found out of the scattering plan. This case is mathematically equivalent to the Néel CW stripes perpendicular to the scattering plane. The Fourier transform of the magnetization won't be written down again

as there are similarities between the Néel results and both Bloch geometry. The DIFFERENCE and SUM intensities yield:

$$I_m^{CL-CR}(\boldsymbol{q} = \boldsymbol{k_y}) = I_m^{CL-CR}(\boldsymbol{q} = -\boldsymbol{k_y}) = 0$$

$$I_m^{CL+CR}(\boldsymbol{q} = \boldsymbol{k_y}) = I_m^{CL+CR}(\boldsymbol{q} = -\boldsymbol{k_y}) = 2|F_1|^2[m_x^2 \cos^2\theta + m_z^2 \sin^2\theta]$$

Thus, the dichroic signal with a Bloch type DW stripes is obtained with the stripes perpendicular to the scattering plane.

2.2.2.2.2 Magnetic stripes perpendicular to the scattering plane

The last situation considered with a stripy magnetic texture is with a Bloch type spin spiral stripes aligned perpendicular to the scattering plan. The magnetization vector is similar to the CW Néel stripes parallel to the scattering plan.

$$\boldsymbol{m} = \begin{pmatrix} 0 \\ m_y \sin\ k_x x \\ m_z \cos\ k_x x \end{pmatrix}$$

Following the same calculation as in equation 47, the scattered intensity in the DIFFERENCE is given by:

$$I_m^{CL-CR}(\boldsymbol{q} = \boldsymbol{k_x}) = -\ I_m^{CL-CR}(\boldsymbol{q} = -\boldsymbol{k_x}) \propto -2(\mathrm{m_z} \sin\theta)(m_y \sin 2\theta)$$

Here, the dichroic signal is shifted by 90° compared to the Néel type DWs, as seen in figure 21.

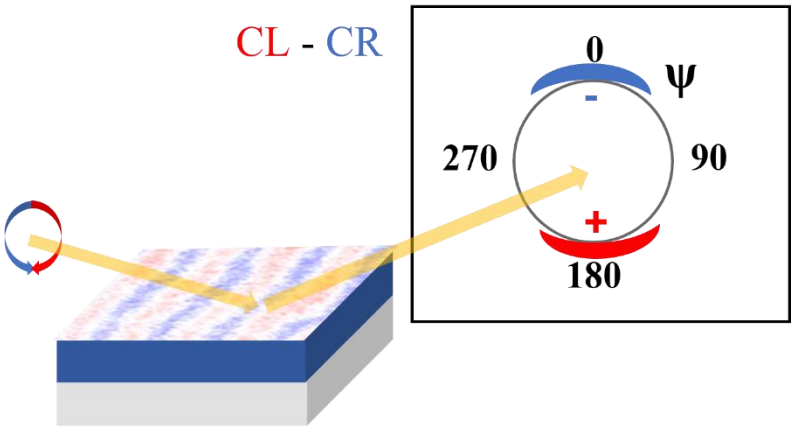

Figure 21: Difference image scheme of a CW Bloch DWs with stripes aligned perpendicularly to the scattering plane.

It also reverses with a change of chirality from CW to CCW and vice versa.

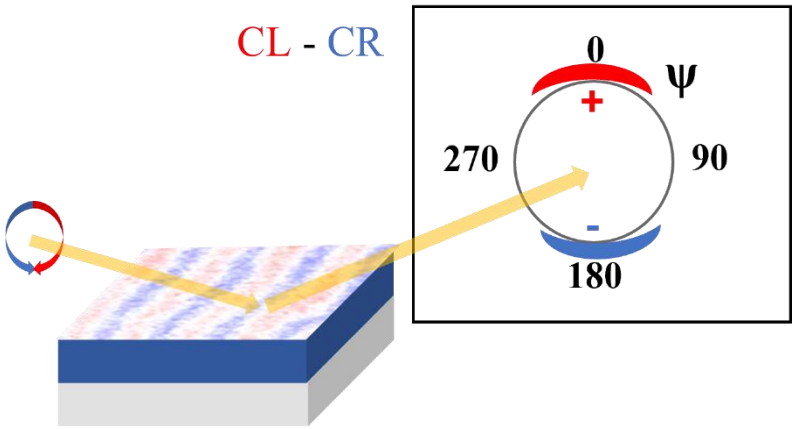

Figure 22: CCW Bloch DWs diffraction pattern in the difference image when the stripes are aligned perpendicularly to the scattering plane.

As the dichroic signal depends on the product of the magnetization component in and out of the scattering plane, this result can be generalized to all chiral magnetic texture, including labyrinthine domain pattern.

The SUM signal doesn't vary a lot with the azimuthal angle. For a spin spiral stripes pattern, only a geometrical factor depending on the incident angle changes.

$$I_m^{CL+CR}(\boldsymbol{q} = \boldsymbol{k_x}) = I_m^{CL+CR}(\boldsymbol{q} = -\boldsymbol{k_x}) = |F_1|^2[2m_z^2 \sin^2\theta + m_y^2 \sin^2 2\theta]$$

In the previous sub-sections, the XRMS signal obtained on the two DW types and chirality have been calculated for a spin spiral stripes pattern with two orthogonal orientations relative to the scattering plane. The results can be extended to the other magnetic textures and stripe orientations relative to the incident beam. However, it is not possible to qualitatively determine the ratio between domains and DWs in a magnetic texture looking separately at the DIFFERENCE and SUM signals. In that regard, the asymmetry ratio helps. It consists in the DIFFERENCE image divided by the SUM, written (CL-CR)/(CL+CR).

2.2.2.2.3 Asymmetry ratio for a spin spiral

We first represent the simulated signal obtained with the simplest magnetic texture to write analytically for an educational purpose. The magnetic spin spiral (represented in figure 4c in chapter 1) is a continuous sinusoidal rotation of the magnetization meaning that the notion of domains and DWs isn't relevant in this particular texture and that both IP and OOP magnetic components have the same amplitude but shifted by 90°. In all the following simulations, the simulated 1D magnetization profile is 100 µm long, which corresponds approximately to one experimental probed dimension with light in this PhD.

The angular dependence of the SUM and DIFFERENCE intensity for a magnetic single layer with chiral Néel spin spiral is plot in figure 23. It gives a maximum in the diffracted signal around 60° and 55°, respectively.

The asymmetric ratio ($\frac{CL-CR}{CL+CR}$) is maximum for a spin spiral magnetic texture which exhibits only the first diffraction order and gives a ratio equal to ~ 0.7. It is sometimes used because it normalizes the magnetic dichroic part by the magnetic signal that does not interfere, allowing a qualitative comparison between different magnetic textures or samples.

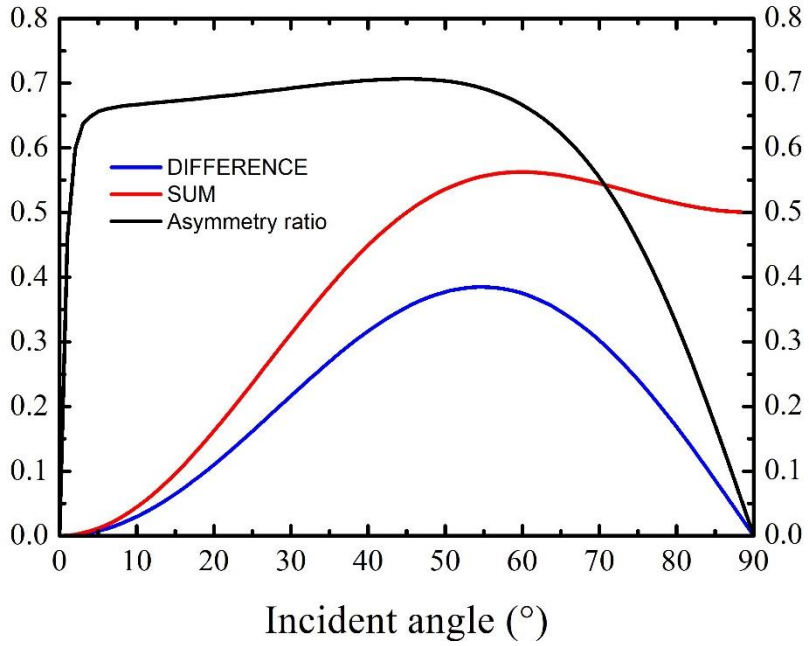

Figure 23: Simulation of the DIFFERENCE (blue) and SUM (red) diffracted intensity with the corresponding asymmetry ratio (black) from a magnetic monolayer with a perfect stripped Néel spin spiral texture parallel to the scattering plane, like figure 19. The DIFFERENCE signal cancels out at 90° from the sample plane, reflecting the fact that no dichroism can be observed in transmission.

$$I_m^{\frac{CL-CR}{CL+CR}}(\boldsymbol{q}=\boldsymbol{k_y}) = \frac{2(\mathrm{m_z}\sin\theta)(m_y \sin 2\theta)}{2m_z^2 \sin^2\theta + m_y^2 \sin^2 2\theta + X} = -I_m^{\frac{CL-CR}{CL+CR}}(\boldsymbol{q}=-\boldsymbol{k_y})$$

To avoid a divergence in the particular case of $\theta = 0$ that is non-physical geometry, we add a small number X in the denominator. As seen previously, the dichroism results from interferences between the magnetic periodic components perpendicular (m_y here) and parallel ($m_x$and m_z) to the scattering plane if there is a spatial shift (of 90°) between them. The usual magnetic texture found in non-vanishing effective anisotropy samples with PMA is composed of domains larger than the DWs. Consequently, it will introduce higher (odd) diffraction orders. The DWs are far more spatially reduced than the domains. The Fourier transform first diffraction order amplitude is thus much more reduced in the magnetization IP components than in the OOP which should lead to a bigger decrease in the DIFFERENCE signal than in the SUM. The SUM and DIFFERENCE signal dependence to the DWs width is explored in the next sub-section.

2.2.2.2.4 Asymmetry ratio for alternating Up/Down magnetic domains separated by DWs

The magnetic texture is composed of stripes domains parallel to the scattering plane with a cycloidal rotation of the magnetization inside the smaller domain walls. The magnetization vector components in a 1D model are written as:

$$M_x(y) = 0$$

$$M_y(y) = M\left[\sqrt{1-\left(\tanh\left(\Lambda\frac{y_1(y)}{w/2}\right)\right)^2} - \sqrt{1-\left(\tanh\left(\Lambda\frac{y_2(y)}{w/2}\right)\right)^2}\right]$$

$$M_z(x) = M\tanh\left(\Lambda\frac{y_3(y)}{2w}\right)$$

(53)

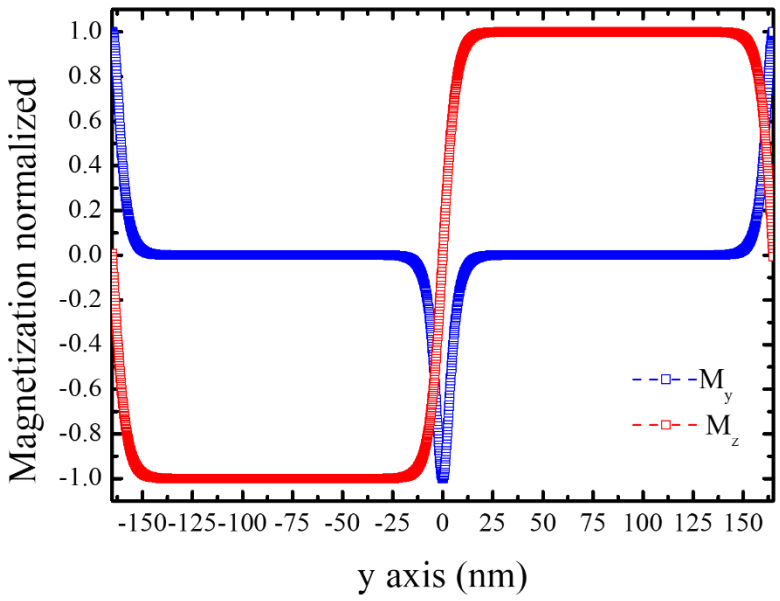

Figure 24: Magnetization profile from the 1D model described in equation 53 for a DW width of 21 nm.

The parameters $y_1(y) = \sin\left(\pi\frac{y+\frac{\Lambda}{4}}{\Lambda}+\frac{\pi}{4}\right)$, $y_2(y) = \sin\left(\pi\frac{y+\frac{\Lambda}{4}}{\Lambda}-\frac{\pi}{4}\right)$ and $y_3(y) = \sin\left(2\pi\frac{y}{\Lambda}\right)$ depends on the position y, taken as the variable. The magnetization amplitude, M, is equal to 1. It is still written here as this model will be expanded for the treatment of the dynamical data later (Annex C).

In the following, we will consider the domain periodicity Λ is taken as a constant and the DW width w is varied in order to illustrate the sensitivity of XRMS to the respective domain and

DWs size. Both are in nanometer. For a DW width equivalent to a quarter of the periodicity, the model gives different magnetization components compared to the spin spiral sinusoidal functions used previously in the formal approach. The validity of the model for a deviation of 1% from the normalization condition, $1 = \sqrt{M_y^2 + M_z^2}$, holds for a periodicity over the DW width ratio bigger than 6. For a periodicity of 330 nm, it corresponds to a maximum DWs width of 55 nm or less, which is at least two times bigger than the DWs width studied in this thesis. The 1D magnetization profile is Fourier transformed and inserted into the XRMS equations described previously. The spatial distribution of the DIFFERENCE and SUM signals are plot in figure 25 for 4 different DW widths.

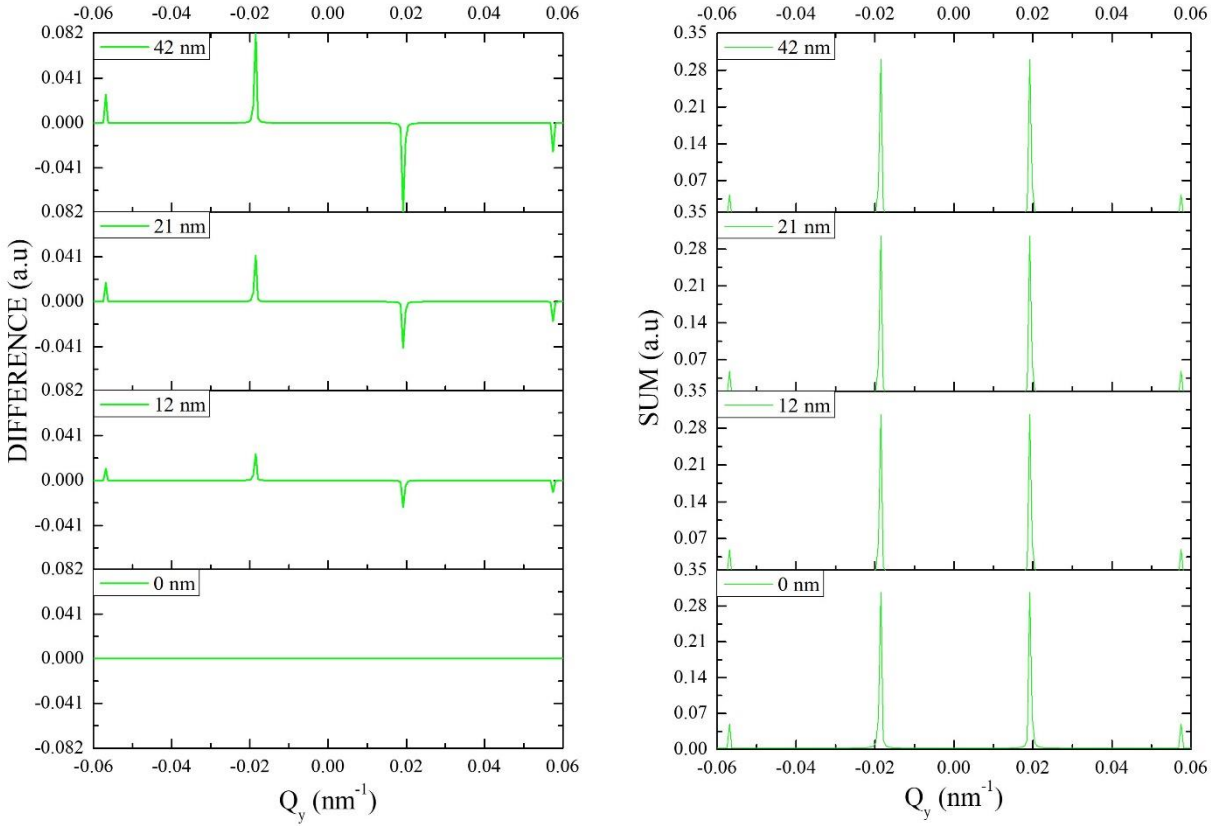

Figure 25: Spatial profile of the DIFFERENCE and SUM signals for different DW widths.

We can notice that there are a first and third order diffraction peaks in the reciprocal space. By integrating the intensity of the simulated magnetic diffraction, we can represent its evolution as function of the DW width.

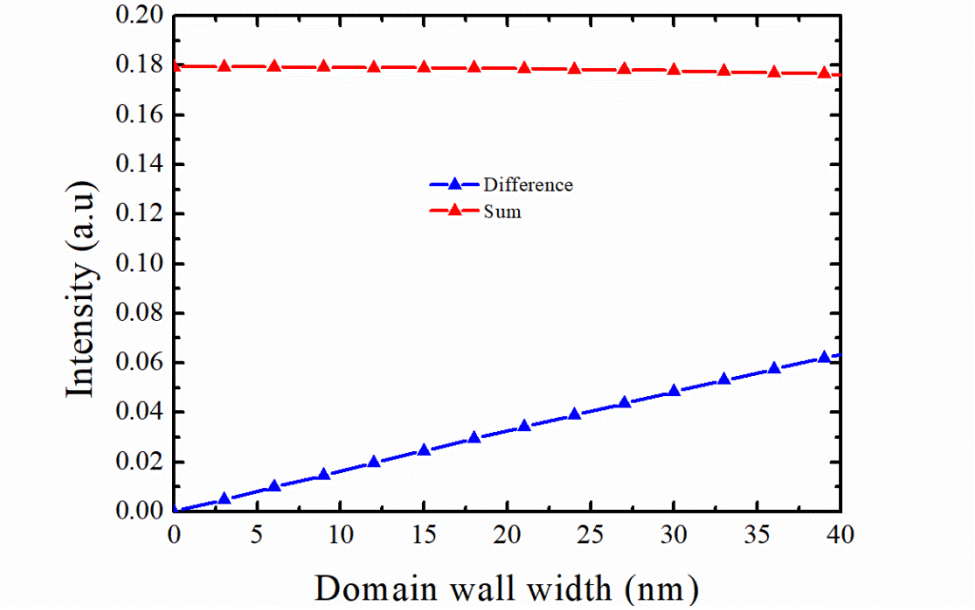

Figure 26: Variation of the magnetic diffracted intensity in the SUM and DIFFERENCE images with the DW width from a magnetic monolayer with stripped Néel domain texture parallel to the scattering plan. The DIFFERENCE signal cancels out in the absence of DW in the magnetic pattern.

The figure 26 displays the SUM and DIFFERENCE signals evolution with respect to the DW width. The simulation has been realized with no Bloch ($M_x(y)$) component and at 45° incident angle, which is the value used at the cobalt $M_{2,3}$ edge, further described in chapter 3. As one can see, the SUM is almost constant when varying the DW width. This implies that the SUM signal is dominated by the $\pm z$ component of the magnetization or in other words, by the domains. The DIFFERENCE signal is null for the absence of DW and increases linearly until 40 nm. The asymmetry ratio reaches $\sim$ 30% maximum. It is more than two times lower than the asymmetry ratio obtained in the spin spiral texture, which is due to the lower spatial ratio between the chiral DWs and the domains in alternating domain textures. The IP component must be an odd function to obtain a dichroism in the diffraction. Thus, the asymmetry ratio is different from zero only if there is a chiral DW.

In figure 27, the asymmetry ratio of the first and third diffraction order is plot. The linear increase of the first order asymmetry ratio with the DW width is due to the increase of the DIFFERENCE signal described above. The third order ratio increases faster than the first order but not linearly. Within the DW width range used in the calculation, the ratio of the first order over the third order asymmetry ratio increases monotonously with the DW width, meaning that in principle, it is possible to retrieve it. However, as seen in figure 26, the third order diffraction signal is smaller than the first order and more subjected to the experimental noise. Thus, this ratio cannot determine the DW width alone.

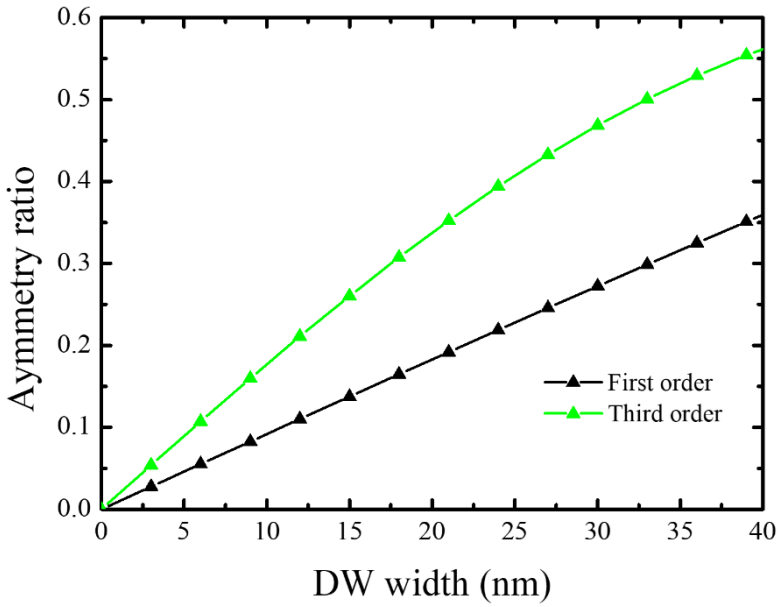

Figure 27: Asymmetry ratio evolution of the first and third diffraction order with the DW width.

In reflection geometry, XRMS is a reliable technique to distinguish between chiral ↑→↓←↑ and non chiral ↑↓↑↓↑ or ↑→↓→↑ magnetic pattern, which is very difficult by magnetic force microscopy for instance. Non chiral magnetic textures exist in samples with a strong PMA and no DMI. However, closure domains can emerge in samples with a smaller anisotropy, i.e., where the cost of the in-plane component at the surface is less expensive in energy compared to the no domain wall case. The depth dependence of closure domains depending on the perpendicular anisotropy has been carried on by Dudzik *et al.*[221] on FePd thin films. It is possible to probe the depth dependence of the magnetic texture without interference effects by varying the X-rays incident angle in single layers. However, dealing with single layers restricts the possibility to engineer the wished chiral magnetic texture. Multilayers offer the possibility to finely tune the different magnetic parameters by varying the stacking order or the composition of the layers and their respective thicknesses for instance.

2.2.3 Chirality in magnetic multilayer studied by XRMS

2.2.3.1 Case of FM multilayers with a homogeneous chirality

In the case of FM multilayers, magnetic and structural period are the same, which gives a maximum scattered intensity to specific angles corresponding to the so-called Bragg peak, as pointed out in figure 28.

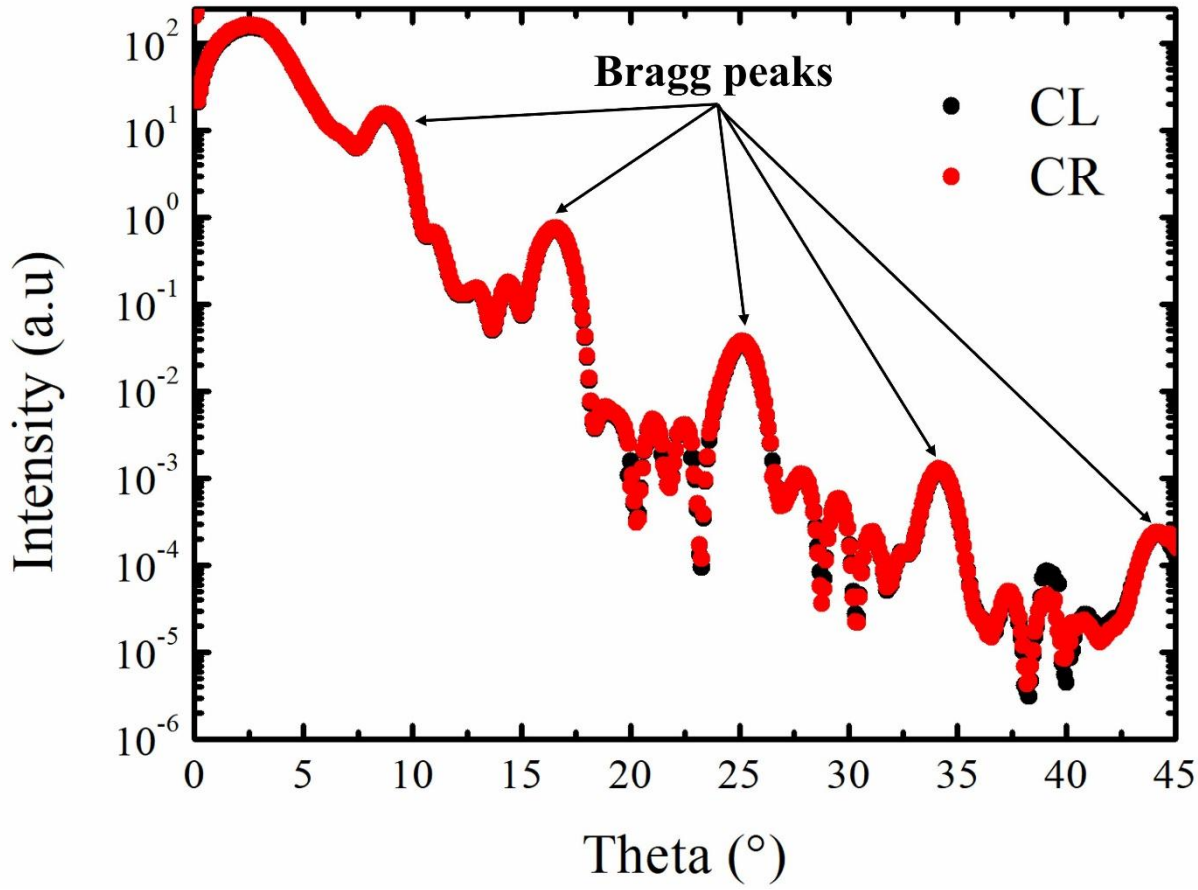

Figure 28: Reflectivity curves of a FM multilayer performed out of a transition metal resonant edge (750 eV) with both circular polarizations. Multiple Bragg peaks are visible and corresponds to the chemical periodicity of the multilayer.

This constructive interference condition maximizes the diffracted magnetic signal and corresponds to a multiple of the multilayer's chemical periodicity in FM multilayers. The first XRMS experiment on asymmetric prototypical Ir/Co/Pt based multilayers has been reported by Chauleau *et al.*[222]. Two samples consisting of five repetitions of the tri-layer, with opposite stacking order, have been grown. The dichroic patterns have been taken at the first multilayer Bragg peak in both samples and show two opposite Néel chirality. The simple and straightforward approach to identify the type of DWs and their chirality is interesting as magnetic multilayers with large interfacial DMI are at the forefront of the spintronic research. It is also a nonperturbative technique and valid on any type of magnetic material, like insulating or metallic magnetic samples due to the element selectivity. Finally, it is not necessary to prepare the sample' surface as the technique is sensitive to a small amount (few nanometers) of magnetic material that can be buried under few nanometer of a layer acting as an oxidation barrier.

The previous formal results are still valid in multilayers with a labyrinthine magnetic pattern as shown in the graphic extracted from Chauleau *et al.*[222] below.

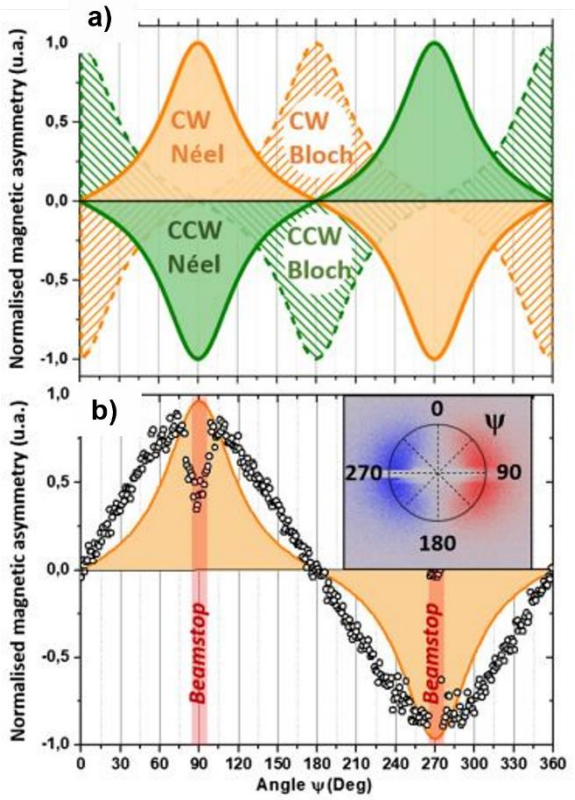

Figure 29: (a) Calculated orthoradial profile of the XRMS images on the multilayer Bragg peak. The orange (green) colour represents the CW (CCW) chirality of the DW and the full (dashed) filling depicts the Néel (Bloch) DW type. (b) A comparison between the calculated CW Néel and the experimental orthoradial profile of a [Ir(1)/Co(0.8)/Pt(1)]x5 multilayer. The red coloured area depicts the beamstop position. The image is taken from Chauleau et al[222].

The first graph in figure 29 (a) condenses the calculated asymmetry ratio orthoradial profile performed for the different DWs configurations. As in the previous section, the Néel and Bloch type DWs diffraction patterns are shifted in angle by 90° and they reverse for opposite chirality. The second part of the same figure compares the calculation and the experimental orthoradial profiles for a multilayer with Néel CW DWs in a labyrinthine pattern. Qualitatively, the behaviour is similar. The drop in intensity around the maximum of the two peaks corresponds to the position of the beamstop, visible in the inset of figure 29 (b). However, there is a clear deviation between the two curves for angles outside of the extremal values. This can be attributed to the kinematical approximation used in the simulation that is not strictly valid in the soft X-ray energy range. More importantly, it doesn't affect the main qualitative conclusion that the type and chirality of a magnetic texture can be directly assessed by XRMS without any assumption.

The possibility to tune the different magnetic interaction parameters in multilayers brought the attention into the nucleation of skyrmion lattice. Increasing the magnetic volume of the skyrmion columnar shape allowed to stabilize skyrmions at RT that were previously observed in bulk materials with no inversion symmetry at temperature usually inferior to 100K.

The skyrmion size could be inferior to 10 nm but are more sensitive to thermal fluctuation. They represent a great opportunity for dense storage applications. XRMS can be a powerful technique to characterize quickly a skyrmion lattice by looking at the diffraction peak radius and their FWHM. A 2017 study focused on the determination of the winding number of skyrmions by XRMS in a Cu_2OSeO_3 bulk sample[223] by analysing the scattered signal symmetry. The skyrmion lattice chirality is determined by the DMI in asymmetric multilayers and will generally be the same as for the DWs. Also, the diffracted intensity is more important in transmission geometry than in reflectivity. The study of systems hosting skyrmion lattices has been performed in transmission geometry in this PhD work and is presented in chapter 3.

The electrical nucleation and control of skyrmions in FM multilayers came with a drawback. The skyrmion doesn't move in straight line. The deviation, called the skyrmion Hall effect, is linked to the topological charge of the skyrmion, N_{sk}. The topological charge, also called winding number, describes the number of turn the skyrmion' spins orientation performs when looking at spins with the same radius with respect to the middle.

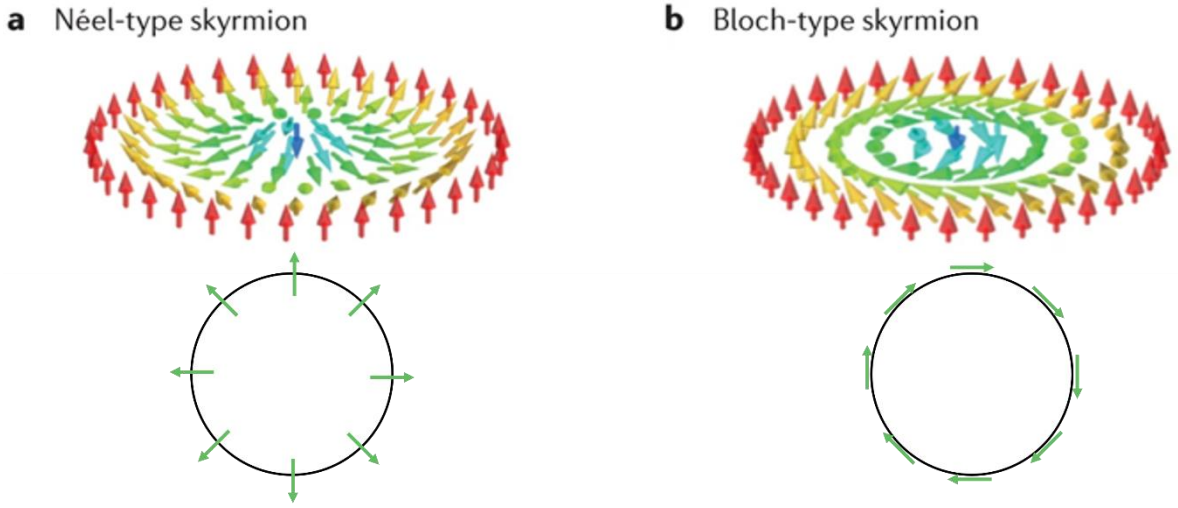

Figure 30: Representation of a Néel (a) and Bloch (b) type skyrmion. Below, the projection of one of the skyrmion radius looking at the top of it. Here the topological number is equal to -1 as the spin direction makes a 360° rotation in the trigonometric direction and the core magnetization points downward. The top images are taken from Fert, A. Reyren, N. & Cros, V. Nat. Rev. Mater. **2**, 17031 (2017)[224].

$$N_{sk} = \frac{1}{4\pi}\int \boldsymbol{m}\cdot\left(\frac{\partial \boldsymbol{m}}{\partial x}\times\frac{\partial \boldsymbol{m}}{\partial y}\right)dx\,dy = \pm 1 \quad (54)$$

There are multiple ways to avoid the skyrmion lateral deflection. For instance, at the edges, the skyrmion hall effect is cancelled due to a repulsive interaction[224]. Another way would be to nucleate skyrmions on FM samples with opposite topological charges in the sample depth.

2.2.3.2 Case of FM multilayers with a hybrid chirality

The magnetization profile has been assumed to be uniform through the multilayers thickness in the previous section. In a recent study originally focusing on the variation of the DWs width in the vertical direction on samples susceptible to host skyrmions, a twisting of the internal DW structure has been found[62]. Different multilayers with different compositions of Pt/Co/X-based trilayer (X=Ir or AlOx) and ranging from five to twenty repetitions with PMA have been explored by XRMS. The XRMS patterns are plot in figure 31 below.

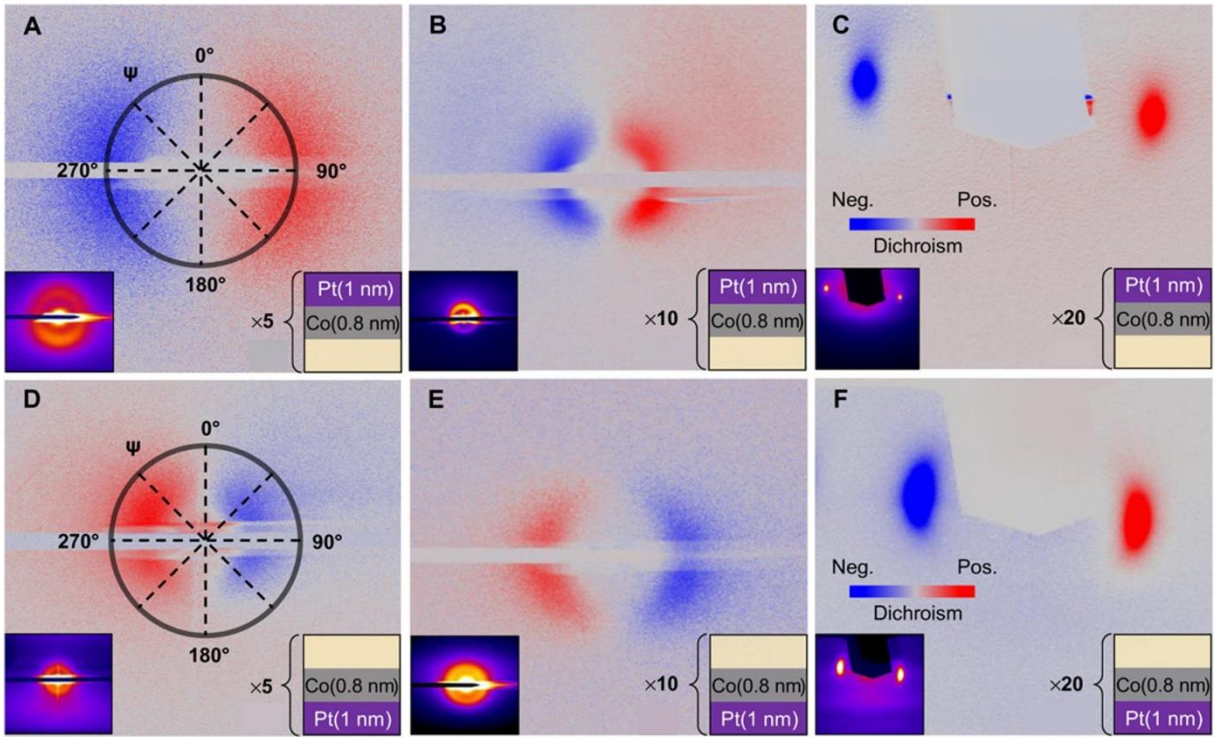

Figure 31: On the top panel, the asymmetry ratio image of multilayers with a DMI favouring a CW Néel DWs texture with 5 (A), 10 (B) and 20 (C) repetitions. On the bottom, the asymmetry ratio images on 5 (D), 10 (E) and 20 (F) repetitions multilayers with a stacking order that should induce CCW Néel DWs. The left inset of each image are the corresponding SUM images while the right inset schemes the multilayers stacking. Figure taken from W. Legrand *et al*. Sci. Adv. **4**, eaat0415 (2018)[62].

In all figure 31 images, the dichroic signal is purely Néel. In the X/Co/Pt stacking (A to C), i.e. with Pt closer to surface than Co, inducing CW Néel DW, the chirality matches the XRMS pattern for all trilayers repetitions. For the stacking with the platinum below the cobalt layer, the dichroic pattern also matches with the stacking order (D and E) inducing CCW Néel DW. However, at twenty repetitions (F), the asymmetry image exhibits an opposite chirality compared to the five and ten repetitions. The XRMS signal mostly originates from the top layers, especially at the first multilayer Bragg peak. It means that the chirality in the topmost layers of the twenty repetitions sample is opposite to the chirality induced by the DMI. This change in the dichroic pattern with the multilayer repetition is the fingerprint of a hybrid chirality in the sample thickness.

The XRMS results has been supported by numerical simulations performed on a twenty repetition multilayers[62]. The DMI strength has been varied from -1.0 mJ m^{-2} to 2.0 mJ m^{-2} with 1 mJ m^{-2} increment. The results are plot below in figure 32.

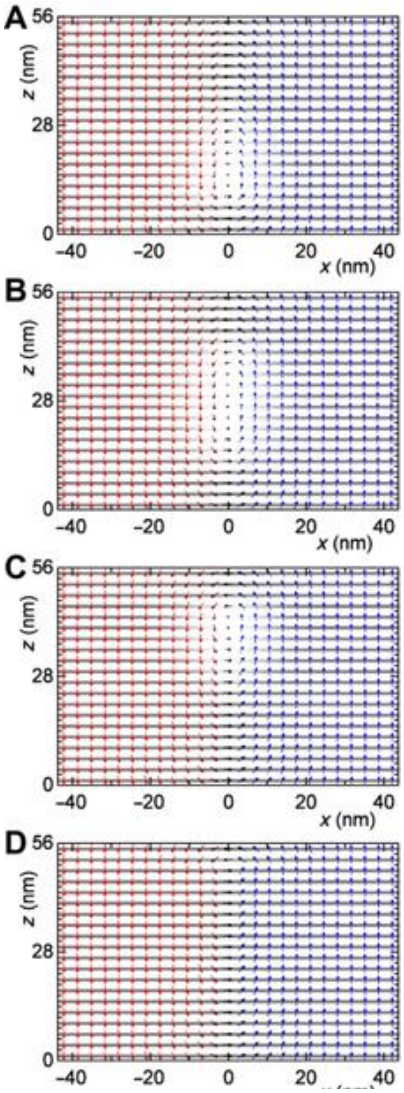

Figure 32: Representation of one DW spin texture cross-section for a twenty-repetition cobalt based asymmetric trilayer. The DMI strength has been varied from -1.0 to 2.0 mJ/cm² (A to D) with a 1 mJ/cm² incremental value. The red (blue) arrows depict the magnetization direction along the -z (+z) direction. The transverse magnetization component (m_y) is represented by the color of the grid from black (m_y=0) to white (m_y=1). Figure taken from W. Legrand *et al.* Sci. Adv. **4**, eaat0415 (2018)[62].

The simulations on the twenty repetitions of an asymmetric trilayer composed of 0.8 nm of cobalt predict that the DW internal structure isn't fully Néel in any case. The simulation performed for a DMI strength of -1.0 mJ/cm², shown in figure 32 (A), exhibits a CW chirality in the topmost layer and a CCW in the bottom. A negative value of the DMI constant is found for a stacking where the cobalt is above platinum, favouring a Néel CCW chirality. The change of chirality is separated by a range of thickness (the white area in the graph) where the magnetization in the DW is oriented along the $\boldsymbol{y}$ axis (Bloch type). In figure 32 (B), the DMI free simulation shows a Bloch type DW in the middle of the stack that surprisingly doesn't dominate all the vertical direction. It is indeed bigger than in the previous simulation but a Néel type DW is still favoured at the top and bottom part of the multilayer due to the large dipolar fields. In the next two simulations, the DMI is positive and favoured a Néel CCW chirality. The Bloch part moves upward as the DMI strength increases (C to D) and decreases vertically in size. Since the hybrid chirality has been observed only in the sample with the higher amount of

magnetic material and that it is the only parameter that changes, the suspicions turn to the dipolar interaction.

As represented in figure 33, the dipolar field closing loops in a domain pattern state favour a CW (CCW) chirality on the top (bottom) layers. Thus, it can result in the stabilization of a hybrid chirality in the sample thickness, with a Bloch point that perform the transition between the two Néel chiralities[62].

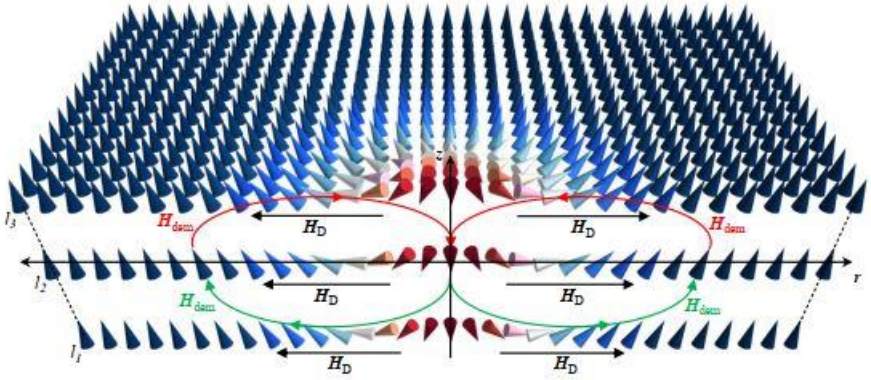

Figure 33: Scheme of the dipolar and DM interaction in a multilayer hosting a skyrmion. The black arrows represent the DM field, acting in the same way through the multilayer i.e., favouring a CCW chirality. The coloured arrows depict the dipolar closing loop field acting on the magnetic moments. In green, the demagnetizing field favours a CCW chirality in the bottom layer, while the red arrows, symbolising the demagnetizing field in the top layers, promote a CW chirality at the top of the sample. The scheme has been taken from William Legrand PhD thesis[76].

As seen in the simulation of figure 32, the Bloch part moves upward or downward depending on the sign and the amplitude of the DMI parameter. The angular dependent study of multilayer hosting hybrid chiral magnetic texture, accompanied by XRMS signal simulation, could determine the depth of the Bloch point which in turn gives the DMI amplitude. However, in multilayers, the range of angle is restricted by the interference effect, which greatly affects an angular dependent study. To get around this issue, it is possible to change the penetration depth by tuning the photon energy around the resonance peak as the dispersion and absorption scattering factors vary strongly around the edge. With the help of micromagnetic and XRMS simulations that account for the interference effect and the magnetic layer differential signal contribution relative to their depth variation, it could be possible. Prior to this PhD work, no such program was available.

Another way to cancel the lateral deviation of the skyrmions would be to have AFM coupled skyrmions. In multilayers, it is possible to achieve an indirect AFM coupling between FM layers through a non-magnetic layer.

2.3 A XRMS study on SAF samples

The samples studied are made of a Pt/CoFeB/Ru trilayer repetition optimized to exhibit a spin spiral texture and antiferromagnetic coupling. The nominal ruthenium thickness is 0.75 nm, which ensures a much stronger AFM coupling between magnetic layers compared to the

second peak around 1.7 nm[225]. The low damping CoFeB and platinum layers thicknesses are chosen to cancel the effective anisotropy. On the one hand, the IEC strength decreases exponentially in the platinum layer, with an attenuation length of 0.3 nm[62,76]. On the other hand, the interfacial anisotropy constant increases with the Pt thickness[226] until saturation around 3 nm. The DMI also increases with the Pt thickness[56]. A non-negligible interfacial anisotropy at the Pt/CoFeB/Ru interfaces is needed to reach a near zero effective anisotropy with a sample in planar geometry. The combination of a vanishing effective anisotropy and dipolar field with a significant DMI should lead to a spin spiral magnetic texture. The nominal thicknesses for the Pt and CoFeB layers are 0.5 nm and 0.9 nm. The 0.5 nm thin platinum layer attenuates the AFM IEC by 80%, but below this thickness the interfacial anisotropy and the DMI drops significantly[76]. The Pt/CoFeB/Ru tri-layer is repeated six, height and ten times on a Ta(5)/Pt(8) buffer layer. The 8 nm platinum buffer layer is dominantly (111) FCC multi-grain oriented. The columnar orientation should propagate, at least partially, into the multilayer[56]. It ensures a higher interfacial anisotropy compared to purely amorphous layers. The samples are capped with 5 nm of aluminium to prevent the oxidation of the topmost magnetic layer.

2.3.1 Sample characterization

2.3.1.1 MFM image

The drawback working with SAF samples is that they are difficult to study. The AFM coupling between FM layers leads to a zero net total magnetization in the multilayer. Thus, the study by Lorentz transmission electronic microscopy or transmission geometry X-ray microscopy such as scanning transmission x-ray microscopy or ptychography is extremely challenging. The other consequence of the AFM coupling is that the stray field is weak compared to FM systems, which makes MFM imaging difficult. However, advanced MFM in vacuum or NV center microscopy allow an contrast to be detected, despite the near cancellation of the stray field.

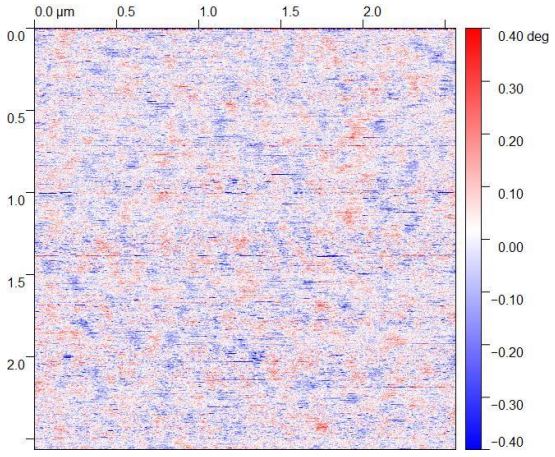

Figure 34: MFM image on a SAF sample in air at 300 K.

The MFM image on the ten repetition SAF displays in figure 34, shows a poor magnetic contrast. The domain periodicity is difficult to estimate directly from the image. The AFM coupling is well established through the multilayer. Its strength as well as the effective anisotropy and

the saturation magnetization can be found directly from the IP and OOP hysteresis curves.

2.3.1.2 Magnetometry at RT

The IP and OOP AGFM curves are plotted in figure 35. The treatment of such hysteresis loop on SAF depends on the curves shape. The straightforward cases are the ones where the effective anisotropy K_{eff}, which can be expressed as a field $\mu_0 H_{eff} = 2K_{eff}/M_S$, is positive and far greater than the AFM coupling field, noted H_{RKKY}, and the one where the effective field is close to zero. In both abovementioned situations, the effective anisotropy field (H_{eff}) and H_{RKKY} can be deduced from the IP and OOP saturation fields. For $H_{eff} \gg H_{RKKY}$, the IP hysteresis curve increases linearly before saturating at $H_{sat} = H_{eff} + 2H_{RKKY}$. When H_{eff} is negligible, the latter expression reduces to $H_{sat} = 2H_{RKKY}$. In the OOP curve, the H_{RKKY} field can be read directly from the abrupt jump in the sample magnetization when $H_{eff} \gg H_{RKKY}$. The magnetization remains around zero during the increase of the absolute field as the system stays AFM coupled. At the H_{RKKY} field, the magnetization reverses in the layers with the magnetization pointing in the opposite direction of the applied OOP field. The sample's magnetization then saturates.

In the present SAF sample, the magnetization increase in the IP and OOP configurations aren't linear. The average magnetization along the measured direction changes with the formation of domains. In the intermediate case, where the effective anisotropy and the AFM coupling field are of the same order of magnitude, only an estimation can be given. The saturation field in the IP hysteresis curve is approximated to $H_{sat} = H_{eff} + 2H_{RKKY}$. The effective anisotropy is obtained by the area difference between the OOP and IP hysteresis curves.

$$W_{mag} = \int_0^{H_S} (M_{hard} - M_{easy})\, dH = K_{eff} \tag{55}$$

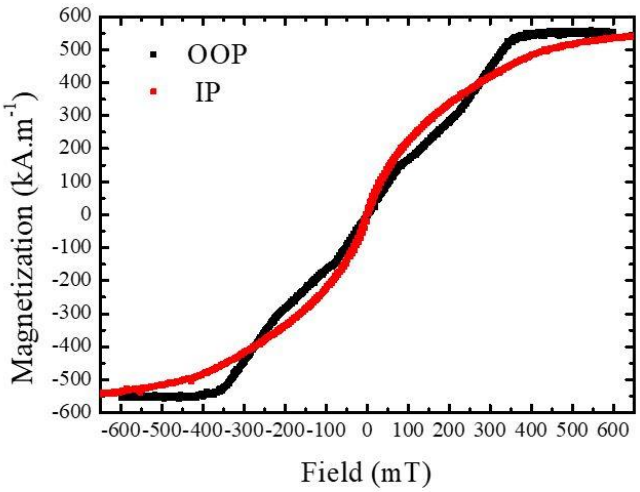

Figure 35: IP and OOP AGFM curves of the SAF ten repetitions sample at 300 K.

From this measurement the effective field is found to be around $\mu_0 H_{eff} \sim 2$ mT and the RKKY field $\mu_0 H_{RKKY} \sim 120$ mT, which seriously put in doubts the assumption made before. Nevertheless, the calculated RKKY field visually agrees with the OOP curve, knowing that each ruthenium/platinum bilayer doesn't mediate exactly the same AFM coupling value as the thickness and the interface quality can vary. This thickness variation could be probed by X-ray reflectivity for instance.

2.3.1.3 X-ray Reflectivity

After the magnetometry technique sensitive to the bulk information, X-ray reflectivity has been performed to characterise the different layers within the sample. The reflectivity curve depicted in figure 36, has been done off resonance at 690 eV on the SAF with eight trilayer repetitions as an example. This specific curve is shown because the fit using DYNA software matches better compared to the other SAF samples. All the experimental data aren't well fit, especially at low angles, but the agreement is better at angles higher than the multilayer Bragg peak. This is quite surprising as the small defects usually affect the high angle part of the curve because of their small periodicity in real space.

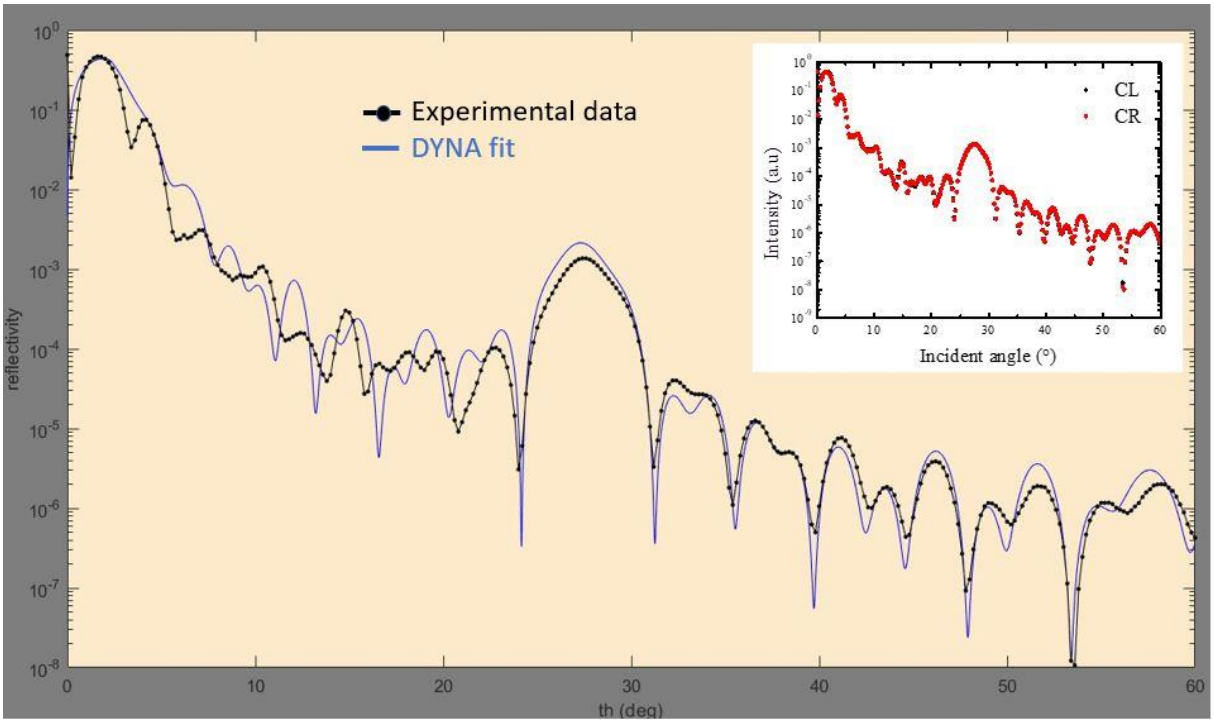

Figure 36: Reflectivity curve performed at 690 eV in black with the fit attempt in blue. The inset shows the reflectivity curves performed with CL and CR polarizations at the same photon energy.

In the figure 36 inset, one can see that the two off-resonant circular polarizations perfectly superimpose, meaning that the reflectivity is reproducible. The DYNA fit has been performed using a multiplicity of 8 for the Pt, Ru and CoFeB layers as described in the table below.

Layer/property	multiplicity	Density (mol/cm^3)	Thickness (nm)		Roughness (nm)
			Fit	Nominal	
Al_2O_3	1	0.041	2	0	0.07
Al	1	0.095	2.5	5	0.22
Pt	8	0.104	0.59	0.5	0.44
Ru	8	0.115	0.55	0.75	0.83
CoFeB	8	0.128	0.81	0.9	0.16
Pt	1	0.104	7.72	8	1.57
Ta	1	0.088	4.97	5	0.27
SiO_2	1	0.044	∞		0.2

Table 2 : Parameters of the fit for the off resonance SAF8 reflectivity curve.

The thicknesses differ by up to 25% from the nominal ones. The same sputtering chamber has been used for those samples and the first Pt/Co/Al based sample studied in scattering geometry. The separation of the tri layer into induvial layers as well as intermixed layers improve a bit the fit but complexifies it a lot. The peak at 4° could be due to a dirt layer above the sample which can also explain the difficulty to fit the oscillations before the Bragg peak. Also, the DYNA software doesn't account for the interface height variation, as the roughness at the interface is taken as an intermixing. Finally, it is not excluded that there is an important intermixing between two layers as their nominal thickness correspond to few atomic layers and that, in the fit, some layers have a roughness comparable to their thickness. As the precise fit of the reflectivity curves isn't the main topic of this work and that even the reflectivity curve at the Cu K_α edge (8.04 keV) on SAF10 can't be fit, no further attempt has been done.

2.3.2 Study of SAF samples using XRMS at RT

The figure below shows the reflectivity curve at resonance of the eight repetitions SAF together with XRMS pattern taken at different angles using RESOXS diffractometer[227]. In figure 37 (a), only the CL reflectivity curve is shown and exhibits a Bragg peak at $\sim 26°$ corresponding to the chemical periodicity (1.95 nm). The SAF samples have been studied at remanence, meaning that both circular polarization reflectivity curves overlap as there is no net magnetic moment in the sample. In previous studies on Ag/Ni[228] and Co/Cu[229] SAF samples, an AFM ordering peak was visible at half the multilayer Bragg peak. It is not visible in the reflectivity curve in figure 37 (a), as well as in the other studied multilayers. Here, the SAFs samples are designed to exhibit a spin spiral magnetic pattern at remanence. Individually, the magnetic layers have zero net magnetization, which explains the absence of a pure AFM peak. However, it doesn't mean the absence of any magnetic diffraction pattern.

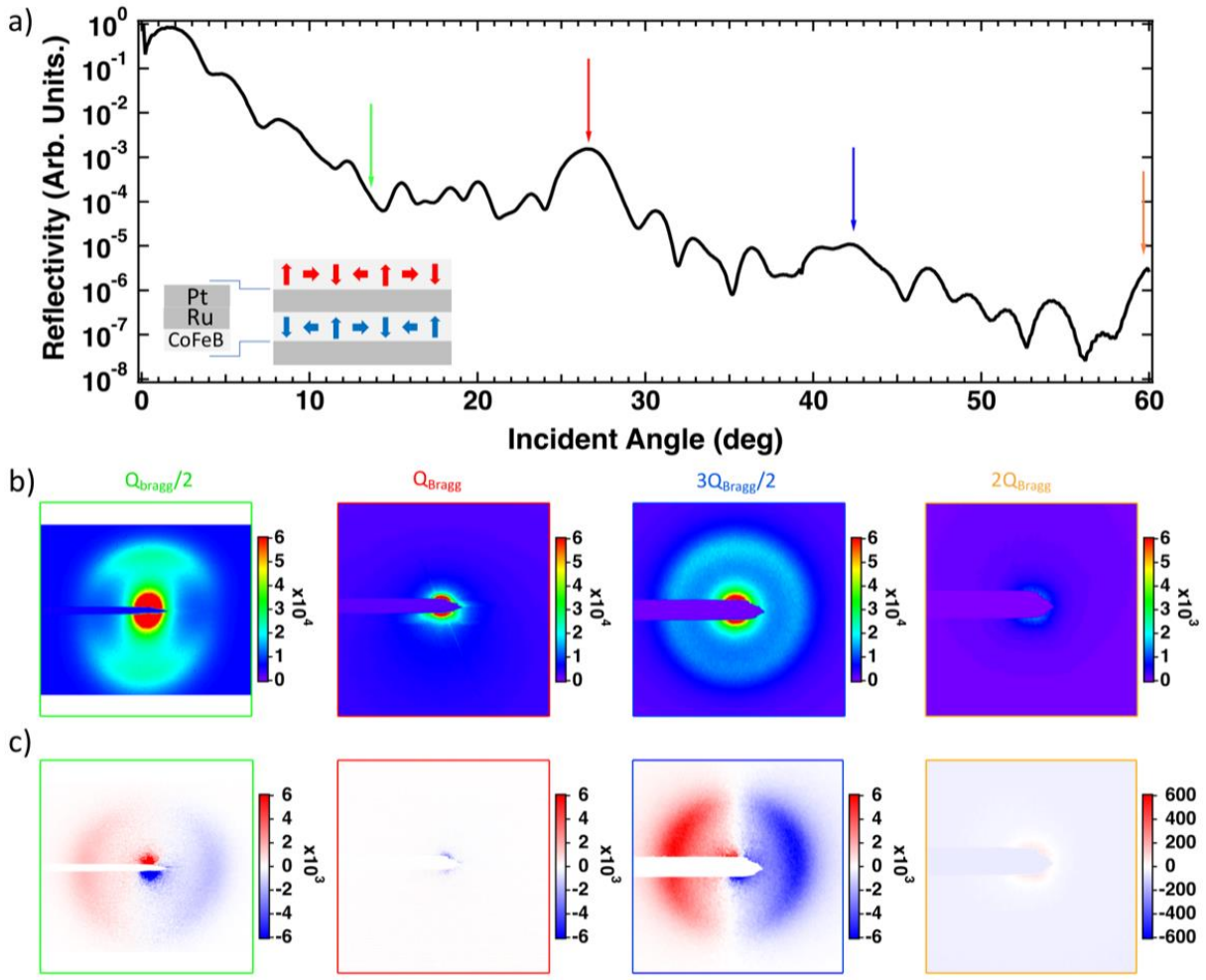

Figure 37: (a) X-ray reflectivity curve recorded on SAF8 at RT and Fe L_3 edge (707 eV) using CL polarized light. The vertical arrows indicate a pair of images taken at the angle with both circular polarizations. The red and orange arrows point toward the multilayer Bragg peak, while the green and blue arrows are placed at half odd order of the multilayer periodicity. (b) Geometrically corrected SUM image (CL + CR) diffraction patterns corresponding to the arrows in the reflectivity curve. (c) Geometrically corrected DIFFERENCE images (CL – CR) vertically aligned with the correspond SUM image and the in-depth reciprocal space periodicity. Image taken from Léveillé *et al*. Phys. Rev. B **104**, L060402 (2021)[227].

The SUM (CL + CR) and DIFFERENCE (CL – CR) 2D images at four different incident angles are shown in figure 37 (b) and (c), respectively. The two images taken at Q_{Bragg} and $2Q_{Bragg}$ in reciprocal space, corresponding to the structural order, show no evidence of a magnetic diffraction pattern. The two other images taken at half odd Bragg peak order, i.e., $Q_{Bragg}/2$ and $3Q_{Bragg}/2$ probe the magnetic order. It is twice the chemical periodicity as the magnetic layers are AFM coupled. A diffraction ring is visible in the SUM images taken at the magnetic periodicity while nothing except the specular beam appears at the Bragg angles. This observation is coherent with the resonant part of the magnetic scattering factor as the magnetization in two adjacent magnetic layers are opposite, the interference effect is destructive at the Bragg peak for the magnetic contribution. The ring depicts the labyrinthine periodic magnetic texture in the sample. The DIFFERENCE images display the same interference behaviour. At half odd integer of the multilayer Bragg peak, a Néel CCW dichroic pattern is observed, as expected from the stacking order with platinum underneath cobalt[222]. The strong dichroic signal

suggests the presence of a fixed chirality through the multilayer, which is coherent with the dipolar interaction cancellation in SAFs. Looking at the SUM and DIFFERENCE diffracted intensity, the maximum asymmetry ratio (CL – CR)/(CL + CR) can be estimated around 10% at 13° and almost 50% at 42°. The theoretical maximum value around 40° for a single magnetic layer with a perfect spin spiral magnetic texture is 70%. This value neglects the experimental noise intrinsic to the camera reading process and any contribution left of the specular signal. Thus, the asymmetry ratio found at 42° in the SAF samples indicates a spin spiral texture.

2.3.3 Temperature dependence of magnetic texture in SAF

2.3.3.1 Temperature dependent magnetometry

Additional hysteresis loops have been performed at different temperature by SQUID. The magnetic parameters extracted from the temperature dependent measurements are plotted in figure 38.

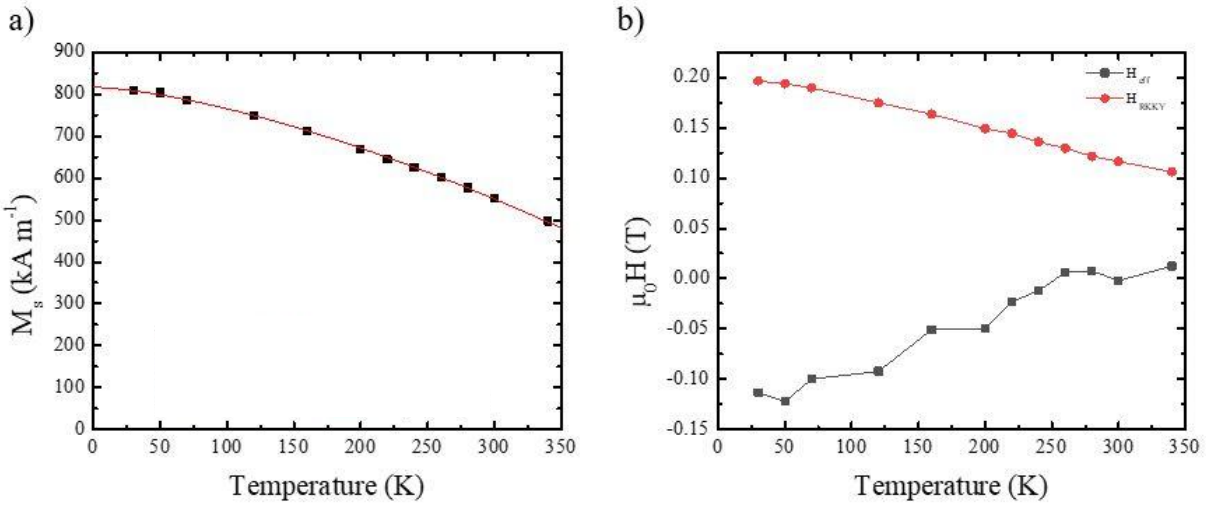

Figure 38: Temperature dependence of the saturation magnetization (a), the RKKY AFM coupling field and the effective anisotropy field (b) obtained from SQUID measurements. The red line in figure (a) results from a fit with a Bloch type law. In (b), the negative field for the anisotropy indicates an IP easy axis.

The first graph in figure 38 (a), shows the experimental evolution of M_s with temperature accompanied by a Bloch power law fit. The saturation magnetization at 0 K is estimated from the fit $M_s(0)$ = 817 kA m^{-1},while at RT it is M_s(RT) = 552 kA m^{-1}. The Bloch $M_0(1 - \left(\frac{T}{T_C}\right)^{\frac{3}{2}})$ power law is common in ferromagnetic at low temperature which derives from magnon excitations. The previously mentioned $M_0\left(1 - \frac{T}{T_{M_S=0}}\right)^{1/3}$ power law is usually valid close to the curie point. A recent study found a large range of validity for this law in CoFeB magnetic layers[230]. Using those two functions yields a curie temperature of Tc = 632K and $T_{M_S=0}$ = 425 K. Considering the value of the saturation magnetization, the FM layers thickness and its stoichiometry with respect to the literature, the $^1/_3$ power law gives a curie temperature more plausible. The evolution of the uniaxial anisotropy can be fit with a power law that yields $K_u \propto$

$M_S^{1.64\pm0.03}$. The power value is low compared to the expected square dependence to M_s in samples where the two-site magnetic anisotropy is mediated by an adjacent Pt layer[231]. The thin platinum layers together with an intermixing could be responsible for the smaller temperature dependence. The AFM RKKY field decreases almost linearly with the temperature increase and drop by a factor of two from 30 K to 340 K. This evolution goes along with a theoretical work which predicted that only the RKKY coupling strength amplitude would be affected by the temperature[232]. However, it contrasts with a study that report a more complex behaviour with temperature in a SAF bilayer[233]. The different changing rate of the magnetic interactions in temperature should induce a visible change in the magnetic pattern periodicity.

In the following, the iron L_3 edge is preferred to the cobalt due to the higher total magnetic moment in iron that induces more dichroic signal.

2.3.3.2 Temperature dependence of magnetic texture in SAF studied by XRMS

The resilience of this spin texture against the different magnetic interaction evolution in temperature has been assessed. The room temperature measurements were acquired first. Then the sample was cooled to the lowest temperature of the experiment and intermediate data points were collected increasing the temperature. A cold trap with liquid nitrogen was set before cooling to reduce the co-deposition of residual molecules at the sample surface. Reflectivity curves performed at different temperatures with a photon energy on and off the iron L_3 resonant edge are plot below.

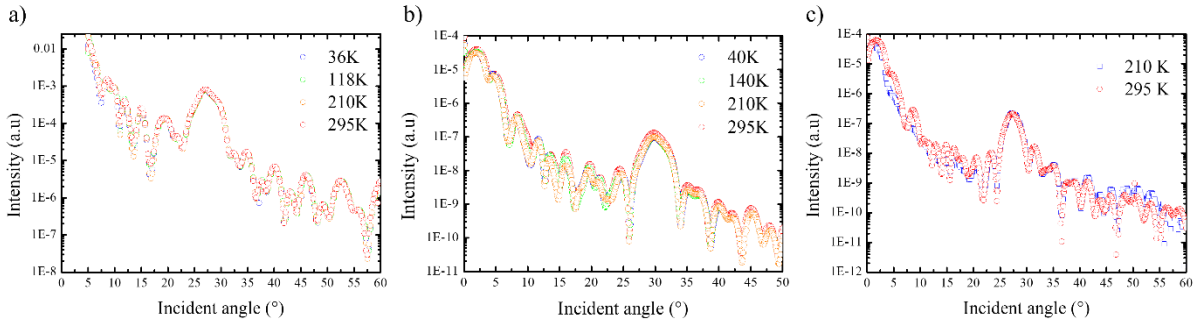

Figure 39: Reflectivity curves performed off resonance and at different temperature on the SAF6 (a), SAF8 (b) and SAF10 (c). The photon energy was 697 eV, 650 eV and 690 eV, respectively.

In the out of resonance graphics in figure 39, the different temperature curves superimpose perfectly for the SAF6, almost perfectly for the SAF8. However, the SAF10 curves show important differences with temperature. Looking at the first degrees of the reflectivity signal, the discrepancy could come from a bad alignment in the 210 K curve as no realignment has been done after the cooling. Moreover, the Keithley instrument that collect the photo-diode signal has a negative off-set value, which affect the measurements at high incident angles,

where the signal is weak. It explains the difference in intensity observed from 40° until the end of the scan at 210 K, as an artificial positive value has been added to the blue curve.

Overall, the off-resonant curves show the same behaviour. As the studied SAF samples are optimized to not only exhibit a zero total magnetization but also a zero net magnetization in each individual magnetic layer and that no external field is applied, the curves in temperature should superimpose.

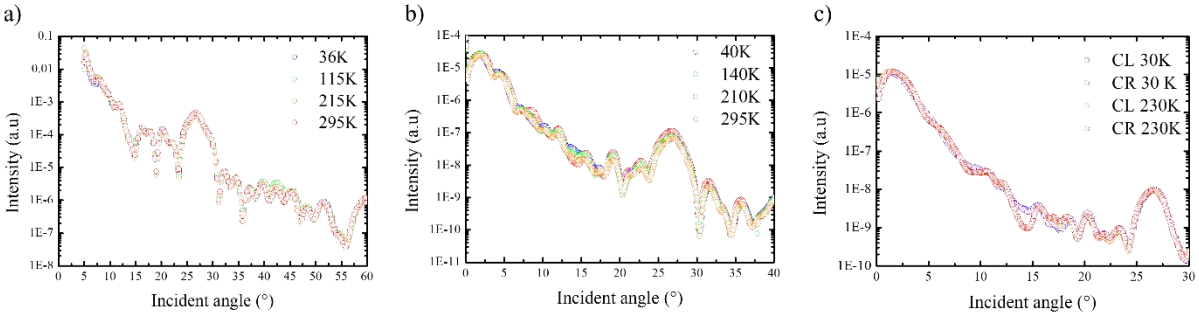

Figure 40: Reflectivity curves performed with the circularly polarized photon energy tuned at the L_3 iron resonant edge and at different temperature on the SAF6 (a), SAF8 (b) and SAF10 (c).

For the SAF6, the reflectivity curves match perfectly except around $3Q_{Bragg}/2$, where the low temperature curves are a bit higher in intensity with respect to the room temperature in red. The eight and ten repetitions samples show a similar and more pronounced trend but around $Q_{Bragg}/2$. As depicted in the figure 40 (c), the CL and CR curves match perfectly, meaning that no net magnetization is present in the sample at low temperature. The signal increasing at Half odd integer of the multilayer Bragg peak at resonance suggests a pure AFM peak that grows while the temperature decreases. From the temperature dependence of the effective anisotropy constant, the magnetic layer easy axis should tilt toward the sample plane as the temperature decreases. This hypothesis shall be confirmed by the fit of the reflectivity signal asymmetry ratio at resonance. Unfortunately, due to the poor agreement in the reflectivity fit itself, no definitive answer can be given.

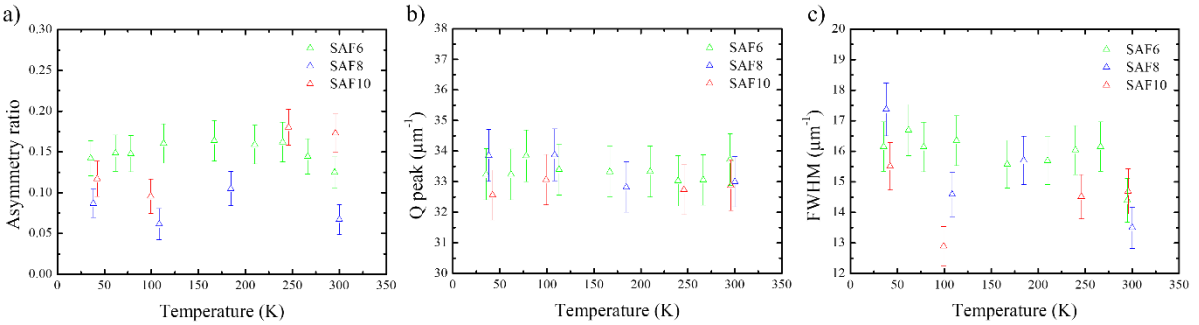

Figure 41: Evolution in temperature of all SAFs asymmetry ratio (a), peak position (b) and FWHM (c).

The evolution of the diffracted signal with temperature has also been measured at $Q_{Bragg}/2$. The data treatment of the 2D images follow the same procedure as described above. Here, a proper specular subtraction is mandatory as its intensity changes with temperature and that the specular geometrical diffusive projection changes with the incident angle. The asymmetry ratio

is defined as the ratio of the signal azimuthal and radial integration subtracted from the specular contribution of the DIFFERENCE over the SUM. Moreover, no mask hides the Bloch type diffraction part (0° and 180°) in the image, which is null in the DIFFERENCE pattern and thus decreases the asymmetry ratio value. In temperature, the asymmetry ratio value seems constant from figure 41 (a). This observation is surprising with regards to the reflectivity results that indicate the growth of an AFM peak. The growth of a net magnetic moment in the magnetic layers should decrease the chiral intensity. No change is neither observed in the peak position nor in the FWHM. Note that the SAFs have similar values for those three parameters, especially the spin spiral periodicity which is about 190 nm. In systems hosting a spin spiral magnetic texture, in which the chirality is dictated by the DMI, the spin spiral period Λ is proportional to the ratio of the exchange stiffness A and the DMI strength D_{ij}, $\Lambda \approx 4\pi A/D$[50,234]. This result would confirm the results that found a similar linear dependence to the saturation magnetization in temperature between the exchange and the DM interactions[231,235,236]. Simulations of the magnetic texture has been performed with MuMax3 to estimate a consistent set of symmetric and asymmetric exchange interactions.

The simulation has been initialized with the SAF10 magnetic parameters at 340 K with the 190 nm magnetic periodicity as a constraint. Its result is displayed in figure 42. A spin spiral-like sinusoidal spatial variation is found for the m_z and m_x magnetization components. The m_y component is negligible as the DMI value is sufficiently large ~ 0.5 mJ m^{-2} to ensure a pure Néel DW type. The associated effective exchange stiffness value is around 5 pJ m^{-1}, which is more than twice lower than the bulk value.

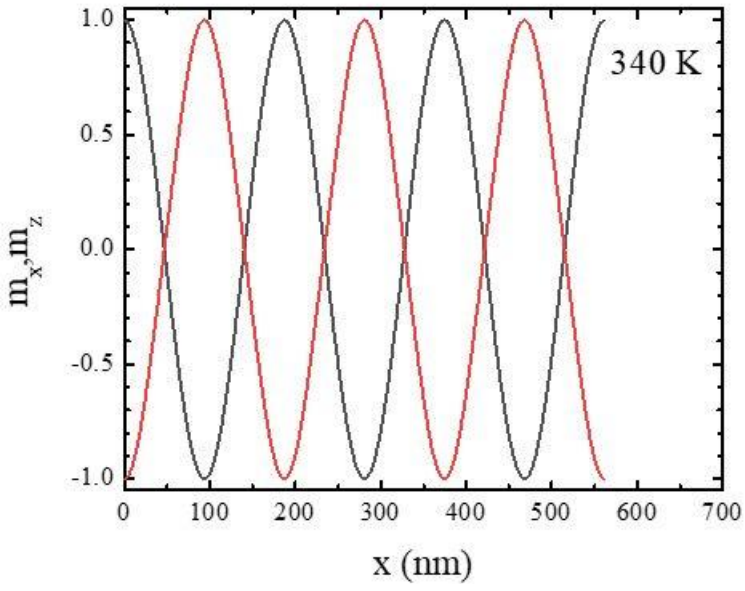

Figure 42: IP and OOP magnetization component profiles at 340 K obtained from a micromagnetic simulation that uses the SAF10 temperature dependent magnetic parameters.

The fact that the same periodicity value is found in SAFs with different tri-layer repetitions confirms the vanishing dipolar contribution, on contrary to FM multilayers. It prevents any

hybrid chirality in the thickness and should be a good playground for the simulation of the XRMS signal angular variation.

2.3.4 XRMS signal dependence to the incident angle

In order to confirm a pure and uniform spin spiral through the sample thickness, we have studied the angular dependence of the magnetic asymmetry ratio. To do so, a software has been developed by Flewett *et al*[195]. It uses the distorted wave born approximation (DWBA) which accounts for the differential transmission of the signal coming from the different buried magnetic layers. This feature is particularly important while dealing with multilayers and soft X-ray as the scattering cross section is much higher than in the hard X-ray regime. To account for the multilayer stacking, the matrix formalism is the same as the one presented in paragraph 1.3.3 in chapter 1, with a classical Maxwell description of the propagation and a dielectric permittivity calculated from the quantum scattering amplitude. The software can use micromagnetic simulation of each magnetic layer or a 3D magnetization vector field as an input. In the multilayer scenario, a stack of 2D map of the magnetization is used. The magnetization maps are transformed into reflection coefficient map, using the expression of the scattering amplitude and the dielectric tensor. The photon incident angle at each magnetic layer interface is calculated with the Snell law and differs from the experiment incident angle. After this first part, the Faraday polarization rotation as well as the intensity attenuation due to the transmission to the different medium are also calculated. Thus, the interference effect is weighted in amplitude by the depth of the scattering event. The optical path in the multilayer also changes the phase of the wave. The wave scattered in the different sample magnetic layers are added to the reflected beam. The propagation in the free space isn't a simple Fourier transform that doesn't account for the Ewald sphere curvature. It mostly plays a role for periodic structures having an off the scattering plane scattered vector contribution (q_y) and causes a q_x dependence of the effective incident angle which increases at grazing incidence. The program can simulate a reflectivity curve taking the zeroth order of the reflected beam. The result for the eight repetitions SAF is displayed in figure 43 (a). The reflectivity curve exhibits two Bragg peaks at ∼26° and ∼60°, similar to the experimental data. However, the intermediate oscillations aren't well reproduced. This is due to the roughness-free idealized sample used, as it is not yet implemented in the program, and that only non-magnetic/magnetic interfaces were considered. Another small contribution comes from the x-ray energy resolution around 707 eV in the experiment that is not considered in the simulations. As the main objective of the software is to reproduce the diffracted XRMS pattern from the magnetic texture. The 2D magnetic layers, used as input in the XRMS simulation, originates from the micromagnetic simulations performed at RT. The simulations (lines) and experimental data (dots) of the SUM (CL + CR) and DIFFERENCE (CL – CR) signal angular dependence are depicted in figure 43 (b) and (c), respectively. They are obtained from the radial profile integration of the magnetic diffracted signal and the simulated 2D pattern for the two circular polarizations on the thicker SAF samples, i.e., SAF8 (blue) and SAF10 (red). Since the sample surface roughness or other deviations from a perfect flat surface isn't considered, the specular spot in the simulations is punctual compared to the experimental one. Thus, the specular signal removal is only performed on the experimental data points.

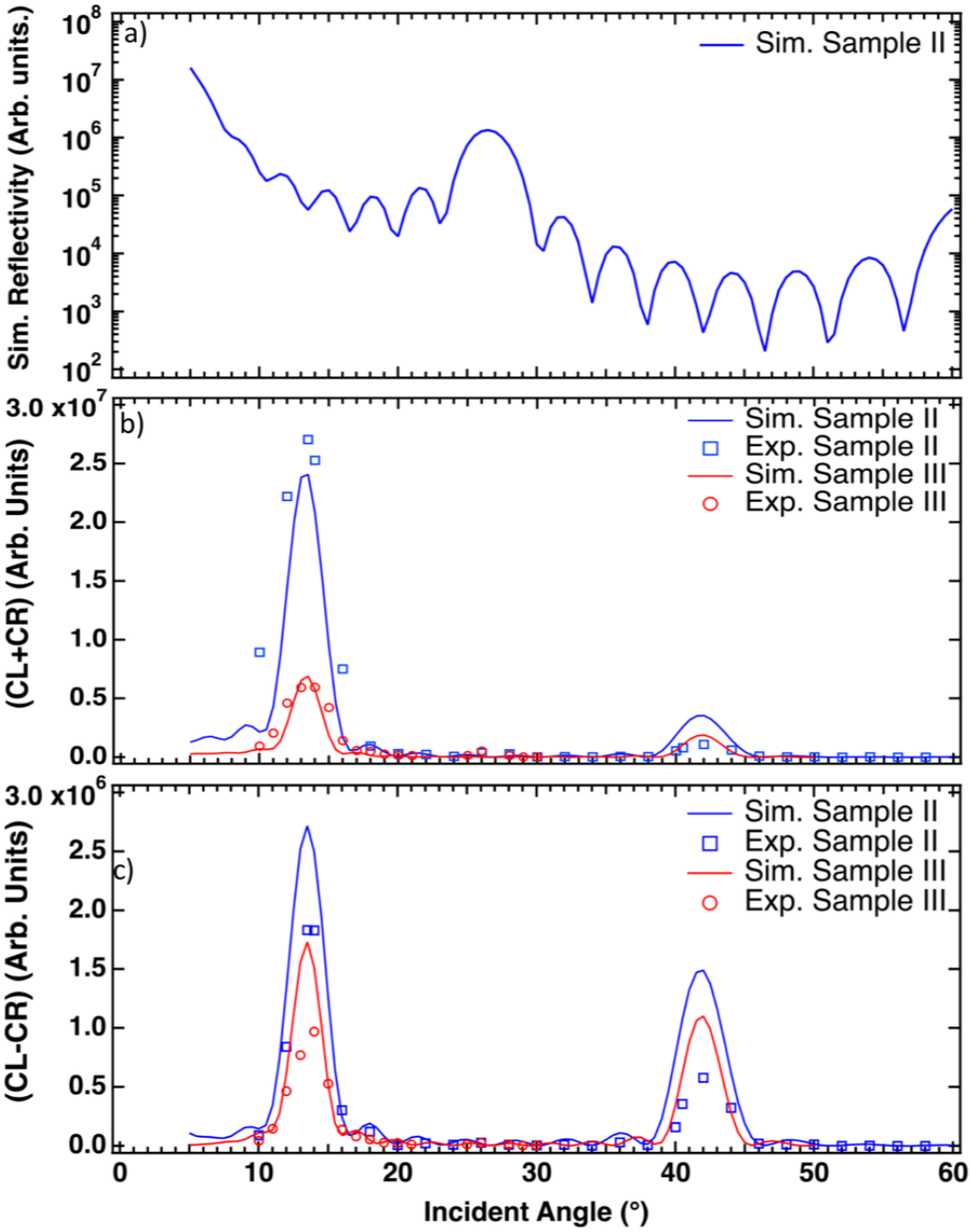

Figure 43: (a) The DWBA XRMS simulation of the eight repetitions SAF sample reflectivity curve. Graphics (b) and (c) display the simulations (lines) and the experimental points (dots) of the SUM (CL + CR) and the DIFFERENCE (CL – CR) signal intensity for the SAF8 (blue) and SAF10 (red). Simulations and experimental data were done for a photon energy of 707 eV. Figure extracted from Léveillé *et al*. **104**, L060402 (2021)[227].

Despite the several difference between the experimental and simulation parameters, the angular dependence is well reproduced at low angle. The intensity is vanishing at the multilayer Bragg peaks and maximum around $Q_{Bragg}/2$ and $3Q_{Bragg}/2$ in the SUM and DIFFERENCE. Both intensities are well reproduced by the simulation at $Q_{Bragg}/2$ but overestimated at $3Q_{Bragg}/2$. This discrepancy can be explained by the idealized sample without any interface roughness which impact more the scattering at high angles.

The XRMS software program is also available to simulate any XRMS diagram as function of field, temperature, time-resolved dependent studies as well as coherent scattering and speckle analysis. The XRMS scattering IP field dependence of a sample with a hybrid chiral texture and a Bloch point has been used as a test bench in Flewett *et al.*[195] publication. The implementation of the interface roughness and polycrystalline grains effects is under way (Flewett *et al.*, private communication). The combination of the micromagnetic and XRMS simulations together with experiments paves the way for the 3D reconstruction of chiral magnetic textures.

In this chapter, the XRMS formalism has been applied on different chiral textures with various DWs type and chirality to illustrate the (dichroic) off-specular diffraction pattern obtained with this technique. XRMS is based on the analysis of the DIFFERENCE (CL – CR) and SUM (CL + CR) images to explore the properties of the (chiral) magnetic texture. The formal XRMS calculations have been performed by considering a single magnetic layer, but it can be extended to multilayers, as shown in Chauleau *et al*[222]. The interference effect between the photons coming from the different magnetic layer is constructive at the multilayer Bragg peak. Thus, XRMS experiments on FM multilayers are usually performed at an incident angle and a photon energy that correspond to an integer of the multilayer chemical periodicity in the reciprocal space. The tunability of the magnetic interactions in multilayers fuelled the research for the optimal composition to obtain a skyrmion lattice state. The transverse motion experienced by the skyrmions when moved with an electrical current, pushed the research toward SAF samples. A SAF sample is a multilayer composed of AFM coupled FM layers. The magnetic periodicity is thus twice the chemical one. The study of SAF is thus performed at half odd integer multiple of the Bragg peak. The temperature variation of spin spiral optimized SAF samples has been performed and shown no variation in the magnetic texture periodicity. It indicates a similar temperature dependence of the exchange stiffness and DMI. Then the SUM and DIFFERENCE signals dependence with respect to the incident angle has been performed. The aim was to fit it with an off-specular diffraction program developed by Flewett *et al*[195] and fed by micromagnetic simulations of the 3D magnetic texture. The results were convincing, even though the roughness isn't yet implemented and compromise the angular dependence fit at high incident angles.

Chapter 3: Time resolved studies on chiral textures

3.1 Ferromagnetic samples with chiral domain walls

3.1.1 Samples description

FM systems have been studied more extensively than SAF samples, making them a straightforward choice for the ultrafast chirality evolution exploration. Multiple FM systems have been studied, statically and in pump probe mode. The first system consists in an asymmetric tri-layer repetition grown by sputter deposition SiO_2||Ta(5)|Pt(5)|[Pt(3)|Co(1.5)|Al(1.4)]x5|Al (0.1) grown at the CNRS/Thales laboratory (thickness in nm). A PLASYS MP900S system with seven 76 mm magnetron sputtering guns (rf or dc) allows to grow complex multilayers on relatively large surfaces, typically 51 mm wafers. A buffer layer made of tantalum (5 nm) deposited on top of the thermally oxidized silicon substrate prevents the delamination of the multilayer. On top of the buffer layer, a 5 nm platinum layer ensures a good (111) texture of the platinum, yielding a strong perpendicular magnetic anisotropy when interfaced with cobalt. The magnetic cobalt layer is sandwiched between platinum (3 nm) and aluminium (1.4 nm). The platinum layer thickness has been chosen to maximize the anisotropy at the Pt/Co interface, which dominates the effective magnetic anisotropy in all cobalt layers. It ensures a homogeneous magnetic anisotropy through the multilayer. Cobalt is used as the magnetic layer due to its strong exchange stiffness, as well as its lower total magnetic moment compared to iron. The latter property enables the growth of thicker magnetic layer with perpendicular magnetic anisotropy, which is further increased by the platinum interface. This feature is important as more magnetic material will give more signal.

As presented in the previous chapter, in planar geometry, it is possible to tune magnetic layer near the spin reorientation transition thickness, where the effective anisotropy cancels, which decreases the domain wall energy cost. The corresponding cobalt thickness is around 1.5 nm. In addition to the magnetic anisotropy, interfacing platinum with a magnetic layer allows a control of the magnetic texture by spin orbit torque. Platinum being a heavy element, with high spin orbit coupling, an electric current flowing into a platinum layer exhibits a spin separation perpendicular to the direction of the current by spin Hall effect[237]. The spatial spin imbalance is an effective spin current, which in planar geometry, can be directed toward another layer. If the other layer is magnetic, (either ferromagnetic or antiferromagnetic) the spin current is absorbed and it applies a torque on the magnetization. The sign of the torque depends on the direction of the current. The ferromagnetic sample was grown with a perspective in such application. Aluminium has been primarily chosen due to the high DMI strength of Pt/Co/Al trilayer[56]. Moreover, the DMI at the Pt/Co interface is among the largest reported[238]. Also, an aluminium thickness of 1 nm or more is sufficient to totally damp the spin current from the platinum layer. After the sputter deposition, the sample have been oxidized under controlled O_2

atmosphere, with a 50 mbar pressure. It ensures a sufficiently thick and dense aluminium oxide top layer to prevent any oxygen diffusion that could oxidize the topmost cobalt layer.

The capping layer have been chosen to be 1.5 nm thick, which is usually the optimal thickness to minimize light absorption. In the X-ray point of view, aluminium is a light element (atomic number, Z=13) with transition edges (~ 73 eV & 118 eV) far from the cobalt $M_{2,3}$ and $L_{2,3}$ edges, which is ideal to maximize the scattered magnetic signal. For the same reason, the tri-layer building block is repeated five times. It was thought to be the upper limit for a uniform chirality in the sample i.e., dominated by the DMI only. It maximizes the number of magnetic elements giving a similar magnetic chiral scattering. More repetitions of the tri-layer increase the dipolar field in the top and bottom magnetic layers, leading to a hybrid texture with non uniform chirality in the sample[62].

3.1.2 Magnetometry

Hysteresis loops have been performed to extract the effective anisotropy and the saturation magnetization. The latter can be deduced from the maximum magnetization observed in the hysteresis curve. The former is deduced from the difference between hard and easy axis hysteresis curve area. The generic formula is given by:

$$K_{eff} = \int M_{hard} \cdot dH - \int M_{easy} \cdot dH$$

(56)

In the particular case of samples with an almost zero saturation field for the magnetization easy axis, the expression of the magnetostatic energy ($\frac{\mu_0 M_s^2}{2}$) is still valid, the effective anisotropy can be directly derived from the saturation field. Otherwise, the perpendicular magnetic moment replace the saturation magnetization in the energy term to take into account the overall domain size evolution[46]. According to the sample easy axis hysteresis curve shape, which is almost saturated at remanence as seen in figure 44 (black open circle), the first case can be considered. Thus, the effective anisotropy is deduced with the saturation field using the hard axis hysteresis curve:

$$H_s = {2K_{eff}}\Big/{\mu_0 M_s}$$

(57)

We found experimentally a saturation field value of ~ 480 kA m^{-1} while the magnetization at saturation reaches ~ 1 MA m^{-1}. The effective anisotropy is estimated ≈ 0.3 MJ m^{-3}, which is small compared to the bulk value[46] of cobalt dipolar interaction 1.27 MJ m^{-3}. The uniaxial anisotropy K_u can be retrieved from equation 6 and yields ~0.93 MJ m^{-3}. As the thickness dependent study of the anisotropy hasn't been performed, it is not possible to extract the contribution of the volume to the overall anisotropy and consequently to compare the interfacial anisotropy with other Co/Pt based multilayers.

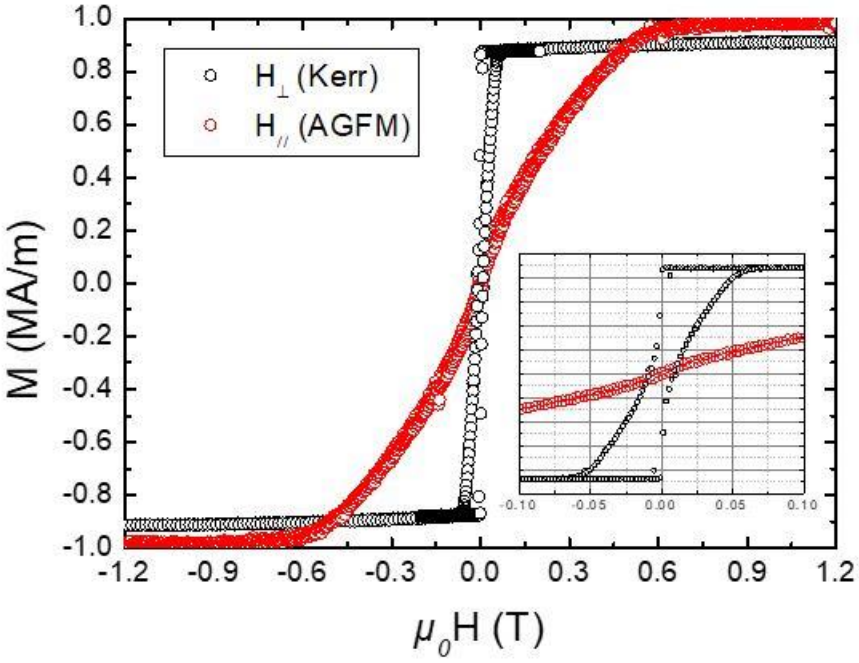

Figure 44: Hysteresis curves with the external field applied perpendicular to the sample plane (magneto optical Kerr effect measurements) and parallel (by alternating gradient field magnetometer). The sample exhibits a clear out of plane easy axis, meaning that the interfacial anisotropy is stronger than the shape anisotropy, as indicated by the positive sign of K_{eff}.

3.1.3 Magnetic force microscopy

MFM images have been performed after out of plane and in-plane demagnetization procedures. It consists in sweeping the magnetic field from the saturation field toward zero by decreasing the amplitude's absolute value of the applied field after each point and alternating the field polarity. As seen in figure 45, the out of plane procedure stabilizes a labyrinthic domain pattern, while the in-plane procedure stabilizes stripes domain along the applied field.

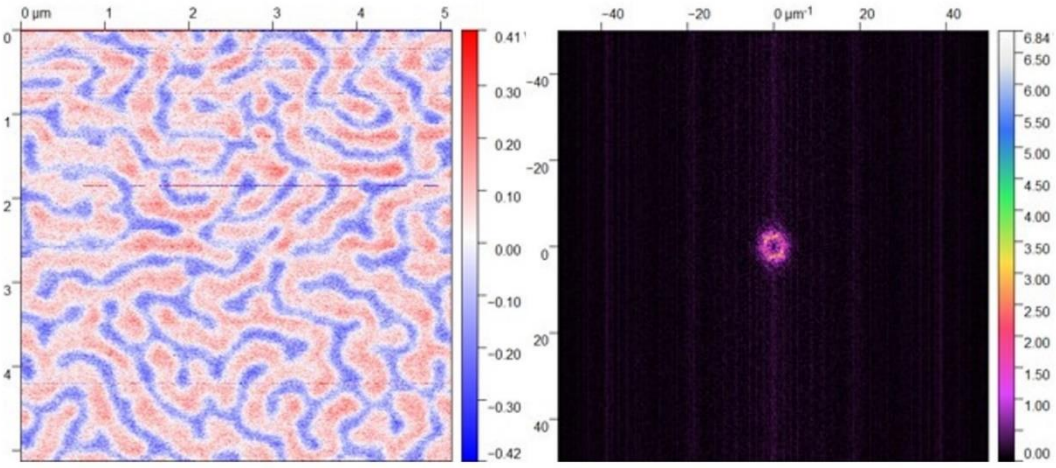

Figure 45: MFM image after an out of plane demagnetization and the corresponding 2D fast Fourier transform applied on the image on the right.

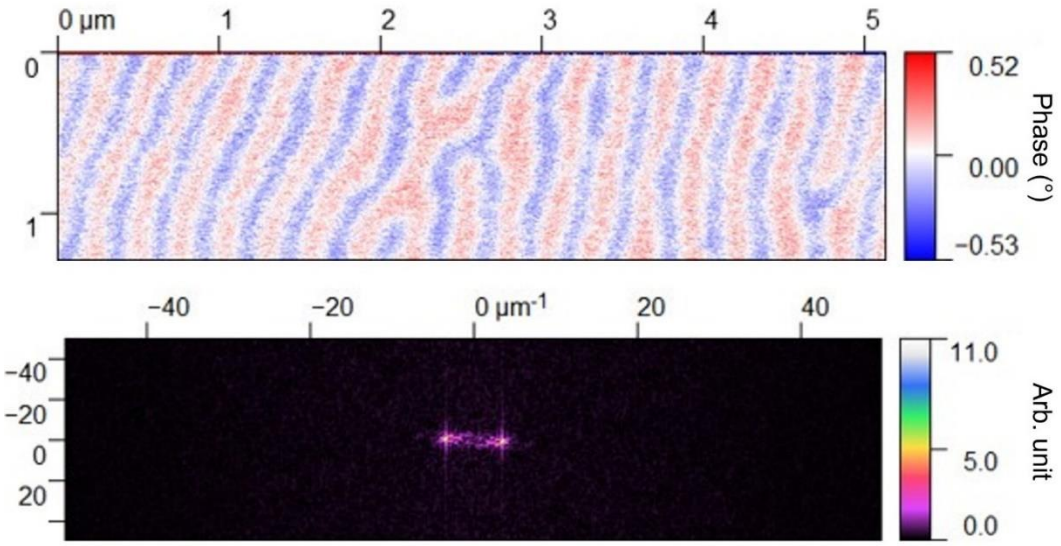

Figure 46: MFM image after an in-plane demagnetization procedure with the corresponding 2D fast Fourier transform below.

The 2D Fourier transform images yield a domain periodicity of 420 $\pm$ 30 nm for the maze domain pattern and 282 $\pm$ 2 nm for the stripes state. This periodicity variation with the magnetic texture can be understood qualitatively. The stripe magnetic domain state is obtained by IP demagnetization. It is a meta-stable state with a dipolar energy contribution larger than in the labyrinthine structure due to the uncompensated dipolar loops in the direction of the stripes.

3.1.4 Soft X-ray (resonant) reflectivity

Reflectivity measurements (cf. chapter 1 for description) have been performed at the L_3 cobalt resonance edge as well as off the resonant peak (750 eV). Each reflectivity was taken with a 0.1° step for the theta incident angle. As a reminder, the incident angle is taken relative to the sample plan. The beamline monochromator was set up to ensure a relatively small (285 meV) energy dispersion in the incoming beam but keeping large photon flux needed for such experiment. It is important to keep a low energy distribution near the x-ray absorption edge, as the optical indices vary drastically (see also chapter 1), even for elemental layers. The photodiode acquires photons during 1 second at each angle. This is typically enough for a good signal to noise ratio until ~30° in the studied multilayers, in RESOXS when the storage ring works with a 500 mA current. With flat interfaces, a few monolayers can be measured up to 85°[239]. The sample was a 3×3 mm² piece and the beam size was below 200 µm. The two information are important to fit the very first experiments data points (theta < ~3°). This angle corresponds to the separation between a fully reflected beam and photons that penetrate in the sample. The corresponding critical angle can be calculated from Snell-Descartes law $\theta_c \approx \sqrt{2\delta}$, with δ the material dispersive index in contact with vacuum (or air). For an aluminium oxide, $\delta \sim 10^{-3}$, which yields a critical angle $\theta_c \approx 2.56°$.

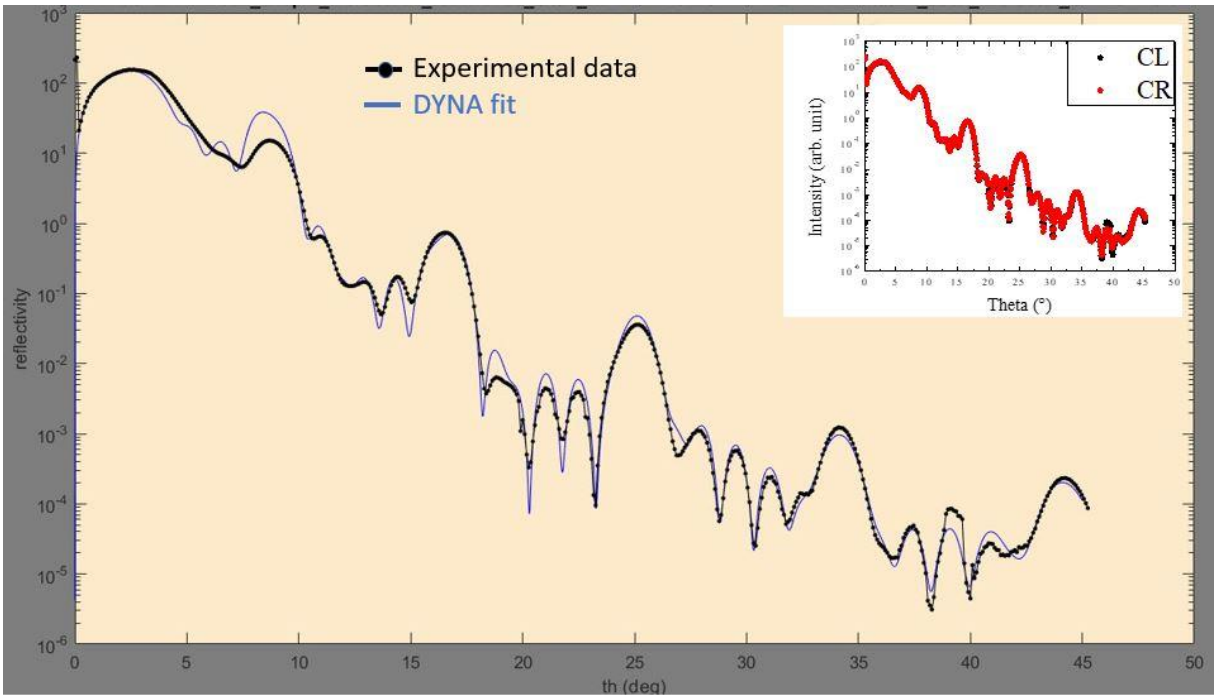

Figure 48: Off resonance data experiment taken at 750 eV (in black) with the reflectivity fit from the DYNA software (in blue). In inset, the CL and CR curve matches. Several chemical Bragg peak can be seen. The small difference between the two curves, observed around 40°, corresponds to the experiment noise limit.

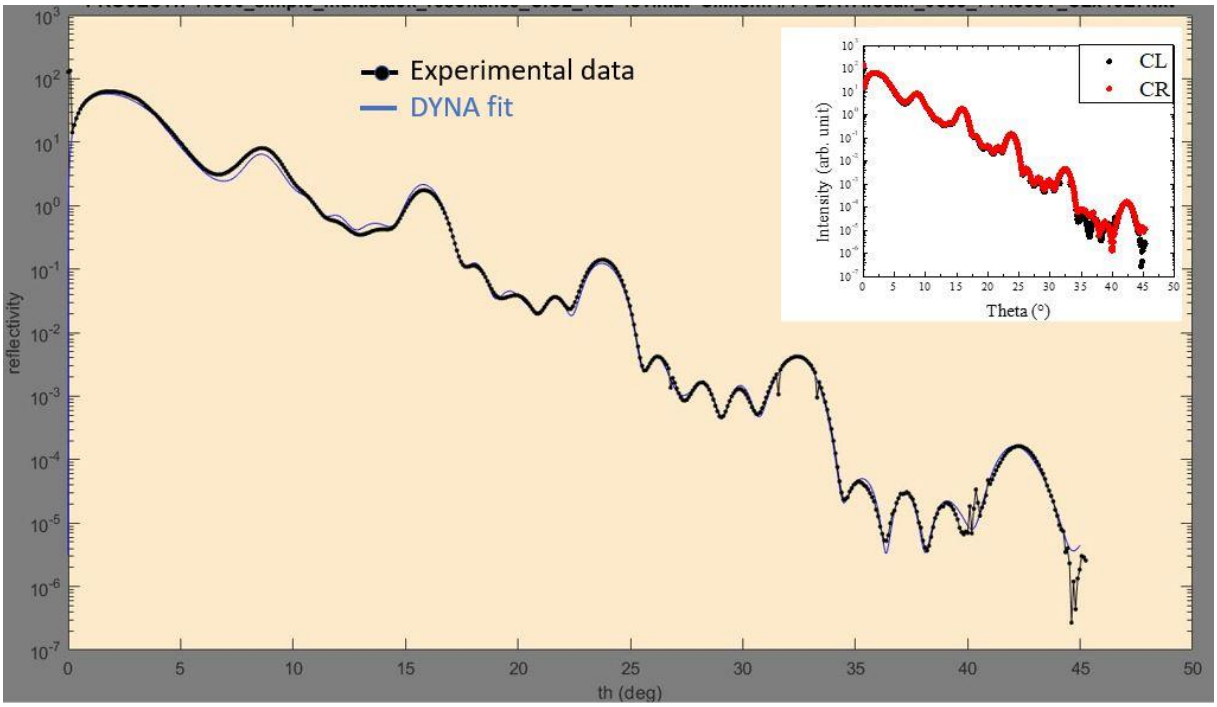

Figure 47: Reflectivity curve taken at the Co L_3 edge, 778.4 eV, (in black) with the reflectivity fit from the DYNA software (in blue). The point jumps observed in the Bragg peak around 33° correspond to a Keithley's range change at around this current intensity. In inset, the CL and CR curve matches, meaning that there is no not magnetic moment in the sample. Several chemical Bragg peak can be seen. The small difference between the two curves, observed around 40°, corresponds once again to the experiment noise limit.

The measurement at resonance is more dominated by the cobalt layers than the off resonance one, where the platinum layers properties have a strong influence on the curve shape due to its high atomic number. It allows a more precise fit of the cobalt layers properties. Also, the fit agrees better to the experimental data points compared to the off resonant one. The results of the fitting procedure show in previous figures give the layers properties i.e., molar density, the thickness and the roughness are displayed in the table below.

Table 3: Values of the reflectivity curve fit with the DYNA software.

Layer \ property	**multiplicity**	**Density (mol/cm^3)**	**Thickness (nm)** Fit	Nominal	**Roughness (nm)**
Al_2O_3	1	0.034	1.67	0	0.27
Al	1	0.089	0.91	1.5	0.22
Co	1	0.133	1.39	1.5	0.45
Pt	4	0.101	3.05	3	0.72
Al	4	0.089	1.49	1.4	0.99
Co	4	0.133	1.39	1.5	0.48
Pt	1	0.101	7.6	8	0.73
Ta	1	0.078	4.6	5	0.72
SiO_2	1	0.044	∞		0.51

The multiplicity column means the number of times the layer is repeated. A layer with the same multiplicity as an adjacent layer is considered as a building block of the multilayer repetition. The SiO_2||Ta(5)|Pt(5)|[Pt(3)|Co(1.5)|Al(1.4)]x5|Al (0.1) sample topmost layers have been separated in the fit due to the aluminium top layer oxidation. The density is in general smaller than the bulk value, which is common for nanometre thin layers except for the substrate. The thicknesses agree quite well with the nominal ones. However, a fly in the ointment must be noted since the platinum and tantalum buffer layers are very close to the fit restriction values. In the roughness, they are a bit high, especially the aluminium in the multilayer. It is more likely to be an artifact of the fitting procedure since the aluminium has a very small influence due to its low atomic number and that the energy used is far from any aluminium edge.

In the reflectivity curves, the multilayer Bragg peaks are clearly visible. They correspond to integer orders of the multilayer chemical periodicity. As the sample magnetic layers are ferromagnetically coupled, the maximum constructive interference for the magnetic signal is obtained at the Bragg peaks since the ferromagnetic periodicity matches the chemical one. The Bragg angle around 8.8° gives the maximum intensity. At the cobalt L_3 edge, the attenuation length in the cobalt is around 80 nm, while in the platinum it is around 62 nm. However, the thickness effectively crossed by the light is shorter with a factor depending on the incident angle sinus. The effective attenuation length at 8.8° becomes 12.2 nm for the cobalt and 9.4 nm for the platinum. Thus, only the topmost layers are probed, which approach to the experimental condition at the cobalt M edge.

3.1.5 Static XRMS results

As seen in the first part of chapter 2, the SUM image (CL + CR) exhibits a full diffraction ring, indicating a labyrinthine magnetic pattern. The modulation along Qx means that the pattern is preferentially oriented toward the x direction, which is parallel to the beam propagation here.

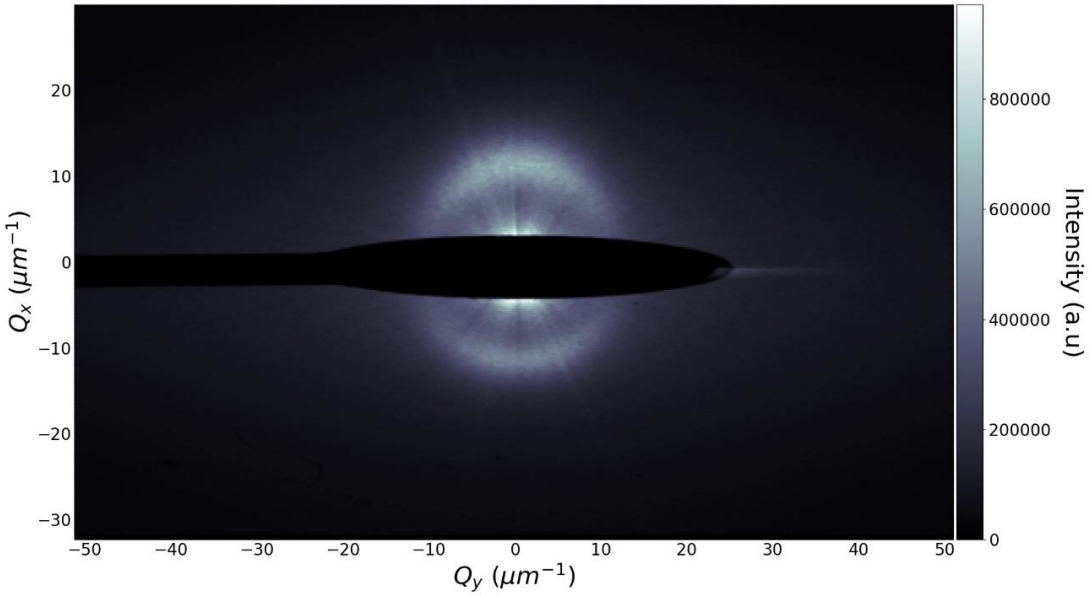

Figure 49: Circular left and circular right SUM image at 8.7°. The intensity modulation of the ring indicates a nearly labyrinthine domain organisation with a small orientation toward the Qx direction.

In the DIFFERENCE image, the dichroic XRMS pattern indicates a Néel type domain walls with a clockwise chirality[222]. This is in apparent contradiction with the sample stacking order. Indeed, a cobalt layer deposited on top of platinum should exhibits a CCW chirality[62].

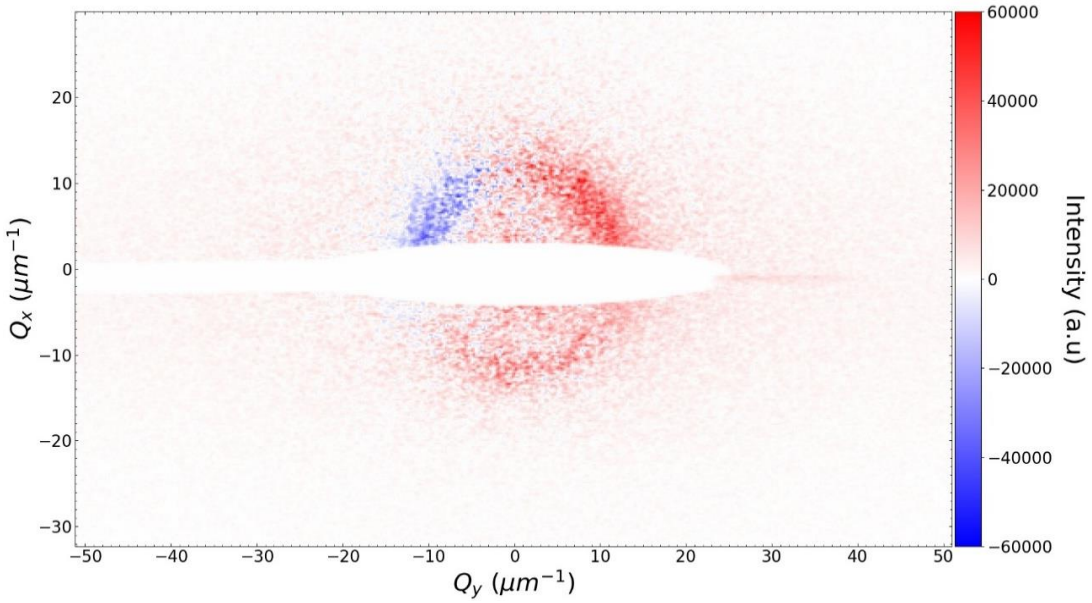

Figure 50: Circular left and circular right DIFFERENCE image, corrected from the projection angle, taken at 8.7°. The sign of the dichroism points toward a Néel type domain wall with a clockwise chirality.

It is further reinforced by the dichroic signal found at 15.8° and 23.7° that correspond to the 2nd and 3rd order multilayer Bragg peak.

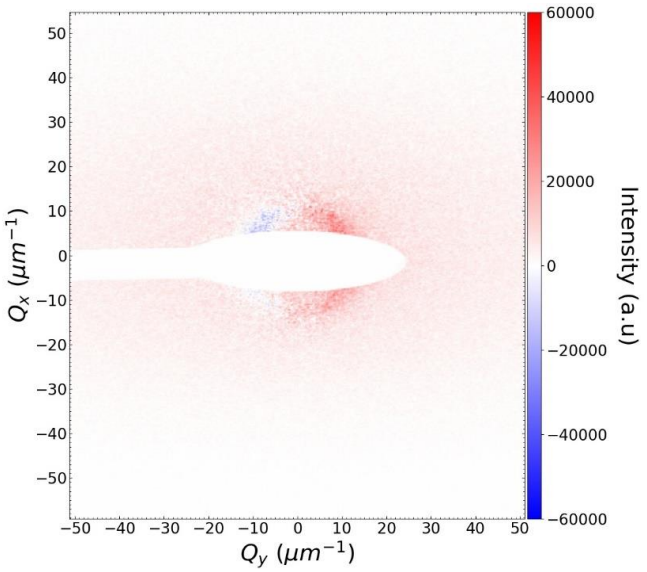

Figure 51: Circular left and circular right DIFFERENCE image corrected from the projection geometry taken at 15.8°. The dichroic sign still indicates a Néel type domain wall with a clockwise chirality but with a smaller intensity compared to the image taken at 8.7°. It originates from the higher incident angle that scatters less. It can also be due to a degradation of the diffracted signal due to hybrid chiral nature of the sample.

In the DIFFERENCE image taken at 15.8°, the dichroic pattern is the same, but the intensity of the diffracted signal is lower compared to the image taken at the first order. The trend of the reflectivity signal to decrease while increasing the angle is the main factor to this observation. A normalization by the SUM is necessary to compare the two angles.

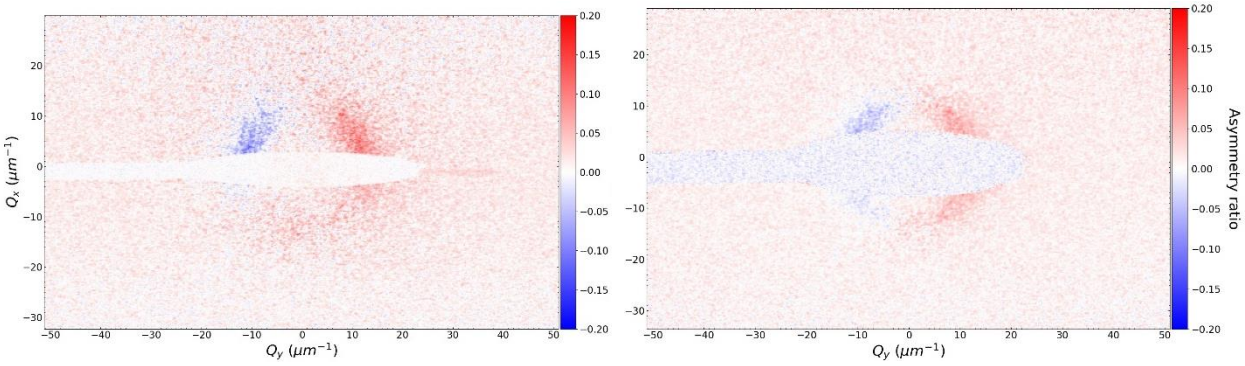

Figure 52: DIFFERENCE divided by the SUM image (asymmetry ratio) for 8.7° (left) and 15.8° (right). The two images exhibit the same domain wall type and chirality (i.e., Néel CW). The amplitude of the signal is a bit higher in the first Bragg peak than in the second.

The amplitude of the magnetic dichroic pattern is larger in the first order Bragg peak than in the second. The more defined ring in the higher angle is ultimately due to the finite dynamic of the CCD camera. Indeed, due to the geometric projection of the beam, the specular beam is elongated by a factor $1/\sin(8.8°)$ in the beam propagation direction. The specular reflection being far more intense than the magnetic signal, despite the use of a beamstop, the

magnetic contrast is lowered at low angle. Additionally, looking at the 3rd order Bragg peak angle, the absence of off-specular magnetic signal clearly indicates a hybrid chirality structure within the sample.

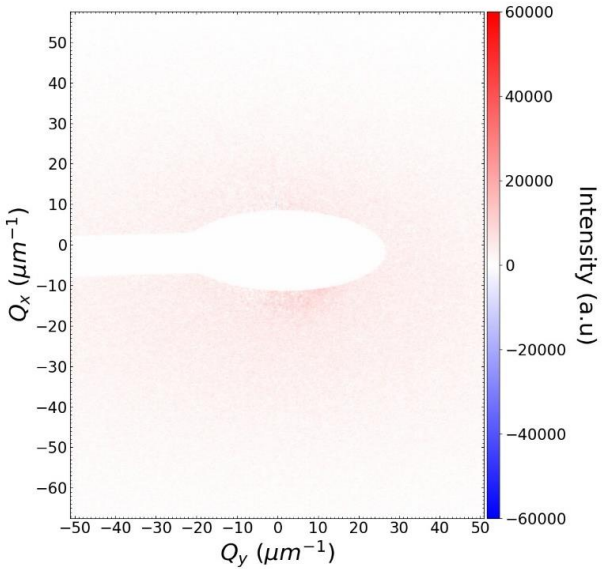

Figure 53: Circular left and circular right DIFFERENCE image corrected from the projection geometry taken at 23.7°. No dichroic signal is found on contrary to the images taken at 8.7° and 15.8°. It probably comes from the diffracted signal cancellation due to the hybrid chiral nature of the sample.

The reciprocal space diffraction ring radius, found in the first two Bragg peak order images, corresponds to a domain periodicity of ~ 530 nm. By comparison with the labyrinthine periodicity observed by MFM (420 nm), the discrepancy is rather large. The periodicity obtained by XRMS usually differs from the MFM measurements due to the refraction index variation at the resonance edge since the wave vector k depends on the refractive index value. The latter directly depends on the scattering amplitude, as seen in the previous chapter.

3.1.6 Micromagnetic simulations

The experimental conclusion of a possible sample with hybrid chiral nature has been further investigated with numerical simulations using MuMax3[240]. In order to facilitate the simulations, by eliminating the random variation inherent to the numeric labyrinthine pattern generation, the focus is brought to the stripe domain pattern. The numerical simulation has been performed by colleagues from UMPhy team, using a cell volume of $0.44 \times 0.8 \times 1.48$ nm^3 along x, y and z directions respectively. The z component is chosen to match the magnetic layer thickness. Also, the tri-layer thickness divided by the cell dimension in the z direction should give a power of 2. This last point increases the calculation speed of MuMax3[240]. It assumes a uniform in depth magnetization profile in each magnetic layer. The exchange length, that corresponds to the distance over which the exchange interaction dominates, is usually around 10 nm or more. Thus, the magnetization should not vary in the layer depth. The cell dimension is smaller in the x direction than in the y because the magnetization isn't supposed to vary with y. The x cell dimension is an important feature, as the angular variation between neighbour spins should be kept lower than 20° to obtain an error of ~1%[240]. An estimation of the domain wall

width can be calculated by $\pi\Delta = \pi\sqrt{A/K_{eff}}$. Taking A ≈ 16 pJ m^{-1} found in multilayers with even thinner cobalt thickness, it approximates the domain wall width of $\pi\Delta \sim$ 23 nm. The x cell size (0.44 nm) has been chosen accordingly. The system size is set to 285× 32 × 25.1 nm^3 with x and y axis repeated with boundary conditions. The repetition together with the periodic boundary condition removes the side effect from the demagnetizing field. The z direction size corresponds to the total multilayer thickness minus the buffer stack and the external non-magnetic layers. The platinum and aluminium thickness between each cobalt layer should prevent any electronic exchange between the magnetic layers, which usually vanishes for platinum thicknesses above 1 nm[12]. The initial magnetization points along +z for small x and along -z for larger x. The central magnetic moment in the domain wall lays along the [1 1 1] direction. The magnetic configuration is minimized from this state, which avoids metastable states (Néel or Bloch) that would pin the convergence into a local minimum.

Some sample magnetic parameters, such as the saturation magnetization and the interfacial anisotropy, have been retrieved by magnetometry measurements and fuelled the numeric simulation. However, the exchange energy as well as the DMI aren't experimentally determined. Their amplitude can be tuned in the simulation to match the experimental MFM periodicity. It is realized by calculation of the system energy density ε with fixed parameters but using different periodicities around the observed one. The numerical derivative of ε can then be calculated from the observed periodicity for a set of exchange stiffness A and DMI strength D.

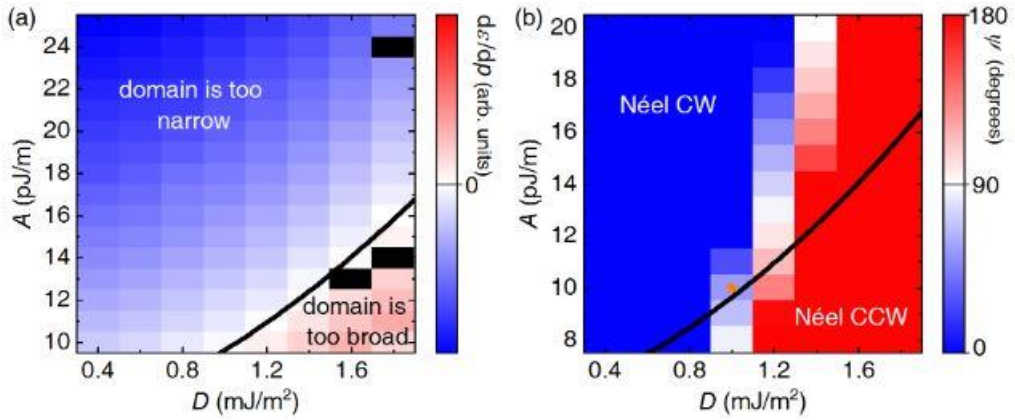

Figure 54: Determination of the symmetric and asymmetric exchange energies. (a) Map of the energy density ε derivative by the domain period p as a function of the effective DMI D and effective exchange energy A. The near zero-derivative zones indicated by the thick black line corresponds to the set of possible parameters minimizing the energy density for the observed period. (b) Corresponding map of the DW magnetization angle ψ of the topmost cobalt layer. The curve of the possible parameters is reported from panel a. The Bloch component is determined by the initial condition of the simulation and is always around ψ = 90°. Black squares indicate discarded values due to convergence error. The orange square corresponds to the selected parameter set for the magnetization profile plots. Taken from Léveillé *et al*[254].

In the figure 54(a), the numerical energy density derivative is plotted as a map, with the effective exchange A and the effective interfacial DMI energies as parameters. The colormap corresponds to the energy density period derivative $\partial\varepsilon/\partial p$ with the observed periodicity p_0. It's numerically computed using simulations with smaller or larger periodicity p with the same set

of magnetic parameters. The size in the x direction is changed for each five periodicities p used for the simulations by step of 10 nm. If the derivative of the energy density with respect to the periodicity is not zero, then the simulation performed with the experimental periodicity isn't the state minimizing the energy of the observed period p_0. The area in blue corresponds to a negative derivative, the set of magnetic parameters favours a larger domain width. This is in adequation with the larger exchange and the low DMI energies value, since DW energy is larger. In the red area, it is the opposite. It is dominated by the DMI contribution that reduces DW energy, and thus, the stable domain size with this set of parameters is smaller than the experimental one. The black curve draws a path of parameters where p_0 is the equilibrium magnetic period state. To determine a valid set of parameters, one has to look at the topmost cobalt layer chirality, that has to be opposite to the one favoured by the DMI, as we observed the XRMS contrast corresponding to CW Néel DW (on figure 50-53). The map in figure 54(b), plots the domain wall magnetization orientation with respect to the exchange and DM energies. The DM energy values that still favour a CCW chirality in the top magnetic layer can be discarded. The solution is thus located around the black curve for D values smaller than the ones favouring a Bloch point ($\psi = 90°$).

Finally, one ends up with a possible magnetic parameter set with D = 1.0 mJ m^{-2} and A =10 pJ m^{-1} indicated by the orange star in Fig. 54(b). From previous studies, using field induced DW propagation[241], the DM strength D is expected around D ≈ 1 mJ m^{-2} in this particular stack, which matches with the estimation. The exchange energy range is a bit low in value compared to the one determined by Brillouin light scattering on similar multilayer with a thinner cobalt layer (A = 16 pJ m^{-1}), that is why we selected the solution with the larger possible A value.

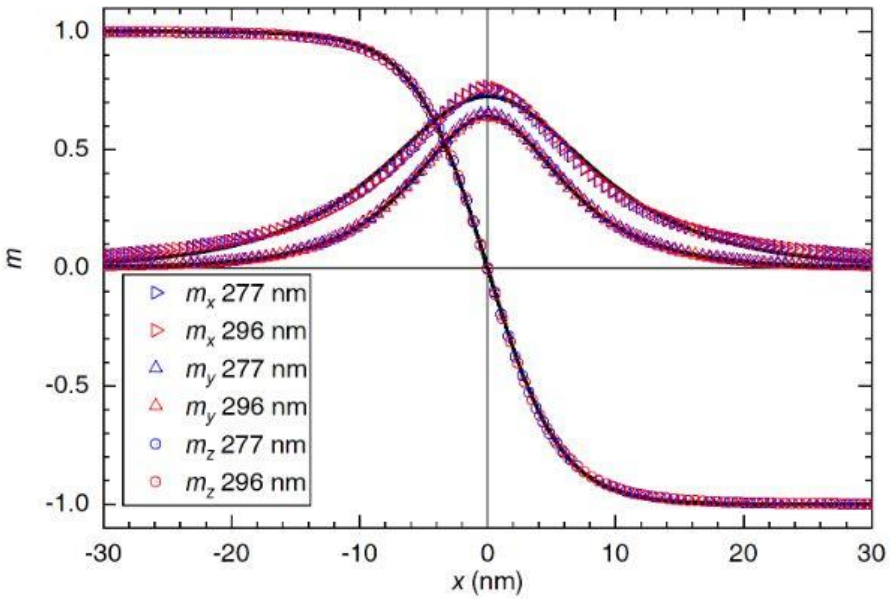

Figure 55: Simulation of the magnetization profile in DW of the topmost cobalt layer. The red (blue) symbols correspond to simulations performed with a + 10 (- 10 nm) domain periodicity with A = 10 pJ m^{-1} and D = 1.0 mJ m^{-2}. Continuous lines are fits using the formula (58) below. The DW width is weakly dependant of the precise period for a variation of 10 nm. The image is taken from supplementary materials in Léveillé *et al*[254].

The DW profile has been explored in conditions close to the expected physical

configuration, with a periodicity 10 nm different than the MFM one. The DW width, is determined from the numerical simulation (18 nm for the z component of the magnetization) and fuel an empirical magnetization profile function draw in continuous line in figure 55.

Both have the same DW width, with a non-pure Néel chirality in the topmost layer. The Bloch contribution is achiral, which is in agreement with the DIFFERENCE XRMS images where no Bloch part is observed. The functions fitting the DW profile is a 1D model, whose complexity will be justified in the discussion of the ultrafast dynamic results.

$$M_x(x,t) = \cos(\Theta(t))\, M(t) \left[\sqrt{1 - \left(\tanh\left(\Lambda \frac{x_1(x)}{w(t)/2} \right) \right)^2} - \sqrt{1 - \left(\tanh\left(\Lambda \frac{x_2(x)}{w(t)/2} \right) \right)^2} \right]$$

$$M_y(x,t) = \sin(\Theta(t))\, M(t) \sqrt{1 - \tanh\left(\left(\Lambda \frac{x_1(x)}{w(t)/2} \right) \right)^2} - \sqrt{1 - \tanh\left(\left(\Lambda \frac{x_2(x)}{w(t)/2} \right) \right)^2}$$

$$M_z(x,t) = M(t) \tanh\left(\frac{\Lambda}{2} \frac{x_3}{w(t)} \right)$$

(58)

With $x_1(x) = \sin\left(\pi \frac{x+\frac{\Lambda}{4}}{\Lambda} + \frac{\pi}{4} \right)$, $x_2(x) = \sin\left(\pi \frac{x+\frac{\Lambda}{4}}{\Lambda} - \frac{\pi}{4} \right)$ and $x_3(x) = \sin\left(2\pi \frac{x}{\Lambda} \right)$. x is the position in the domain while Λ corresponds to the domain periodicity, in the same units as x. Θ is a tilting angle defining the hybrid DW type. For Θ = 0° (90°), it corresponds to a pure Néel (Bloch) DW. The empirical model also considers the time evolution of the magnetization *M*(*t*), which is proportional to $\sqrt{CL + CR}$, and the temporal evolution of DW width *w*(*t*)~πΔ. As the asymmetry ratio amplitude depends on the relative width of the DW over the domains, a clean separation between the specular tail and the diffraction signal is performed for experiments performed in reflection geometry. Indeed, the specular signal is spread due to its projection on the sample and overlaps with the off-specular signal. Before introducing the data analysis method, the experimental parameters are briefly presented as some intervene in the data treatment.

3.1.7 XRMS Data-analysis

During the few experiments performed, the laser spot size was 384×239 µm² and the smaller FEL spot 247×181 µm², given in 4σ. The difference in size between the two beams ensures that the diffracted signal comes only from the pumped region. The scattering patterns have been recorded with a PI-MTE CCD square 2048 pixels camera with a pixel size of 13.5 µm. It is located at 12 cm from the sample. At each delay between the horizontally polarized IR pump and the XUV probe, 500 shots were accumulated and stored in a single image in the HDF5 format used nowadays at most of the large facilities as FERMI, SOLEIL... Two accumulation images were taken for each delay and each polarization of the probe. To reduce the CCD reading time, the images have been binned by a factor 2 in the two directions. The

accumulation is performed by the CCD software and the binned image saved in the HDF5 file. The latter also contains other experiment contextual data, such as the FEL wavelength, the laser pump energy per pulse or the XUV shot intensity.

A four-quadrant photodiode, placed upstream the experimental chamber, collects the tails of each XUV shot. The four-quadrant photodiode intensity is used to normalize the image, diminishing the image-to-image variation due to black shots. In addition, a choice has been made to remove all the x-ray images that differ by 20% from the average of the four-quadrant diode total intensity of all the images. Before and after each delay scan, a CCD background image ("darks") is taken with the same acquisition dynamic (50Hz) and accumulation (500 shots). The darks images are averaged and subtracted from the diffraction images. Each processed image is sorted by delay value and separated in circular left and right polarization. The images are resized by a geometric factor that accounts for the 45° incident angle projection. The SUM (CL + CR), DIFFERENCE (CL – CR) and asymmetry ratio [(CL-CR) / (CL + CR)] images are calculated. Due to the non-perfect normalization between the two circular polarizations and to the FEL spatial jitter between polarizations, some erratic points can be found at the

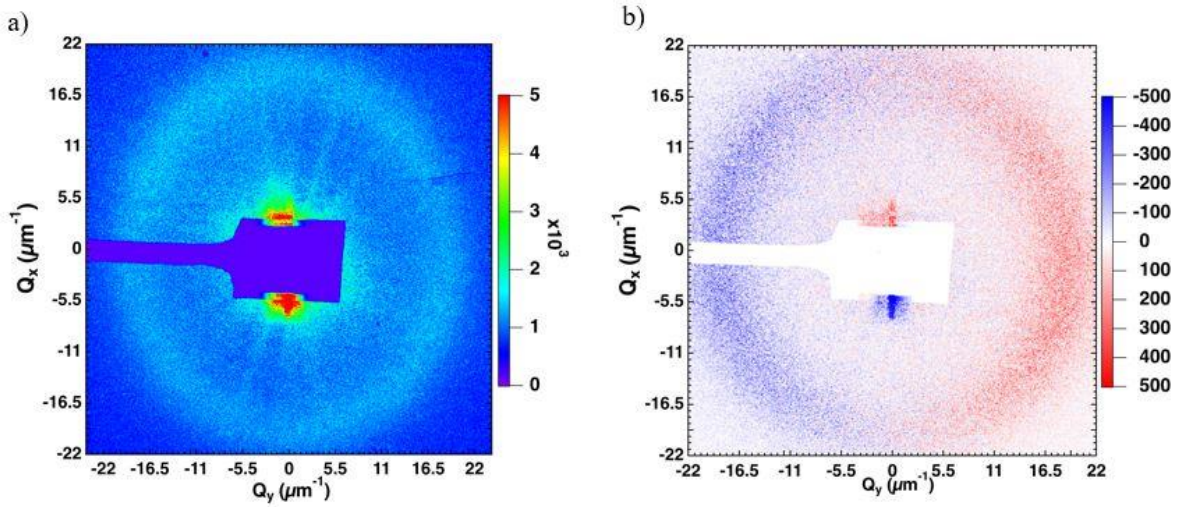

Figure 56: (a) SUM image (CL + CR) without intensity modulation in the ring, typical of a labyrinthine domain pattern. (b) Dichroic diffraction pattern (CL – CR) exhibiting a clockwise Néel DW signal. The two images have been geometrically corrected from the projection angle. Both images were taken at a negative delay time and are from Léveillé *et al*[254].

edges of the beamstop, as observed in the DIFFERENCE image in Fig. 56(b). After a manual determination of the center of the diffraction pattern, a radial mask is applied to mask the beamstop. A symmetric angular mask is also applied to remove any spurious effect due to the beamstop support. Another mask consists in replacing directly in the image the value by zero. Then, an azimuthal average is performed excluding zero pixels outside the radial mask. This is done to keep the full range of the images' radial profile in the graph. It also ensures that the averaged radial profile is performed on non-zero-pixel values. Note that it is not applied in the two images in figure 56.

Then, the diffuse signal is removed in a large disk around the specular position. It is particularly important for the SUM (CL+CR) images as the specular tail contribution is far greater than the

diffracted magnetic signal. In X-ray diffraction, a peak is usually fit by a Voigt function. The function is a convolution product between a Gaussian and a Lorentzian function. In our case, the specular peak is hidden by the beamstop and the off-specular magnetic signal is located at approximately 300 pixels of the estimated center. The pixel width is 27 µm in both directions due to the 2×2 binning, meaning that the signal is 8.1 mm away from the center. It is more than one order of magnitude greater than the FEL spot size. The use of a smaller beamstop, to fit better the specular signal, would hide almost totally the magnetic scattering due to the finite CCD dynamic range. Thus, several simpler functions (Gaussian, exponential, Lorentzian or polynomial functions) have been tried to fit the specular tail. The green dotted lines in figure 57 have been chosen to maximize the number of points with only the specular signal at the maximum of demagnetization. The latter is the more critical to fit due to the low magnetic signal.

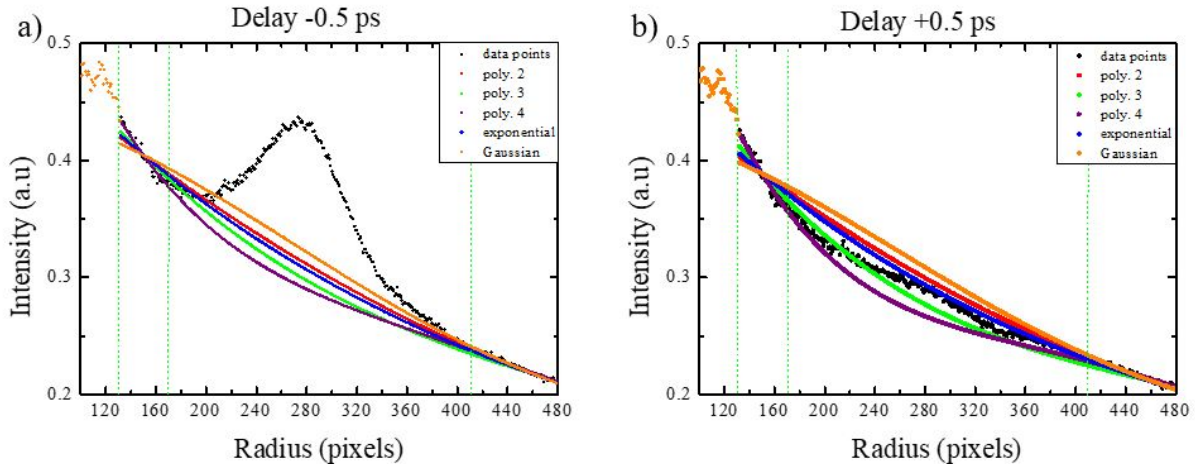

Figure 57: Fit attempt of the specular signal under the diffracted magnetic peak by different functions at negative delays (a) and around the maximum of demagnetization (b). The orange points before the first green dotted line at 130 pixels correspond to the experimental radial profile. The non-regular shape is due to the non-circularity of the beamstop.

Gaussian or exponential functions in the fitting procedure struggle to appropriately simulate the diffusive part under the diffracted magnetic signal at negative and positive delays. Note that, the Lorentzian decay is too abrupt to reproduce properly the specular and the fit didn't converge. The order 2 polynomial curve can't follow the data points decreases, while the 3rd and 4th order are able to. From figure 57, the 4th order polynomial curve could look better than the 3rd order, but it takes too much curvature under the peak, leading to an overestimation of the magnetic signal. Moreover, the prefactor of the 4th power is extremely small, indicating that the 3rd order polynomial can be sufficient. Noteworthy, the possibility to use inverse functions such as $a/x^n + b$ haven't been explored during the data treatment. The use of this kind of function to fit the tail of gaussian-like repartition has been widely spread in different themes[242].

The resulting specular signal removal with the parameters used in the data analysis, i.e., a third order polynomial function at each delay and a fixed fit range is plotted in figure 58 at two delays for the SUM image. The fit (red line in figure 58) seems to simulate well the specular curvature, even at the maximum of demagnetization. Since the range is the same for all the delay, the pre-peak one catches a bit the magnetic signal for negative delay to improve the fit when the signal is close to its minimum. The result dispersion depending on the fit parameters

has been studied and is discussed later.

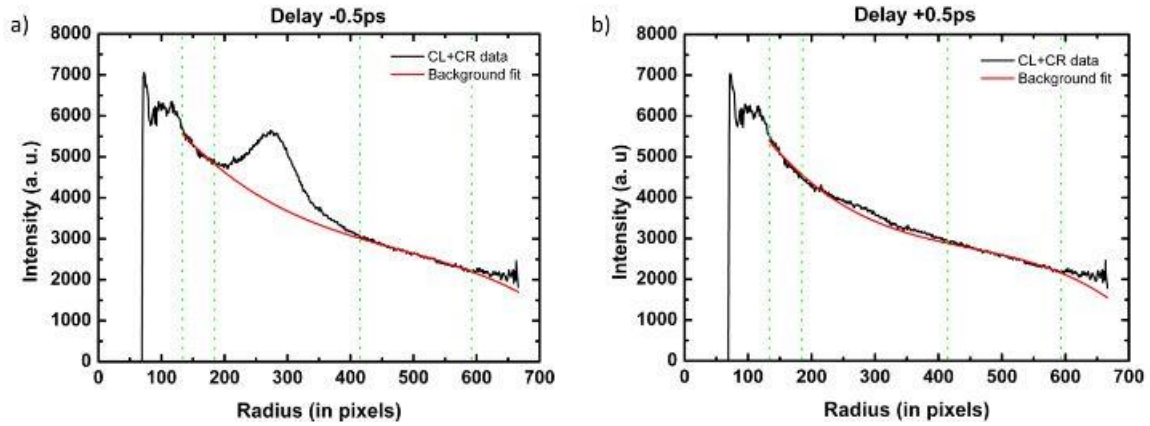

Figure 58: Radial profile of the SUM image for delay times of -0.5 ps (a) and 0.5 ps (b) that corresponds to the maximum of demagnetization. The red line is a cubic function that simulates the specular signal fitting data enclosed in the two areas marked by the vertical green dots. Taken from Léveillé *et al*[254].

After the specular fit removal, the remaining diffraction peak is fitted. For the SUM and DIFFERENCE signal, a Gaussian function works well as seen in figure 59. The amplitude, the full width at half maximum (FWHM) and the peak position are displayed in wave vector units (μm^{-1}).

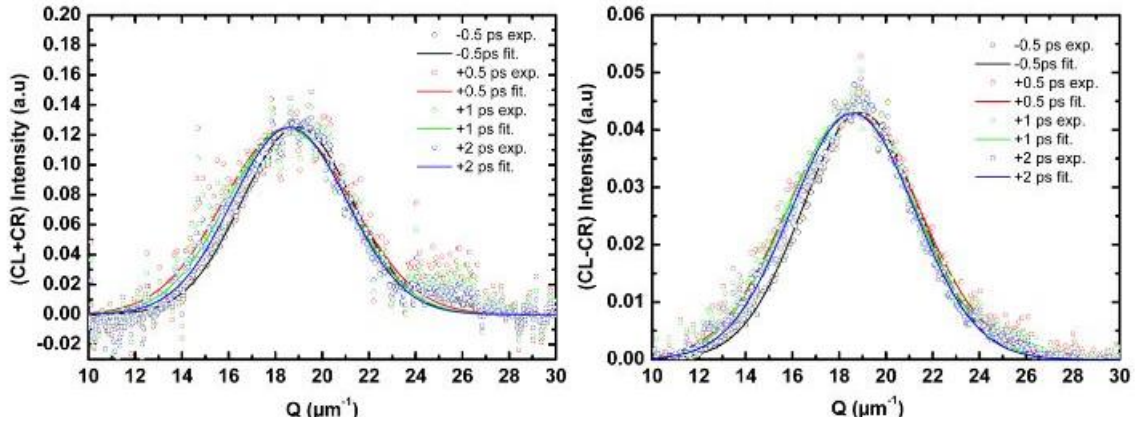

Figure 59: Experimental data points for the SUM image (a) and the DIFFERENCE (b) after specular subtraction. The coloured lines are Gaussian fit of the different delays. The curves and fits have been rescaled to the -0.5 ps value for clarity. Image taken from supplementary materials of Léveillé *et al*[254].

The amplitude is used as a verification of the gaussian signal fit since it should give the same result as the direct integration of magnetic peak radial profile (see Fig. 60(a)). The orthoradial profile is also extracted from the CL – CR images at all delays to check if a change of chirality occurs after the optical excitation. Some orthoradial profile are displayed for different delays corresponding to the unpumped system, the maximum of demagnetization and the recovery phases.

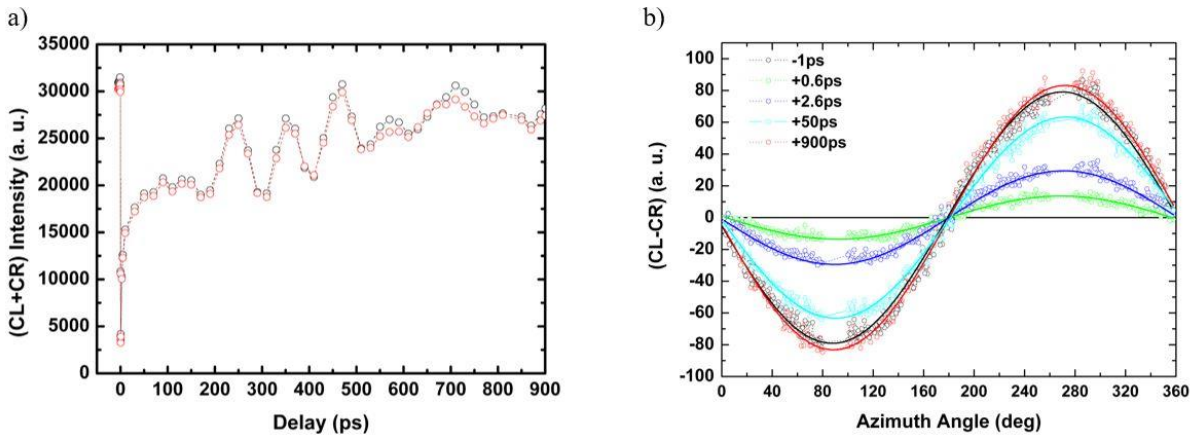

Figure 60: (a) The SUM signal resulting from the direct signal integration under the magnetic peak and the amplitude of the Gaussian fit. (b) Orthoradial profile in the DIFFERENCE image for different delays. The symmetrical mask, removing potential signal artifact from the beamstop holder is visible at 90° and 270°.

The different azimuthal profiles keep their sinusoidal shape with the maximum (minimum) at 270° (90°) at all delays. Only a symmetrical variation in the amplitude at +90° and 270° is observed, meaning that the CW Néel chirality persist even at the ultrafast time scale (see chapter 2). Note that the azimuthal profile isn't corrected from any background or specular signal residue, showing that the spatial FEL jitter has a negligible influence if the signal is far enough from the beamstop. The robustness of the radial profile specular fit is explored in the Annex A.

3.1.8 Time resolved studies

In the following, the time resolved study on the chiral FM multilayer are presented. The determination of the probe fluence and the potential issues that can emerge while dealing with interface sensitive multilayers. Then, the artifact-free time-resolved results are presented, beginning with the ultrafast regime (delays < 5 ps) and a specially developed model that gives insights about the underlying mechanism that could be responsible of the ultrafast behaviour. It is followed by the sub-nanosecond dynamics which is completed by MOKE and VNA-FMR experiments, as well as magnetic mode simulations to understand the sub-nanosecond dynamics. Then, the effect of the pump circular polarization at different fluences on the SUM and DIFFERENCE signals is explored on the same sample.

3.1.8.1 Optimization of the free electron laser fluence

After setting up the data analysis procedure, dynamical diffraction patterns have been analysed. The following delay scan have been performed with two different laser fluences and with a XUV FEL fluence of ~1.1 mJ/cm^2. The two graphs containing the SUM and DIFFERENCE signals at the two different IR pump fluence performed at two different areas, separated by 1 mm, are reported in figure 61.

In Fig. 61(a), both SUM signals exhibit an ultrafast demagnetization followed by a recovery that is not completed at 900 ps after t0, which is not concerning if the amount of absorbed energy by the magnetic layer is high. In some extreme cases, where the electronic and

spin temperatures exceed the Curie point, the recovery dynamic can be slowed down to the nanosecond timescale.

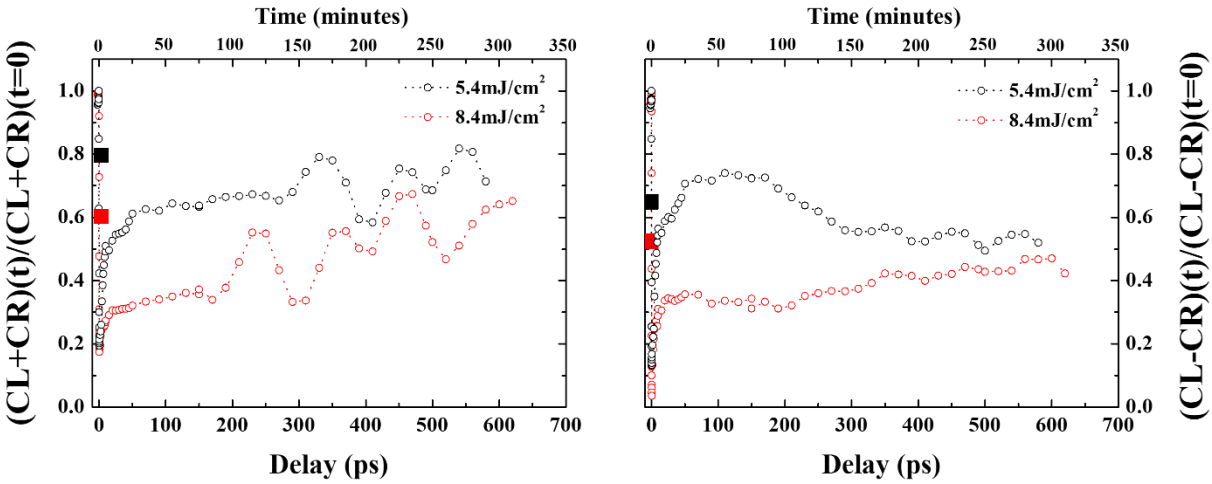

Figure 61: Time dependence of the SUM (CL + CR) and DIFFERENCE (CL – CR) magnetic intensity normalized for two IR laser fluences. The big squares represent points taken after the delay scan at a negative delay.

Oscillations with different on-set and periods are visible in both curves at hundreds of ps, which is a new feature not observed in previous time-resolved XRMS study on magnetic domain texture. But this results has to be taken with care as the two points taken after each delay scan don't recover the initial value of their respective scan. The drop corresponds approximately to their respective last scan value, but it is surprising that the intensity didn't fully recover even for a high pump fluence as the big square points have been recorded at least 20 ms after a laser shot. Looking now at the DIFFERENCE signal (figure 61.b), a peculiar evolution is found once again at the hundreds of picosecond time scale. For the delay scan with an IR pump fluence of 8.4 mJ/cm², the curve (empty red circles) recovers after the ultrafast drop and stabilize at 30% of the maximum signal, then increases slowly with the delay. But the red square point, indicating a point taken at a negative delay after the experiment in the same probed area, recovers at a value a bit above the last scan value but at 50% of the initial scan value. In the 5.4 mJ/cm² delay scan (empty black circles), the decrease is directly visible through the scan. After reaching 70% of its initial value around 100 ps, the DIFFERENCE signal decreases constantly until the end of the scan, dropping to 50% at 900 ps. As previously observed in the SUM and 8.4 mJ/cm² curves, the negative delay point (black square point) taken after the scan doesn't recover the initial value.

The fact that the behavior is more pronounced in the DIFFERENCE curve with the smaller IR fluence, indicates that it is not pump fluence related. Moreover, the IR pump fluence used for the measurement are typical for ultrafast demagnetization studies[16], an order of magnitude away from the damage threshold. The fact that the process is observed after five hours long scan and is visible only in the hundreds of picosecond timescale indicates a thermal diffusion heat assisted effect. Moreover, the chiral signal is more impacted than the SUM. It could mean that it originates from a thermal effect occurring at the interface. Intermixing affects the value of the DMI but it does not vanish[243], explaining that the signal doesn't fall to zero for the highest IR fluence. Another feature observed in the curves is the pronounced damped oscillation with a characteristic timescale of ~165 ps (~6 GHz). It is more visible in the SUM than in the

DIFFERENCE. The origin of those oscillations is discussed later. In the results presented thereafter, the FEL intensity has been attenuated by ~50% (I = 0.5 mJ/cm²). Also, a systematic measurement on the probed area at negative delay (-1 ps) has been performed to check the sample integrity after each delay scan but won't systematically be presented in the following.

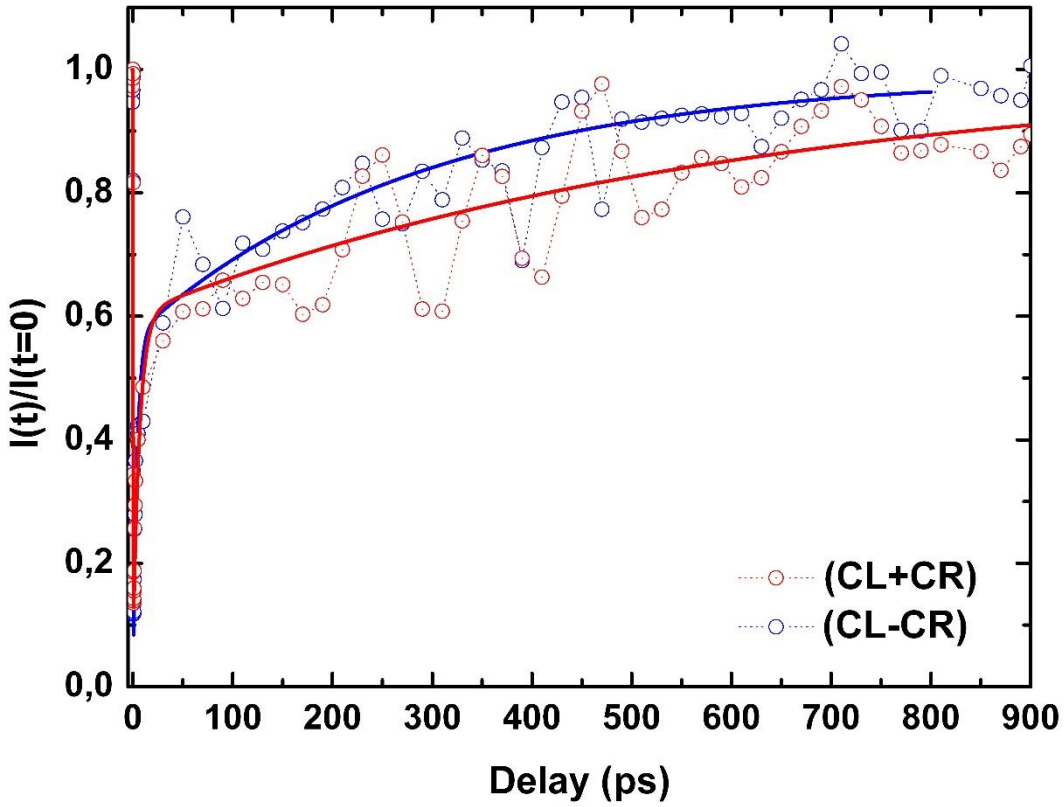

Figure 62: Time-resolved evolution of the SUM (CL + CR) and the DIFFERENCE (CL – CR) signal. The red and blue curves are fits from the experimental data points corresponding the SUM and DIFFERENCE, respectively.

As seen in figure 62, the recovery is (partially) completed at 800 ps for the DIFFERENCE (SUM) signal. The XFEL fluence doesn't induce a deterioration of the interfaces, at least during a full delay scan. Thus, an artifact free data analysis interpretation can be performed. First, the focus is made on the ultrafast regime, i.e., t < 5 ps. The slower dynamics is discussed in a second step.

3.1.8.2 Ultrafast time scale (0 – 5 ps)

The ultrafast time evolution of the diffraction ring (CL + CR) and of the dichroism (CL – CR) absolute value is displayed in figure 63 (a). A subpicosecond demagnetization is observed.

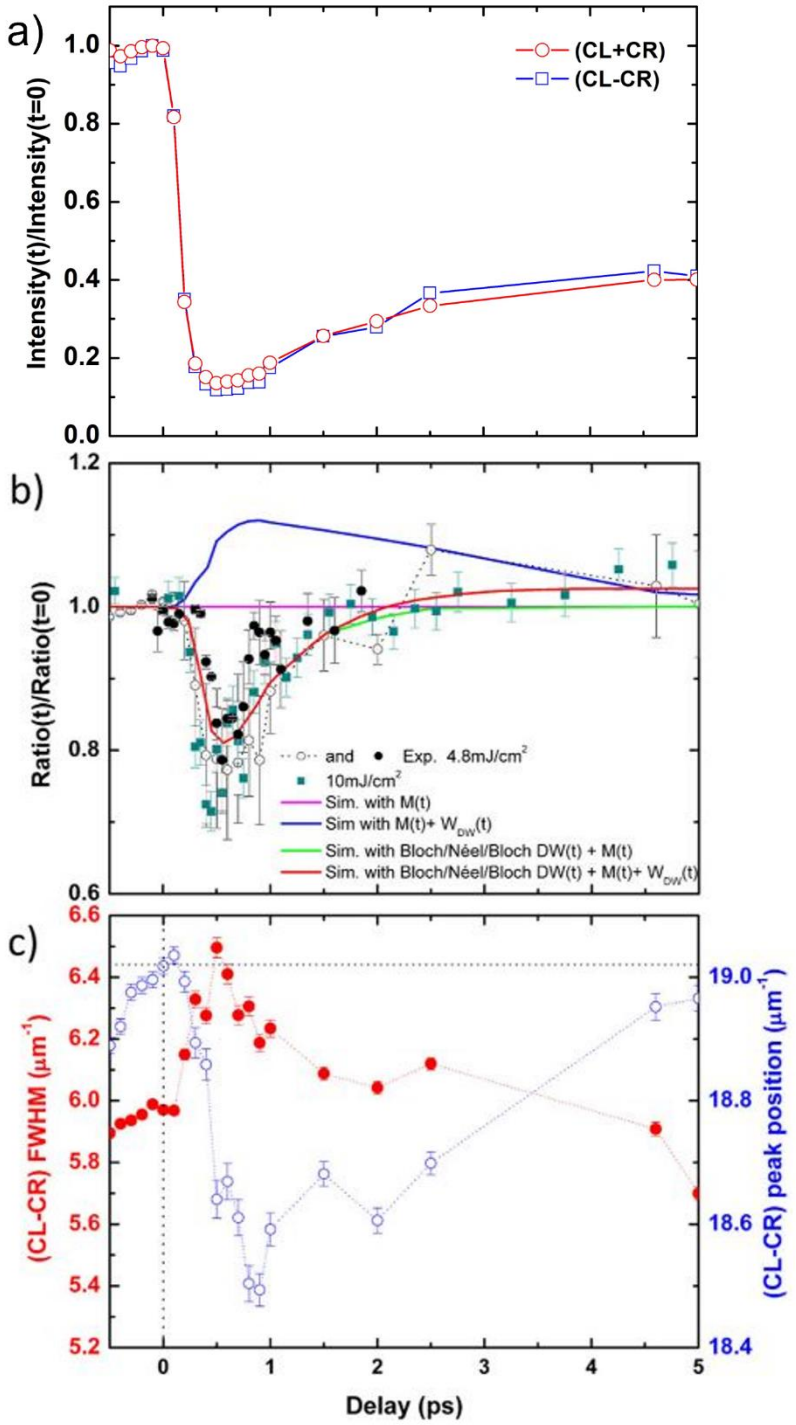

Figure 63: a) Integration of the diffraction ring CL + CR) and dichroism (CL – CR) signal normalized by their respective value at negative time delays. b) the asymmetry ratio obtained from the experimental data shown above (empty circles) and two additional delay scans, performed at a different beamtime, with one at the same pump fluence (4.8 mJ/cm²) in black dots and the other higher IR pump fluence (10 mJ/cm²) in cyan. The coloured lines represent simulations with different models. They are explained in detail below. c) FWHM (red dots) and position of the diffracted peak (empty blue circles) in reciprocal space time evolution. Image taken from Léveillé *et al*[254].

As already observed in metallic magnetic layers[16,169], the demagnetization time constant obtain from the fit is around 150±30 fs for the SUM signal. In the DIFFERENCE, the value isn't different (140 ±20 fs) within the error bar that doesn't contain the time resolution of the experiment, 120 fs. Due to the square relationship between the intensity and the magnetization

(see chapter 2), the characteristic time scales have been obtained by fitting the square root of both curves with an empirically crafted three exponential functions convoluted by a Gaussian function with a FWHM $\sigma_{probe} = \sqrt{\sigma_{IR}^2 + \sigma_{FEL}^2} = \sqrt{100^2 + 60^2} = 120$ fs.

$$\sqrt{I(t)} = [a + H(t - t_0)\Delta M(t)] * G(t, \sigma_{probe})$$

$$\Delta M(t) = -(c \cdot e^{-\frac{t-t_0}{t_2}} - b \cdot e^{-\frac{t-t_0}{t_1}} + f \cdot e^{-\frac{t-t_0}{t_3}})$$

(59)

I(t) is the intensity in the curve, whose square root is related to the magnetization *M*(t). $H(t\text{-}t_0)$ and $G(t, \sigma_{probe})$ stands for a Heaviside and a Gaussian function. The latter mimic the limited experimental time resolution due to the finite length of the XUV and IR pulses. The characteristic times t_1, t_2 and t_3, refer to the demagnetization time, the fast recovery and the slow recovery time, respectively. The different constant a, c, b and f stand for the initial magnetization level, the amplitude of the fast recovery, of the demagnetization and of the slow recovery process, respectively. The classical phenomenological response function, often used to retrieve the different bath temperature and containing two exponential functions, usually fail to fit data set with final delay times above 100 ps[168].

After the ultrafast quenching reaches a maximum around 0.5 ps, it is followed by a log-like increase over the next ps. One notices that the dichroic curve (CL – CR) drops more than the SUM. Also, the recovery of the chiral signal seems to be faster than in the SUM, even if the time constants found by the fits are similar for the DIFFERENCE (2.0 ±0.5 ps) and the SUM (2 ±1 ps). Similar observations have been also found for another ferromagnetic chiral multilayer in Kerber *et al*. work[244]. In figure 63(b), the asymmetry ratio (CL-CR)/(CL+CR) time evolution shows a 15% dip for the data taken with an IR fluence of 4.8 mJ/cm² around 0.7 ps. It is reproducible within the error bars and even larger for the experiment performed at a pump fluence twice larger. The normalized asymmetry ratio remains below unity up to 2 ps.

The FWHM and Gaussian peak position time evolution, determined by the Gaussian fit on the DIFFERENCE image, are displayed in figure 63(c). The result is far less fit dependent than the SUM. From its initial value (330 $\pm$20 nm), a shift of the peak position toward smaller Q values can be observed, similar to what has been observed in the literature[172]. However, as observed in the figure 59(b), there is no peak asymmetry within our signal to noise ratio, as previously observed by Pfau *et al*[169]. The link between the peak shift toward higher domains width value and an actual growth or reorganization of the domains and DWs is still debated. The DW velocity required is between one and two orders of magnitude larger than the usually observed DW speed ($\sim$100 m s^{-1})[169].

The deviation of the asymmetry ratio cannot be explained by an ultrafast change in the scattering factor, which would be induced by hot electrons filling the d bands. The laser fluence of the experiment is at least one order of magnitude lower than the one used to probe the optically-induced change of electron occupation in X-ray absorption spectroscopy[245]. We propose an alternative explanation, which relies on a different variation of the magnetic moment inside

domains and DWs. A constant unity ratio in time would mean that the domain walls and domains magnetization dynamics would be equivalent. It is depicted by the magenta curve in figure 63(b). The XRMS model used to fit the ratio is described in Annex B. If a DW expansion is considered, as stated in Pfau *et al.*, and taken as a 10% expansion versus its equilibrium value (~20 nm), the asymmetry ratio should increase up to 1.1 as shown in the blue curve in figure 63(b). This is in opposition to the experimental data. The hypothesis made for the following is that the decrease of the asymmetry ratio below unity is due to a reduction of the magnetic chirality. This decrease can come from a change in the ratio of the in-plane and out of plane magnetic moment or a loss in the coherent Néel rotation inside the DW. The asymmetry should drop below unity due to a different demagnetization inside the DWs and the domains. Note that, a scenario where only the magnetization recovery is faster inside the DWs would result in an asymmetry ratio larger than unity, similar to the DW expansion model. To understand the different dynamic between DWs and domains, a model relying on a torque induced by the flow of polarized hot electrons in the DWs has been developed.

In the sub-picosecond regime, an intense flow of spin currents generated by the IR pulse can affect the DWs. These spin currents can transfer spin angular momentum inside the magnetic layer or toward another layer. The angular momentum transfer and dissipation can lead to enhanced demagnetization as well as faster magnetization recovery. This mechanism has been explored for the non colinear magnetization texture dynamics inside DWs. The enhanced spin scattering within DWs has been previously invoked as a static magnetoresistance contribution[246]. It could also play a role in the induced spin-transfer torques leading to the current-induced DW displacement. To describe the two aforementioned effects, a ballistic model has been developed and is adaptable to the ultrafast demagnetization scenario. The ballistic spin carriers are described as classical spin particles perceiving a varying exchange field while crossing the domain wall[247]. The particles are coupled by exchange interaction to the localized magnetic moment through the *s-d* Hamiltonian. In the case of the sample studied, the localized magnetic moments rotate in a Néel fashion. Added to the fact that the particle velocity component perpendicular to the DW is related to their momentum in the k-space. The problem, within a proper renormalization, is equivalent to the “fast adiabatic passage” in the nuclear magnetic resonance theory. The spin time evolution can be described by the Landau-Lifshitz equation:

$$\frac{d\boldsymbol{s}}{dt} = \frac{J_{ex}S}{\hbar}\boldsymbol{m} \times \boldsymbol{s} \tag{60}$$

The equation contains the carrier spin direction $\boldsymbol{s}$, the exchange energy J_{ex} with the localized moment S. The direction of the time-varying exchange field felt by the ballistic electrons is given by $\boldsymbol{m}$. In the electronic rotating frame, the spins are precessing around the effective field from the localized moment. Since the hot electrons come from the domains, being polarized up or down, they acquire a component out of the chiral plane of rotation. The carrier spin precession angle ω is proportional to the carrier velocity v and inversely proportional to the exchange times and the DW width $w = \pi\Delta$[246].

$$\langle \omega \rangle = \frac{\pi \hbar v}{J_{ex} S 2\pi \Delta}$$

(61)

In the case of a DW with of 15 nm, with electrons at the Fermi level, the precession angle can reach about 7 degrees. The precession angle could be quite different in the case of hot electrons, that are produced during the demagnetization process. However, the relevant hot electron parameters values are challenging to estimate. Their velocity should not be far from the electron Fermi level velocity $\sim 10^6$ m s^{-1} [17]. The exchange energy in bands 1 eV or more above the Fermi level is reduced down to tenth of eV. Thus, the precession angle could be greater than 7° for a large part of the hot electrons' distribution. The hot electron spin interaction with the localized moment shall in turn generate a torque on the latter, parallel to the chiral vector: $\boldsymbol{m}_i \times \boldsymbol{m}_j$ [248]. The spin current carried by the hot electrons is flowing in an isotropic manner, meaning that the mistracking angles can be either positive or negative. Consequently, on average the net torque acting on the DWs shall cancel.

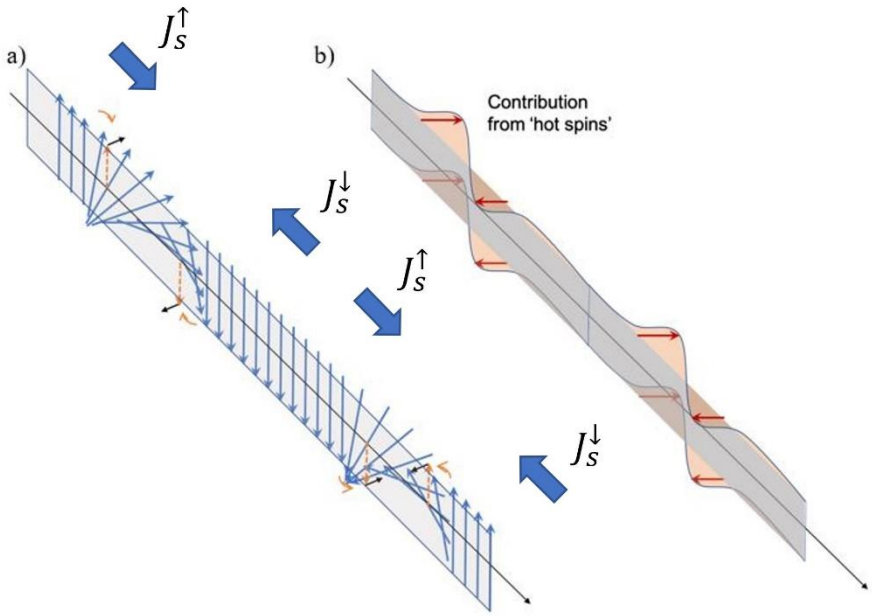

Figure 64: a) Schematic representation of the torque (black arrows) action induced by the spin polarized hot electrons flowing from the domains toward and perpendicularly to the DWs. The orange arrows represent the magnetic moment Néel rotation in the hot electron frame. The resulting transient DW magnetization configuration is illustrated in b). Image extracted from Léveillé *et al*[254].

To relate the experimental observation with the previously discussed model, the overall effect of the incoherent precession induced by the hot electrons must be considered. The domains being almost an order of magnitude larger than the DWs, there is a spin current flowing in the DWs after some 100 fs (~ domain width / hot electron velocity). The spin current applies a torque, which in turn acts on the local magnetization. The spin current is of opposite sign on each side of the DW. It induces an opposite torque on the local magnetic moment, which cancels out in the middle of the DWs, further increasing their incoherent precession. In the case where the spin current arrives perpendicularly to the DWs, a coherent precession can be induced, tilting the localized moments out of the chiral rotation plane (figure 64(a)). A new transient DW

structure made of a pure Néel type at its center together with two opposite Bloch type components on both DW sides, as depicted in figure 64(b).

The presence of this Bloch type component results in a decrease of the dichroic signal compared to a pure Néel rotation. The amplitude of this DW distortion can be estimated. The large amount of hot electrons produced after each optical pulse, typically 0.5 electrons per cobalt atom for the used IR fluence[17]. Importantly, the timescale for the torque onset is given by the exchange field, which falls in the 10-fs range. This ensures that the wall distortion doesn't lag in time with the hot electrons passing through the DWs. If one considers that the additional loss of magnetization inside the DWs is uniquely due to the coherent torque effect, a quantitative estimation gives a tilting angle larger than 10°. In addition, the onset of the Bloch components in the DW should spill out into the domains, which slightly increase the DW width. This is a common conclusion of several recent studies dealing with labyrinthine magnetic domain pattern[169,172]. In the simulation, the assumption has been made that the DW width reaches a maximum at 1 ps when the quenched demagnetization starts to recover. After reaching its maximum expansion, the simulation considers that the DW width recovers its unpumped value.

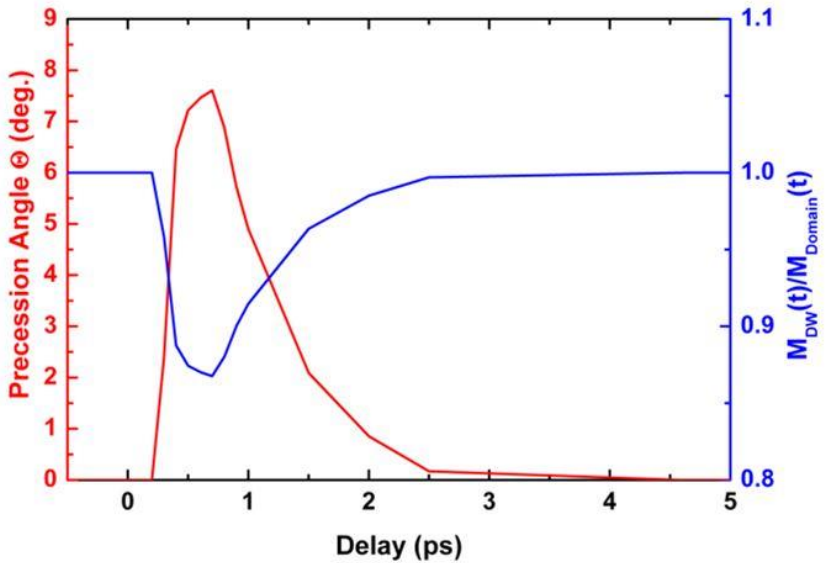

Figure 65: Out of the chiral rotation plane precession angle tilt of the DW (in red) and the DW magnetization dynamics normalized by the domain magnetization. Image extracted from Léveillé *et al*[254].

A 1D magnetization profile XRMS model has been used to fit the asymmetry ratio evolution (Annex B). First, one extracts the magnetization variation directly from the square root of the CL + CR intensity. Then, the time evolution of the asymmetry ratio can be simulated considering a 15% further demagnetization inside the DW due to both incoherent and coherent processes. Although, it is not possible from the current experimental data to disentangle the two effects. A measurement with the observation of multiple diffraction orders or a potential satellite peak from the transient DW type would allow to separate the two contributions. A reasonable simulation output gives a maximum precession angle of 8.5° at ~0.6 ps with a DW magnetization reduction relatively to domains of 87% as drawn in figure 65.

The resulting asymmetry ratio time evolution obtained with this model corresponds to the green curve in figure 63(b). It is in excellent agreement with the experiment data obtained with a pump fluence of 4.8 mJ/cm². In addition, if one considers a DW expansion of 10%, the small asymmetry ratio unity overshoot after 2 ps can also be fit. The agreement is found for a DWs angle distortion of 10.5°. It corresponds to the red curve in figure 63(b). Even though the exchange driven distortion in the DWs is established in hundreds of fs, it shouldn't vanish until longer timescale around the nanosecond. On contrary, the incoherent contribution should accelerate the relaxation of the magnetization inside the DWs, which could explain that the asymmetry ratio exceed unity in the experimental results.

3.1.8.3 sub-nanosecond timescale (100 ps – 1 ns)

In this paragraph we concentrate on the longer timescale dynamics up to 900 ps. The FEL results are accompanied by MOKE and VNA-FMR experiment as well as magnetic mode calculations to look for the origin of the GHz damped oscillation clearly observed in the SUM signal as well as in the SUM and DIFFERENCE respective peak position evolution in the hundreds of picosecond time scale.

The fits performed on the experimental data in figure 62, give a smaller long recovery time constant for the DIFFERENCE (270 ± 20 ps) signal than the SUM (440 ± 30 ps). At 900 ps the dichroic signal has recovered its original value while the SUM is still 10% lower. It confirms the faster chiral recovery with respect to the domains, even at hundreds of ps, as observed in Kerber *et al*[244].

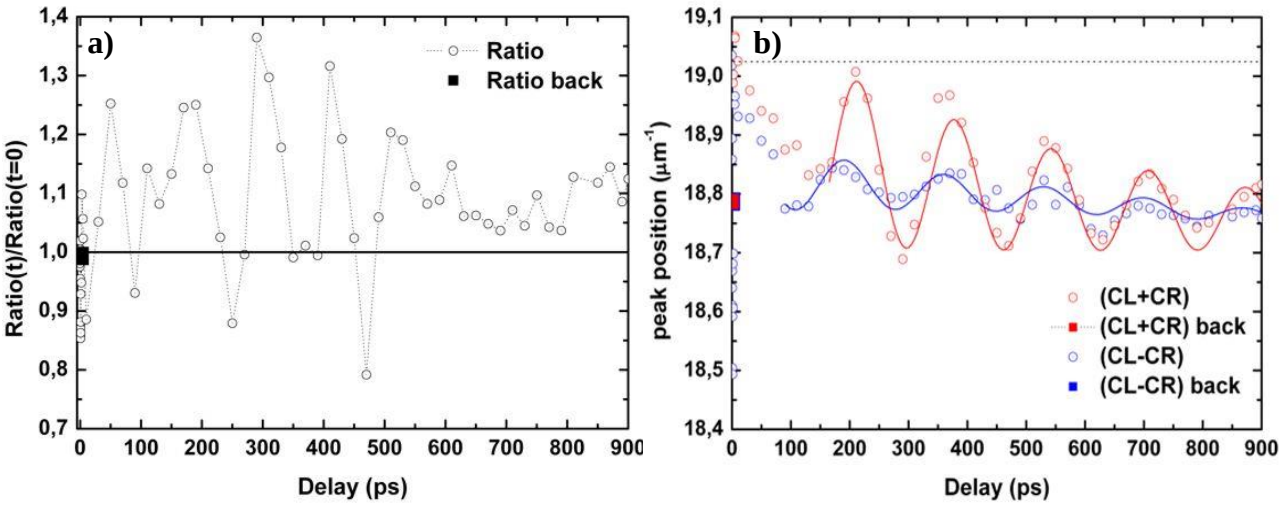

Figure 66: a) Evolution of the magnetic asymmetry ratio (CL - CR)/(CL + CR) up to 900 ps. The big black square represents the measurement performed at negative delays (t = -1 ps) recorded right after the delay scan. b) the peak position of the CL + CR and CL – CR signals. The red and blue squares are the data points taken at negative delay (t = - 1 ps) after the delay scan. The lines fit the experimental curve with a periodic function of ~ 165 ps period.

In the hundreds of ps time, the asymmetry ratio is mostly above unity with a peak around 1.4 and slowly drifts toward its initial value. A 6 GHz damped oscillation is observed and mainly come from the SUM signal variation. A frequency equivalent damped oscillation is also present in the CL + CR and CL – CR maximum scattering intensity positions, with a more pronounced amplitude in the SUM. The points taken after the delay scan, represented by big

and coloured squares in the two graphs, show that there is no sample degradation during the scan. The onset of this phenomenon starts around 50-100 ps. At this timescale, the magnetization recovering dynamics is dominated by the slow process, as suggested in figure 62. Even if, the magnetization in the DWs and domains haven't yet fully recovered, it is typically the timescale at which the classical LLG micromagnetic dynamic can take over.

If one considers that the oscillations are present in the SUM and not in the DIFFERENCE, it implies that the magnetization oscillation in the domain and domain walls shouldn't be in phase or shifted by $\pi/2$. Indeed, at 45°, the CL + CR signal is proportional to $m_z^2 + m_y^2$ while the CL - CR probes $m_y m_z$. Thus, a time-periodic magnetization oscillation should be two times slower than the one found in the signal. Different scenarios explaining the experimental 6 GHz oscillation has been checked, such as coherent magnetization precession, domains or DWs breathing mode.

3.1.8.3.1 Time-resolved magneto-optical Kerr effect

First, a time resolved magneto-optical Kerr effect (TR-MOKE) measurements performed on a piece of the same sample has been performed to investigate the magnetization dynamics in the absence of domains. An out of plane magnetic field of ± 0.2 T was applied during experiments to uniformly saturate the multilayer. In the TR-MOKE setup, an amplified Ti:Sapphire laser provides a 800 nm beam at a frequency of 1 kHz to pump the multilayer at normal incidence. A small fraction of the pump beam is picked up, then frequency doubled (400 nm) by a β-Barium Borate crystal. The probe is focused to a 10 µm diameter beam making an angle of 45° with respect to the probe (figure 67(a)). Both pulses duration is ∼100 fs long. In the MOKE, the light polarization state after reflection on a magnetic surface depends on the magnetization amplitude and direction. Therefore, any change in the magnetization properties should be detected, being in the ultrafast window or in the ns regime. The time resolved rotation of the reflected beam polarization is analyzed using a set of half-lambda waveplates, Wollaston prism and balanced photodetector. In general, the TR-MOKE signal contains an optical and a magnetic contribution. To obtain the curves in figure 67 (b, c, d and e), the experiment is performed at positive and negative saturation field. The difference of the two saturated measurements gives the magnetic signal (b,c) while the sum gives the optical contribution, which can be related to the multilayer charge density.

The TR-MOKE measurements of figure 67(b,d) were performed at two different fluences that are lower than the one used at Fermi because the reflection is more than twice bigger at 45° than at normal incidence. The scans focusing on the few ps regime show a typical ultrafast magnetization dynamic, with a sub picosecond demagnetization followed by a picosecond characteristic time recovery. The long delay scan shows a smooth behavior with no oscillation. It rules out the hypothesis of a coherent magnetic oscillation in the sample. On the optical curves, a short peak can be observed at the ultrafast timescale. It is related to the photoinduced generation of hot carriers. At longer times in the reflectivity curve of figure 67(e), a damped oscillation emerges with a main frequency of 60 GHz and a beating around 3.5 GHz. The absence of this signal in the magnetic contribution and the oscillation frequency points toward acoustic modes in the topmost portion of the metallic multilayer. Theoretical calculations performed with the multilayer composition and layers thicknesses, developed in Annex C, give an oscillation frequency close to the experimental value.

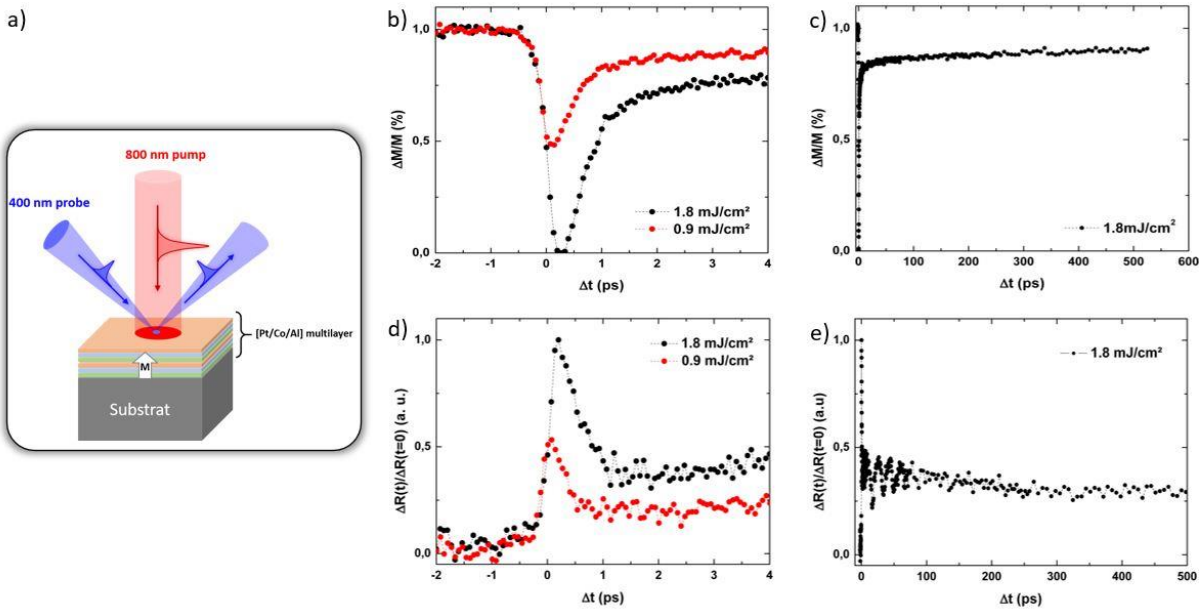

Figure 67: (a) Experimental set-up with the probe (400 nm) and pump (800 nm) beams impinging on the sample saturated busing a permanent magnet. The time resolved magneto-optical Kerr effect measurements at the ultrafast (b) and hundreds of ps timescale (c). The ultrafast (d) and nanosecond (e) regimes of the reflectivity signal. All the curves have been normalized.

3.1.8.3.2 Magnetic modes simulations

The domains contribution to the magnetic signal has still to be explored, as the MOKE experiment is performed at saturation. The magnetic layers in the stack have an out-of-plane magnetic anisotropy and are in multi-domains state at zero field. The nonuniformity of the magnetic pattern can mediate excitation of magnetic precessional modes. An estimation of the lowest precession frequency associated to the magnetic domains is given by:

$$f = \gamma \mu_0 (H_A - H_d + H_{ex})$$

(62)

Where γ=28 GHz/T is the gyromagnetic ratio, μ_0 the vacuum permeability, H_A is the out of

plane anisotropy field, H_d and H_{ex} are the demagnetizing and exchange fields. From the in-plane and out of plane AGFM measurements, the anisotropy field part yields $\mu_0(H_A - H_d) = {2K_{eff}}/{M_s} \cong 0.55$ T. The associated frequency mode, $\gamma\mu_0(H_A - H_d) \cong 15.4$ GHz, corresponds to the sample uniform ferromagnetic resonance mode (FMR) without bias magnetic field. The exchange field contribution to the magnetic mode originates from the nonuniform domain pattern. Considering a striped domain pattern, the standing wave frequency is given by $\gamma\mu_0 H_{\text{ex}} = 2\gamma A k^2/M_s$, where k is the wave number. The exchange constant A is taken equal to 12 pJ m^{-1} from the micromagnetic simulations. The spin wave wavelength corresponds to twice the domain size. Thus, for $\Lambda = {2\pi}/{k} \cong 290$ nm, the exchange field excitation frequency yields $\gamma\mu_0 H_{\text{ex}} \cong 0.3$ GHz. The contribution from the DMI should be smaller than the exchange. The lowest frequency associated with the magnetic domains' precession is $f \cong 15.7$ GHz. It is twice larger than the experimentally observed frequency. Measurements of VNA-FMR have been carried out to verify experimentally the previous calculation.

3.1.8.3.3 Vector network analyzer ferromagnetic resonance experiment

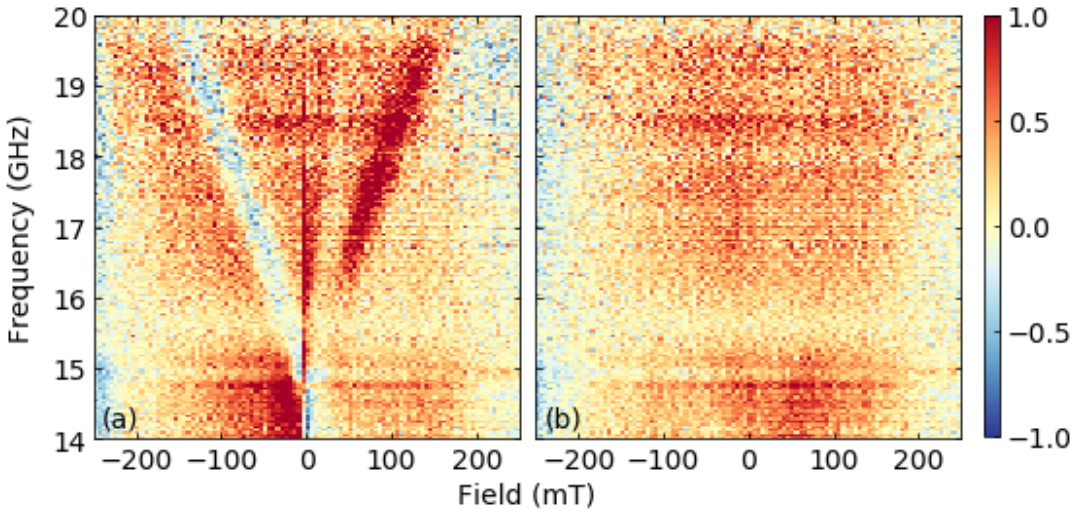

Figure 68: VNA-FMR measurement with the bias field applied (a) out of the sample plane and (b) in the sample plane. In both cases, the applied rf field is perpendicularly to the bias and in the sample plane.

The figure 68 shows the measurements performed with a bias DC field applied out of the sample plane (a) and in the sample pane (b). In both, the rf field is applied in the plane and perpendicularly to the bias field. No feature has been observed for a rf field below 15 GHz. In addition, the signal absorption is only found for a bias applied out of the sample plane. At zero field, the maximum rf field absorption is located around 15 GHz, close to the magnetic mode calculation. Also, the maximum absorption increases with the bias and correspond to FMR uniform precession. The evolution of the rf field frequency maximum absorption with respect to the field allows to estimate precisely the remanent magnetic mode as well as the effective magnetic anisotropy.

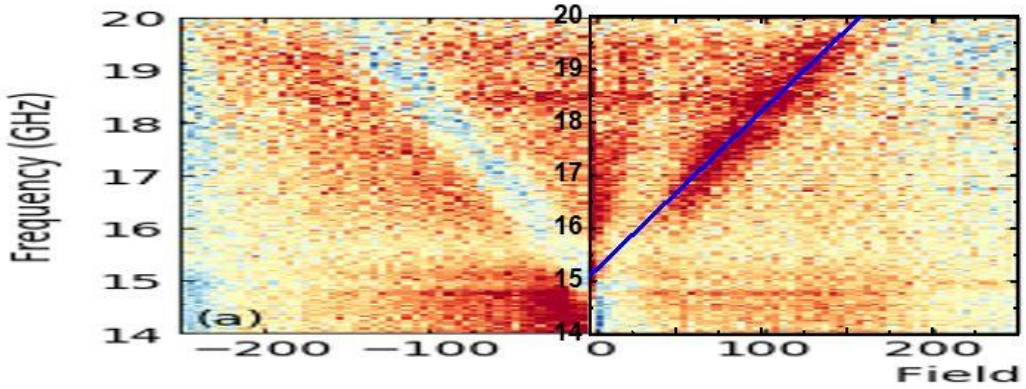

Figure 69: VNA-FMR out of plane bias field map of the rf field absorption superimposed with a linear fit of the frequency versus field evolution.

The linear fit of the signal $f = f_0 + \vartheta B_z$ yields f_0= 15.1 GHz and ϑ= 0.031 GHz/T. The origin of the graph gives an equivalent field of $B_0 = {f_0 2\pi}/{\gamma}$ = 540 mT, which is in excellent agreement with the anisotropy field found previously (550 mT). Note that, even at the hundreds of picosecond timescale, the sample hasn't fully evacuated the heat from the pump pulse. The different magnetic parameters change with temperature. Therefore, the direct comparison of the VNA-FMR measurements with the experimental result isn't straightforward.

3.1.8.4 Discussion

The temperature variation study of some magnetic parameters has recently been performed in perpendicularly magnetized magnetic films[230,231,235,236,249,250]. Temperature dependent magnetometry measurements found that the saturation magnetization (M_s) evolves as $\left(1 - {T}/{T_c}\right)^{\frac{1}{3}}$ between room temperature and the curie point (T_c) for various compounds[230]. The effective magnetic anisotropy temperature dependence is a bit more complex as it is proportional to the square of M_s but also contains an interfacial anisotropy contribution K_s, which is proportional to $M_s^{2.5\pm0.3}$ and independent of the material combination[230]. Finally, the exchange stiffness can be estimated performing an IP field cooling. The fit of the M_s temperature evolution with a Bloch law, which considers that the loss of M_s is due to magnon excitations, links the exchange stiffness with Ms. A recent study found that the exchange stiffness A varies as $A(T) = A_0 \left(\frac{M_s(T)}{M_s(0)}\right)^{1.7152}$ with A_0 and $M_s(0)$ the values of A and M_s at T= 0 K[231] for temperature ranging between 150 and 300 K. This power law is close to the power of two given by the mean field theory and experimentally found in another paper[230] on a similar CoFeB multilayer sample. For the DMI, the results are more diversified. In a study on a Pt/CoFeB/Ru multilayer hosting a skyrmion state, the DMI strength has been estimated combining the above-mentioned procedures and x-ray magnetic circular dichroic photoemission electron microscopy (XMCD-PEEM) to determine the domain width. The DMI parameter is adjusted to fit the average domains width using a static multilayer domain energy model[251]. The DMI has been found to be

linear with $M_S^{1.86}$. It is close to the exchange stiffness variation as found in IP permalloy[235] or in Pt/Co/MgO samples[236]. However, two other studies performed on Pt/Co thin films, using the average domains width numerical fit procedure[249] or Brillouin light scattering (BLS)[250] found $D \propto M_S^{\sim 5}$ for temperatures above 300 K. In general, the unambiguous monotonous variation of the different magnetic parameters with temperature excludes a pure thermal induced mechanism for the GHz oscillations found in the SUM signal.

The last remaining hypothesis is a DWs breathing that propagates in the domains. It could be explained by the DWs type perturbation due to the spin current induced torque that lasts until some hundreds of picoseconds. The DWs would recover their initial pure Néel type through a breathing mode. This explanation could explain the ratio overshoot at long timescale as well as the maximum peak oscillation seen in the DIFFERENCE and the SUM images. No simulations have been performed yet to explore this assumption.

In this section, the time evolution of the chirality and the domains dominated signal have been compared using linearly polarized pump. In the following, inspired by the helicity dependent all-optical switching found in symmetric Co/Pt multilayers[252], the effect of a circularly polarized IR pump on both signal is assessed for different fluence values on a non-symmetrically stacked sample. The latter having the same composition as the sample studied in this section.

3.1.9 IR pump circular polarization

In this section, we explore the effect of the pump circular polarization on a FM chiral sample.

3.1.9.1 Reproducibility of the delay scans

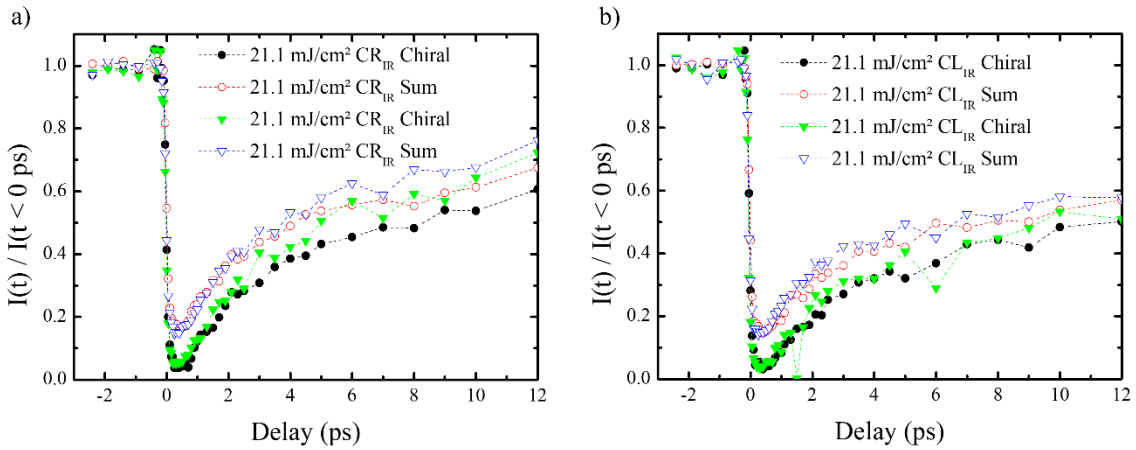

Figure 70: Repeatability measurements taken at the maximum fluence (21.1 mJ/cm²) value for each pump polarization. The circular right polarization (a) and circular left (b) curves show a relatively good repeatability of the results.

In this experiment, the FEL and IR beam size were respectively 215×330 µm² and 560×550 µm². The pump beam has been circularly polarized with a quarter waveplate set-up that can be rotated CW or CCW to switch between CL and CR polarizations, which should have

the same fluence. As in the previous section, a delay scan contains the data taken with both FEL circular polarization and a single pump polarization. In the following, CL_{IR} and CR_{IR} indicate the IR polarization. The DIFFERENCE image data treatment is named chiral to avoid any possible confusion. The IR polarization order for each pump fluence has been switched to get rid of any experiment artifact due to the relatively high IR beam fluence. Also, each pump fluence for each polarization has been performed two times on the same sample area to verify the results repeatability. It is important for the statistic but also due to the specific demagnetization procedure described later in the text.

In figure 70, the two graphs taken with CR_{IR} (a) and CL_{IR} (b) pump polarization show a good reproducibility of the results. Moreover, the chiral signal demagnetizes more than the SUM as in the previous section. It is more pronounced due to the higher laser fluence. Although, there is a difference in the chiral CR_{IR} curves, the green CR_{IR} chiral curve (a) was recorded after the black CR_{IR} (a) one but between the CL_{IR} repeatability curves (b). In comparison to the previous section, two hundred of nm thick zirconium filters have been added to decrease the FEL power by a factor of 5. It would prevent any thermally induced damage due to the increased laser fluence. The pump laser shot-to-shot variation doesn't exceed 2%. Thus, the variation shouldn't be due to a sample degradation.

3.1.9.2 Variation of the laser fluence

The delay scans with distinct pump polarizations have been carried out for three different fluences, taken on two different sample spots and reported in the figure 71 below. A spot change occurred between the two pairs of 13 mJ/cm² fluence repeatability scans performed, which is after the 8.5 mJ/cm² delay scans but before the 21.1 mJ/cm². The data treatment has been adapted to the lower signal to noise ratio due to the FEL intensity reduction. In the data analysis, two different specular fit range has been used. One for the delays around the maximum demagnetization and the other for the remaining points. It affects no more than 10 delay points around the maximum demagnetization. No "jump" is observed around 0.5 ps in the figure 71 graphics, confirming that the change of range affects smoothly the analysis.

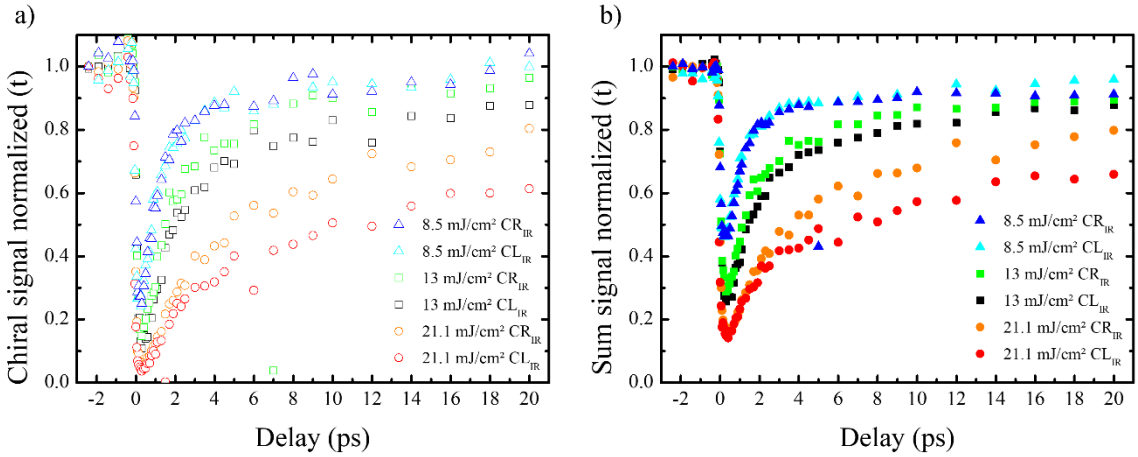

Figure 71: Chiral (a) and SUM (b) normalized signal for three different laser fluences and the two circular polarizations. The shape of the point indicates the fluence, while the symbol's colour corresponds to the pump polarization.

In both graphs, the highest fluences causes more demagnetization in the sample, which is a common feature. Then, if one looks at the 8.5 mJ/cm² curves for the chiral and SUM signals in blue (CR_{IR}) and cyan (CL_{IR}) triangles, they follow the same trend with very little deviations. No circular pump polarization switch effect is noticed. Increasing the fluence to 13 mJ/cm² reveals a small separation between the green (CR_{IR}) and black (CL_{IR}) squares in the chiral (a) and SUM (b) signal. In both graphs, the CR_{IR} curve is above the CL_{IR}. The effect is even more pronounced at a fluence of 21.1 mJ/cm² (orange and red circular point curves). From figure 72, it is not straight forward to conclude if the separation between the two polarizations curve of a single fluence is different in the chiral and SUM signals.

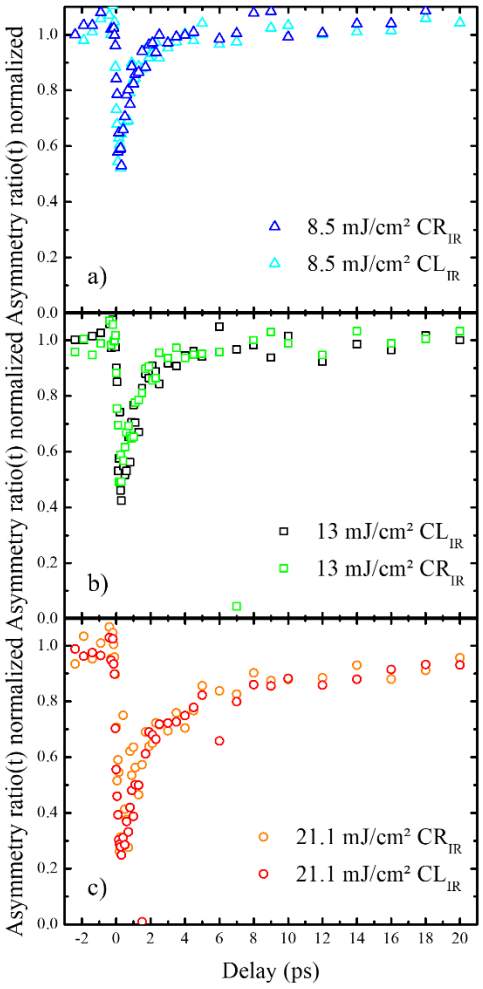

Figure 72:Asymmetry ratio normalized for 8.5 mJ/cm² (a), 13 mJ/cm² (b) and 21.1 mJ/cm² pump fluence with both circular polarizations.

In figure 72, the asymmetry ratio (chiral / SUM) curve for each fluence and polarization have been plotted. In the three graphs, the CL_{IR} and CR_{IR} pump curves are equivalent. It means that one IR circular polarization influences the chiral and SUM signal demagnetization proportionally in the same manner. In other words, the CL_{IR} laser polarization demagnetizes more the sample than the CR_{IR} polarization. This additional demagnetization is proportionally the same in the chiral and SUM signal. Thus, the additional demagnetization results from a larger (or more efficient) laser energy absorption for CL_{IR} than CR_{IR}. It raises the question of the sample magnetic state during the experiment, as the two pump polarizations have the same fluence.

The sample used for this experiment is similar in composition but hasn't seen any magnetic field prior to the beamtime. The coils, used in the next section to produce a magnetic field out of the sample plane, were not mounted. Thus, a beamtime specific demagnetization procedure was performed to demagnetize the sample. The 50Hz repetition IR pump was set to a fluence of 24.3 mJ/cm² and illuminated the sample during one second. This procedure was enough to locally nucleate a chiral domain pattern like the one in the previous section, not visible on laser-virgin sample areas. However, the magnetic texture non-homogeneity in the sample could disturb the energy state, due to the "as grown" dipolar interaction with the probed area. It would explain the discrepancy obtained for the maximum peak position displayed in figure 73. The green, black, orange and red coloured symbols correspond to the same scan used in the previous graphs while the magenta and purple curves are reproducibility scans.

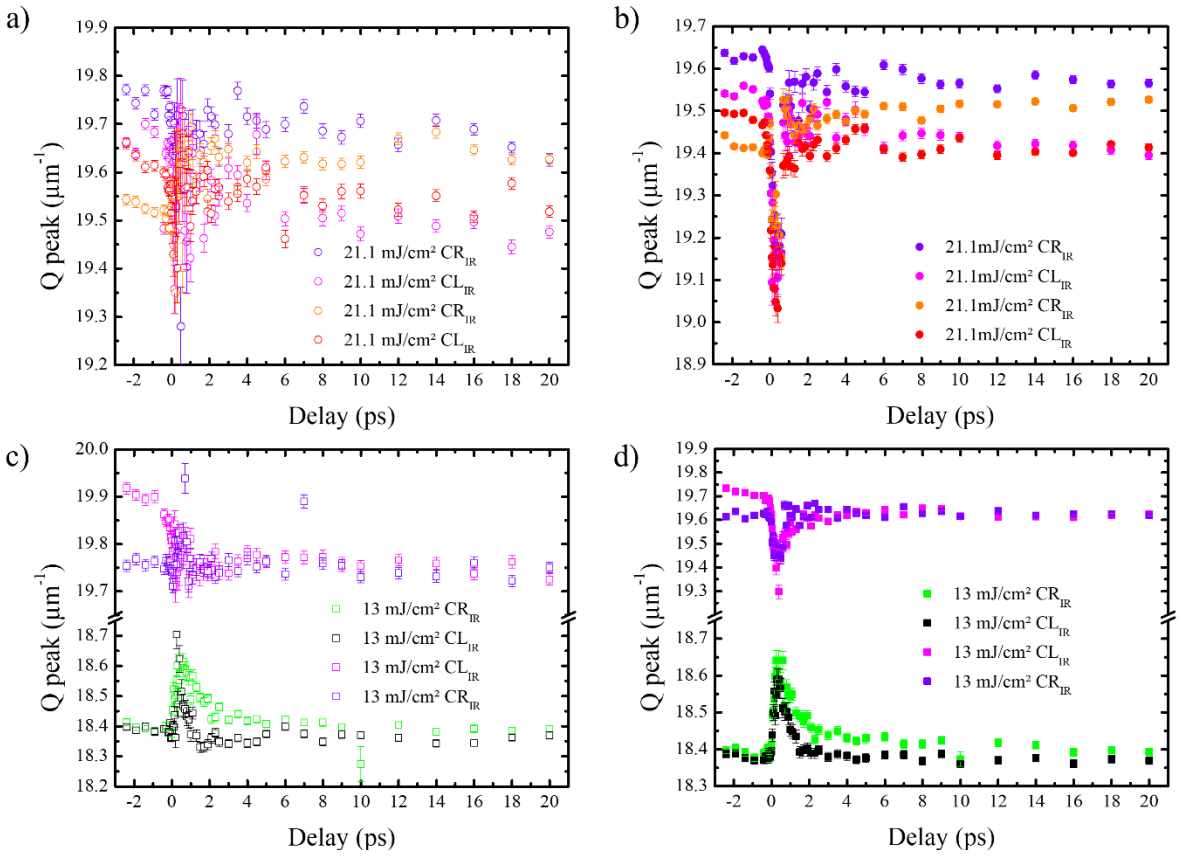

Figure 73: Maximum peak position of delay scans taken with the same pump fluences and two pump's circular polarizations. The top panel (a,b) shows the peak position's evolution for a fluence of 21.1 mJ/cm² in the chiral (a) and SUM (b) images. On the bottom part, the repeatability measurements perform for a fluence of 13 mJ/cm² are plot. The graph with empty symbols curves (c) is from the chiral image data treatment while the symbol-filled curves on the bottom right part (d) are extracted from the SUM image. In the legend, the data are sorted in chronological order, the first scan being at the top.

As seen in figure 73, the ultrafast peak position evolution differs from scan to scan. No repeatability scan has been done for the 8.5 mJ/cm² fluence. In the graphs' legend, the labels position corresponds to the delay scan order. In the figure 73 top panels (a,b), corresponding to the 21.1 mJ/cm² fluence, the peak position values at negative delays are above the previous section negative delay Q peak value (19 µm^{-1}) for both images. Note that the previous ultrafast decrease of the position is once again found. After the ultrafast decrease, the peak position

seems to shift toward 19 μm^{-1} delay scan after delay scan. Moreover, in the tens of picosecond timescale, the peak position varies toward a value corresponding to the next scan negative delay peak position, with the exception of the last delay scan (in red), which converges toward the previous scan value (orange). Since no sign of sample damage has been found in the intensity, it could indicate that the magnetic state isn't at its minimum energy value.

In the smaller fluence graphs (figure 73 c,d), the Qpeak has two opposite behaviours. It either increases or decreases during the first ps. This is due to the change of probed area between the two delay scans taken with CL pump polarization. Note that the two delay scans taken at a pump fluence of 8.5 mJ/cm^2 have qualitatively the same ultrafast increase. Both sample areas have been demagnetized with the same laser power and length.

The Q peak evolution of a sample locally demagnetized by a laser shows that the initial magnetic pattern state can determine the ultrafast maximum diffraction peak variation. It could be a starting point to explain the different Q peak ultrafast evolution reported in literature. However, the "instability" of the initial magnetic pattern in the above experiment weakens the amplitude signal interpretation, as the square of the domains' number that scatter in the probed region is proportional to the diffracted intensity. Those results need to be completed by a study on a chiral system but with an opposite topmost layer chirality and uniformly demagnetized as we suspect that this effect comes from a stronger absorption of the IR light when the circular polarization sense of rotation is the same as the chirality. The same Pt/Co/Al tri-layer building block could be used but with three repetitions or less.

3.2 Skyrmion lattices in FM samples

After the study of chiral domains texture, the focus turned on the study of skyrmion lattice in field. As the magnetic diffracted signal depends on the ordering coherent length, which varies with the applied field, the experiment was done in transmission geometry to maximize the signal to noise ratio and drastically decrease the specular signal under the magnetic peak.

3.2.1 Description of the Ru based sample

In this section two different skyrmion lattice systems have been studied. They have been growth on Si_3N_4 membranes, which has a high transmission at both the cobalt L edge (~ 650 nm) and M edge (~ 52 nm). The first system is a ten repetitions Pt/CoFeB/Ru multilayer growth on Ta(5)/Pt(8) buffer layer and capped with a 3 nm Pt layer. A strong DM parameter (|D|~ 0.75 mJ m^{-2}) is usually found in Pt/Co/Ru trilayers[56] for non-magnetic layer thicknesses above 1 nm. In this sample, the nominal 1.4 nm ruthenium layers favour a ferromagnetic coupling of the magnetic layers. The platinum layer is 1 nm thin, and the low damping (relative to Co) $Co_{40}Fe_{40}B_{20}$ magnetic layer thickness is 0.8 nm. The use of thinner layers and of a magnetic alloy also reduce the interfacial anisotropy value. In skyrmion lattice system, the effective magnetic anisotropy is usually (but it is not necessarily) tuned slightly to negative value as it increases the field stability range of the skyrmionic state[76] but it is not the case for our samples.

3.2.2 Magnetometry and MFM

Following the same data treatment as in the previous section, the effective anisotropy is obtained from the magnetization at saturation, M_s = 687 kA m^{-1}, and the IP saturation field $H_{sat(||)}$ = 0.38 T. The effective anisotropy constant yields K_{eff} = 132 kJ m^{-3}.

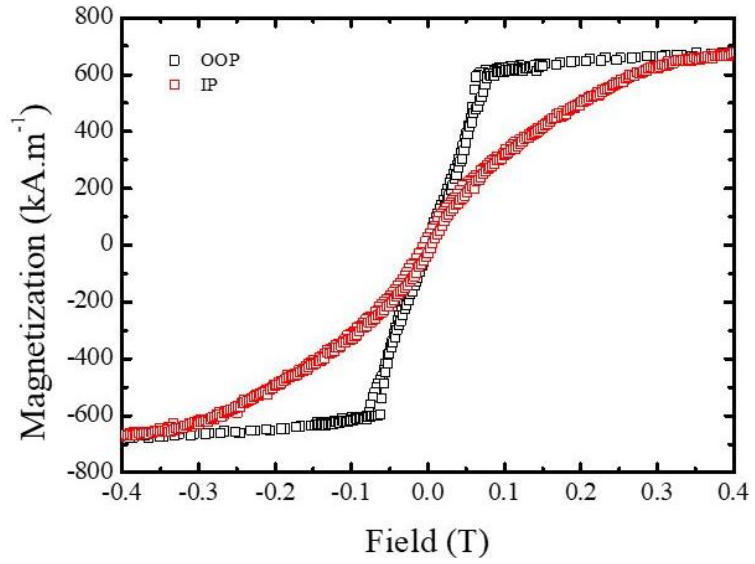

Figure 74: IP and OOP AGFM curve of the Pt/CoFeB/Ru based multilayer.

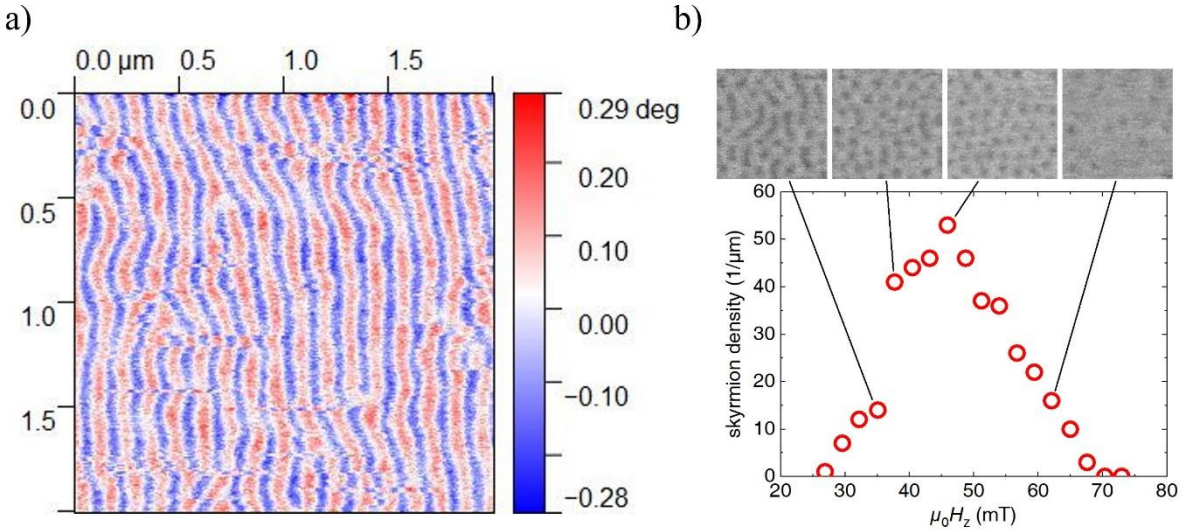

Figure 75: (a) MFM image of the Pt/CoFeB/Ru multilayer after an IP demagnetization procedure. (b) MFM images (1×1 µm²) of the same multilayer with at different applied OOP fields with the related skyrmion density plot.

The magnetic domain stripe, shown in figure 75 (a), has been obtained after sweeping a

decreasing IP field parallel to the stripes in the final state. In the image, there are some lines that look shifted in phase. It is due to the reversing of the MFM tip during the scan. The domain pattern periodicity estimated from a line profile on the MFM image is 130 nm. An OOP field dependent MFM run has been performed and exhibits a skyrmion lattice state. The skyrmion density found in the 1×1 μm² MFM images is maximum around 45 mT.

3.2.3 XRMS images hysteresis loop

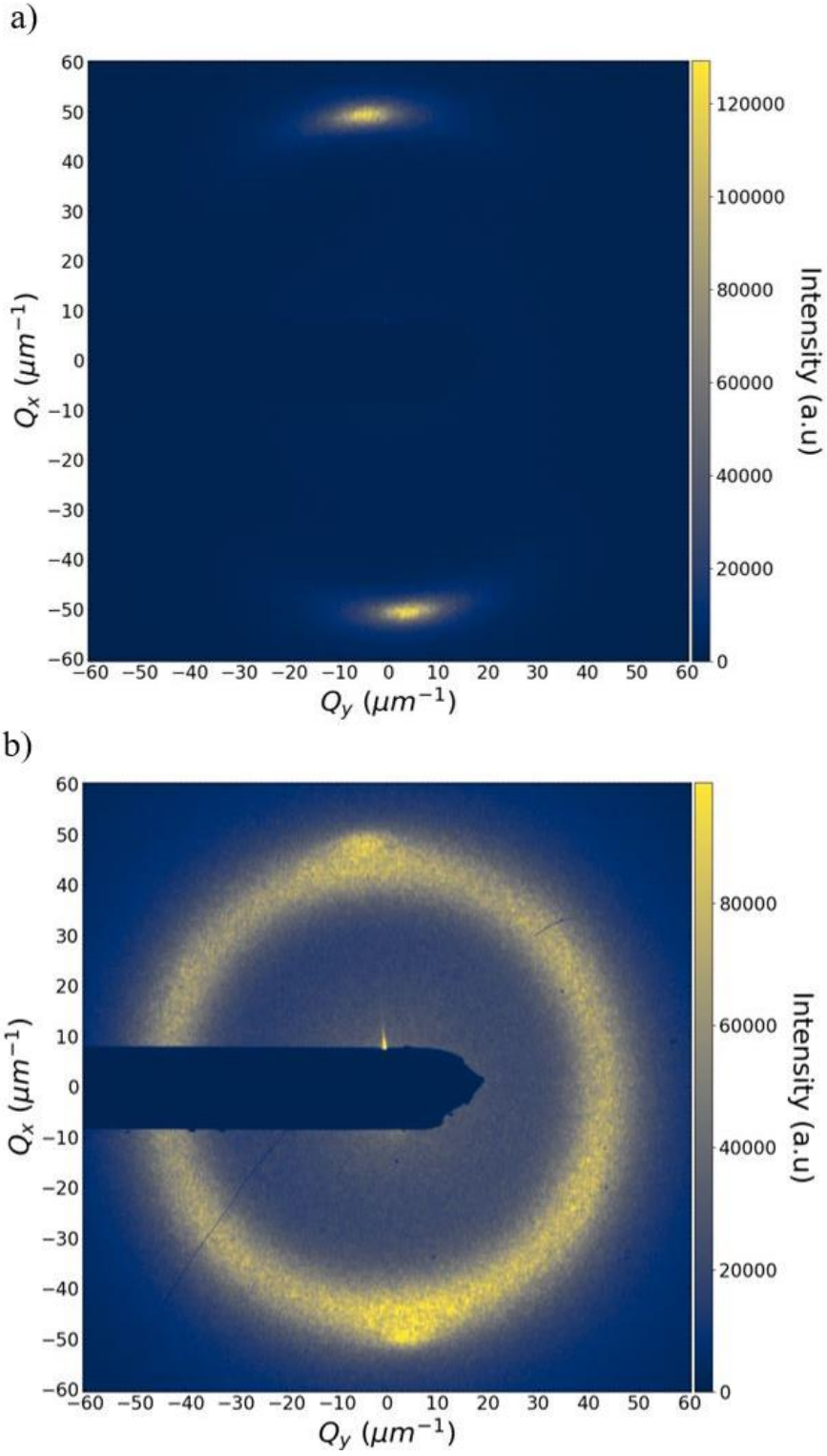

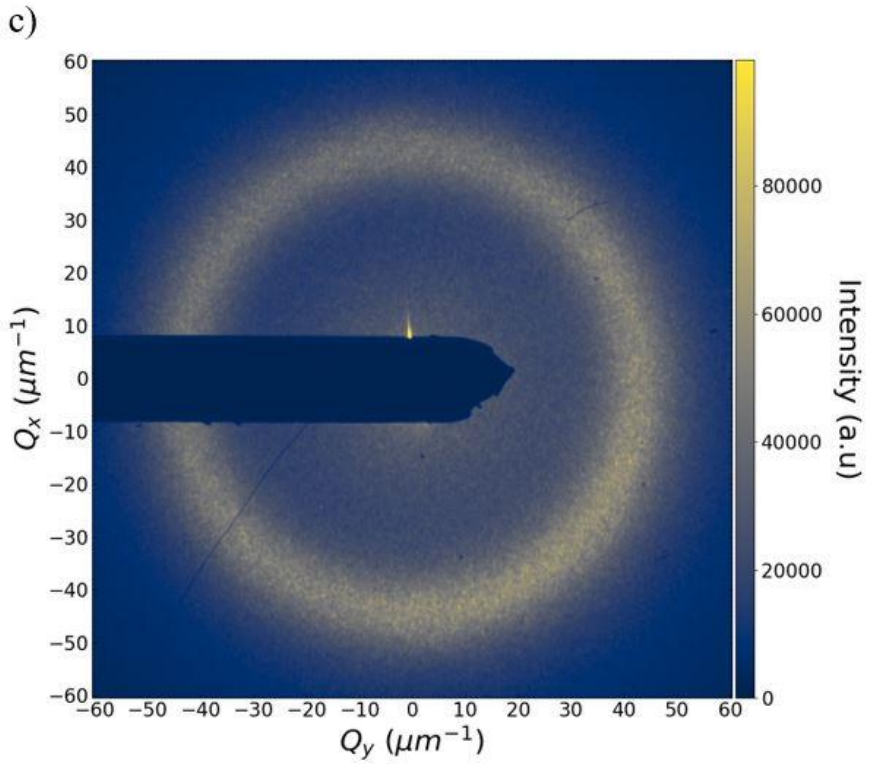

Figure 76: Images taken at 0 mT (a) 45 mT (b) and 54 mT at 300 K.

The hysteresis loops XRMS images have been acquired at the Iron edge since the dichroic signal is usually larger in Fe than in Co. The external field has been applied OOP and the scattered signal collected with a single circular polarization, since no chiral signal should be observed in transmission geometry. The accumulation time per image as well as the attenuators has been adapted from field to field depending on the maximum intensity collected. The same total exposure time over the acquisition time for one image ratio has been kept. The exit slits after the monochromator stayed at 30 μm during the experiment. Only one sweep from 0 T to a positive field beyond saturation has been done.

In the first image of figure 76, taken at 0 field, two spots, symmetric with respect to the beamstop, are visible. This is a stripe diffraction pattern fingerprint. Increasing the field to 45 mT, a less intense diffraction ring is superimposed to the previous stripe spots. The stripe signal disappears at 54 mT. The normalized image's orthoradial profiles at different fields are plot in figure 77.

From zero field to 37 mT, there is no evidence of a skyrmion lattice sixfold symmetry diffraction pattern. The modulation is visible at 38 mT and disappear after 54 mT. The ortho-radial profile has been performed with a rather large radial area to account for any magnetic pattern periodicity variation.

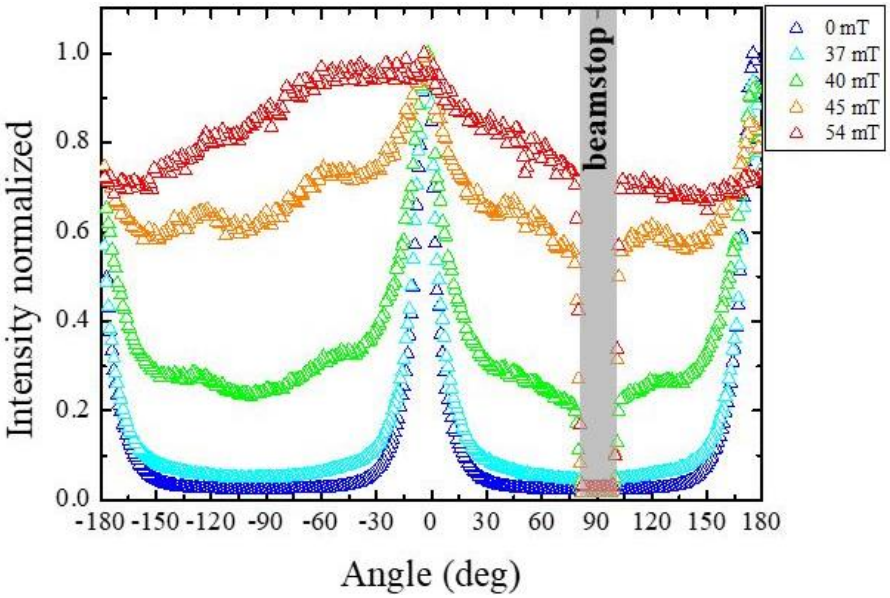

Figure 77: Normalized orthoradial profile of images taken at 0 mT (blue), 37 mT (cyan), 40 mT (green), 45 mT (orange) and 54 mT (red). The beamstop is located around 90°.

The intensity as well as the maximum peak position and the FWHM variation with field, extracted from the images' radial profile, is plot in figure 78 below.

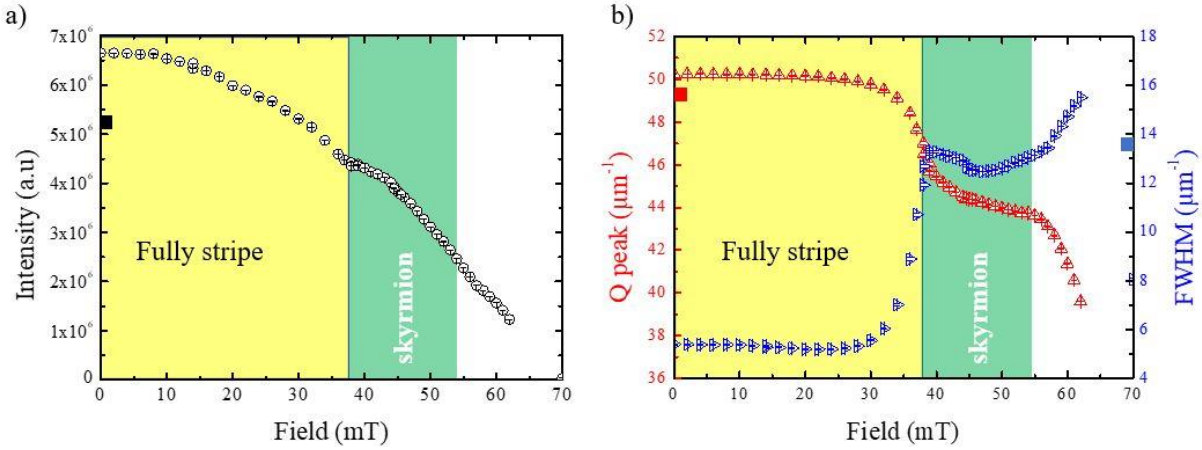

Figure 78: Evolution of the diffracted peak area (a), position and FWHM (b) with respect to the external OOP field. The black, red and blue filled squares are a measurement taken a zero field after saturation. The yellow area represents the stripe state at the beginning of the experiment, while the green area delimits the skyrmion lattice phase. The error bars only contain the uncertainty of the fit.

The yellow and green areas are defined from the presence of a sixfold modulation in the orthoradial profile. In the yellow area, as the field increases, the intensity of the two diffraction spots decreases. The maximum peak position and the FWHM stays constant until 30 mT where they decrease and increase with the field, respectively. At 38 mT, where the sixfold modulation is visible in the orthoradial profiles, the intensity slope with field changes and seems to reach a plateau until a drastic decrease around 45 mT with a higher initial slope again. This plateau is

also present in the peak position and the FWHM. In the former, the plateau has the length of the skyrmion area. Those results correspond to a superposition of the stripe and skyrmion lattice variation in field. The magnetic stripe domain order is gradually destroyed upon increasing the OOP field and isn't reversible as indicated by the filled squares in figure 78. To isolate the skyrmion signal, a symmetric numerical 60° polar mask has been applied to best hide and exclude the two diffraction spots from the radial profile data analysis. It is a good compromise to minimise the alteration of the skyrmion lattice signal but still reduce drastically the intensity of the stripe diffraction pattern. The results are gathered in figure 79.

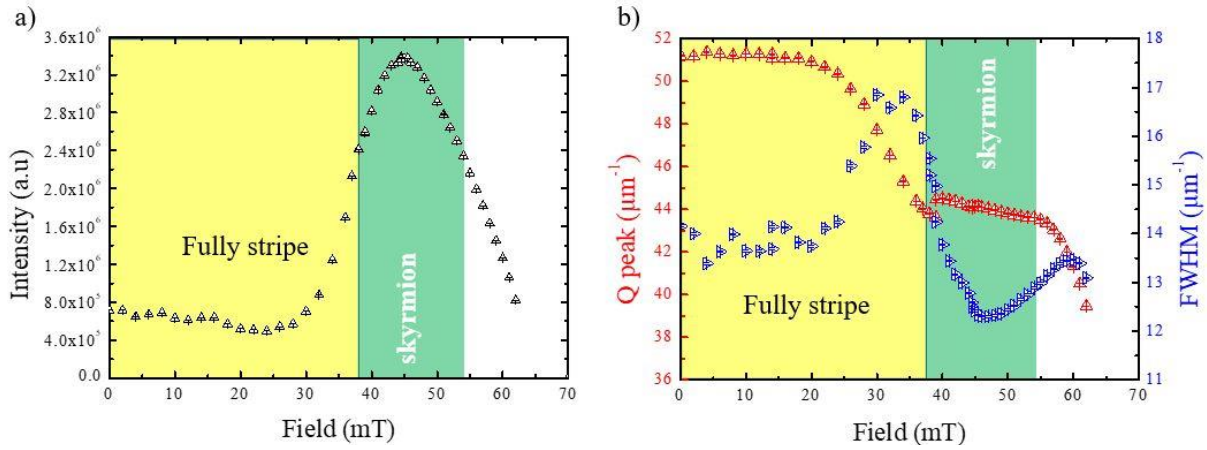

Figure 79: Evolution of the diffracted peak area (a), position and FWHM (b) with respect to the external OOP field on the images where the stripe diffraction spot has been hidden. The yellow and green areas are the same stripe and skyrmion state zones, as in figure 78. The error bars only contain the uncertainty of the fit.

As one can see, the intensity variation with field in figure 79 (a) differs from the full image. The slight decrease between zero and 28 mT originates from the stripe pattern signal not hidden by the mask. It is followed by an increase and reaches a maximum at ~45 mT, similarly to figure 75 (b). This maximum value is close to the value at the same field in the data treatment without mask. The subsequent decrease follows the same trend with values close to the one in figure 78 (a), meaning that the stripe signal was negligible in that part. The peak position in the masked images has a similar shape and values with the full image. With the exception that the first decrease starts at 20 mT and that around 38 mT, the curve seems discontinuous. The maximum position in the vicinity of the skyrmion phase is more reliable here, as the peak is fit with a gaussian. In the full image, the two peaks superimpose. The fit position of the peak's maximum slowly shifts toward the skyrmion phase one, while the transition can be more abrupt reducing the stripe signal as in the masked image. The gaussian fit function isn't appropriate in the vicinity of both phases if one signal isn't suppressed. The smaller field area of the FWHM is dominated by the tail of the stripe diffraction, explaining the larger value (~14 μm^{-1}) compared to the fully stripe state (~5 μm^{-1}). At ~20 mT, the FWHM increases, reaches a maximum around 30 mT, which also corresponds to the change of curvature in the period decrease. After 30 mT, the FWHM value drop to ~12 μm^{-1} at 45 mT and increases again. The FWHM represents the coherence length of the probe texture. It means that the skyrmion lattice is best organised at 45 mT. The skyrmionics phase isn't as dense as in the beginning of the peak position plateau but much more organised. The intensity of the diffracted signal is also maximum for a 45 mT OOP field.

3.2.4 First attempt of a time-resolved study at M edge

Unfortunately, it was not possible to extract a signal with a good signal over noise ratio at the cobalt or iron M_3 edges, compromising the chance to perform the pump and probe experiment. The multilayer x-ray absorption around 60 eV is too high in comparison to the magnetic layer signal. It is mostly due to the total platinum (20.4 nm) and ruthenium (14 nm) thicknesses together with their low attenuation length, i.e., ~9 nm and ~7.5 nm, respectively. Also, the multilayer has been grown on a 200 nm thick Si_3N_4 membrane, which has an attenuation length of ~51 nm. Note that the attenuation length is underestimated as the value given above are valid for a density close to the bulk value, while it is usually smaller in thin films. The attenuation lengths of the different elements used in our sample at different transition metal edges is gathered in Annex D. The next skyrmion lattice-based multilayer has been optimized to absorb less x-ray at 60 eV.

3.2.5 Description of the aluminium based sample

The next multilayer is made with five repetitions of a Pt(2.5)/Co(1.9)/Al(1.4) building block. The aluminium layers absorb much less the x-ray around 60 eV than the ruthenium. Despite the larger platinum thickness in the building block, the signal to noise ratio should drastically increase as the tri-layer repetition is lower and that the magnetic layer is fully composed of thicker metallic cobalt. Moreover, the buffer layer has been reduce to Ta(3)/Pt(2) and deposited on a 100 nm Si_3N_4 membrane.

3.2.6 Magnetometry and field dependent MFM images

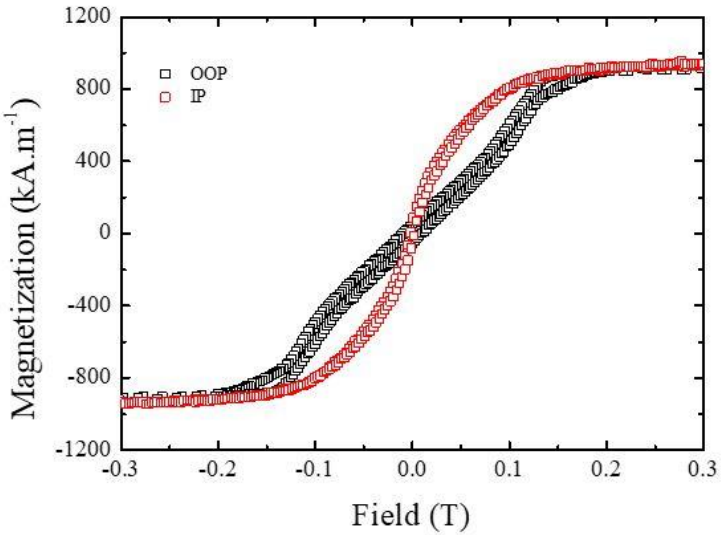

Figure 80: IP and OOP AGFM curves of the Pt/Co/Al based skyrmion lattice.

The sample with 1.9 nm cobalt layer thickness has been characterized performing AGFM measurements that are plot in figure 80. The system exhibits a slightly IP easy axis with a magnetization at saturation around 910 kA m^{-1}. The anisotropy is obtained from the OOP

saturation field ≈ 0.15 T which is equal to $H_{sat(\perp)} = {}^{2K_i}/_{\mu_0 M_s}$. The interfacial anisotropy K_i is related to the effective anisotropy constant $K_{eff} = -0.45$ MJ m^{-3}. In absolute value, it is more important than the previous Pt/Co/Al multilayer which doesn't exhibit a skyrmion lattice state. Those figures have to be handled with care as the similar saturation magnetization field for both, IP and OOP curves, indicates a way smaller effective anisotropy. Additionaly, the sample was $\sim 7 \times 7$ mm², which is too big to give an accurate saturation magnetization value in AGFM, with an error that can exceed 20%.

MFM images at different OOP field has been performed on a multilayer grown on top of the 50 nm Si_3N_4 membrane after an IP demagnetization. The images have been taken on the cliff between the Si_3N_4 membrane and the bulk. It was too complicated to perform the images in field at the center of the membrane due to the set-up vibration. The sample has seen the AGFM field before. The MFM field was varied from 0 to 133 mT.

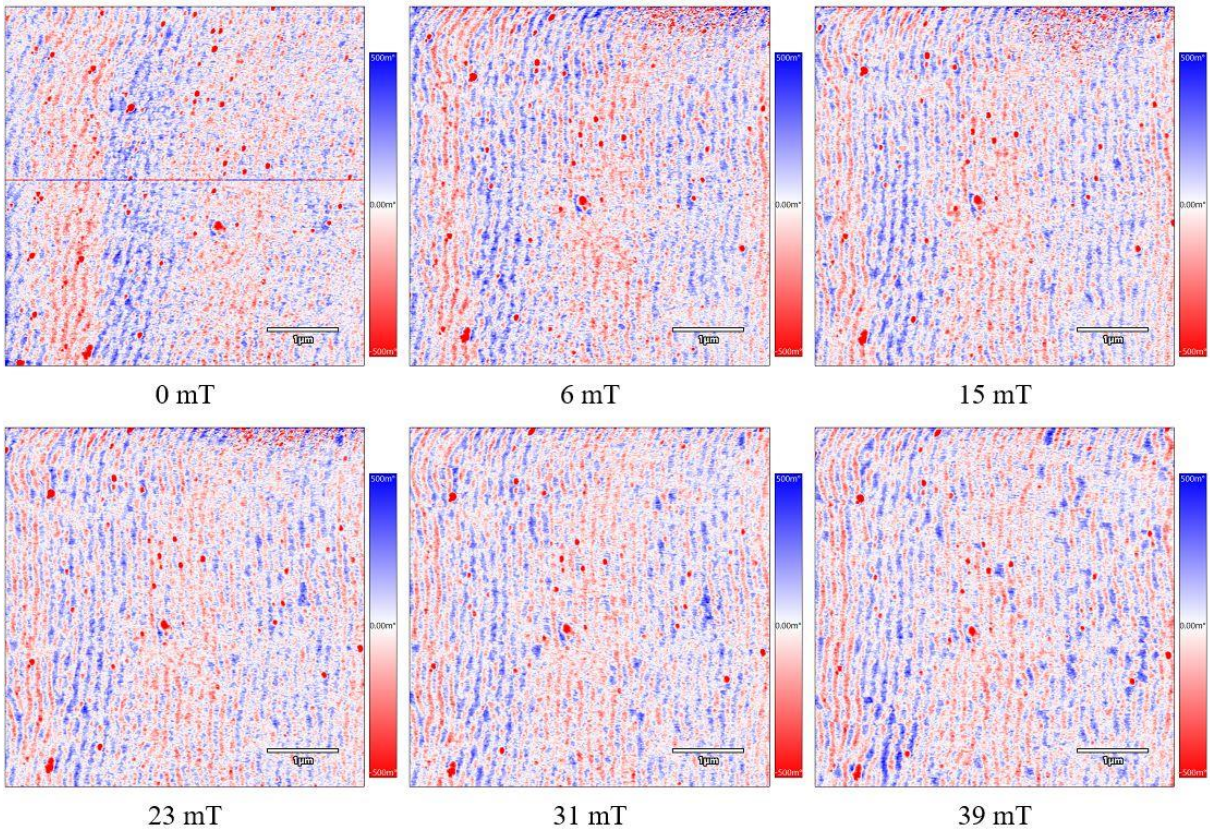

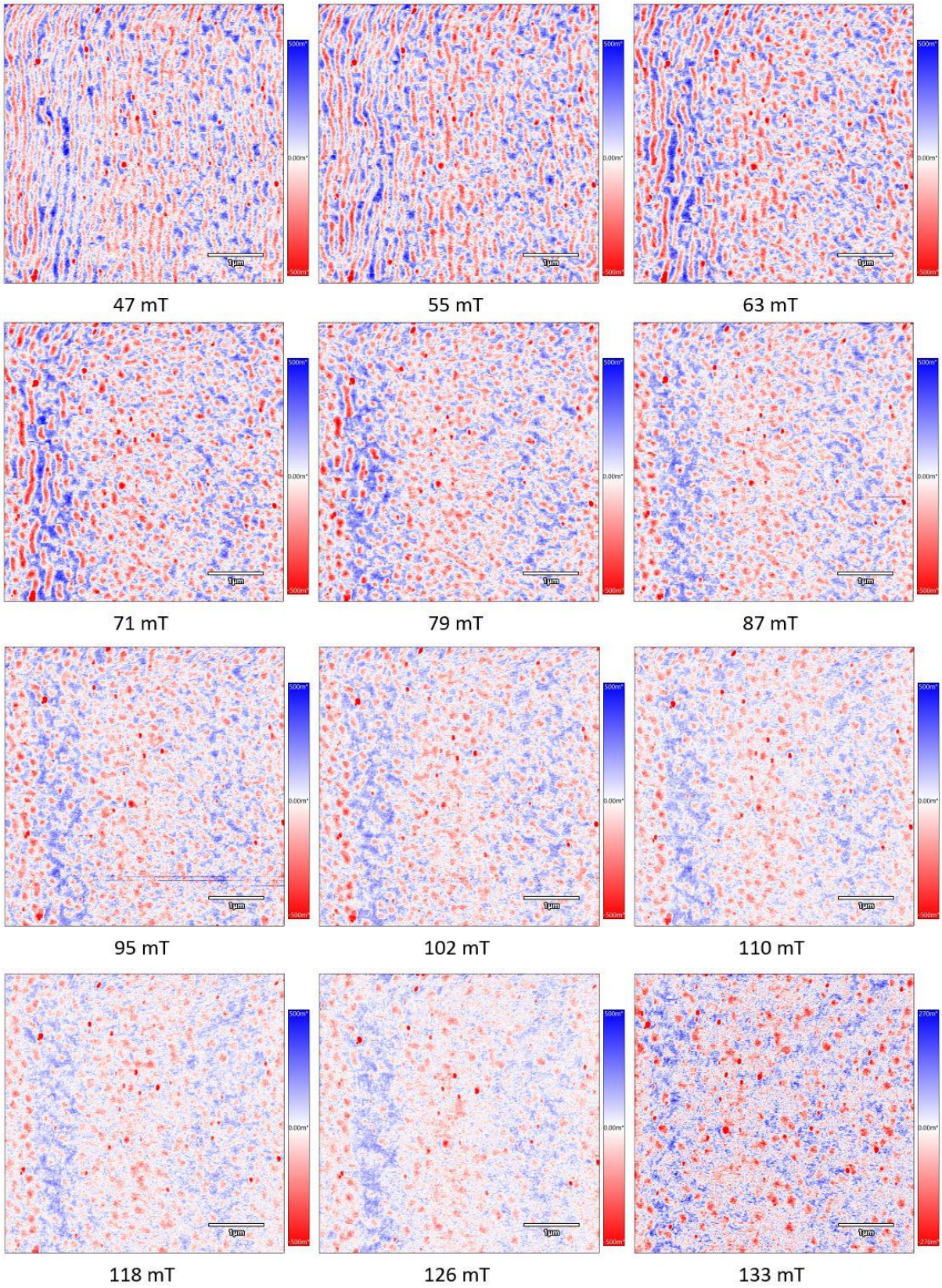

Figure 81: MFM images performed on the membrane at different OOP fields taken from 0 to 133 mT .

In the images, the stripy domain phase resulting from the IP demagnetization procedure is well ordered at zero field, where its periodicity is estimated to 150 nm. It dominates the magnetic texture until ~63 mT. Beyond that field, a disordered skyrmionics phase appear,

where the skyrmion size is above 100 nm. At this field, the typical distance between skyrmions is approximately of 300 nm. There is a large distribution in the skyrmion size and distance, making a precise image analysis complicated.

3.2.7 XRMS Hysteresis loop.

The XRMS cobalt L edge hysteresis loop images have been performed in the COMET chamber on SEXTANTS beamline. The required OOP field to saturate the sample is around 150 mT and RESOXS can produce a field up to 110 or 120 mT maximum. In this experiment, as well as in the M edge dynamic performed at Fermi FEL, a CMOS sensor has been used[253]. It offers a higher acquisition rate compared to the previously used CCD detector. For instance, at Fermi, a factor of 30 in collection time is gained. In COMET experimental chamber, the CMOS is mounted on a detector stage that can move in the direction of the beam. The sample to CMOS distance can thus be adapted to maximize the diffracted ring contrast. The following static and dynamic results have been obtained with a single sample containing multiple membranes. It is an important feature as the signal can result from different membranes since they are separated by 500 µm in both directions. Consequently, a 50 µm pinhole was placed 200 mm upstream to the sample and the incident X-ray centered on one membrane. Despite our effort, a signal was still detected from a different membrane and the bigger beamstop was used.

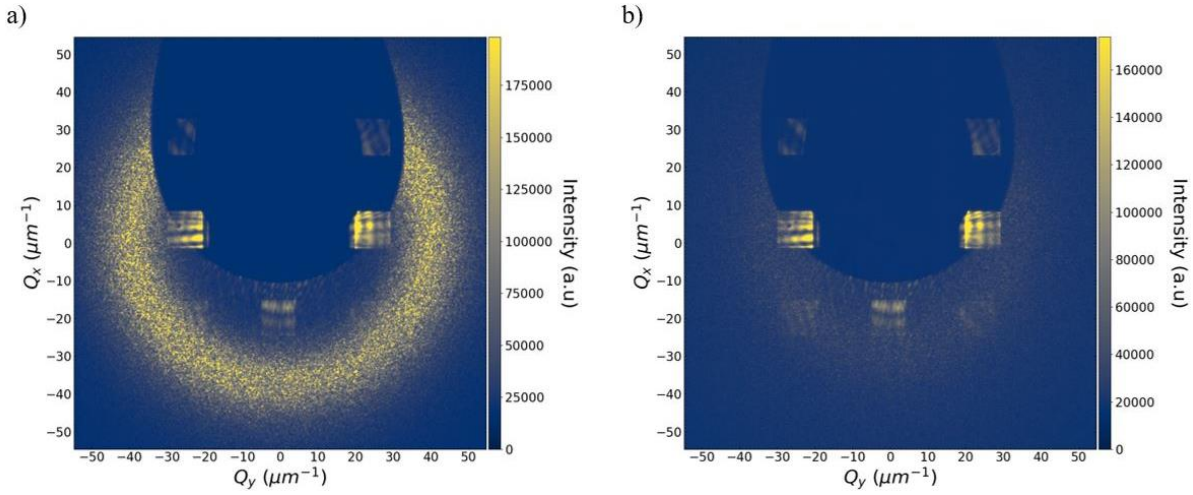

Figure 82: Images taken at 0 mT (a) and 150 mT (b) applied OOP.

In figure 82 (a), the image taken at zero field displays a ring without any intensity modulation visible by eye. It indicates a labyrinthine domain pattern. In figure 82 (b), corresponding to an image taken at 150 mT, no diffraction ring is observed. The signal around the beamstop, comes from at least one other membrane and is relatively close to the diffraction ring. The image at saturation have been subtracted to every image in field to reduce drastically the component coming from the multi-membrane specular. An image was acquired for each field between $\pm$150 mT, beginning at 0 mT toward positive values. During the hysteresis loop, each time the field sweep reached $\pm$150 mT, a field of $\pm$300 mT was applied without taking any image. It ensures that the sample was saturated before changing the field evolution sign. The orthoradial profiles of images taken at different field during the first field sweep is plot in figure

83.

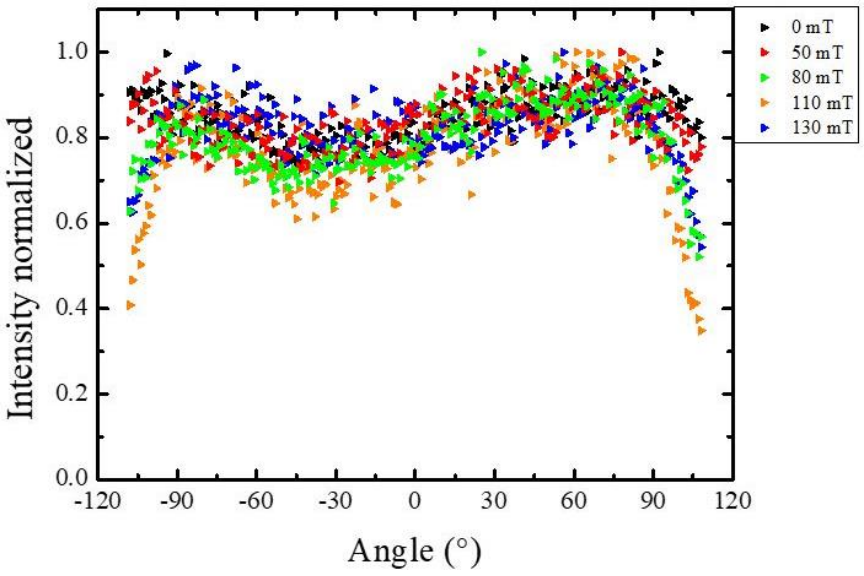

Figure 83: Orthoradial profile of images taken at 0 mT (black), 50 mT (red), 80 mT (green), 110 mT (orange) and 130 mT (blue).

The orthoradial profile doesn't cover the $\pm 180°$ range because a polar mask covering 140° has been applied where the beamstop is. No sign of modulation is observed, which confirms the poor skyrmion lattice ordering seen in the MFM images. The radial profile exploitation, done in the same manner as in the previous skyrmion lattice, is displayed in figure 84. In the intensity hysteresis loop, the increasing and decreasing field curves don't match. The shift between the two curves is about 10 mT, which is almost an order of magnitude bigger than the COMET magnet remanent field. The shoulder around ± 90 mT could be a sign of the skyrmion lattice.

The maximum peak position at zero field corresponds to a periodicity of ~ 160 nm. It is larger than the stripe periodicity found in the MFM image but qualitatively coherent with the higher period found in labyrinthine domain patterns. The shift in the Q peak hysteresis curves is around 20 mT. As the field increment is 10 mT, it is legitimate to question the accuracy of the specular and gaussian fit. In transmission geometry, with a diffracted signal hundreds of pixels away to the beamstop, the specular contribution is almost zero. Thus, the gaussian fit doesn't depend on the specular signal removal. A similar hysteresis loop has been performed on RESOXS (not show here) and found a 15 mT shift, knowing that the field step was 5 mT. In RESOXS, the magnetic field is produced with four electromagnets, on contrary to COMET that uses four permanent magnets. The RESOXS quadrupole remanent field isn't larger than 2 mT, meaning that the shift effect between increasing and decreasing field curves comes probably from a hysteretic behaviour of the sample magnetic pattern. As in the previous skyrmion lattice sample, increasing the field in absolute value results in an increase of the magnetic period. A small shoulder, similar to the intensity curve one, is also observed around ± 90 mT with the black and red curves amplitude antisymmetric to each other with respect to the field. The

asymmetry is more pronounced in the FWHM curves but more erratic for fields above 90 mT. The FWHM value is close to the previous skyrmion lattice sample FWHM.

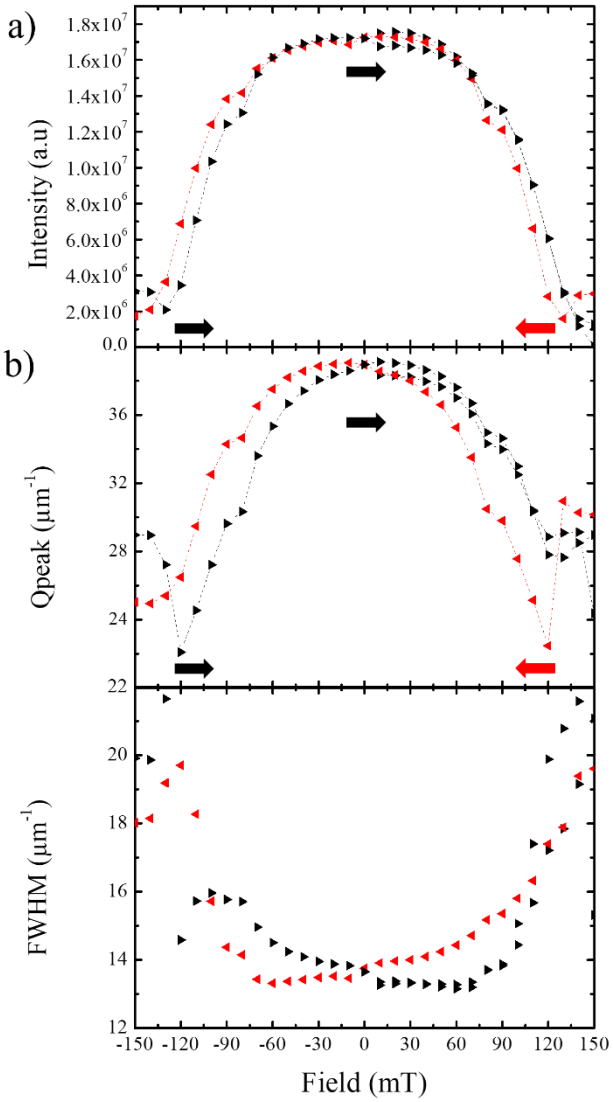

Figure 84: Intensity (a), peak position (b) and FWHM (c) of the diffraction peak's radial profile at different field during the hysteresis loop. The black triangles depict the points taken with an increasing field while the red triangles are points from the decreasing part of the field sweep.

Despite the lack of sixfold symmetry signal, the sample dynamics has been studied. At Fermi, the gain in the data collection time using the CMOS came at the cost of the sample to detector distance that couldn't be as close as the CCD. Together with the smaller CMOS pixel size and the relatively small magnetic domain periodicity, it was not possible to get the full diffraction ring. A polar mask selects the signal that is used in the data treatment. The acceptance angle is around 80°. It prevents any artifact in the radial profile that could come from

the signal proximity with the image's limit but also reduces the error due to the center determination. The latter is higher compared to the images with a full diffraction ring.

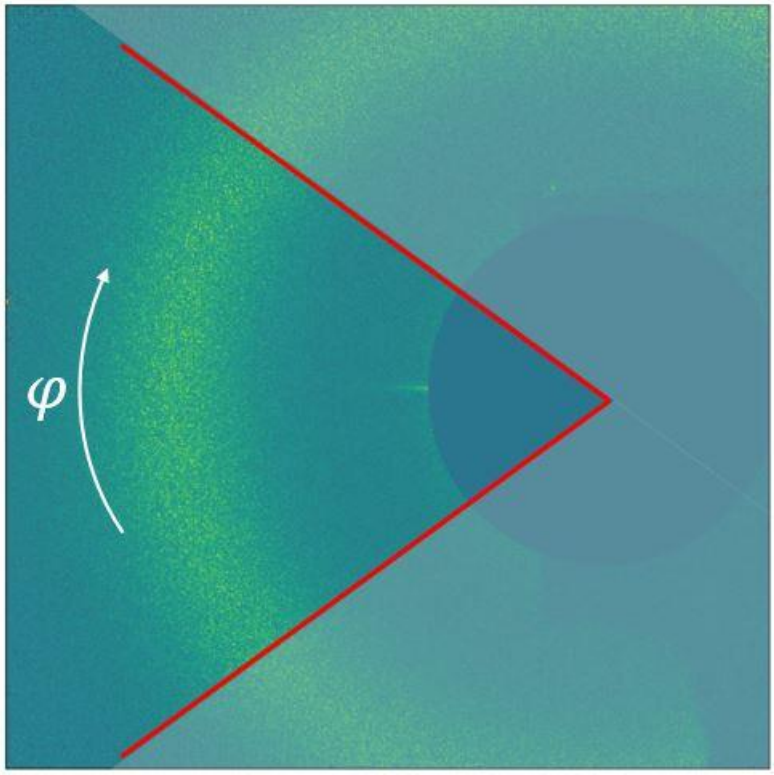

Figure 86: Image taken with the CMOS detector at negative delay. The red lines depict the polar mask used in the analysis to avoid any influence due to the image's limit proximity. The black circle at the right of the image is a numerical beamstop that hides the specular.

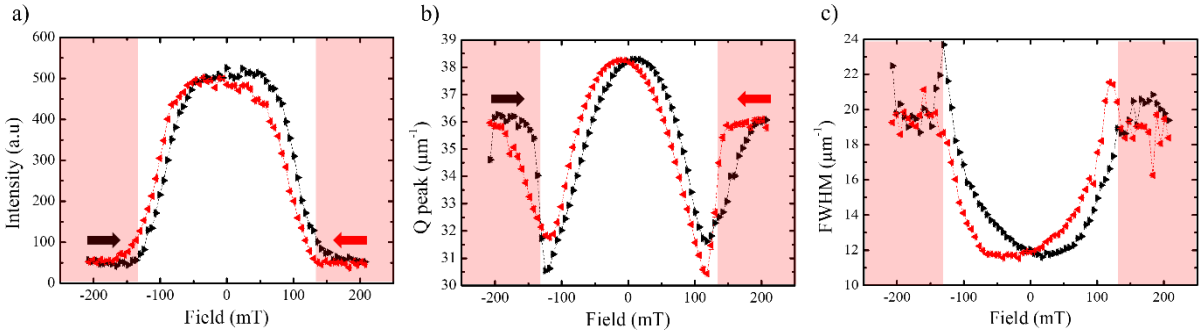

Figure 85: Intensity (a), peak position (b) and FWHM (c) of the magnetic diffracted signal in the 80° mask window. The red rectangles indicate the part of the curves where the signal is almost negligible.

The hysteresis measurement has been reproduced at the cobalt M_3 edge. In the DiProI chamber, the magnetic field is produced by four electromagnets. During the static measurement, the field step was 5 mT. The asymmetry shift between the positive and negative field don't go over 7 mT and is maximum for small coil current. The intensity, maximum peak position and the FWHM are plotted in figure 86. A rapid comparison with the hysteresis loop performed at the L edge, shows that the antisymmetric shift is still present. Its value is still around 10 mT in the intensity curve, 20 mT in the periodicity and even higher in the FWHM. The values are sensibly the same as at the cobalt L_3 edge. However, there is no more visible shoulder around

90 mT. The different behaviour could come from the higher signal to noise ratio in the experiment performed at the L_3 edge (1.59 nm) in COMET than the one at cobalt M_3 edge (20.8 nm) in DiProI.

3.2.8 Time-resolved study

The sub-nanosecond dynamic has been performed with the laser and FEL fluences set at 1.55 mJ/cm^2 and ~2 mJ/cm^2, respectively. The fields applied during the delay scans ranged from zero to ±88.8 mT with steps of 29.6 mT. The field delay scans have been realized by pair of field absolute value without following a specific order. Between each delay scan, the sample was saturated at +200 mT. Then, some fields have been measured again to check the reproducibility. The domains' diffraction intensity variation at different fields is plot in figure 87.

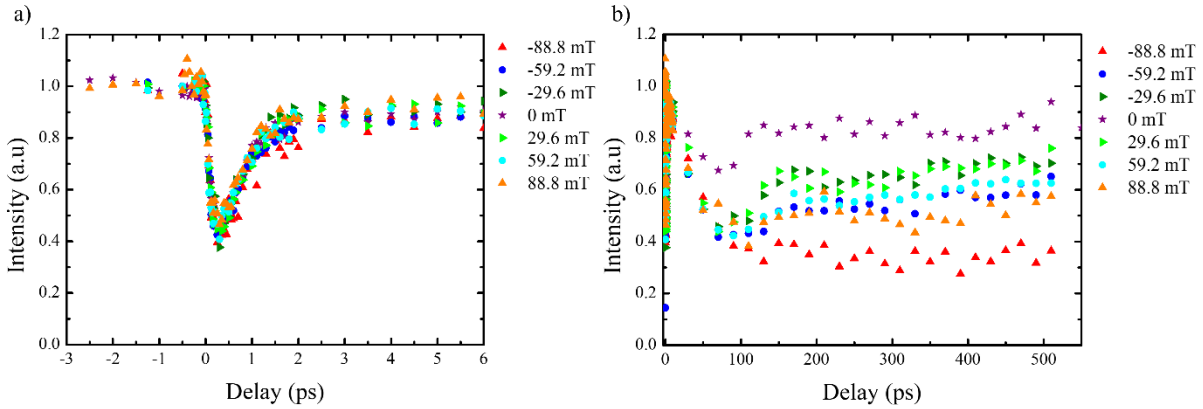

Figure 87: Plots of delay scans performed at different field which are focused on the ultrafast (a) and hundreds of picosecond regime. The scans that have the same field in absolute value share the same point type.

In the graph focusing on the ultrafast time scale, all delay scans exhibit a typical subpicosecond and follow the same curve. The demagnetization time constant (~160 ±20 fs) is close to the one found in reflection geometry on a similar sample composition, but the magnetization minimum is reached at (~300 fs). The remagnetisation time is almost three time smaller (~360 ±50 fs). It qualitatively corresponds to the trend observed in literature, i.e., the remagnetisation time decreases with the fluence. Between 10 and 30 ps, the diffracted signal suddenly decreases until 100 ps. The drop is of 30% at zero field and increases with the field to reach 60% at ±88.8 mT. The results are reproducible, as well as the separation between the ±88.8 mT curves after 100 ps that may result from the asymmetry in the hysteresis loop. However, after each scan, the scattered intensity decreases without significant change in the peak position and FWHM, which indicates an absence of sample degradation. This observation is quite surprising as in transmission geometry the beam is more homogeneously distributed between the layers than in reflection, where sample degradation was observed for a FEL fluence twice smaller. The data collection time is also much shorter than previously, the normalized data reproducible and the signal slowly recovering. To determine if the effect originates from a sample degradation, a delay scan has been performed on a $[Co(0.6)/Pt(0.8)]_{20}$ multilayer grown on $Si_3N_4(50)/Ta(2)$ and capped

with 2 nm of aluminium. The result of one stripe domain diffracted spot pattern is plot in figure 88.

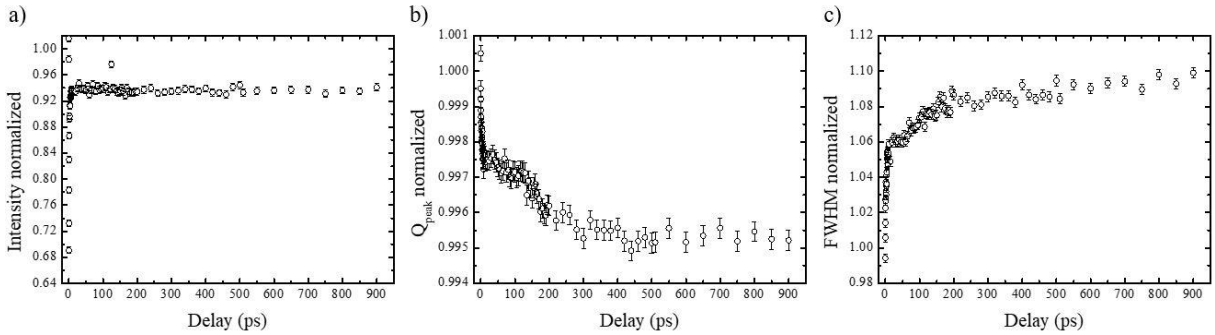

Figure 88: Evolution with the delay of the intensity (a), the peak position (b) and the FWHM (c) of the symmetric Co/Pt multilayer.

As one can see, the intensity drop isn't present in figure 88 (a). The intensity doesn't fully recover at 900 ps. Looking at the peak position and the FWHM, they respectively decrease and increase, indicating a change in the domain pattern toward a more labyrinthine state, which could explain the 6% intensity decrease due to loss of long-range ordering.

The intensity drop observed in the skyrmion lattice system around 30 ps should not originate from the sample degradation since the effect is abrupt compared to the degradation observed in reflection. Also, the CMOS delay scans are way faster (~45 minutes) than the ones performed with CCD (more than 300 minutes). Thus, if the physical behaviour is real, the change in the intensity could originate from the change of effective anisotropy favouring the in-plane magnetization in the domains. Indeed, the interfacial anisotropy depends to the power of 2.5 to the magnetization saturation while the dipolar, responsible for the IP easy axis in planar geometry, evolves with the square of M_s. As the saturation magnetization decreases when the temperature increases, the magnetization easy axis should tend more IP. This qualitative explanation doesn't explain why the sudden magnetization drop between 10 and 30 ps as well as the small oscillations after 100 ps. The periodicity of the latter is about 8.3 GHz, which is a bit higher than in the other Pt/Co/Al multilayer.

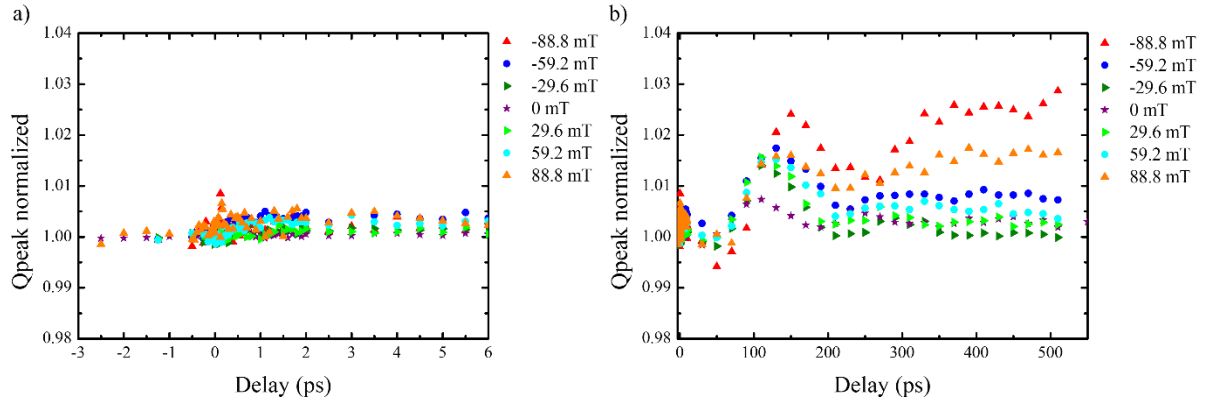

Figure 89: Peak position evolution of delay scans performed at different field which are focused on the ultrafast (a) and hundreds of picosecond regime (b). The scans that have the same field in absolute value share the same point type.

The normalized peak position evolution in the ultrafast regime shows almost no evolution as depicted in figure 89 (a). At longer timescale, no signal evolution is seen before 30 ps. Then, an increase of the peak position kicks in and is followed by a ~8 GHz oscillation. The first oscillation maximum seems to increase in delay and in amplitude with the field absolute value. The variation in the peak position doesn't exceed 3% of the initial value at any applied field. Thus, only a strong variation in the FWHM could explain the intensity drop by a domain magnetic pattern variation.

At zero applied field, a small (2%) monotonous decrease at negative delays would indicate a gradual domain pattern change toward a more ordered state due to the laser pulses if it wasn't below the error bar value (~2.5%). In the ultrafast regime, the FWHM decreases by 10%, which is different to the behaviour typically observed. A smaller decrease (~5%) is observed for ±29.6 mT. At ±59.2 mT almost no change is observed and at ±88.9 mT the FWHM increases by few percent in the sub picosecond regime. At this timescale, no noticeable difference has been found in the intensity signal with field. The FWHM in the sub-nanosecond regime fluctuates by few percent around 95% of their initial value for all fields except ±88.8 mT that increase around 30 ps and then tend toward the same value. The peak position and FWHM's evolution diversity in time at different field as well as the low variation percentage discards the magnetic pattern origin for the intensity drop between 10 and 30 ps.

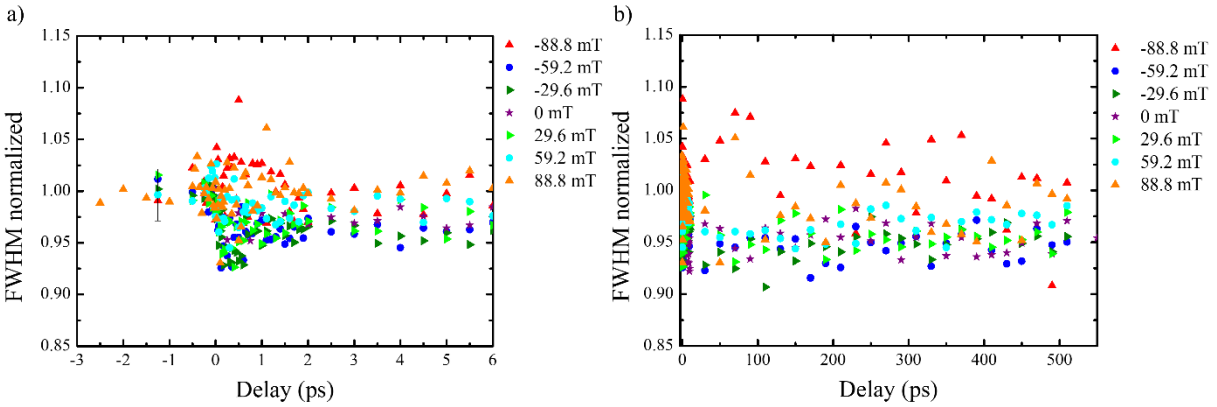

Figure 90: Normalized FWHM at the ultrafast (a) and sub-nanosecond regimes (b).

To further investigate the origin of the intensity variation, the diffracted signal field dependence, only swept from negative to positive field due to time restriction, at 300 ps has been realized and is plot in figure 91.

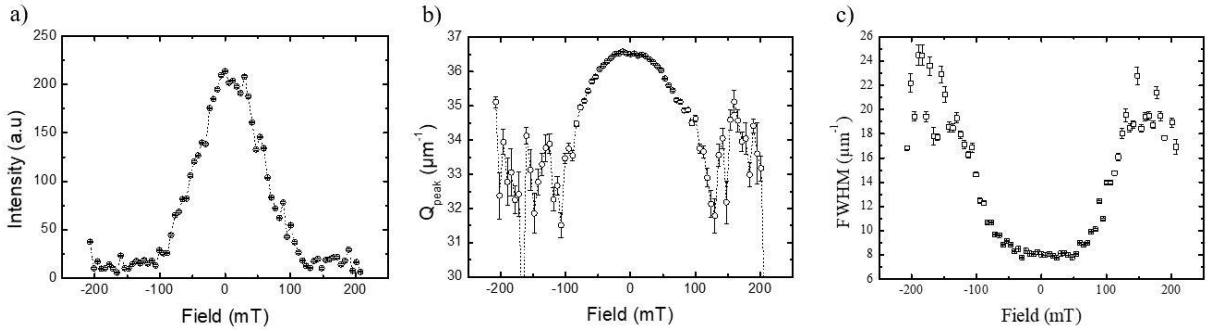

Figure 91: The single field sweep data analysis intensity (a), peak position (b) and FWHM (c) evolution.

Compared to the hysteresis performed at negative delay, the intensity and peak position drop quickly with field, while the FWHM evolves similarly as the black curve in figure 86 (c). At field inferior to 70 mT in absolute value, the FWHM value at 300 fs is inferior to the negative delay one. The domain magnetic pattern is thus less resilient against an external magnetic field but, according to the FWHM, more ordered.

The explanation of the intensity drop's origin observed in the skyrmion lattice sample but not in symmetrical Co/Pt or multilayers with the same Pt/Co/Al composition is still missing. Overall, at the M edge, well-ordered skyrmion lattices are required to obtain a noticeable sixfold symmetry modulation in the signal. It could be obtained from an IP demagnetization of the samples, with the drawback that the stripe state isn't fully reversible with field and laser. However, little skyrmions are preferred for potential high density storage applications. The study of skyrmion lattice samples at the L edge provides better results as the magnetic dichroism is stronger but also, the use of ruthenium, giving more ordered skyrmion lattices than Al-based multilayers, is less detrimental to the magnetic contrast. The skyrmion dynamics is yet to be properly performed on a sixfold symmetry diffraction pattern.

In that chapter, the time-resolved behaviour of different chiral systems has been studied. First, the evolution of the SUM and DIFFERENCE (chiral) signals in reflection geometry has been performed on a Pt/Co/Al multilayer exhibiting a labyrinthine domain pattern with chiral DWs. It results that the DIFFERENCE signal demagnetizes more and recovers faster than the SUM signal, the former mostly originates from the chiral DWs while the latter from the domains. A model that relies on spin polarized hot electrons currents from the domains flowing into the DWs has been developed to explain our results. The hot electrons coming from both sides of the DWs are opposite in polarisation and interact with the DWs magnetization. The torque that comes from the hot electrons flow, induced a transient distortion of the DW type and further demagnetizes the DWs compared to the domains. The faster recovery of the chiral signal is visible at the sub nanosecond time scale. Indeed, the DIFFERENCE intensity recover its initial value while the SUM is at 90% of the negative delays value. In the SUM, 6 GHz damped oscillation have been observed. MOKE, VNA-FMR and magnetic modes calculations have been realised to get its origin, but no such frequency has been found. On the same sample, the effect of the pump circular polarization has been studied. A different evolution between the CL_{IR} and CR_{IR} pump polarization is noticed and scales with the pump fluence. The results must be confirmed with an experiment realised on a sample with an opposite chirality. Finally, time-

resolved experiments on samples hosting a skyrmion lattice state was done in transmission geometry to get more signal. The results obtained on a sample with a rather poor skyrmion lattice order, didn't show any specific behaviour in field at the ultrafast regime. However, a drop in intensity has been found around 30 ps and increases with an external magnetic field. Its origin is still unclear.

Conclusion and perspectives

Conclusion

During this PhD work, the static and the time-resolved evolution of different chiral magnetic textures has been studied with XRMS. XRMS gives access to the magnetic DWs sense and type of winding analysing the dichroism in the off-specular scattering diffraction pattern. The sense of winding corresponds to the magnetic chirality (CW or CCW) and the type of winding indicates the cycloidal (Néel) or helicoidal (Bloch) rotation of the spin inside the DWs. This information can be found in the DIFFERENCE image with the orthoradial distribution. The intensity of the diffracted signal is obtained by radial integration of the diffracted signal in the DIFFERENCE (CL – CR) and SUM (CL + CR) images. The intensity of the DIFFERENCE image is linked to the interference between the magnetization in and out of the scattering plane, which is defined by the incoming and out-going photons wave vector. In a magnetic domain state, the SUM signal is dominated by the OOP component of the magnetization, that we can assigned to the domains and the DIFFERENCE by the interference between domains and DWs magnetization. The comparison of the SUM and DIFFERENCE signals evolution with time gives a qualitative information on the domains and DWs behaviour, respectively. A part of the experiment has been performed in reflection geometry. Due to the geometrical projection, the specular beam doesn't vanish and both, off specular and specular contributions coexist. Consequently, a python analysis code has been written to fit and subtract the specular signal, which is often stronger than the magnetic one. It has been first tested in static condition in order to validate it.

The formal XRMS calculations presented in chapter 2 considered a single magnetic layer. It holds true for multilayers, as shown experimentally by Chauleau *et al*[222]. The difference is that each magnetic layers re-emit a part of the incoming beam. The different beams interfere with each other, but some are coming from more layers that are more buried and thus attenuated. The constructive interference effect is obtained at the multilayer Bragg peak since the chemical and magnetic periodicities are equal. Thus, XRMS experiments on FM multilayers are usually performed at an integer of the multilayer chemical periodicity in the reciprocal space. The tunability of the magnetic interactions in multilayers fuelled the research for the optimal composition for applications. In spintronics, a project aims to use ultra-small magnetic textures for storage devices. Skyrmion is a good candidate to that purpose as it is usually tens of nanometer large. Isolated skyrmions have already been stabilized in FM multilayers but their electrically driven displacement exhibits a transverse motion. A way to cancel this effect is to nucleate skyrmions in SAF samples, which are multilayers composed of AFM coupled FM layers. For the XRMS study, the magnetic period is thus twice the chemical one meaning that SAFs studies have to be performed at half odd integer multiple of the Bragg peak. In this PhD work, SAF samples have been tailored to stabilize a spin spiral magnetic texture at RT. The spin spiral periodicity gives a direct information about the exchange energy over the DMI strength ratio. The XRMS signals temperature dependent study of SAF samples with different repetitions indicates that both contributions vary similarly in temperature. Then, the incident angle

dependence of the SUM and DIFFERENCE signal has been done at RT. The variation of the incident angle towards higher values increases the depth probed by the X-rays. Thus, the change in the XRMS signals depends on the 3D magnetic texture and the interference effect. A program, fuelled by a micromagnetic simulation of the magnetic texture, has been developed to simulate the on and off-specular signal. It was able to reproduce the angular variation around the first half Bragg peak but failed to reproduce the variation at $3Q_{Bragg}/2$ because the roughness isn't yet taken into account.

It paves the way toward the 3D reconstruction of spin texture with XRMS that ideally will have a wavelength limited only spatial resolution (i.e. few nm in the soft x-ray range). It has been done in Flewett *et al*[195]., where the authors reproduce the signal from a sample with an hybrid chiral texture containing a Bloch part, a Bloch orientation of the DWs texture sandwiched between two opposite Néel chiral DWs in the vertical direction. The evolution of the Bloch part depth with field has been successfully tracked. This kind of FM sample stabilize with the dipolar interaction, two opposite chirality in the vertical direction.

In the time-resolved study part of that PhD work, multiple chiral samples have been studied. The first one is a Pt(3)/Co(1.5)/Al(1.4) (nm) trilayer with PMA, repeated five times and tailored to exhibit a high interfacial DMI strength. All time-resolved results on that sample were obtained in reflection geometry (45°) at the cobalt $M_{2,3}$ edge (~20.6 nm) which has a low attenuation length (~4 nm) in Pt and Co. Thus, only the topmost CW Néel layers are probed but mostly dominated by the top one. Despite the unexpected hybrid chirality found in our sample, the probed layers are of the same chirality allowing a safe analysis of the diffraction pattern. During the experiment, the sample was in a labyrinthine state. The evolution of the DIFFERENCE and SUM signals with time revealed a bigger demagnetization in the DIFFERENCE than in the SUM. Also, the DIFFERENCE signal recovers faster at few ps times scale as well as at the sub-nanosecond one, as found in Kerber *et al*[244]. This result is reproducible and can be explained by a model relying on the generation of spin polarized hot electrons coming from the domains. The hot electrons' spin, coming from both sides of the DW with opposite polarization, interact with the DWs magnetization. The interaction induces a torque $\boldsymbol{\tau} \propto \boldsymbol{m} \times \boldsymbol{s}$, with $\boldsymbol{m}$ the DW local moment and $\boldsymbol{s}$ the spin carrier polarization, which should have two effects. The first one is an incoherent effect due to the isotropic emission of the hot electrons that causes a disorder in the DW structure, increasing the effective temperature of the DWs' spin. The other effect comes from the hot electrons that comes perpendicularly toward the DWs. It induces two opposite transient spin precession components out of the DW magnetization rotation plane on both DWs side. Due to the reduced exchange energy in the excited *s-p* levels, the precession angle could reach ~10° at the ultrafast regime and should remain on longer time scale. The determination of the ratio between the incoherent and coherent effect is not possible in our case. It requires another diffraction order in the off-specular diffraction pattern as the two effects shouldn't affect the intensity of the higher order peak(s). In the peak maximum position in the reciprocal space, which indicates the magnetic pattern periodicity, an ultrafast decrease of 2.6 % can be seen. A similar results has been found in Pfau *et al*.[169] work realised in transmission geometry on a symmetric Co/Pt multilayer with a labyrinthine magnetic texture, while other

studies either found a change at few picoseconds[172] after the laser pulse or no change in labyrinthine and stripes structures, respectively[173,174].

At hundreds of picosecond delays, a damped 6 GHz oscillation is seen in the SUM signal as well as in the peak position of both signals. The origin of those oscillations has been explored, performing MOKE, VNA-FMR experiments and magnetic modes calculations. Except the MOKE reflectivity results that matches the theoretical calculations of the multilayer phonons modes, the magnetic oscillation frequency hasn't been found. At hundreds of picoseconds, the system hasn't yet released all the heat received by the laser pulse, knowing that temperature affects the different magnetic contributions.

On the very same sample, the effect of the circular polarization of the pump has been explored. At the lower tested fluences, no changes were detected between CL_{IR} and CR_{IR}. At higher laser fluences, the CL_{IR} polarization is below in signal than CR_{IR} in both, the DIFFERENCE, and the SUM. The result is reproducible but a further study with a sample of opposite chirality must be performed before concluding about its origin. Nevertheless, the asymmetry ratio of CL_{IR} and CR_{IR} were equal at a given fluence, indicating that the separation between the two pump polarization results from a higher absorption of the CL_{IR} polarization. We suspect that this effect is due to a stronger absorption of the IR light when the circular polarization sense of rotation is the same as the chiral winding sense.

The final part of this PhD work deals with skyrmion lattice samples. The skyrmion lattice was nucleated by increasing an OOP field from a labyrinthine magnetic domain pattern. At the ultrafast regime, no change was noticed in field. However, from 30 ps, a surprising drop of the off-specular scattered intensity is observed. This drop increases with the field. Neither a dramatic change in the peak position or of the FWHM is noticed. Thus, a sudden change of magnetic texture is excluded. The origin of that phenomena is still unclear and will be subject of further investigation.

Perspectives

Through this PhD thesis, the different behaviour between the SUM and DIFFERENCE off-specular signals has been found by two different teams[244,254] in different FM samples in the ultrafast regime. However, the results on the evolution of the peak position are still debated as well as its link with the mechanism explaining this change. One hypothesis is that the DWs width varies. To investigate this point, FM samples with a good signal to noise ratio in the intensity of the higher diffraction orders is needed. The experiment should also be performed in the labyrinthine and stripes state to disentangle a potential magnetic texture dependence. The other perspective on chiral FM is to pursue the study on the pump circular polarization effect on two opposite chiral system. Finally, we could think about performing a time-resolved experiment at various angle on FM sample with a hybrid chirality to follow the Bloch part depth at a transition metal L edge. Supported by micromagnetic calculations, it could give a more precise insight on the different magnetic contributions' evolution at the ultrafast time scale.

Then, the study of systems hosting a well ordered skyrmionics state could also be achieved. In our results, no sixfold symmetry has been found, despite the clear evidence of a skyrmion lattice nucleation with field shown in MFM but lacking of long range order. The tracking of the sixfold symmetry signal evolution, decorrelated from the other magnetic texture should give a good insight about the skyrmionics state evolution after a laser pulse. It should also provide a comparison with the drop of intensity found in our sample.

Finally, more study on SAF samples should be performed. The first should be static to characterize the robustness of the spin spiral texture with field, as electrically done by Maccariello *et al.*[255] but with XRMS in this case. The second is the laser-induced behaviour of the spin spiral state, that we attempt at the cobalt $M_{2,3}$ edge, performed at the L edge of a transition metal at $Q_{Bragg}/2$ or $3Q_{Bragg}/2$. The ultrafast model proposed to explain the higher demagnetization in the DWs assumes that the domains are far bigger than the DWs. In a spin spiral state, there is no such distinction. Thus, the DIFFERENCE and SUM signal should have a similar time-resolved behaviour if our spin polarized hot electron model dominates the demagnetization mechanism.

ANNEX A: Variability of the results with the fit parameters for the specular signal removal

The diffraction center determination is also important for the data radial profile. Considering that one can manually find it with a precision of 10 pixels or less, a perturbation test has been performed.

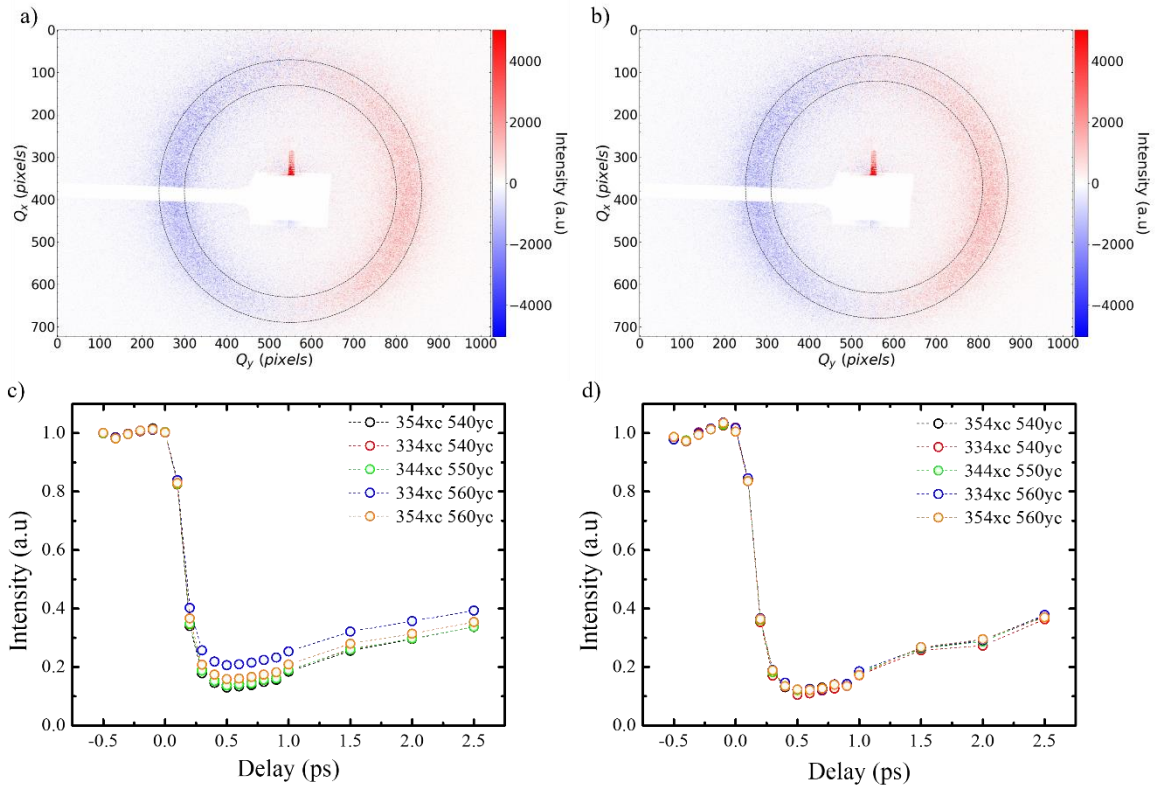

Figure S1 : Same difference image taken at negative delay with two concentric circles but with a different center, shifted by 10 pixels in both directions (a&b). In graph c), the curves correspond to analysis performed with different center position for the sum (CL + CR) signal. The figure d is the same but for the difference image. The way the signal is obtained at each delay is further described in the main text.

As noticed in figure S1 (a&b), the 10 pixels shift in the center of the concentric circles is visible. The associated influence on the data analysis of the 10 pixels shift in absolute value and in both directions is plotted for the sum image (figure S1(c)) and the difference (figure S1(d)). The center position, within an uncertainty of 10 pixels, has almost no influence on the difference signal. The sum signal is more sensitive to it. However, except one center point, the variation is relatively small (less than 10%) indicating a good manual choice for the center with a third order polynomial fit.

Another crucial parameter for the data analysis, is the range used for the specular fit. There are two areas separated by the diffracted magnetic signal. The range with a radius delimitation greater than the magnetic signal is larger since it imposes a fit curvature where there is only the

specular signal at all delays. The variation of the magnetic signal amplitude, depending on the range fit, using the third order polynomial function has been addressed.

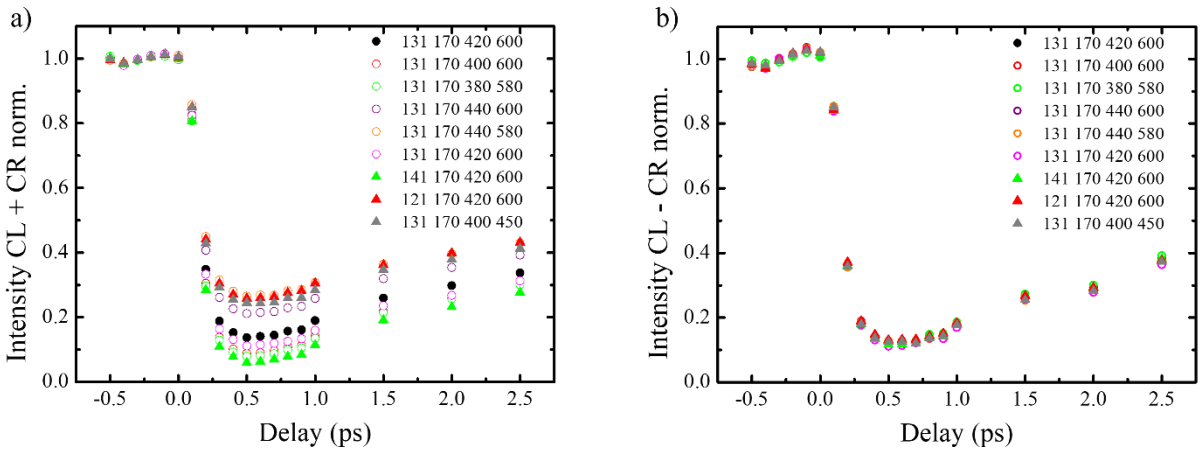

Figure S2 : Influence of the parameter range for the third order polynomial fit in the sum (a) and the difference (b) signal.

ANNEX B : Simulation of the XRMS asymmetry ratio with a transient mixed Bloch/Néel/Bloch DWs

A one-dimension magnetization profile of a mixed Bloch/Néel/Bloch type DWs with a time dependence can be written as follows:

$$M_x(x,t) = \cos(\Theta(t))\, M(t) \left[\sqrt{1-\left(\tanh\left(\lambda\frac{x_1(x)}{w(t)/2}\right)\right)^2} - \sqrt{1-\left(\tanh\left(\lambda\frac{x_2(x)}{w(t)/2}\right)\right)^2}\right];$$

$$M_y(x,t) = \sin(\Theta(t))\, M(t) \sqrt{1-\tanh\left(\left(\lambda\frac{x_1(x)}{w(t)/2}\right)\right)^2} - \sqrt{1-\tanh\left(\left(\lambda\frac{x_2(x)}{w(t)/2}\right)\right)^2};$$

$$M_z(x,t) = M(t)\tanh\left(\frac{\lambda}{2} * \frac{x_3}{w(t)}\right);$$

With $x_1(x) = \sin\left(\pi\frac{x+\frac{\lambda}{4}}{\lambda}+\frac{\pi}{4}\right)$, $x_2(x) = \sin\left(\pi\frac{x+\frac{\lambda}{4}}{\lambda}-\frac{\pi}{4}\right)$ and $x_3(x) = \sin\left(2\pi\frac{x}{\lambda}\right)$, x is the position center around 0 and λ the domain periodicity. Both are in nanometer. $\Theta(t)$ is the out of the DW rotation plane tilt angle due to the torque induced by the spin polarized hot electrons, $w(t)$ is the DW width that changes with time and $M(t)$ is the time dependent magnetization which is proportional to $\sqrt{SUM}$ intensity.

In figure S3(a), the simulated magnetization profile for $\Theta = 0°$ and $\Theta = 40°$ and a DW width of 20 nm is displayed. The corresponding resonant magnetic scattering amplitude in dipolar approximation[190,220,256] is given by:

$$f_{EI}^{REXS} = \begin{pmatrix} 0 & \boldsymbol{k} \\ -\boldsymbol{k}' & \boldsymbol{k}'\times\boldsymbol{k} \end{pmatrix}\cdot\boldsymbol{M}$$

The diffracted intensity for a given incident polarization expressed with the scattering amplitude is written as follows[190]:

$$I = Tr\left[\tilde{f}\rho\tilde{f}^{\dagger}\right]$$

Where $\tilde{f}$ and $\tilde{f}^{\dagger}$ are the Fourier transform of the scattering amplitude f_{EI}^{REXS} and its complex conjugate, respectively, and ρ is the density matrix relative to the incident x-ray beam. The density matrix for a CL and CR polarized beam in the Stoke-Poincaré representation[220] is expressed as follows:

$$\rho_{CL} = \frac{1}{2}\begin{pmatrix} 1 & -i \\ i & 1 \end{pmatrix} \text{ and } \rho_{CR} = \frac{1}{2}\begin{pmatrix} 1 & i \\ -i & 1 \end{pmatrix}$$

The simulated asymmetry ratio variation with the wiggling angle is plot in figure S3(a). We can see that considering a similar demagnetization inside DWs and domains leads to a wiggling angle of ~23°, which is quite high as discussed in **chapter 3**. The additional demagnetization experienced by the DW spins is written as dependent on the wiggling angle and is proportional to $\cos(\Theta)$, $\cos^2(\Theta)$ or $1- \sin(\Theta)$, as depicted in figure S3(b). These analytical functions were chosen arbitrarily for their simplicity and any other model could be used. In this PhD, the DWs magnetization amplitude has been chosen to evolve as $1- \sin(\Theta)$. It is the function that gives the smaller and more reasonable wiggling angle among the three. The asymmetry ratio variation with the DW width is plot in figure S3(c). It is normalized by the simulation performed for a DW width of 20 nm and a 0° wiggling angle Θ that corresponds to the static value found in the micromagnetic simulations (see **chapter 3**). This model can account for the DWs width dilatation as well as the greater demagnetization in the DWs and the tilt angle, both due to hot electrons' induced torque.

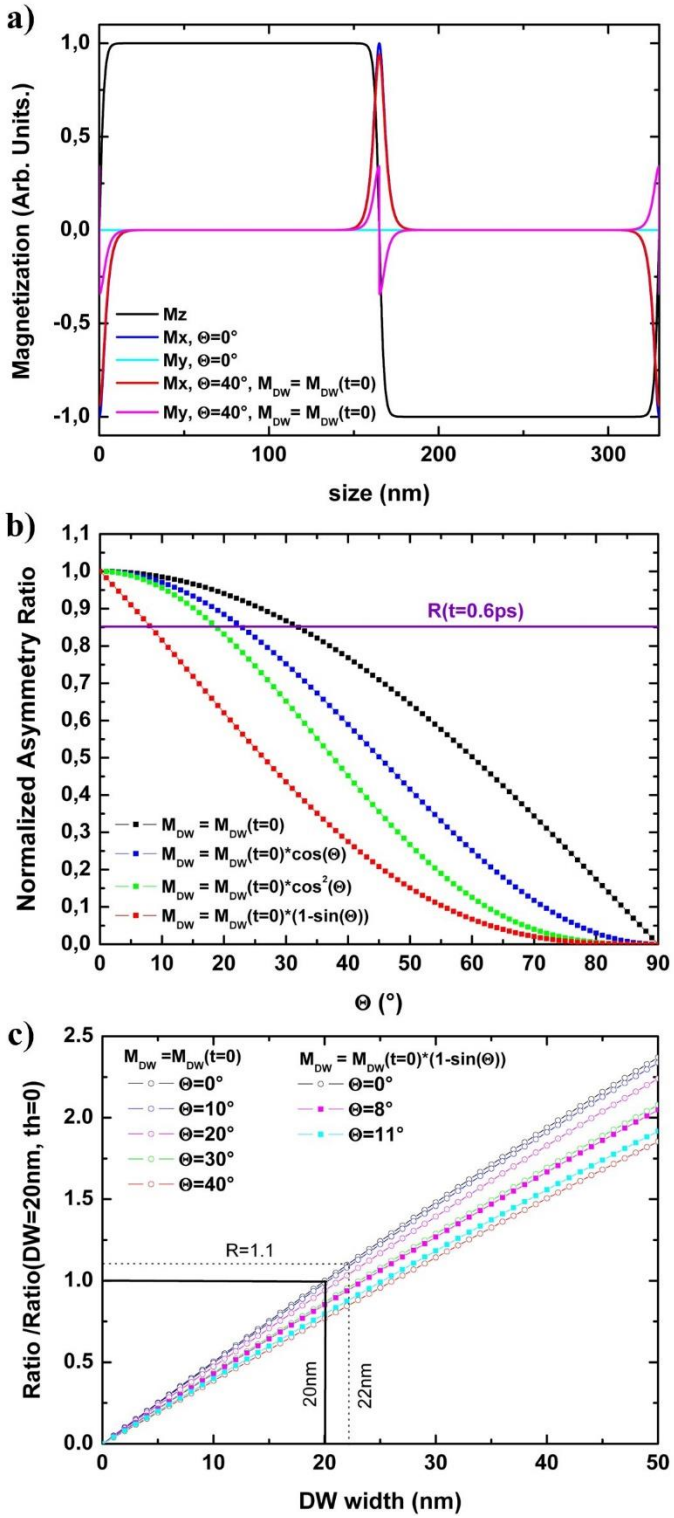

Figure S3 : (a) Representation of the magnetization profile for a wiggling angle equals to Θ=0° and Θ=40°. (b) Simulation of the asymmetry ratio (CL-CR)/(CL+CR) for different precession angles. (c) Simulation of the asymmetry ratio normalized by the value at a DW width of 20 nm and wiggling angle Θ=0°.

ANNEX C: Frequencies of acoustic modes

The optical pump pulse generates transient elastic strain near the surface of the multi-layer stack Si | SiO_2 | Ta (5) | Pt (8) | [Co (1.5) | Al (1.4) | Pt (3)] ×4 | Co (1.5) | Al (1.5) (thicknesses in nm). The strain pulse propagates from the surface into the inner part of the stack, experiencing multiple reflections from the interlayer interfaces and outer surfaces. These reflections lead to proliferation of strain pulses bouncing back and forth between various interfaces. The interference between these pulses leads to formation of standing waves. Their characteristic frequencies, which may be present in the time-resolved signals measured from the topmost part of the sample, are determined by the times of the pulse round trips across the individual layers or sets of those and by additional phase shifts that may be produced by reflections. The strongest wave amplitude is expected for confinement between interfaces causing the strongest reflections. The strength of a reflection from an interface increases as the mismatch of the acoustic impedances of the adjacent layers increases.

	K (GPa)	G (GPa)	ρ (kg m^{-3})	c_l (km s^{-1})	c_t (km s^{-1})	Z_l (MPa s m^{-1})	Z_t (MPa s m^{-1})
Co	153	83	8800	5.5	3.1	48	27
Pt	236	62	21500	3.8	1.7	83	37
Al	81	25	2700	6.5	3.0	18	8
Ta	204	69	16700	4.2	2.0	70	34
Si	37	80	2300	7.9	5.9	18	14
SiO_2	40	28	2200	5.9	3.6	13	8

Table S1 Properties of the stack's constituent layers.

Table S1 summarizes the values of the bulk modulus, K, the shear modulus, G, and the density, ρ, of the stack's constituent layers, together with the corresponding values of the speed of longitudinal, $c_\mathrm{l} = \sqrt{\left(K + \frac{4}{3}G\right)/\rho}$, and transverse, $c_\mathrm{t} = \sqrt{G/\rho}$, sound and those of the longitudinal, $Z_\mathrm{l} = \rho c_\mathrm{l}$, and transverse, $Z_\mathrm{t} = \rho c_\mathrm{t}$, acoustic impedances. The strongest impedance mismatch occurs at the SiO_2 | Ta interface. This promotes formation of a standing wave across the metallic stack with a total thickness of $L = 39.6$ nm. Due to the impedance of the substrate being lower than that of the metallic stack, the wave's wavelength is equal to $2L$, while its frequency is equal to the inverse of the round-trip time of the acoustic pulse. Table S2 presents the wave's frequencies for speeds of the order of those shown in Table S1. The frequencies corresponding to sound speed values characteristic for longitudinal phonons in the sample have a similar

magnitude to the 60 GHz value observed experimentally in TR-MOKE experiment. This is consistent with the fact that optical pump pulses cannot couple to transverse phonons in our experimental geometry, in which the optical spot size is greater than the film thickness by orders of magnitude.

Speed of sound (km s^{-1})	2	3	4	5	6
Frequency (GHz)	25	38	50	63	76

Table S2 Estimates of the standing wave frequency for different values of the speed of sound.

These considerations can be put on a more rigorous footing by calculating the spectral response of a one-dimensional stack of elastic materials to a time-periodic force source at its outer surface. The real part of the velocity response is then peaked at the resonant frequencies of the structure. The response can be easily found by solving the one-dimensional wave equation, for which we employed a custom-made simulation. The figure S4 shows the result of this calculation for the surface of a structure with properties described in Table S1 and subjected to a longitudinal force, i.e. acting normal to the film plane. The response exhibits several resonant peaks. The finite widths of the peaks, of about 4-5GHz, are due to the sound escaping from the stack into the semi-infinite space representing the substrate. The three lowest resonant frequencies are 48.6, 104.9, and 155.8 GHz, respectively. This further confirms the identification of the 60 GHz contribution to the reflectivity signal (figure 67 (d&e) in the main text) as an acoustic mode.

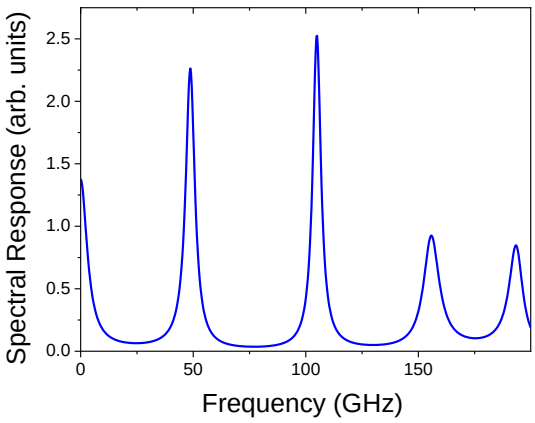

Figure S4 : The calculated longitudinal acoustic spectral response of the studied sample.

ANNEX D: Attenuation lengths at different transition edges

The following attenuation length values are taken from Henke data booklet[257].

Element\ transition	Co L_3 edge	Co M_3 edge	Fe L_3 edge	Fe M_3 edge
Al	1560 nm	710 nm	1210 nm	570 nm
Co	100 nm	10.5 nm	477 nm	21 nm
Pt	62 nm	8.9 nm	55.5 nm	9.3 nm
Ru	85.5 nm	7.5 nm	71 nm	6.4 nm
Fe	88.5 nm	9.5 nm	70 nm	34 nm

Table S3 : Attenuation lengths for various elements and transition edges.

With: Co L_3 edge = 778.1 eV, Co M_3 edge = 59.9 eV

And Fe L_3 edge = 706.8 eV, Fe M_3 edge = 52.7 eV

List of the different figures

List of tables

References

1. Lacheisserie, E. D. T. D. & Tremolet De Lacheisserie, E. D. *MAGNETISME : I. Fondements*. (Presses universitaires de Grenoble, 1999).
2. Baibich, M. N. *et al.* Giant Magnetoresistance of (001)Fe/(001)Cr Magnetic Superlattices. *Phys. Rev. Lett.* **61**, 2472–2475 (1988).
3. Binasch, G., Grünberg, P., Saurenbach, F. & Zinn, W. Enhanced magnetoresistance in layered magnetic structures with antiferromagnetic interlayer exchange. *Phys. Rev. B* **39**, 4828–4830 (1989).
4. Fullerton, E. E. & Childress, J. R. Spintronics, Magnetoresistive Heads, and the Emergence of the Digital World. *Proceedings of the IEEE* **104**, 1787–1795 (2016).
5. Thiaville, A., Rohart, S., Jué, É., Cros, V. & Fert, A. Dynamics of Dzyaloshinskii domain walls in ultrathin magnetic films. *EPL* **100**, 57002 (2012).
6. Parkin, S. S. P., Hayashi, M. & Thomas, L. Magnetic Domain-Wall Racetrack Memory. *Science* **320**, 190–194 (2008).
7. Boulle, O. *et al.* Room-temperature chiral magnetic skyrmions in ultrathin magnetic nanostructures. *Nature Nanotech* **11**, 449–454 (2016).
8. Woo, S. *et al.* Observation of room-temperature magnetic skyrmions and their current-driven dynamics in ultrathin metallic ferromagnets. *Nature Mater* **15**, 501–506 (2016).
9. Moreau-Luchaire, C. *et al.* Additive interfacial chiral interaction in multilayers for stabilization of small individual skyrmions at room temperature. *Nature Nanotech* **11**, 444–448 (2016).
10. Sampaio, J., Cros, V., Rohart, S., Thiaville, A. & Fert, A. Nucleation, stability and current-induced motion of isolated magnetic skyrmions in nanostructures. *Nature Nanotech* **8**, 839–844 (2013).
11. Fert, A., Cros, V. & Sampaio, J. Skyrmions on the track. *Nature Nanotech* **8**, 152–156 (2013).

12. Legrand, W. *et al.* Room-temperature stabilization of antiferromagnetic skyrmions in synthetic antiferromagnets. *Nat. Mater.* **19**, 34–42 (2020).
13. Yang, S.-H., Ryu, K.-S. & Parkin, S. Domain-wall velocities of up to 750 m s−1 driven by exchange-coupling torque in synthetic antiferromagnets. *Nature Nanotech* **10**, 221–226 (2015).
14. Joachim Stöhr & Hans Christoph Siegmann. *Magnetism: From fundamentals to nanoscale dynamics*. (Springer, 2006).
15. Baltz, V. *et al.* Antiferromagnetic spintronics. *Rev. Mod. Phys.* **90**, 015005 (2018).
16. Beaurepaire, E., Merle, J.-C., Daunois, A. & Bigot, J.-Y. Ultrafast Spin Dynamics in Ferromagnetic Nickel. *Phys. Rev. Lett.* **76**, 4250–4253 (1996).
17. Kampfrath, T. *et al.* Terahertz spin current pulses controlled by magnetic heterostructures. *Nature Nanotech* **8**, 256–260 (2013).
18. Qiu, H. *et al.* Ultrafast spin current generated from an antiferromagnet. *Nat. Phys.* **17**, 388–394 (2021).
19. Stanciu, C. D. *et al.* All-Optical Magnetic Recording with Circularly Polarized Light. *Phys. Rev. Lett.* **99**, 047601 (2007).
20. Radu, I. *et al.* Transient ferromagnetic-like state mediating ultrafast reversal of antiferromagnetically coupled spins. *Nature* **472**, 205–208 (2011).
21. Hellman, F. *et al.* Interface-induced phenomena in magnetism. *Rev. Mod. Phys.* **89**, 025006 (2017).
22. Boeglin, C. *et al.* Distinguishing the ultrafast dynamics of spin and orbital moments in solids. *Nature* **465**, 458–461 (2010).
23. Siegrist, F. *et al.* Light-wave dynamic control of magnetism. *Nature* **571**, 240–244 (2019).
24. Spencer Jeppson & Roopali Kukreja. Capturing ultrafast magnetization phenomenon using femtosecond x rays: APL Materials: Vol 9, No 10. *APL Materials* **9**, 100702 (2021).
25. Willems, F. *et al.* Optical inter-site spin transfer probed by energy and spin-resolved transient absorption spectroscopy. *Nat Commun* **11**, 871 (2020).

26. Hofherr, M. *et al.* Ultrafast optically induced spin transfer in ferromagnetic alloys. *Science Advances* (2020) doi:10.1126/sciadv.aay8717.

27. II. The Doctor's Dissertation. in *Niels Bohr Collected Works* (eds. Rosenfeld, L. & Nielsen, J. R.) vol. 1 163–393 (Elsevier, 1972).

28. Leeuwen, H.-J. van. Problèmes de la théorie électronique du magnétisme. *J. Phys. Radium* **2**, 361 (1921).

29. Kittel, C. *Introduction to solid state physics*. (John Wiley & Sons, 2005).

30. N. W. Ashcroft & N. D Mermin. *Solid State Physics*. (Saunders, 1976).

31. Legrand, W. *et al.* Modeling the Shape of Axisymmetric Skyrmions in Magnetic Multilayers. *Phys. Rev. Applied* **10**, 064042 (2018).

32. Stoner, E. C. Collective electron ferromagnetism. *Proceedings of the Royal Society of London. Series A. Mathematical and Physical Sciences* **165**, 372–414 (1938).

33. Metaxas, P. J. *et al.* Creep and Flow Regimes of Magnetic Domain-Wall Motion in Ultrathin Pt/Co/Pt Films with Perpendicular Anisotropy. *Phys. Rev. Lett.* **99**, 217208 (2007).

34. Devolder, T. *et al.* Exchange stiffness in ultrathin perpendicularly magnetized CoFeB layers determined using the spectroscopy of electrically excited spin waves. *Journal of Applied Physics* **120**, 183902 (2016).

35. Belmeguenai, M. *et al.* Exchange stiffness and damping constants in diluted CoxFeyB1-x-ythin films. *J. Phys. D: Appl. Phys.* **50**, 415003 (2017).

36. Eyrich, C. *et al.* Exchange stiffness in thin film Co alloys. *Journal of Applied Physics* **111**, 07C919 (2012).

37. Eyrich, C. *et al.* Effects of substitution on the exchange stiffness and magnetization of Co films. *Phys. Rev. B* **90**, 235408 (2014).

38. Zeeman, P. On the influence of magnetism on the nature of the light emitted by a substance. *The London, Edinburgh, and Dublin Philosophical Magazine and Journal of Science* **43**, 226–239 (1897).

39. Kittel, C. Theory of the Structure of Ferromagnetic Domains in Films and Small Particles. *Phys. Rev.* **70**, 965–971 (1946).

40. Néel, L. Anisotropie magnétique superficielle et surstructures d'orientation. *J. Phys. Radium* **15**, 225–239 (1954).

41. Gradmann, U. & Müller, J. Flat Ferromagnetic, Epitaxial 48Ni/52Fe(111) Films of few Atomic Layers. *physica status solidi (b)* **27**, 313–324 (1968).

42. Fert, A. R. Magnetic and Transport Properties of Metallic Multilayers. *Materials Science Forum* **59–60**, 439–480 (1990).

43. Carcia, P. F., Suna, A., Onn, D. G. & van Antwerp, R. Structural, magnetic, and electrical properties of thin film Pd/Co layered structures. *Superlattices and Microstructures* **1**, 101–109 (1985).

44. Carcia, P. F. Perpendicular magnetic anisotropy in Pd/Co and Pt/Co thin-film layered structures. *Journal of Applied Physics* **63**, 5066–5073 (1988).

45. van Kesteren, H. W., den Broeder, F. J. A., Bloemen, P. J. H., van Alphen, E. A. M. & de Jonge, W. J. M. Antiparallel and perpendicular magnetization alignment for Co / Ru multilayers. *Journal of Magnetism and Magnetic Materials* **102**, L9–L14 (1991).

46. Johnson, M. T., Bloemen, P. J. H., Broeder, F. J. A. den & Vries, J. J. de. Magnetic anisotropy in metallic multilayers. *Rep. Prog. Phys.* **59**, 1409–1458 (1996).

47. Dzyaloshinsky, I. A thermodynamic theory of "weak" ferromagnetism of antiferromagnetics. *Journal of Physics and Chemistry of Solids* **4**, 241–255 (1958).

48. Moriya, T. Anisotropic Superexchange Interaction and Weak Ferromagnetism. *Phys. Rev.* **120**, 91–98 (1960).

49. Fert, A. & Levy, P. M. Role of Anisotropic Exchange Interactions in Determining the Properties of Spin-Glasses. *Phys. Rev. Lett.* **44**, 1538–1541 (1980).

50. Bode, M. *et al.* Chiral magnetic order at surfaces driven by inversion asymmetry. *Nature* **447**, 190–193 (2007).

51. Ferriani, P. *et al.* Atomic-Scale Spin Spiral with a Unique Rotational Sense: Mn Monolayer on W(001). *Phys. Rev. Lett.* **101**, 027201 (2008).

52. Heide, M., Bihlmayer, G. & Blügel, S. Dzyaloshinskii-Moriya interaction accounting for the orientation of magnetic domains in ultrathin films: Fe/W(110). *Phys. Rev. B* **78**, 140403 (2008).

53. Haraldsen, J. T. & Fishman, R. S. Control of chirality normal to the interface of hexagonal magnetic and nonmagnetic layers. *Phys. Rev. B* **81**, 020404 (2010).

54. Chen, G. *et al.* Tailoring the chirality of magnetic domain walls by interface engineering. *Nat Commun* **4**, 2671 (2013).

55. Chen, G. *et al.* Novel Chiral Magnetic Domain Wall Structure in Fe/Ni/Cu(001) Films. *Phys. Rev. Lett.* **110**, 177204 (2013).

56. Legrand, W. *et al.* Spatial extent of the Dzyaloshinskii-Moriya interaction at metallic interfaces. *Phys. Rev. Materials* **6**, 024408 (2022).

57. Yu, X. Z. *et al.* Real-space observation of a two-dimensional skyrmion crystal. *Nature* **465**, 901–904 (2010).

58. Heinze, S. *et al.* Spontaneous atomic-scale magnetic skyrmion lattice in two dimensions. *Nature Phys* **7**, 713–718 (2011).

59. Mühlbauer, S. *et al.* Skyrmion Lattice in a Chiral Magnet. *Science* **323**, 915–919 (2009).

60. Jiang, W. *et al.* Blowing magnetic skyrmion bubbles. *Science* **349**, 283–286 (2015).

61. Pollard, S. D. *et al.* Observation of stable Néel skyrmions in cobalt/palladium multilayers with Lorentz transmission electron microscopy. *Nat Commun* **8**, 14761 (2017).

62. Legrand, W. *et al.* Hybrid chiral domain walls and skyrmions in magnetic multilayers. *Science Advances* (2018) doi:10.1126/sciadv.aat0415.

63. Ruderman, M. A. & Kittel, C. Indirect Exchange Coupling of Nuclear Magnetic Moments by Conduction Electrons. *Phys. Rev.* **96**, 99–102 (1954).

64. Kasuya, T. A Theory of Metallic Ferro- and Antiferromagnetism on Zener's Model. *Progress of Theoretical Physics* **16**, 45–57 (1956).

65. Yosida, K. Magnetic Properties of Cu-Mn Alloys. *Phys. Rev.* **106**, 893–898 (1957).

66. Bruno, P. & Chappert, C. Oscillatory coupling between ferromagnetic layers separated by a non-magnetic metal spacer. *Phys. Rev. Lett.* **67**, 1602–1605 (1991).

67. Bruno, P. & Chappert, C. Ruderman-Kittel theory of oscillatory interlayer exchange coupling. *Phys. Rev. B* **46**, 261–270 (1992).

68. Friedel, J. Metallic alloys. *Nuovo Cim* **7**, 287–311 (1958).

69. Anderson, P. W. Localized Magnetic States in Metals. *Phys. Rev.* **124**, 41–53 (1961).

70. Dieny, B. *et al.* Magnetotransport properties of magnetically soft spin-valve structures (invited). *Journal of Applied Physics* **69**, 4774–4779 (1991).

71. Barman, A., Mondal, S., Sahoo, S. & De, A. Magnetization dynamics of nanoscale magnetic materials: A perspective. *Journal of Applied Physics* **128**, 170901 (2020).

72. Dürr, H. A. *et al.* Chiral Magnetic Domain Structures in Ultrathin FePd Films. *Science* (1999) doi:10.1126/science.284.5423.2166.

73. Olivier Fruchart. Lectures on nanomagnetism, European School of Magnetism.

74. Nandy, A. K., Kiselev, N. S. & Blügel, S. Interlayer Exchange Coupling: A General Scheme Turning Chiral Magnets into Magnetic Multilayers Carrying Atomic-Scale Skyrmions. *Phys. Rev. Lett.* **116**, 177202 (2016).

75. Tokunaga, Y. *et al.* A new class of chiral materials hosting magnetic skyrmions beyond room temperature. *Nat Commun* **6**, 7638 (2015).

76. Legrand, W. Crafting magnetic skyrmions at room temperature : size, stability and dynamics in multilayers. (Université Paris-Saclay (ComUE), 2019).

77. Landau, L. & Lifshitz, E. 3 - On the theory of the dispersion of magnetic permeability in ferromagnetic bodies. in *Perspectives in Theoretical Physics* (ed. Pitaevski, L. P.) 51–65 (Pergamon, 1935). doi:10.1016/B978-0-08-036364-6.50008-9.

78. Gilbert, T. A phenomenological theory of damping in ferromagnetic materials. *IEEE Transactions on Magnetics* (2004) doi:10.1109/TMAG.2004.836740.

79. Stiles, M. D. & Miltat, J. Spin-Transfer Torque and Dynamics. in *Spin Dynamics in Confined Magnetic Structures III* (eds. Hillebrands, B. & Thiaville, A.) 225–308 (Springer, 2006). doi:10.1007/10938171_7.

80. Manchon, A. *et al.* Current-induced spin-orbit torques in ferromagnetic and antiferromagnetic systems. *Rev. Mod. Phys.* **91**, 035004 (2019).

81. Gambardella, P. & Miron, I. M. Current-induced spin–orbit torques. *Philosophical Transactions of the Royal Society A: Mathematical, Physical and Engineering Sciences* **369**, 3175–3197 (2011).

82. Dieny, B. & Chshiev, M. Perpendicular magnetic anisotropy at transition metal/oxide interfaces and applications. *Rev. Mod. Phys.* **89**, 025008 (2017).

83. Jhuria, K. *et al.* Spin–orbit torque switching of a ferromagnet with picosecond electrical pulses. *Nat Electron* **3**, 680–686 (2020).

84. Cubukcu, M. *et al.* Ultra-Fast Perpendicular Spin–Orbit Torque MRAM. *IEEE Transactions on Magnetics* **54**, 1–4 (2018).

85. Kimel, A. V., Kirilyuk, A., Tsvetkov, A., Pisarev, R. V. & Rasing, T. Laser-induced ultrafast spin reorientation in the antiferromagnet TmFeO3. *Nature* **429**, 850–853 (2004).

86. Gómez-Abal, R., Ney, O., Satitkovitchai, K. & Hübner, W. All-Optical Subpicosecond Magnetic Switching in NiO(001). *Phys. Rev. Lett.* **92**, 227402 (2004).

87. Gomonay, O., Baltz, V., Brataas, A. & Tserkovnyak, Y. Antiferromagnetic spin textures and dynamics. *Nature Phys* **14**, 213–216 (2018).

88. Sun, C.-K., Vallée, F., Acioli, L. H., Ippen, E. P. & Fujimoto, J. G. Femtosecond-tunable measurement of electron thermalization in gold. *Phys. Rev. B* **50**, 15337–15348 (1994).

89. Fann, W. S., Storz, R., Tom, H. W. K. & Bokor, J. Electron thermalization in gold. *Phys. Rev. B* **46**, 13592–13595 (1992).

90. Suárez, C., Bron, W. E. & Juhasz, T. Dynamics and Transport of Electronic Carriers in Thin Gold Films. *Phys. Rev. Lett.* **75**, 4536–4539 (1995).

91. Vaterlaus, A. *et al.* Different spin and lattice temperatures observed by spin-polarized photoemission with picosecond laser pulses. *Journal of Applied Physics* **67**, 5661–5663 (1990).

92. Vaterlaus, A., Beutler, T. & Meier, F. Spin-lattice relaxation time of ferromagnetic gadolinium determined with time-resolved spin-polarized photoemission. *Phys. Rev. Lett.* **67**, 3314–3317 (1991).

93. Dalla Longa, F., Kohlhepp, J. T., de Jonge, W. J. M. & Koopmans, B. Influence of photon angular momentum on ultrafast demagnetization in nickel. *Phys. Rev. B* **75**, 224431 (2007).

94. Bigot, J.-Y. Femtosecond magneto-optical processes in metals. *Comptes Rendus de l'Académie des Sciences - Series IV - Physics* **2**, 1483–1504 (2001).

95. Shim, J.-H. *et al.* Role of non-thermal electrons in ultrafast spin dynamics of ferromagnetic multilayer. *Sci Rep* **10**, 6355 (2020).

96. Illg, C., Haag, M. & Fähnle, M. Ultrafast demagnetization after laser irradiation in transition metals: Ab initio calculations of the spin-flip electron-phonon scattering with reduced exchange splitting. *Phys. Rev. B* **88**, 214404 (2013).

97. Zhang, G. P. & Hübner, W. Laser-Induced Ultrafast Demagnetization in Ferromagnetic Metals. *Phys. Rev. Lett.* **85**, 3025–3028 (2000).

98. Zhang, G. P., Bai, Y., Hübner, W., Lefkidis, G. & George, T. F. Understanding laser-induced ultrafast magnetization in ferromagnets: First-principles investigation. *Journal of Applied Physics* **103**, 07B113 (2008).

99. Bigot, J.-Y., Vomir, M. & Beaurepaire, E. Coherent ultrafast magnetism induced by femtosecond laser pulses. *Nature Phys* **5**, 515–520 (2009).

100. Kimel, A. V. *et al.* Ultrafast non-thermal control of magnetization by instantaneous photomagnetic pulses. *Nature* **435**, 655–657 (2005).

101. Kimel, A. V. *et al.* Inertia-driven spin switching in antiferromagnets. *Nature Phys* **5**, 727–731 (2009).

102. Koopmans, B., van Kampen, M., Kohlhepp, J. T. & de Jonge, W. J. M. Ultrafast Magneto-Optics in Nickel: Magnetism or Optics? *Phys. Rev. Lett.* **85**, 844–847 (2000).

103. Koopmans, B., Kampen, M. van & Jonge, W. J. M. de. Experimental access to femtosecond spin dynamics. *J. Phys.: Condens. Matter* **15**, S723–S736 (2003).

104. Beaurepaire, E. *et al.* Coherent terahertz emission from ferromagnetic films excited by femto-second laser pulses. *Appl. Phys. Lett.* **84**, 3465–3467 (2004).

105. Dewhurst, J. K., Elliott, P., Shallcross, S., Gross, E. K. U. & Sharma, S. Laser-Induced Intersite Spin Transfer. *Nano Lett.* **18**, 1842–1848 (2018).

106. Schütz, G. *et al.* Absorption of circularly polarized x rays in iron. *Phys. Rev. Lett.* **58**, 737–740 (1987).

107. Thole, B. T., Carra, P., Sette, F. & van der Laan, G. X-ray circular dichroism as a probe of orbital magnetization. *Phys. Rev. Lett.* **68**, 1943–1946 (1992).

108. Carra, P., Thole, B. T., Altarelli, M. & Wang, X. X-ray circular dichroism and local magnetic fields. *Phys. Rev. Lett.* **70**, 694–697 (1993).

109. Carva, K., Legut, D. & Oppeneer, P. M. Influence of laser-excited electron distributions on the X-ray magnetic circular dichroism spectra: Implications for femtosecond demagnetization in Ni. *EPL* **86**, 57002 (2009).

110. Eich, S. *et al.* Band structure evolution during the ultrafast ferromagnetic-paramagnetic phase transition in cobalt. *Science Advances* **3**, e1602094 (2017).

111. Teichmann, M., Frietsch, B., Döbrich, K., Carley, R. & Weinelt, M. Transient band structures in the ultrafast demagnetization of ferromagnetic gadolinium and terbium. *Phys. Rev. B* **91**, 014425 (2015).

112. Mathias, S. *et al.* Probing the timescale of the exchange interaction in a ferromagnetic alloy. *Proceedings of the National Academy of Sciences* **109**, 4792–4797 (2012).

113. Stamm, C. *et al.* Femtosecond modification of electron localization and transfer of angular momentum in nickel. *Nature Mater* **6**, 740–743 (2007).

114. Bergeard, N. *et al.* Ultrafast angular momentum transfer in multisublattice ferrimagnets. *Nat Commun* **5**, 3466 (2014).

115. Hennecke, M. *et al.* Angular Momentum Flow During Ultrafast Demagnetization of a Ferrimagnet. *Phys. Rev. Lett.* **122**, 157202 (2019).

116. Töws, W. & Pastor, G. M. Many-Body Theory of Ultrafast Demagnetization and Angular Momentum Transfer in Ferromagnetic Transition Metals. *Phys. Rev. Lett.* **115**, 217204 (2015).

117. Dornes, C. *et al.* The ultrafast Einstein–de Haas effect. *Nature* **565**, 209–212 (2019).

118. Unikandanunni, V. *et al.* Anisotropic ultrafast spin dynamics in epitaxial cobalt. *Appl. Phys. Lett.* **118**, 232404 (2021).

119. B. Frietsch, *et al.* The role of ultrafast magnon generation in the magnetization dynamics of rare-earth metals. *Sci. Adv.* **6**, eabb1601 (2020).

120. Dewhurst, J. K. *et al.* Angular momentum redistribution in laser-induced demagnetization. *Phys. Rev. B* **104**, 054438 (2021).

121. Eschenlohr, A. *et al.* Ultrafast spin transport as key to femtosecond demagnetization. *Nature Mater* **12**, 332–336 (2013).

122. Vodungbo, B. *et al.* Indirect excitation of ultrafast demagnetization. *Sci Rep* **6**, 18970 (2016).

123. Bergeard, N. *et al.* Hot-Electron-Induced Ultrafast Demagnetization in Co/Pt Multilayers. *Phys. Rev. Lett.* **117**, 147203 (2016).

124. Seifert, T. S. *et al.* Femtosecond formation dynamics of the spin Seebeck effect revealed by terahertz spectroscopy. *Nat Commun* **9**, 2899 (2018).

125. Gort, R. *et al.* Early Stages of Ultrafast Spin Dynamics in a 3d Ferromagnet. *Phys. Rev. Lett.* **121**, 087206 (2018).

126. Cardin, V. *et al.* Wavelength scaling of ultrafast demagnetization in Co/Pt multilayers. *Phys. Rev. B* **101**, 054430 (2020).

127. Chekhov, A. L. *et al.* Ultrafast Demagnetization of Iron Induced by Optical versus Terahertz Pulses. *Phys. Rev. X* **11**, 041055 (2021).

128. Krauß, M., Aeschlimann, M. & Schneider, H. C. Ultrafast Spin Dynamics Including Spin-Orbit Interaction in Semiconductors. *Phys. Rev. Lett.* **100**, 256601 (2008).

129. Krauß, M. *et al.* Ultrafast demagnetization of ferromagnetic transition metals: The role of the Coulomb interaction. *Phys. Rev. B* **80**, 180407 (2009).

130. Carpene, E. *et al.* Dynamics of electron-magnon interaction and ultrafast demagnetization in thin iron films. *Phys. Rev. B* **78**, 174422 (2008).

131. Mueller, B. Y. *et al.* Feedback Effect during Ultrafast Demagnetization Dynamics in Ferromagnets. *Phys. Rev. Lett.* **111**, 167204 (2013).

132. Steiauf, D. & Fähnle, M. Elliott-Yafet mechanism and the discussion of femtosecond magnetization dynamics. *Phys. Rev. B* **79**, 140401 (2009).

133. Koopmans, B., Ruigrok, J. J. M., Longa, F. D. & de Jonge, W. J. M. Unifying Ultrafast Magnetization Dynamics. *Phys. Rev. Lett.* **95**, 267207 (2005).

134. Pickel, M. *et al.* Spin-Orbit Hybridization Points in the Face-Centered-Cubic Cobalt Band Structure. *Phys. Rev. Lett.* **101**, 066402 (2008).

135. Schaack, G. Observation of circularly polarized phonon states in an external magnetic field. *J. Phys. C: Solid State Phys.* **9**, L297–L301 (1976).

136. Koopmans, B. *et al.* Explaining the paradoxical diversity of ultrafast laser-induced demagnetization. *Nature Mater* **9**, 259–265 (2010).

137. Carva, K., Battiato, M., Legut, D. & Oppeneer, P. M. Ab initio theory of electron-phonon mediated ultrafast spin relaxation of laser-excited hot electrons in transition-metal ferromagnets. *Phys. Rev. B* **87**, 184425 (2013).

138. Schellekens, A. J. & Koopmans, B. Comparing Ultrafast Demagnetization Rates Between Competing Models for Finite Temperature Magnetism. *Phys. Rev. Lett.* **110**, 217204 (2013).

139. Carva, K., Battiato, M. & Oppeneer, P. M. Ab Initio Investigation of the Elliott-Yafet Electron-Phonon Mechanism in Laser-Induced Ultrafast Demagnetization. *Phys. Rev. Lett.* **107**, 207201 (2011).

140. Turgut, E. *et al.* Stoner versus Heisenberg: Ultrafast exchange reduction and magnon generation during laser-induced demagnetization. *Phys. Rev. B* **94**, 220408 (2016).

141. Carpene, E., Hedayat, H., Boschini, F. & Dallera, C. Ultrafast demagnetization of metals: Collapsed exchange versus collective excitations. *Phys. Rev. B* **91**, 174414 (2015).

142. Atxitia, U., Chubykalo-Fesenko, O., Walowski, J., Mann, A. & Münzenberg, M. Evidence for thermal mechanisms in laser-induced femtosecond spin dynamics. *Phys. Rev. B* **81**, 174401 (2010).

143. Haag, M., Illg, C. & Fähnle, M. Theory of scattering of crystal electrons at magnons. *Phys. Rev. B* **87**, 214427 (2013).

144. Knut, R. *et al. Inhomogeneous magnon scattering during ultrafast demagnetization*. http://arxiv.org/abs/1810.10994 (2018) doi:10.48550/arXiv.1810.10994.

145. Beens, M., Duine, R. A. & Koopmans, B. Modeling ultrafast demagnetization and spin transport: The interplay of spin-polarized electrons and thermal magnons. *Phys. Rev. B* **105**, 144420 (2022).

146. Malinowski, G. *et al.* Control of speed and efficiency of ultrafast demagnetization by direct transfer of spin angular momentum. *Nature Phys* **4**, 855–858 (2008).

147. Battiato, M., Carva, K. & Oppeneer, P. M. Superdiffusive Spin Transport as a Mechanism of Ultrafast Demagnetization. *Phys. Rev. Lett.* **105**, 027203 (2010).

148. Battiato, M., Carva, K. & Oppeneer, P. M. Theory of laser-induced ultrafast superdiffusive spin transport in layered heterostructures. *Phys. Rev. B* **86**, 024404 (2012).

149. Schönhense, G. & Siegmann, H. C. Transmission of electrons through ferromagnetic material and applications to detection of electron spin polarization. *Annalen der Physik* **505**, 465–474 (1993).

150. Aeschlimann, M. *et al.* Ultrafast Spin-Dependent Electron Dynamics in fcc Co. *Phys. Rev. Lett.* **79**, 5158–5161 (1997).

151. Wieczorek, J. *et al.* Separation of ultrafast spin currents and spin-flip scattering in Co/Cu(001) driven by femtosecond laser excitation employing the complex magneto-optical Kerr effect. *Phys. Rev. B* **92**, 174410 (2015).

152. Schellekens, A. J., Kuiper, K. C., de Wit, R. R. J. C. & Koopmans, B. Ultrafast spin-transfer torque driven by femtosecond pulsed-laser excitation. *Nat Commun* **5**, 4333 (2014).

153. Chen, J. *et al.* Competing Spin Transfer and Dissipation at Co/Cu(001) Interfaces on Femtosecond Timescales. *Phys. Rev. Lett.* **122**, 067202 (2019).

154. Chardonnet, V. *et al.* Toward ultrafast magnetic depth profiling using time-resolved x-ray resonant magnetic reflectivity. *Structural Dynamics* **8**, 034305 (2021).

155. Chardonnet, V. Etude du role des interfaces dans la desaimantation ultrarapide. (Sorbonne université, 2018).

156. Hofherr, M. *et al.* Speed and efficiency of femtosecond spin current injection into a nonmagnetic material. *Phys. Rev. B* **96**, 100403 (2017).

157. Melnikov, A. *et al.* Ultrafast Transport of Laser-Excited Spin-Polarized Carriers in Au/Fe/MgO(001). *Phys. Rev. Lett.* **107**, 076601 (2011).

158. Rudolf, D. *et al.* Ultrafast magnetization enhancement in metallic multilayers driven by superdiffusive spin current. *Nat Commun* **3**, 1037 (2012).

159. Turgut, E. *et al.* Controlling the Competition between Optically Induced Ultrafast Spin-Flip Scattering and Spin Transport in Magnetic Multilayers. *Phys. Rev. Lett.* **110**, 197201 (2013).

160. Razdolski, I. *et al.* Analysis of the time-resolved magneto-optical Kerr effect for ultrafast magnetization dynamics in ferromagnetic thin films. *J. Phys.: Condens. Matter* **29**, 174002 (2017).

161. Groeneveld, R. H. M., Sprik, R. & Lagendijk, A. Femtosecond spectroscopy of electron-electron and electron-phonon energy relaxation in Ag and Au. *Phys. Rev. B* **51**, 11433–11445 (1995).

162. Elsayed-Ali, H. E., Norris, T. B., Pessot, M. A. & Mourou, G. A. Time-resolved observation of electron-phonon relaxation in copper. *Phys. Rev. Lett.* **58**, 1212–1215 (1987).

163. Kabanov, V. V. Electron-electron and electron-phonon relaxation in metals excited by optical pulse. *Low Temperature Physics* **46**, 414–419 (2020).

164. Shim, J.-H. *et al.* Ultrafast dynamics of exchange stiffness in Co/Pt multilayer. *Commun Phys* **3**, 1–8 (2020).

165. Atxitia, U. *et al.* Multiscale modeling of magnetic materials: Temperature dependence of the exchange stiffness. *Phys. Rev. B* **82**, 134440 (2010).

166. Moreno, R. *et al.* Temperature-dependent exchange stiffness and domain wall width in Co. *Phys. Rev. B* **94**, 104433 (2016).

167. Roth, T. *et al.* Temperature Dependence of Laser-Induced Demagnetization in Ni: A Key for Identifying the Underlying Mechanism. *Phys. Rev. X* **2**, 021006 (2012).

168. Wang, F. *et al.* Magnetization relaxation dynamics in [Co/Pt]3 multilayers on pico- and nanosecond timescales. *Phys. Rev. Research* **3**, 033061 (2021).

169. Pfau, B. *et al.* Ultrafast optical demagnetization manipulates nanoscale spin structure in domain walls. *Nat Commun* **3**, 1100 (2012).

170. Miron, I. M. *et al.* Fast current-induced domain-wall motion controlled by the Rashba effect. *Nature Mater* **10**, 419–423 (2011).

171. Vogt, K. *et al.* All-optical detection of phase fronts of propagating spin waves in a Ni81Fe19 microstripe. *Appl. Phys. Lett.* **95**, 182508 (2009).

172. Zusin, D. *et al.* Ultrafast domain dilation induced by optical pumping in ferromagnetic CoFe/Ni multilayers. *arXiv:2001.11719 [cond-mat]* (2020).

173. Vodungbo, B. *et al.* Laser-induced ultrafast demagnetization in the presence of a nanoscale magnetic domain network. *Nat Commun* **3**, 999 (2012).

174. Hennes, M. *et al.* Laser-induced ultrafast demagnetization and perpendicular magnetic anisotropy reduction in a Co88Tb12 thin film with stripe domains. *Phys. Rev. B* **102**, 174437 (2020).

175. Faraday, M. S. (Great B. On the magnetization of light and the illumination of magnetic lines of force c. 1. https://library.si.edu/digital-library/book/onmagnetizationo01fara (1846).

176. Bloch, F. On the Magnetic Scattering of Neutrons. *Phys. Rev.* **50**, 259–260 (1936).

177. Schwinger, J. S. On the Magnetic Scattering of Neutrons. *Phys. Rev.* **51**, 544–552 (1937).

178. Halpern, O. & Johnson, M. H. On the Theory of Neutron Scattering by Magnetic Substances. *Phys. Rev.* **51**, 992–992 (1937).

179. Broglie, M. de. Recherches sur la diffraction des rayons de Röntgen par les milieux cristallins. *Radium (Paris)* **10**, 245–249 (1913).

180. Compton, K. T. & Trousdale, E. A. The Nature of the Ultimate Magnetic Particle. *Phys. Rev.* **5**, 315–318 (1915).

181. Compton, A. H. & Rognley, O. Is the Atom the Ultimate Magnetic Particle? *Phys. Rev.* **16**, 464–476 (1920).

182. Yensen, T. D. Evidence Obtained by X-Ray Analysis of Films of Iron in Magnetic Fields as to the Ultimate Nature of Magnetism. *Phys. Rev.* **32**, 114–123 (1928).

183. Platzman, P. M. & Tzoar, N. Magnetic Scattering of X Rays from Electrons in Molecules and Solids. *Phys. Rev. B* **2**, 3556–3559 (1970).

184. De Bergevin, F. & Brunel, M. Observation of magnetic superlattice peaks by X-ray diffraction on an antiferromagnetic NiO crystal. *Physics Letters A* **39**, 141–142 (1972).

185. Hubbell, J. H., Gimm, H. A. & Overbo, I. Pair, Triplet, and Total Atomic Cross Sections (and Mass Attenuation Coefficients) for 1 MeV-100 GeV Photons in Elements Z=1 to 100. *Journal of Physical and Chemical Reference Data* **9**, 1023–1148 (1980).

186. Compton, A. H. Scattering of X-Rays by a Spinning Electron. *Phys. Rev.* **50**, 878–881 (1936).

187. Blume, M. & Gibbs, D. Polarization dependence of magnetic x-ray scattering. *Phys. Rev. B* **37**, 1779–1789 (1988).

188. Blume, M. Magnetic scattering of x rays (invited). *Journal of Applied Physics* **57**, 3615–3618 (1985).

189. Stirling, W. G. & Cooper, M. J. X-ray magnetic scattering. *Journal of Magnetism and Magnetic Materials* **200**, 755–773 (1999).

190. Hannon, J. P., Trammell, G. T., Blume, M. & Gibbs, D. X-Ray Resonance Exchange Scattering. *Phys. Rev. Lett.* **62**, 2644–2644 (1989).

191. Chauleau, J.-Y. *et al.* Electric and antiferromagnetic chiral textures at multiferroic domain walls. *Nat. Mater.* **19**, 386–390 (2020).

192. Stojić, N., Binggeli, N. & Altarelli, M. Mn L2,3 edge resonant x-ray scattering in manganites: Influence of the magnetic state. *Phys. Rev. B* **72**, 104108 (2005).

193. Materlik, G., Sparks, C. J. & Fischer, K. *Resonant anomalous X-ray scattering : theory and applications*. (Elsevier Science Ltd, 1994).

194. Elzo, M. *et al.* X-ray resonant magnetic reflectivity of stratified magnetic structures: Eigenwave formalism and application to a W/Fe/W trilayer. *Journal of Magnetism and Magnetic Materials* **324**, 105–112 (2012).

195. Flewett, S. *et al.* General treatment of off-specular resonant soft x-ray magnetic scattering using the distorted-wave Born approximation: Numerical algorithm and experimental studies with hybrid chiral domain structures. *Phys. Rev. B* **103**, 184401 (2021).

196. Parratt, L. G. Surface Studies of Solids by Total Reflection of X-Rays. *Phys. Rev.* **95**, 359–369 (1954).

197. Bourzami, A., Lenoble, O., Féry, Ch., Bobo, J. F. & Piecuch, M. Enhancement of polar Kerr rotation in Fe/Al2O3 multilayers and composite systems. *Phys. Rev. B* **59**, 11489–11494 (1999).

198. Zak, J., Moog, E. R., Liu, C. & Bader, S. D. Magneto-optics of multilayers with arbitrary magnetization directions. *Phys. Rev. B* **43**, 6423–6429 (1991).

199. Mansuripur, M. Analysis of multilayer thin-film structures containing magneto-optic and anisotropic media at oblique incidence using 2×2 matrices. *Journal of Applied Physics* **67**, 6466–6475 (1990).

200. Elder, F. R., Gurewitsch, A. M., Langmuir, R. V. & Pollock, H. C. Radiation from Electrons in a Synchrotron. *Phys. Rev.* **71**, 829–830 (1947).

201. Iwanenko, D. & Pomeranchuk, I. On the Maximal Energy Attainable in a Betatron. *Phys. Rev.* **65**, 343–343 (1944).

202. Rowe, E. M. & Mills, F. E. Tantalus. 1. A Dedicated Storage Ring Synchrotron Radiation source. *Part. Accel.* **4**, 211–227 (1973).

203. History. *Lightsources.org* https://lightsources.org/history/ (2017).

204. Balerna, A. & Mobilio, S. Introduction to Synchrotron Radiation. in *Synchrotron Radiation: Basics, Methods and Applications* (eds. Mobilio, S., Boscherini, F. & Meneghini, C.) 3–28 (Springer, 2015). doi:10.1007/978-3-642-55315-8_1.

205. David T. Attwood. *Soft X-Ray and EUV Radiation*. (Cambridge University Press, 1999).

206. Sasaki, S. *et al.* Design of a new type of planar undulator for generating variably polarized radiation. *Nuclear Instruments and Methods in Physics Research Section A: Accelerators, Spectrometers, Detectors and Associated Equipment* **331**, 763–767 (1993).

207. Chiuzbăian, S. G. *et al.* Design and performance of AERHA, a high acceptance high resolution soft x-ray spectrometer. *Review of Scientific Instruments* **85**, 043108 (2014).

208. Sacchi, M. *et al.* The SEXTANTS beamline at SOLEIL: a new facility for elastic, inelastic and coherent scattering of soft X-rays. *J. Phys.: Conf. Ser.* **425**, 072018 (2013).

209. Popescu, H. *et al.* COMET: a new end-station at SOLEIL for coherent magnetic scattering in transmission. *J Synchrotron Rad* **26**, 280–290 (2019).

210. Jaouen, N. *et al.* An apparatus for temperature-dependent soft X-ray resonant magnetic scattering. *J Synchrotron Rad* **11**, 353–357 (2004).

211. Sacchi, M. *et al.* IRMA-2 at SOLEIL: a set-up for magnetic and coherent scattering of polarized soft x-rays. *J. Phys.: Conf. Ser.* **425**, 202009 (2013).

212. Abualrob, H. *et al.* Horizontal Emittance Reduction on a Synchrotron Radiation Light Source with a Robinson Wiggler. *arXiv:1806.09354 [physics]* (2018).

213. Madey, J. M. J. Stimulated Emission of Bremsstrahlung in a Periodic Magnetic Field. *Journal of Applied Physics* **42**, 1906–1913 (1971).

214. Deacon, D. A. G. *et al.* First Operation of a Free-Electron Laser. *Phys. Rev. Lett.* **38**, 892–894 (1977).

215. Schmüser, P., Dohlus, M., Rossbach, J. & Behrens, C. One-Dimensional Theory of the High-Gain FEL. in *Free-Electron Lasers in the Ultraviolet and X-Ray Regime: Physical Principles, Experimental Results, Technical Realization* (eds. Schmüser, P., Dohlus, M., Rossbach, J. & Behrens, C.) 39–61 (Springer International Publishing, 2014). doi:10.1007/978-3-319-04081-3_4.

216. Amann, J. *et al.* Demonstration of self-seeding in a hard-X-ray free-electron laser. *Nature Photon* **6**, 693–698 (2012).

217. Lambert, G. *et al.* Injection of harmonics generated in gas in a free-electron laser providing intense and coherent extreme-ultraviolet light. *Nature Phys* **4**, 296–300 (2008).

218. Capotondi, F. *et al.* Multipurpose end-station for coherent diffraction imaging and scattering at FERMI@Elettra free-electron laser facility. *J Synchrotron Rad* **22**, 544–552 (2015).

219. Allaria, E. *et al.* Control of the Polarization of a Vacuum-Ultraviolet, High-Gain, Free-Electron Laser. *Phys. Rev. X* **4**, 041040 (2014).

220. van der Laan, G. Soft X-ray resonant magnetic scattering of magnetic nanostructures. *Comptes Rendus Physique* **9**, 570–584 (2008).

221. Dudzik, E. *et al.* Influence of perpendicular magnetic anisotropy on closure domains studied with x-ray resonant magnetic scattering. *Phys. Rev. B* **62**, 5779–5785 (2000).

222. Chauleau, J.-Y. *et al.* Chirality in Magnetic Multilayers Probed by the Symmetry and the Amplitude of Dichroism in X-Ray Resonant Magnetic Scattering. *Phys. Rev. Lett.* **120**, 037202 (2018).

223. Zhang, S. L., van der Laan, G. & Hesjedal, T. Direct experimental determination of the topological winding number of skyrmions in Cu2OSeO3. *Nat Commun* **8**, 14619 (2017).

224. Fert, A., Reyren, N. & Cros, V. Magnetic skyrmions: advances in physics and potential applications. *Nat Rev Mater* **2**, 1–15 (2017).

225. Bloemen, P. J. H., van Kesteren, H. W., Swagten, H. J. M. & de Jonge, W. J. M. Oscillatory interlayer exchange coupling in Co/Ru multilayers and bilayers. *Phys. Rev. B* **50**, 13505–13514 (1994).

226. den Broeder, F. J. A., Hoving, W. & Bloemen, P. J. H. Magnetic anisotropy of multilayers. *Journal of Magnetism and Magnetic Materials* **93**, 562–570 (1991).

227. Léveillé, C. *et al.* Chiral spin spiral in synthetic antiferromagnets probed by circular dichroism in x-ray resonant magnetic scattering. *Phys. Rev. B* **104**, L060402 (2021).

228. Tonnerre, J. M. *et al.* Soft X-Ray Resonant Magnetic Scattering from a Magnetically Coupled Ag/Ni Multilayer. *Phys. Rev. Lett.* **75**, 740–743 (1995).

229. Spezzani, C. *et al.* Hysteresis curves of ferromagnetic and antiferromagnetic order in metallic multilayers by resonant x-ray scattering. *Phys. Rev. B* **66**, 052408 (2002).

230. Iwata-Harms, J. M. *et al.* High-temperature thermal stability driven by magnetization dilution in CoFeB free layers for spin-transfer-torque magnetic random access memory. *Sci Rep* **8**, 14409 (2018).

231. Zhou, Y., Mansell, R., Valencia, S., Kronast, F. & van Dijken, S. Temperature dependence of the Dzyaloshinskii-Moriya interaction in ultrathin films. *Phys. Rev. B* **101**, 054433 (2020).

232. Kundu, A. & Zhang, S. Temperature dependence of RKKY interaction. *Journal of Magnetism and Magnetic Materials* **393**, 331–333 (2015).

233. Li, Y. *et al.* Temperature-dependent interlayer exchange coupling strength in synthetic antiferromagnetic [Pt/Co] 2/Ru/[Co/Pt]4 multilayers. *Chinese Phys. B* **27**, 127502 (2018).

234. Meckler, S. *et al.* Real-Space Observation of a Right-Rotating Inhomogeneous Cycloidal Spin Spiral by Spin-Polarized Scanning Tunneling Microscopy in a Triple Axes Vector Magnet. *Phys. Rev. Lett.* **103**, 157201 (2009).

235. Nembach, H. T., Shaw, J. M., Weiler, M., Jué, E. & Silva, T. J. Linear relation between Heisenberg exchange and interfacial Dzyaloshinskii–Moriya interaction in metal films. *Nature Phys* **11**, 825–829 (2015).

236. Kim, S. *et al.* Correlation of the Dzyaloshinskii–Moriya interaction with Heisenberg exchange and orbital asphericity. *Nat Commun* **9**, 1648 (2018).

237. Hirsch, J. E. Spin Hall Effect. *Phys. Rev. Lett.* **83**, 1834–1837 (1999).

238. Ajejas, F. *et al.* Interfacial potential gradient modulates Dzyaloshinskii-Moriya interaction in Pt/Co/metal multilayers. *Phys. Rev. Materials* **6**, L071401 (2022).

239. Tonnerre, J. M. *et al.* Depth Magnetization Profile of a Perpendicular Exchange Coupled System by Soft-X-Ray Resonant Magnetic Reflectivity. *Phys. Rev. Lett.* **100**, 157202 (2008).

240. Vansteenkiste, A. *et al.* The design and verification of MuMax3. *AIP Advances* **4**, 107133 (2014).

241. Ajejas, F. *et al.* Tuning domain wall velocity with Dzyaloshinskii-Moriya interaction. *Appl. Phys. Lett.* **111**, 202402 (2017).

242. Bak, P., Tang, C. & Wiesenfeld, K. Self-organized criticality: An explanation of the 1/f noise. *Phys. Rev. Lett.* **59**, 381–384 (1987).

243. Zimmermann, B. *et al.* Dzyaloshinskii-Moriya interaction at disordered interfaces from ab initio theory: Robustness against intermixing and tunability through dusting. *Appl. Phys. Lett.* **113**, 232403 (2018).

244. Kerber, N. *et al.* Faster chiral versus collinear magnetic order recovery after optical excitation revealed by femtosecond XUV scattering. *Nat Commun* **11**, 6304 (2020).

245. Mahieu, B. *et al.* Probing warm dense matter using femtosecond X-ray absorption spectroscopy with a laser-produced betatron source. *Nat Commun* **9**, 3276 (2018).

246. Viret, M. *et al.* Spin scattering in ferromagnetic thin films. *Phys. Rev. B* **53**, 8464–8468 (1996).

247. Vanhaverbeke, A. & Viret, M. Simple model of current-induced spin torque in domain walls. *Phys. Rev. B* **75**, 024411 (2007).

248. Waintal, X. & Viret, M. Current-induced distortion of a magnetic domain wall. *EPL* **65**, 427 (2004).

249. Schlotter, S., Agrawal, P. & Beach, G. S. D. Temperature dependence of the Dzyaloshinskii-Moriya interaction in Pt/Co/Cu thin film heterostructures. *Appl. Phys. Lett.* **113**, 092402 (2018).

250. Zhang, Y. *et al.* Direct observation of the temperature dependence of the Dzyaloshinskii–Moriya interaction. *J. Phys. D: Appl. Phys.* **55**, 195304 (2022).

251. Lemesh, I., Büttner, F. & Beach, G. S. D. Accurate model of the stripe domain phase of perpendicularly magnetized multilayers. *Phys. Rev. B* **95**, 174423 (2017).

252. Lambert, C.-H. *et al.* All-optical control of ferromagnetic thin films and nanostructures. *Science* **345**, 1337–1340 (2014).

253. Léveillé, C. *et al.* Single-shot experiments at the soft X-FEL FERMI using a back-side-illuminated scientific CMOS detector. *J Synchrotron Rad* **29**, 103–110 (2022).

254. Léveillé, C. *et al.* Ultrafast time-evolution of chiral Néel magnetic domain walls probed by circular dichroism in x-ray resonant magnetic scattering. *Nat Commun* **13**, 1412 (2022).

255. Maccariello, D. *et al.* Electrical Signature of Noncollinear Magnetic Textures in Synthetic Antiferromagnets. *Phys. Rev. Applied* **14**, 051001 (2020).

256. Hill, J. P. & McMorrow, D. F. Resonant Exchange Scattering: Polarization Dependence and Correlation Function. *Acta Cryst A* **52**, 236–244 (1996).

257. Henke, B. L., Gullikson, E. M. & Davis, J. C. X-Ray Interactions: Photoabsorption, Scattering, Transmission, and Reflection at E = 50-30,000 eV, Z = 1-92. *Atomic Data and Nuclear Data Tables* **54**, 181–342 (1993).

Résumé étendu en français

Pendant ce travail doctoral, l'évolution en champ et/ou résolue en temps de différentes textures magnétiques ont été étudiées par diffusion magnétique résonante des rayons X (XRMS). La XRMS donne accès au type et au sens de l'enroulement de l'aimantation dans les parois de domaines (DW) par le motif dichroïque dans le signal diffracté hors du spéculaire. Le sens de l'enroulement de l'aimantation correspond à la chiralité magnétique (sens horaire, CW ou anti horaire, CCW) et le type d'enroulement indique la rotation cycloïdale (Néel) ou hélicoïdale (Bloch) du moment angulaire de spin dans les DWs. Cette information peut être trouvée dans le profile ortho-radiale de l'image DIFFERENCE des polarisations circulaires gauche et droite.

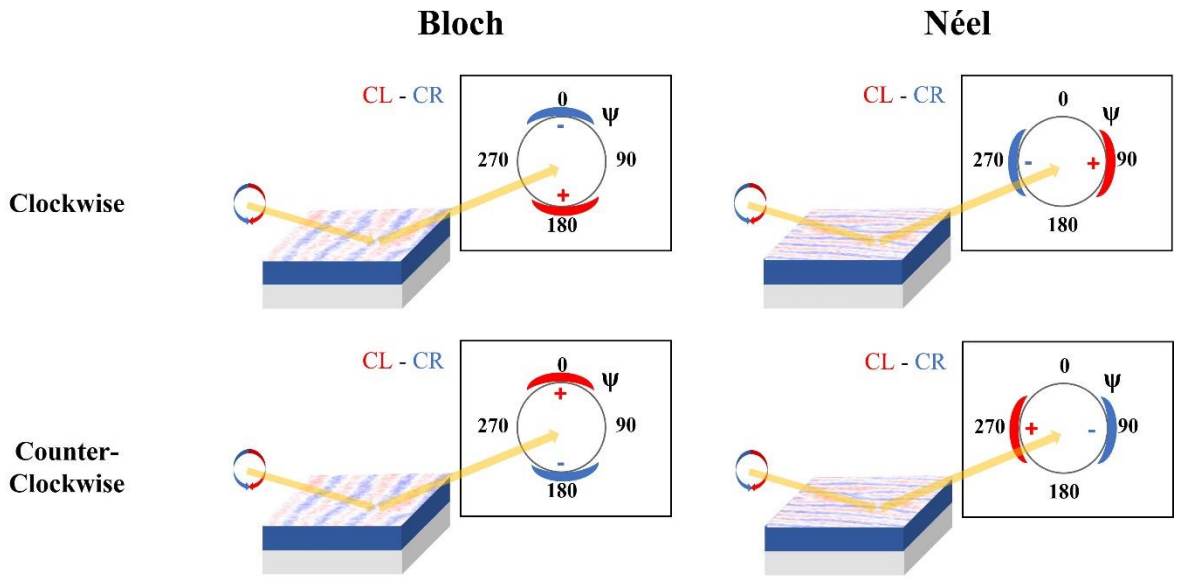

Figure R1 : Motifs dichroïques de diffraction pour différents types et chiralités magnétiques des DWs

L'intensité du signal diffractée est obtenue par intégration radiale des images DIFFERENCE (CL – CR) et SOMME (CL + CR). L'intensité de l'image DIFFERENCE est liée à l'interférence des composantes de l'aimantation situées hors et dans le plan de diffusion, défini par les vecteurs d'ondes incidents et partants des photons. Dans un état magnétique avec des domaines, le signal SOMME est dominé par la composante de l'aimantation hors du plan de l'échantillon (OOP), que l'on peut assigner aux domaines. Le signal DIFFERENCE provient de l'interférence de l'aimantations des domaines et des parois de domaine. La comparaison de l'évolution temporelle des signaux de SOMME et DIFFERENCE donne une information qualitative sur le comportement relatif des DWs et des domaines. L'expérience a été réalisée en géométrie de réflexion. A cause de la projection géométrique du faisceau incident, la réflexion spéculaire se superpose au signal magnétique diffracté hors du spéculaire. Cela est particulièrement vrai pour l'image SOMME. Par conséquent, une code python a été développé pour

simuler et soustraire le signal spéculaire, qui par ailleurs peut être plus important que le signal magnétique pour les faibles angles d'incidence.

Le formalisme de la XRMS est présenté dans le chapitre 2 en considérant une seule couche magnétique. La XRMS est également valable dans les multicouches FM, comme montré expérimentalement par Chauleau *et al*.[1] La différence est que chaque couche magnétique réémet une partie du rayonnement incident. Les différents faisceaux interférents entre eux mais leur somme est tout de même dominée par les couches plus en surface du fait de leur plus faible atténuation. Dans les multicouches FM, l'interférence constructive est obtenue au pic de Bragg de la multicouche car les périodicités magnétique et chimique sont égales. Par conséquent, les images de XRMS sur les multicouches FM sont effectuées à un angle correspondant à un multiple entier de la périodicité chimique dans l'espace réciproque. Le fait de pouvoir moduler les interactions magnétiques dans les multicouches a motivé les recherches pour trouver les compositions optimales pour différentes applications. Dans la spintronique, un objectif est d'utiliser des textures de spin très petite pour coder l'information pour des dispositifs de stockage de données. Les skyrmions magnétiques sont de bons candidats pour réaliser cet objectif car ils peuvent être aussi petit que quelques nanomètres. Des skyrmion magnétique isolées ont été stabilisés dans des multicouches FM mais à cause de leur texture de spin qui s'enroule, ils subissent une force latérale à leur direction de déplacement quand ils sont contrôlés électriquement. Cet enroulement est aussi responsable de leur plus grande stabilité par rapport aux DWs. Cette propriété est appelée protection topologique. Un moyen d'annulé la force transverse serait de nucléer des skyrmions magnétiques dans des échantillons antiferromagnétiques de synthèse (SAF). Les SAFs sont des multicouches composées de couches FM couplées antiferromagnetiquement (AFM) entre elles. Pour l'étude par XRMS de ce type de multicouche, l'angle d'incidence des rayons X doit correspondre à un multiple impair et demi entier du pic de Bragg dans l'espace réciproque. En effet, la périodicité magnétique est deux fois plus grande que la périodicité chimique dans l'espace réel du fait du couplage AFM. Une interférence constructive du signal magnétique est obtenu pour un multiple impair et demi entier du pic de Bragg alors qu'une interference destructive est obtenu pour un multiple entier du pic de Bragg comme montré dans la figure R2.

Dans ce travail de thèse, les échantillons SAF ont été conçus pour stabiliser une texture en spirale de spin à température ambiante (RT). Cette texture correspond à une rotation sinusoïdale de l'aimantation. La périodicité de la spirale de spin donne une indication sur le rapport entre l'énergie d'échange et l'interaction Dzyaloshinskii-Moriya (DMI) dans le cas où le champ dipolaire est négligeable tout comme l'anisotropie effective, ce qui est le cas ici. La dépendance en température du signal XRMS d'échantillons SAF avec différentes répétitions de la multicouche indique que le ratio échange-DMI ne change pas en température. Ensuite, la variation angulaire des signaux de SOMME et DIFFERENCE à température ambiante a été effectuée à température ambiante. La variation de l'angle d'incidence vers des valeurs plus élevées augmente la profondeur sondée par les rayons X mais diminue la périodicité des interférences observées dans l'espace réel. Par conséquent, la variation d'intensité du signal XRMS dépend de la structure 3D de la texture du spin mais aussi des effets d'interférences.

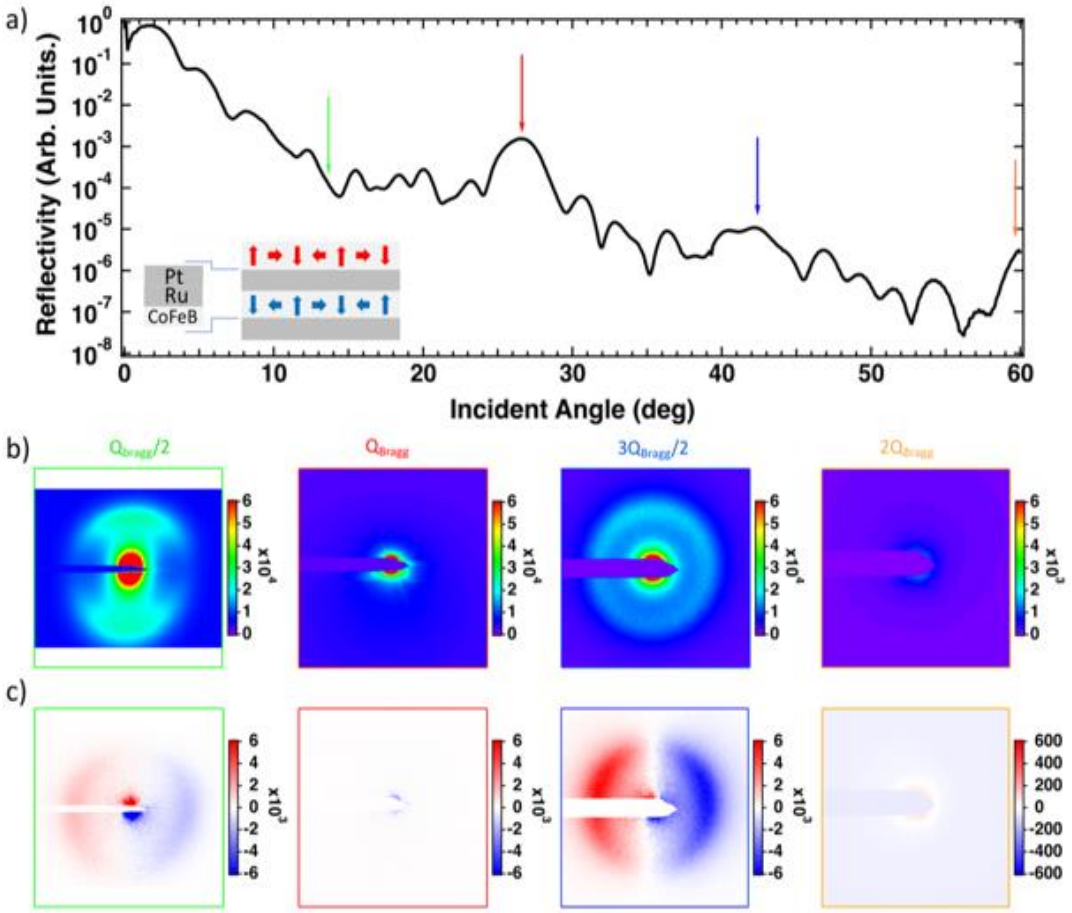

Figure R2 : (a) Courbe de réflectivité X effectuée sur un échantillon SAF avec8 répétitions à température ambiante et au seuil L_3 (707 eV) du Fer en utilisant une lumière polarisée circulairement. Les flèches verticales indiquent l'angle utilisé pour chaque paire d'images prise avec deux lumières polarisées circulairement. Les flèches rouges et oranges pointent vers les angles correspondant aux multiples entiers du pic de Bragg alors que les flèches verte et bleue sont placées aux multiples demi entier impairs de la multicouche. (b) Images SOMME (CL + CR) corrigées de la projection géométrique correspondant aux flèches sur la courbe de réflectivité. (c) Images DIFFERENCE corrigées de la projection géométrique alignées verticalement avec les images SOMME correspondantes.

Pour simuler cette dépendance, un programme prenant comme donnée d'entrée les simulations micromagnétiques des différentes couches magnétiques a été développé par S. Flewett *et al.*[2] pour simuler les signaux dans et hors du spéculaire. Ce programme est capable de reproduire la variation angulaire des signaux XRMS atour du premier demi pic de Bragg ($Q_{Bragg}/2$) mais n'a pas été capable de bien reproduire celle à $3Q_{Bragg}/2$ car la rugosité n'est pas encore prise en compte.

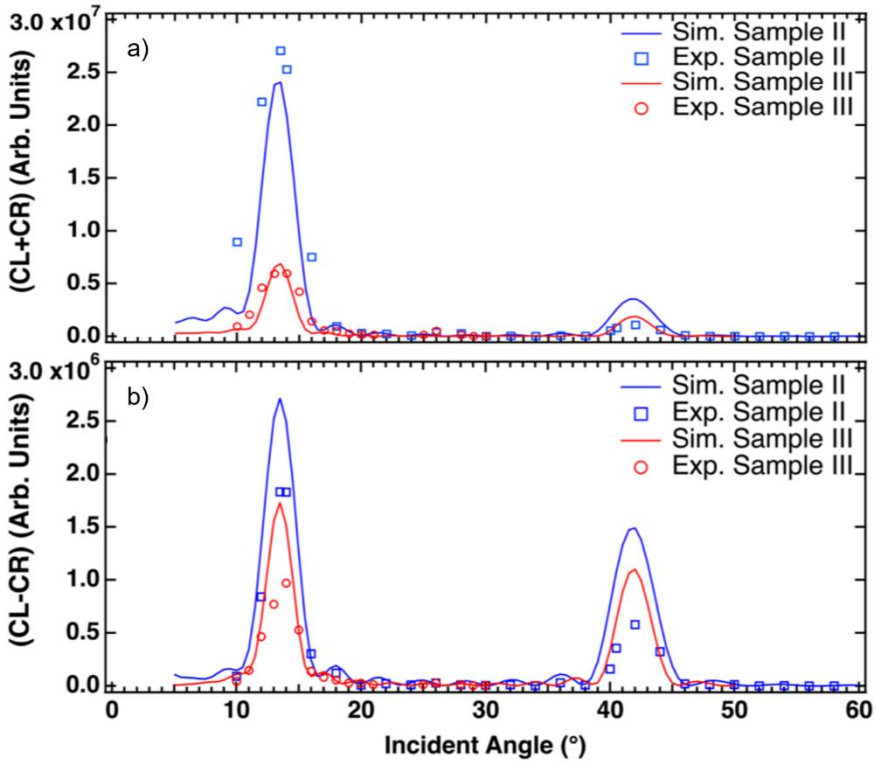

Figure R3: Les graphiques (a) et (b) montrent les simulations (lignes) et les points expérimentaux (points) de l'intensité des signaux SOMME (CL + CR) et DIFFERENCE (CL – CR) pour le SAF 8 répétitions (bleu) et 10 répétitions (rouge). Les points expérimentaux comme les simulations ont été réalisées à une énergie de photon de 707 eV.

Cette méthode ouvre la voie vers la reconstruction 3D de texture de spin avec la XRMS qui idéalement a une résolution spatiale seulement limitée par la longueur d'onde (c'est-à-dire quelques nm dans la gamme des rayons X mous). Cela a été fait pour la première fois par Flewett *et al.*[2] Qui ont réussi à reproduire la variation du signal en angle et en champ dans un échantillon avec une chiralité Néel hybride avec entre les deux une partie Bloch dans la direction verticale. Plus spécifiquement, l'évolution de la profondeur de cette partie Bloch en fonction du champ magnétique appliqué a été réalisée. La chiralité Néel hybride dans la direction verticale peut être stabilisé dans des échantillons FM par la fermeture des boucles de champ démagnétisant qui favorise un chiralité Néel CW près de la surface et Néel CCW en profondeur.

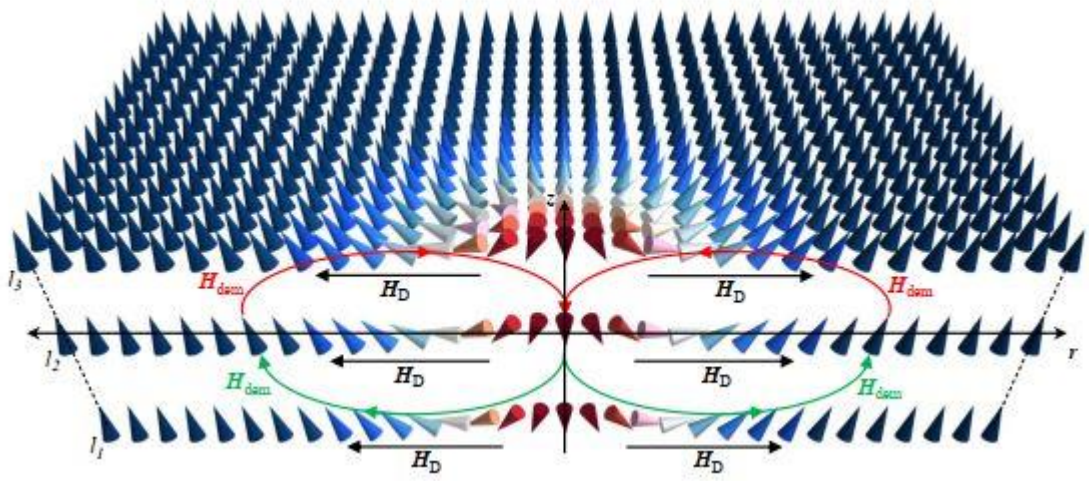

Figure R4: Schéma des interactions dipolaire et DM dans une multicouche accueillant un skyrmion magnétique. Les flèches noires représentent le champ du DMI qui agit uniformément dans l'échantillon, favorisant une chiralité CCW. Les flèches colorées représentent les boucles du champ dipolaire qui agissent sur les moments magnétiques. En vert, le champ démagnétisant favorise une chiralité CCW dans les couches les plus enterrées alors que les flèches rouges, symbolisant le champ démagnétisant dans les couches supérieures, promeuvent une chiralité CW

Dans la partie temps résolus de ce doctorat, plusieurs échantillons avec une texture de spin chirale ont été étudiés. Le premier est un échantillon composé d'une tri-couche Pt(3)/Co(1.5)/Al(1.4) (nm), ayant une anisotropie magnétique perpendiculaire (PMA) au plan de l'échantillon, répétée cinq fois and optimisée pour avoir un DMI interfaciale élevé. Tous les résultats obtenus en temps résolus sur cet échantillon ont été obtenue en géométrie de réflexion (45°) et au seuil M_3 du cobalt (~20.6 nm) qui a une longueur d'atténuation faible (~9 nm) dans le cobalt et le platine. Par conséquent, seule la couche magnétique la plus en surface sera sondée. Malgré la chiralité hybride de notre échantillon, seul une couche magnétique est sondée permettant l'analyse du motif de diffraction avec une interférence des couches du dessous négligeable. L'échantillon a été étudié avec une texture labyrinthique des domaines magnétiques. L'évolution des signaux DIFFERENCE et SOMME avec le temps révèle une désaimantation plus importante ainsi qu'une ré-aimantation plus rapide de la DIFFERENCE que de la SOMME que ça soit à des temps de quelques picoseconde mais aussi de quelques nanosecondes. Ce résultat confirme ce qui a été trouvé en premier lieu par Kerber *et al.*[3]

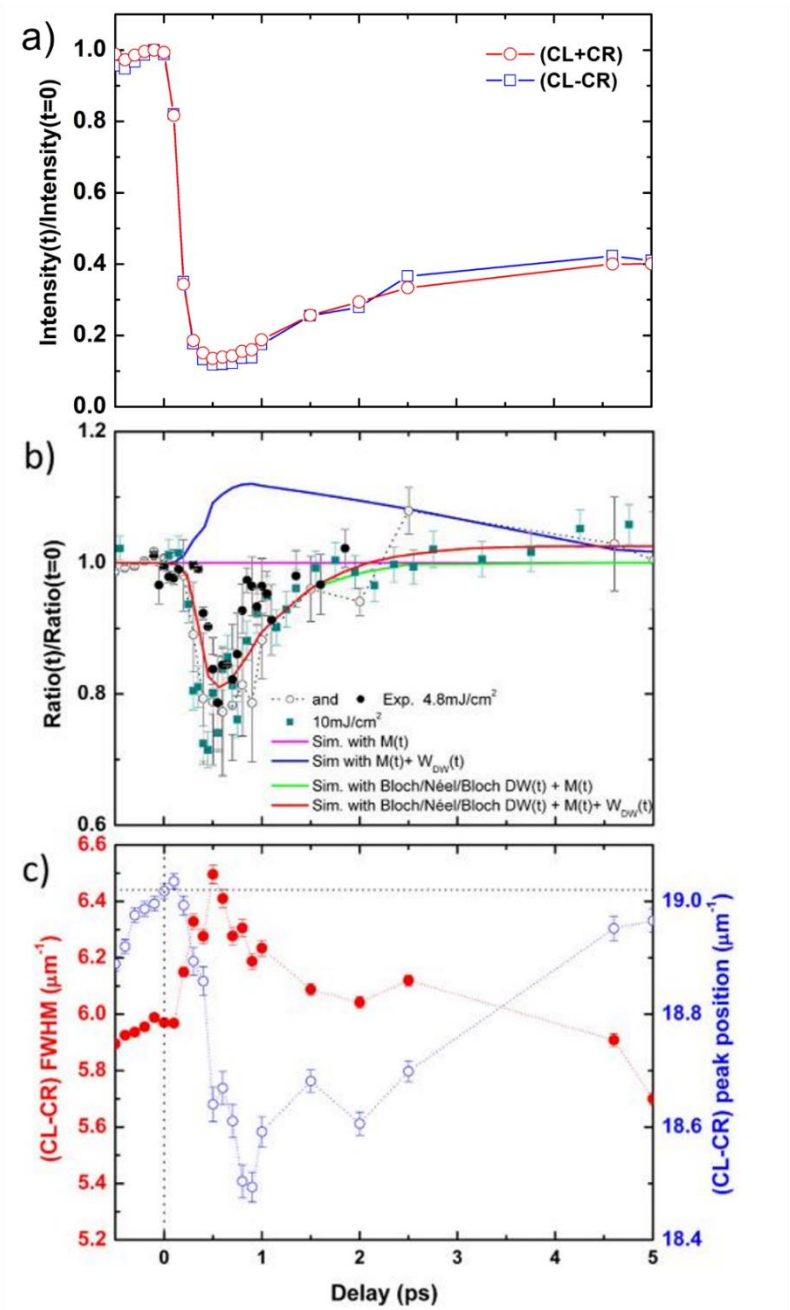

Figure R5: (a) Intégration du signal magnétique dans l'anneau de diffraction dans l'image SOMME (CL + CR) ainsi que dans l'image DIFFERENCE (CL – CR). (b) Ratio asymétrique (DIFFERENCE/SOMME) normalisé obtenu des données expérimentales mentionnées précédemment (cercles vides) ainsi que de deux autres balayages en temps effectués à la même fluence laser (4.8 mJ/cm², cercles noirs) et l'autre à une fluence plus élevée (10 mJ/cm², cercles cyans). Les lignes colorées sont des simulations effectuées avec différents modèles. En rose, le modèle considère une désaimantation similaire entre les DWs et les domaines. En bleu, le modèle reprend la même base que précédemment mais y ajoute une expansion des parois de domaines. En vert, la simulation prend en compte l'effet des électrons chauds polarisés en spin sur l'aimantation des DWs (expliquer plus en détail ci-dessous). En rouge, la simulation reprend le modèle vert mais y ajoute une expansion des DWs. (c) Evolution de la largeur à mi-hauteur du pic (FWHM) représentée par les points rouges ainsi que de la position du maximum du pic dans l'espace réciproque (cercles bleus vides).

Ce résultat est reproductible et peut être expliqué par un modèle reposant sur la génération d'électrons chauds polarisés en spin venant des domaines situés des deux côtés des DWs. Les domaines magnétiques de part et d'autre des DWs sont opposés en polarisation de spin. Le

spin des électrons chauds interagit avec l'aimantation locale dans les DWs et induit un couple $\boldsymbol{\tau} \propto \boldsymbol{m} \times \boldsymbol{s}$, avec $\boldsymbol{m}$ l'aimantation local dans le DW et $\boldsymbol{s}$ le spin de l'électron chaud. Le couple devrait avoir deux effets. Le premier est un effet incohérent due à l'émission isotrope des électrons chauds qui cause un désordre des moments magnétiques dans les DWs, augmentant « la température effectives » des spin dans la paroi. L'autre effet (cohérent) vient des électrons chauds venant perpendiculairement aux DWs. Il induit une précession différente des spins en dehors du plan de rotation de l'aimantation initiale du DWs, opposée de chaque coté du DWs. Du fait de la réduction de l'énergie d'échange dans les niveaux excités *s-p* par rapport aux niveaux *d*, l'angle de précession hors du plan du DW peut atteindre ~10° dans le régime ultra-rapide et devrait rester pendant quelques picosecondes.

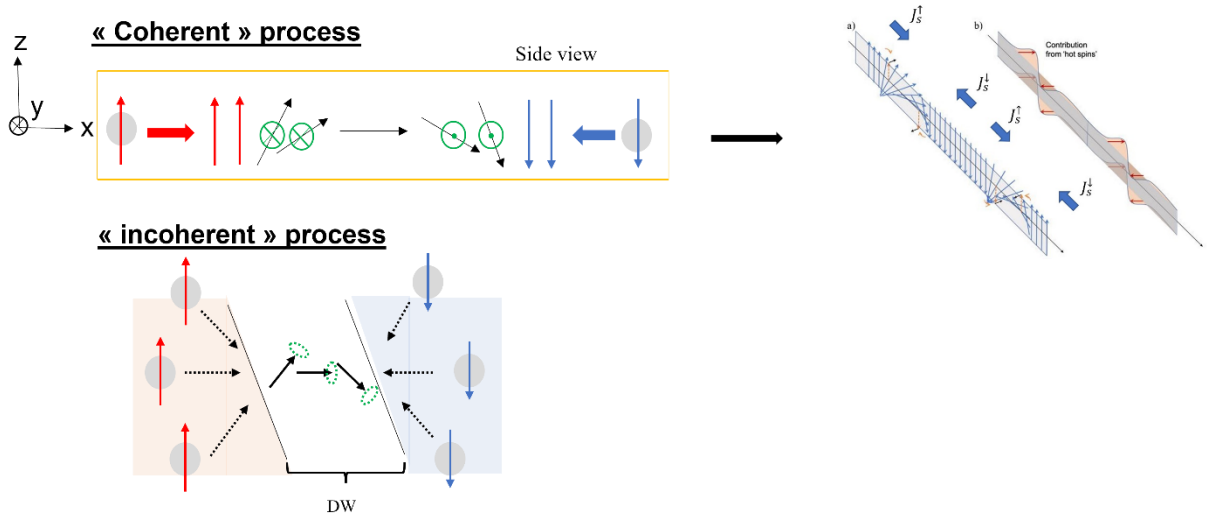

Figure R6: Schéma des processus induit par les électrons chauds polarisés en spin venant des domaines.

Dans notre cas, il n'est pas possible de déterminer la prédominance d'un processus sur l'autre. Cela nécessiterait l'observation d'un ordre de diffraction plus grand (ordre 3, 5…) hors du spéculaire car chaque processus affecterait différemment l'intensité des pics de diffraction suivant leur ordre. La position du maximum du pic magnétique dans l'espace réciproque indique la périodicité de la texture magnétique. Dans notre cas, une augmentation de 2.6% peut être constatée à l'échelle ultra-rapide. Un résultat similaire a été obtenu par Pfau *et al.*[4] en 2012 sur un échantillon avec empilement symétrique de Co/Pt étudié en transmission avec des domaines magnétiques dans un état labyrinthique. D'autres études ont trouvé un changement à l'échelle de la picoseconde[5] après l'impulsion laser ou alors aucun changement de la position du pic dans des échantillons avec des domaines labyrinthique ou en bande[6,7], respectivement[8].

A des délais de plusieurs centaines de picoseconde, une oscillation de 6 GHz dont l'amplitude s'atténue avec le temps est observé dans l'intensité du signal SOMME mais aussi dans la position du pic de la DIFFERENCE et de la SOMME. L'intensité diffractée est proportionnelle au carré de l'aimantation, ce qui donne une fréquence d'oscillation de 3 GHz de l'aimantation. L'origine de cette oscillation a été explorée par MOKE résolue en temps (tr-MOKE) et par résonance ferromagnétique à réseau d'analyseur vectoriel (VNA-FMR). Aucune oscillation

n'a été trouvée dans le signal magnétique du tr-MOKE. Dans la courbe de réflectivité, une oscillation correspondant aux modes de phonon théoriques de la multicouche a été observée. La mesure par VNA-FMR montre une fréquence de 15 GHz à rémanence, corroborée par le calcul des modes d'oscillation attribuable aux domaines. La mesure de VNA-FMR a été effectuée à température ambiante alors qu'à des temps de l'ordre de la nanoseconde, toute la chaleur de l'impulsion laser n'a pas été évacuée. Cependant, cela ne peut expliquer un si grand écart de fréquence.

Sur le même échantillon, l'effet de la polarisation circulaire de la pompe a été exploré (jusqu'alors, la pompe était polarisée linéairement). Aux fluences les plus faibles (8.5 mJ/cm²), aucun changement n'est observé entre CL_{IR} et CR_{IR}. A des fluences plus grandes (13 & 21 mJ/cm²), les courbes DIFFERENCE et SOMME obtenues avec la polarisation de la pompe CL_{IR} sont inférieurs en intensité que celles obtenues avec CR_{IR}. Le résultat est reproductible mais la même étude avec un échantillon de chiralité opposée doit être faite afin de conclure sur l'origine de cet effet. Néanmoins, les rapports d'asymétrie (DIFFERENCE/SOMME) sont égaux pour CL_{IR} et CR_{IR} à fluence égale, ce qui indique de la séparation des courbes résultat de la plus grande absorption de CL_{IR} par rapport à CR_{IR}. On suspecte que cet effet pourrait être due à une absorption plus forte de la polarisation circulaire quand celle-ci tourne dans le même sens que la chiralité.

La dernière partie de ce travail de thèse se focalise sur des multicouches FM accueillant un état skyrmionique liquide. Cet état est nucléé en augmentant le champ extérieur hors du plan de l'échantillon depuis un état de domaines magnétiques labyrinthique. L'échantillon a été étudié en géométrie de transmission pour maximiser le rapport signal sur bruit. A des temps inférieurs à 5 ps, aucune différence n'est observée en champ. Cependant, à partir de ~20 ps, un décroît soudain de l'intensité diffractée par les domaines est observé avant sa stabilisation autour de 100 ps. L'intensité décroit d'autant plus que l'on augmente le champ appliqué. Ni la périodicité des domaines, via la position du pic, ni la largeur de ce pic ne change dramatiquement à ces temps-là. Par conséquent, un changement de texture magnétique est exclu. De même, l'ordre de réalisation des courbes ainsi que leur temps d'acquisition exclu un mécanisme de dégradation comme origine. L'origine de ce phénomène serait plutôt liée au changement de signe de l'anisotropie effective, passant d'un axe facile hors du plan à un axe dans le plan. Cela expliquerait la baisse de l'intensité diffracté car en géométrie de transmission, seule la composante de l'aimantation hors du plan participe au signal.

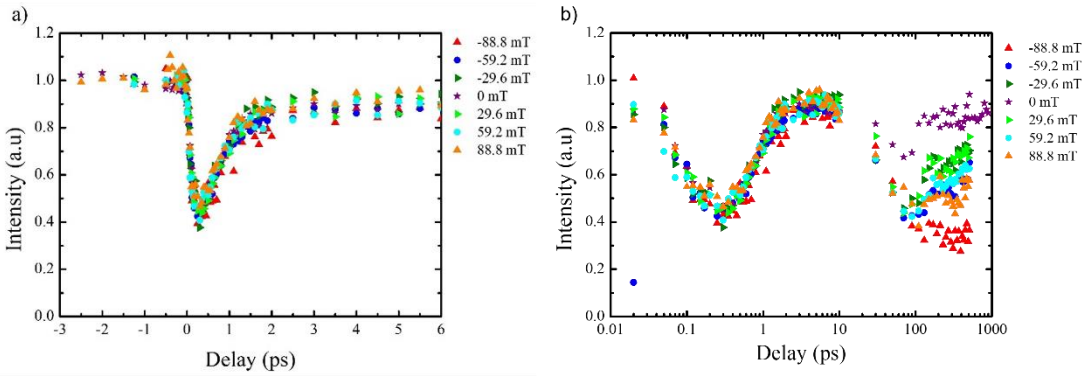

Figure R7: Graphiques des balayages temporels à différents champ appliqués hors du plan focalisés sur les temps ultra-rapide (a) et sur les temps sous la nanoseconde (b). Les balayages ayant la même valeur de champ en valeur absolue partagent la même forme de point.

Références :

1. Chauleau, J.-Y. *et al.* Chirality in Magnetic Multilayers Probed by the Symmetry and the Amplitude of Dichroism in X-Ray Resonant Magnetic Scattering. *Phys. Rev. Lett.* **120**, 037202 (2018).
2. Flewett, S. *et al.* General treatment of off-specular resonant soft x-ray magnetic scattering using the distorted-wave Born approximation: Numerical algorithm and experimental studies with hybrid chiral domain structures. *Phys. Rev. B* **103**, 184401 (2021).
3. Kerber, N. *et al.* Faster chiral versus collinear magnetic order recovery after optical excitation revealed by femtosecond XUV scattering. *Nat Commun* **11**, 6304 (2020).
4. Pfau, B. *et al.* Ultrafast optical demagnetization manipulates nanoscale spin structure in domain walls. *Nat Commun* **3**, 1100 (2012).
5. Zusin, D. *et al.* Ultrafast domain dilation induced by optical pumping in ferromagnetic CoFe/Ni multilayers. *arXiv:2001.11719 [cond-mat]* (2020).
6. Vodungbo, B. *et al.* Laser-induced ultrafast demagnetization in the presence of a nanoscale magnetic domain network. *Nat Commun* **3**, 999 (2012).
7. Hennes, M. *et al.* Laser-induced ultrafast demagnetization and perpendicular magnetic anisotropy reduction in a Co88Tb12 thin film with stripe domains. *PHYSICAL REVIEW B* 12 (2020).
8. Hagström, N. Z. *et al.* Symmetry-dependent ultrafast manipulation of nanoscale magnetic domains. *arXiv:2112.09587 [cond-mat]* (2021).